

**Glass and Jute fibers modified with CNT-based functional  
coatings for high performance composites**

**DISSERTATION**

zur Erlangung des akademischen Grades

Doktor rerum naturalium

(Dr. rer. nat.)

vorgelegt

der Fakultät Mathematik und Naturwissenschaften

der Technischen Universität Dresden

von

**Lazaros Tzounis**

**geboren am 02.12.1987 in Volos-Magnesia, Griechenland**

**Eingereicht am:** \_\_\_\_\_

Die Dissertation wurde in der Zeit von Dezember 2010 bis Dezember 2013 im Leibniz-Institut für  
Polymerforschung Dresden e.V. angefertigt







# Acknowledgements

It is very important to start first with a number of people who gave me an invaluable help for completing this research work, during the last three years. I feel cordially indebted towards these people and I would like to acknowledge them one by one, because without their contribution, this thesis would not come to the end.

First of all, I would like to express my sincere gratitude to my supervisor, Prof. Dr. Manfred Stamm, who has given me a strong and contributing guidance, as well as for providing me the opportunity to join his group and work in one of the most well-known institutes for polymer research in Europe (IPF). My grateful thanks and appreciation are also addressed to Prof. Dr. Edith Mäder for giving me a lot of inspiring ideas, for her guidance and her unfailing willingness to support me at every time throughout the whole period of my work. I should extend my sincere thanks to Dr. Martin Kirsten for his valuable suggestions and motivation at the early stages of my thesis.

I will use further the opportunity to acknowledge Dr. Petr Formanek who introduced me into the fantastic world of electron microscopy, and for his positive attitude to provide his help at any time it was needed. Mr. Michael Göbel is also acknowledged for the preparation of the FIB lamellae. I am very thankful also to Mr. Andreas Janke for training me with AFM, Dr. Frank Simon for conducting the XPS experiments, Dr. Dieter Jehnichen for XRD investigations, Dr. Dieter Fischer for Raman analysis, Mrs. Kerstin Arnhold and Mrs. Liane Häussler for TGA, Dr. Mikhail Malanin for FTIR and Mrs. Steffi Pressler for carrying out the single fiber pull-out tests.

I would like to extend my warm appreciation to Dr. Petra Pötschke, Dr. Jürgen Pionteck and Dr. Amit Das for several discussions and fruitful scientific advice during my PhD.

Last but not least, I would like to thank colleagues and friends from IPF, especially Mr. Marco Liebscher, Mr. Soumyadip Choudhury, Mr. Leonard Schellkopf, Mr. Niclas Wiegand, Mr. Guido-Sebastian Sommer, Dr. Roman Tkachov, and all fellow members of our group and whole IPF for their great cooperation. Besides that, I would like to thank my girlfriend Kristi for her patience, understanding, and for always being there for me all the time I was working on my thesis, even if I was not able sometimes to meet with her via Skype video-calls. I also thank all my dear family for their ungrudging emotions and

psychological support all these years, and friends from Greece for pushing me towards science, as well as friends here, in Dresden, for the very nice moments we spent together.

I am very thankful to our secretaries Mrs. Janett Forkel and Mrs. Nicole Crause for their excellent and immediate assistance in many cases.

Finally, I am deeply grateful to IPF Dresden for the financial support of this research work.

# Table of Contents

<b>List of Abbreviations and Symbols</b> .....	<b>9</b>
<b>Chapter 1 Introduction</b> .....	<b>12</b>
<b>Chapter 2 Theoretical background and literature overview</b> .....	<b>15</b>
2.1 Structure and properties of Carbon Nanotubes (CNTs).....	15
2.1.1 Introduction: Discovery of CNTs .....	15
2.1.2 Bonding of carbon atoms in carbon nanotubes.....	15
2.1.3 Structure and types of CNTs.....	16
2.1.4 Electronic properties of CNTs .....	18
2.1.5 Applications of CNTs .....	20
2.1.6 CNTs in polymer composites.....	20
2.2 Nanoparticles and their physicochemical properties.....	22
2.2.1 Silica nanoparticles (SiO <sub>2</sub> NPs) .....	22
2.2.2 Silver nanoparticles (Ag NPs).....	24
2.2.2.1 Origin of surface plasmon resonance (SPR) .....	25
2.2.2.2 SERS effect and SERS substrates.....	27
2.2.2.3 Synthetic routes for preparation of silver nanoparticles ....	32
2.3 Block copolymer (BCP) nanostructures .....	35
2.4 Fiber Reinforced Polymer Composites (FRPCs) .....	37
2.4.1 Fibers used to reinforce a polymer matrix .....	38
2.4.2 Polymer matrices .....	42
2.4.3 Interphase between fiber and matrix and interfacial interactions ...	44
<b>Chapter 3 Experimental techniques</b> .....	<b>47</b>
3.1 Analytical methods .....	47
3.1.1 Fourier transform infrared spectroscopy (FT-IR) .....	47
3.1.2 Raman and Surface-enhanced Raman spectroscopy.....	47
3.1.3 Ultraviolet-visible spectroscopy (UV-vis).....	52
3.1.4 Electrokinetic analysis .....	52
3.1.5 Thermogravimetric analysis (TGA).....	52
3.1.6 X-ray Photoelectron spectroscopy (XPS) .....	53
3.2 Atomic force microscopy (AFM) .....	53
3.3 Scanning electron microscopy (SEM) .....	55

3.4	Transmission electron microscopy (TEM).....	55
3.5	Electrical resistance measurements.....	56
<b>Chapter 4</b>	<b>Synthesis and properties of nano-sized colloidal systems.....</b>	<b>57</b>
4.1	Chemical modifications of carbon nanotubes (CNTs).....	57
4.1.1	Acid treatment of MWCNTs .....	57
4.1.2	Grafting of MWCNTs with Polystyrene (PS) chains.....	59
4.2	Synthesis of silica spheres (~120 nm).....	59
4.3	Synthesis of silica@silver hybrid particles for SERS and catalytic applications .....	60
4.3.1	Decoration of SiO <sub>2</sub> spheres with Ag seeds (SiO <sub>2</sub> @Ag-seed) .....	61
4.3.2	Silver growth using SiO <sub>2</sub> @Ag-seed as templates .....	61
4.3.3	Characterisation techniques .....	62
4.3.4	Results and discussion .....	64
4.3.4.1	Fourier transformed infrared spectroscopy (FT-IR) .....	64
4.3.4.2	Zeta potential measurements.....	65
4.3.4.3	UV-vis spectroscopy of SiO <sub>2</sub> and SiO <sub>2</sub> @Ag particles.....	66
4.3.4.4	XRD of SiO <sub>2</sub> @Ag nanohybrids.....	67
4.3.4.5	Electron microscopy investigations .....	67
4.3.4.6	SERS experiments .....	68
4.3.4.7	Catalytic reduction of 4-nitrophenol to 4-aminophenol.....	70
4.4	Synthesis of superparamagnetic Fe <sub>3</sub> O <sub>4</sub> nanoparticles .....	74
<b>Chapter 5</b>	<b>Epoxy/BCP nanostructured thermosetting materials.....</b>	<b>75</b>
5.1	Introduction.....	75
5.2	Experimental part.....	77
5.2.1	Materials .....	77
5.2.2	Synthesis of P2VP-b-PMMA.....	77
5.2.3	Synthesis of the ionic liquid block copolymer.....	79
5.2.4	Synthesis of paramagnetic ionic liquid block copolymer .....	79
5.2.5	Protocol for blending epoxy and PIL block copolymer .....	80
5.2.6	Experimental techniques .....	80
5.3	Results and discussion .....	82
<b>Chapter 6</b>	<b>Epoxy/Glass fiber nanostructured interphases .....</b>	<b>91</b>
6.1	The interphase microstructure and electrical properties of glass fibers covalently and non-covalently bonded with multiwall carbon nanotubes .....	91
6.1.1	Introduction.....	92



6.1.2	Experimental .....	94
6.1.2.1	Materials .....	94
6.1.2.2	Glass fiber cleaning – silanisation treatment .....	95
6.1.2.3	MWCNT functionalization .....	95
6.1.2.4	Deposition of MWCNTs onto single glass fibers via chemical or physical bonds .....	96
6.1.2.5	Characterization techniques .....	97
6.1.3	Results and discussion .....	101
6.1.3.1	MWCNT analysis .....	101
6.1.3.2	XPS analysis .....	101
6.1.3.3	Glass fiber surface microstructures.....	105
6.1.3.4	TEM interphase microstructures of single fiber composites .....	107
6.1.3.5	Electrical properties of single MWCNT-coated glass fibers and single fiber composites.....	109
6.1.3.6	Interfacial adhesion properties.....	112
6.2	MWCNT-grafted glass fibers as a smart tool for the epoxy cure monitoring, UV-sensing and thermal energy harvesting .....	115
6.2.1	Introduction.....	116
6.2.2	Experimental .....	119
6.2.2.1	Materials .....	119
6.2.2.2	Chemical grafting of MWCNTs onto the GF surface.....	120
6.2.3	Characterization techniques .....	121
6.2.3.1	Scanning and Transmission electron microscopy (SEM, TEM).....	121
6.2.3.2	Electrical resistance and conductivity measurements .....	121
6.2.3.3	In-situ cure monitoring of epoxy using the GF-CNT smart tool .....	122
6.2.3.4	Thermal analysis of the resin cure by differential scanning calorimetry (DSC).....	123
6.2.3.5	Rheology .....	124
6.2.3.6	UV-sensing .....	124
6.2.3.7	Thermoelectric energy harvesting.....	124
6.2.3	Results and discussion .....	125
6.2.3.1	Surface morphology of MWCNT-grafted glass fibers ....	125

6.2.3.2	Single fiber composite interphase microstructure.....	126
6.2.3.3	Epoxy cure monitoring and position detection using the GF-CNT sensor .....	127
6.2.3.4	UV sensing properties.....	130
6.2.3.5	Electrical resistance and conductivity of GF-CNT and GF-CNT/epoxy composites.....	131
6.2.3.6	Thermoelectric power generation .....	134
6.2.3.4	UV sensing properties.....	136
<b>Chapter 7</b>	<b>Jute fibers covered with CNT-networks as hybrid fillers for the reinforcement of a natural rubber matrix .....</b>	<b>137</b>
7.1	Introduction.....	140
7.2	Experimental .....	140
7.2.1	Materials .....	140
7.2.2	Purification and functionalization of MWCNTs.....	140
7.2.3	Jute fiber alkali treatment and deposition of MWCNTs .....	141
7.2.4	Preparation of NR/a-JF and NR/JF-CNT composites.....	142
7.2.5	Characterisation techniques .....	144
7.3	Results and Discussions .....	144
7.3.1	Infrared spectroscopy (FT-IR) .....	145
7.3.2	Raman spectroscopy .....	146
7.3.3	Thermogravimetric analysis (TGA).....	147
7.3.4	Contact angle measurements.....	148
7.3.5	Electron microscopy investigations .....	151
7.3.6	Cure and physical properties of NR and NR/JF composites.....	156
7.3.7	Dynamic mechanical thermal analysis of NR and NR/JF composites .....	159
<b>Chapter 8</b>	<b>General Conclusions and Outlook.....</b>	<b>159</b>
	<b>References .....</b>	<b>161</b>
	<b>Full list of publications and contribution to conferences.....</b>	<b>174</b>

## List of abbreviations and symbols

AgNO <sub>3</sub>	Silver nitrate
Ag NPs	Silver nanoparticles
AFM	Atomic force microscopy
ASTM	American society for testing and Materials
ATRP	Atom Transfer Radical Polymerization
BCP	Block copolymer
C-AFM	Conductive Atomic Force Microscopy
CNT/CNTs	Carbon nanotube(s)
CTAB	Cetyltrimethylammonium bromide
CVD	Chemical vapour deposition
DC, dc	Direct current
DGEBA	Diglycidyl ether of bisphenol-A
DMTA/DMA	Dynamic mechanical (thermal) analysis
DMSO	Dimethyl sulfoxide
DSC	Dynamic scanning calorimetry
EFM	Electric force microscopy
EFTEM	Energy-filtered transmission electron microscopy
EKA	Electrokinetic analysis
Fe(acac) <sub>3</sub>	Iron (III) acetylacetonate
Fe <sub>3</sub> O <sub>4</sub>	Iron oxide
FFT	Fast Fourier Transform
FIB	Focused ion beam
FT-IR	Fourier transform infrared spectroscopy
GFRP/GFRPs	Glass fiber reinforced polymer(s)
GF/GFs	Glass fiber/Glass fibers
GF-ad-CNT	Glass fibers adsorbed CNTs
GF-g-CNT/GF-CNT	Glass fibers chemically grafted with CNTs
GPC	Gel Permission Chromatography
H-T	Halpin-Tsai model
IEP	Isoelectric point
IFS	Interface friction strength
IFSS	Interfacial shear strength
JF/JFs	Jute fiber/Jute fibers
JF-CNT	Jute fibers coated with CNTs

KBr	Potassium bromide
KCl	Potassium chloride
LSPR	Localized surface plasmon resonance
Mn	Number average molecular mass
Mw	Weight average molecular mass
MWNTs/MWCNTs	Multi-walled carbon nanotube(s)
NaBH <sub>4</sub>	Sodium borohydride
NaOH	Sodium hydroxide
NP/NPs	Nanoparticle(s)
NR	Natural rubber
ODT	Order-disorder transition
PDI	Polydispersity index
PEI	Polyethyleneimine
PMMA	Polymethyl methacrylate
PS	Polystyrene
P2VP	Poly(2-vinylpyridine)
P4VP	Poly(4-vinylpyridine)
PS-b-P2VP	Poly(styrene-block-2-vinylpyridine)
PS-b-P4VP	Poly(styrene-block-4-vinylpyridine)
RMS	Root-mean-square roughness of the surface
RT	Room temperature
R6G	Rhodamine
SAXS	Small-angle X-ray scattering
SD	Standard deviation
SEF	Surface enhancement factor
SEM	Scanning electron microscopy
SERS	Surface enhanced Raman spectroscopy
SE2	Secondary electron detector
SPM	Scanning probe microscopy
SPR	Surface plasmon resonance
SiO <sub>2</sub>	Silica or Silicon dioxide
SiO <sub>2</sub> @Ag	Silica spheres decorated with silver dots
SiOH	Silanol or Silicon hydroxide
SWCNTs	Single-walled carbon nanotube(s)
T	Thermodynamic (absolute) temperature

$T_g$	Glass transition temperature
TEM	Transmission electron microscopy
TEMPO	2,2,6,6-Tetramethyl-piperidin-1-oxyl
TEOS	Tetraethyl orthosilicate
TGA	Thermogravimetry or thermogravimetric analysis
THF	Tetrahydrofuran
TM	Tapping Mode
UV-vis	Ultra-violet visible spectroscopy
XPS	X-Ray photoelectron spectroscopy
XRD	X-Ray Diffraction
ZP	Zeta-potential
$\gamma$ -APS/3-APS	gamma- or 3-aminopropyltriethoxysilane
4-Nip/4-Amp	4-Nitrophenol/4-Aminophenol
$\vec{a}$	Unit vectors of the hexagonal lattice
$\vec{C}_h$	Chiral vector
$V_f$	Fiber volume fraction
$\theta$	Chiral angle
$d$	Fiber diameter
$\tau$	Interfacial shear strength (IFSS)
$\alpha$	The degree of conversion or degree of cure during isothermal cure
$\alpha_R$	Electrical degree of cure
$R_0$	The initial resistance of the specimen
$e$	Electronic charge
$\mu$	The mobility of charge carriers for a percolating CNT-network
$\rho$	Specific volume electrical resistivity
$\sigma$	Electrical conductivity

## Introduction

**Motivation:** Carbon nanotubes are known as one of the strongest materials in nature and since their discovery; they have triggered the scientific interest for fabricating multi-functional polymer composites. However, a well-known problem associated to the incorporation of nanoparticulate materials in polymer matrices is their tendency to agglomerate in order to reduce their surface energy, and the extreme increase of the polymer viscosities (i.e melts, solutions, etc), which makes it very difficult to process them. Polymers can be efficiently reinforced by fibers for applications where high strength and stiffness are required. Micro-scale short fiber reinforced polymer composites have been an alternative way to obtain fiber reinforced composites since the long fiber incorporation is a painful job and not always feasible and easy to produce composites in big scale. Therefore, use of long glass fibers as the support for depositing CNTs as well as CNTs+other kind of nanoparticles was made, and the resulting interfaces were investigated in detail by single fiber model composites. This approach can bring the CNT functionality, fiber strength and toughness to the final composite, and simultaneously alleviate the manufacturing process from increase of the polymer high viscosities. Finally, very logically the question of whether to improve or destroy the interface integrity comes before implementing the hybrid hierarchical reinforcements in bigger scales, and an output out of this work will be given. Furthermore, several information and functionalities arising from the CNTs at the interphase region will be elucidated like cure monitoring of the epoxy resin matrix, UV-sensing ability, and thermoelectric energy harvesting, giving rise to multi-functional structural composites. CNT-modified natural fibers also have been utilised to fabricate short fiber reinforced composites, and have shown a promising reinforcement effect due to the CNT nanostructured interfaces.

The ‘interface’ in fiber reinforced polymer composites (FRPCs) is known as a very crucial parameter that has to be considered in the design of a composite with desired properties. Interfaces are often considered as surfaces however, they are in fact zones or areas with compositional, structural, and property gradients, typically varying from that of the fiber and the matrix material. Characterization of the mechanical properties of interfaces is necessary for understanding the mechanical behavior of scaled-up composites. In fact, the mechanical characteristics of a fiber/resin composite depend mainly on *i*) the mechanical properties of the component materials, *ii*) the surface of the fiber, and *iii*) the nature of the fiber/resin bonding as well as the mode of stress transfer at the interface. Among the many factors that govern the characteristics of composites involving a glass, carbon, natural or ceramic fiber, and a macromolecular matrix, the adhesion between fiber and matrix plays a

predominant role. In specific, the stress transfer at the interface requires an efficient coupling between fiber and matrix. Therefore, it is important to optimize the interfacial bonding since a direct linkage between fiber and matrix gives rise to a rigid, low impact resistance composite material.

**Aims & objectives:** The main aims and objectives of this study are summarized within the bullets indicated below:

- Modify the surface of conventional fibers (glass and jute) with MWCNTs, and incorporate them in a polymer matrix.
- Strengthen the composite interfaces by the use of MWCNTs.
- Investigate the composite interfacial adhesion strength by single fiber model composites.
- Provide the CNT- and/or any other kind of desired functionality in the composite by depositing CNTs and/or different kind of nanoparticles on the fiber surface. Create hierarchical structures and hybrid composite multi-functional interfaces.
- Use the fiber/CNT reinforcement as a smart tool for providing information about the structure (epoxy cure state) and the health condition of the composite (UV-sensing).
- Use the densely packed CNT-networks at the interface region for the effective thermoelectric energy harvesting, upon exposition of the composite to a temperature gradient.
- Use the CNT-coated fibers as support for depositing superparamagnetic  $\text{Fe}_3\text{O}_4$  nanoparticles via ionic interactions, endowing the fibers with increased conductivity and showing a response to an external magnetic field; potential applications: *i*) recyclable fibers, *ii*) electromagnetic shielding effectiveness, *iii*) data storage, *iv*) magnetic strain sensor showing the existence of cracks or voids at the interface region which can accumulate resulting further in the materials' failure.
- Incorporate a big amount of nano-scale filler in the final composites using the fiber as the agent/support to immobilize any kind of different nanoparticles.

**Thesis outline:** The first chapter provides an introduction to the structure and properties of CNTs as well as their use in polymer composites. In chapter 2, the theoretical background about the physicochemical properties of colloids which have been used in this thesis are also provided, whereas rare information about block copolymers is also given because BCPs can successfully induce nanostructuring to an epoxy, used as the matrix throughout this thesis. The definition and classification of fiber reinforced polymer composites (FRPCs) are

described as well in this chapter and special focus is given to make understandable the big importance of the ‘interphase’ in composite materials. In the next chapter (chapter 3), all the experimental techniques used within this thesis are described, and their principles are briefly explained. The chapter 4 deals with the chemical protocols we applied to synthesize different kinds of nanocolloids as well as their micro-structural and physical characterisation. Epoxy blended with BCP was prepared and their properties as well as special functionalities are discussed in chapter 5. Then, chapter 6 describes the anchorage of MWCNTs onto the GF surfaces via covalent and non-covalent bonds, and the resulting interphases in an epoxy matrix were extensively characterized. In addition, this chapter demonstrates the functionality of the hybrid interfaces which have been developed and discussed for the first time within the research accomplished within this thesis. Making use of the results we obtained on single fiber level of GF-CNT/epoxy model composite investigations regarding the strengthening of the composite interfaces, we extended the idea of CNT-modified fibers, and especially natural fibers, in order to effectively reinforce a natural rubber matrix (chapter 7). The final, chapter 8 presents the general conclusions and gives an outlook for future work.



## Chapter 2

### Theoretical background and literature overview

#### 2.1 Structure and properties of Carbon Nanotubes (CNTs)

##### 2.1.1 Introduction: Discovery of CNTs

Since the discovery of closed graphite shells dubbed buckminsterfullerene by Kroto *et al.* [2] in 1985, carbon has started to obtain a significant interest in nanoscale science including chemistry, biology and engineering. Carbon Nanotubes were first discovered around 1952 by Radushkevich *et al.* [3] and possibly have been around for much longer. However, it is only after Iijima's observation of CNTs in 1991, which gave rise to an extreme interest from the scientific community all over the world for many wide-ranging disciplines. [4]

##### 2.1.2 Bonding of carbon atoms in carbon nanotubes

The structure of a carbon nanotube can be thought as a single graphene sheet rolled up into a cylinder, as illustrated in Fig. 2.1.

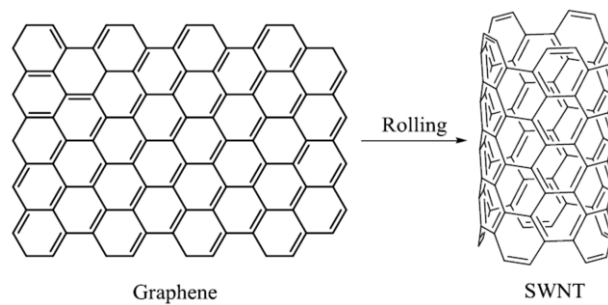


Fig. 2.1 - Schematic view of carbon nanotube structure derived from a rolled up graphene sheet.<sup>[1]</sup>

CNTs can be considered as long seamless cylinders consisting of an hexagonal honeycomb lattice of carbon atoms, the ends of which can either be capped by two halves of fullerene or left open. A carbon atom has six electrons of which two are accommodated in the 1s orbital and the remaining four occupy the 2s and 2p orbitals, responsible for bonding. CNTs have deformed  $sp^2$  hybridization due to the circular curvature [5], and this causes the shifting of the three  $\sigma$  bonds which lie in the  $sp^2$  plane to out of plane. As a result the  $\pi$

<sup>[1]</sup> [http://eed.gsfc.nasa.gov/562/SA\\_CarbonNanotubes.htm](http://eed.gsfc.nasa.gov/562/SA_CarbonNanotubes.htm)

orbital is more delocalized outside to compensate as shown in Fig. 2.2. This type of symmetry change in the  $sp^2$  orbital makes nanotubes chemically more reactive, mechanically more strong, and electrically and thermally more conductive than graphite. [5]

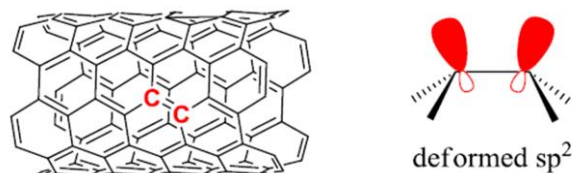


Fig. 2.2 - Schematic representation of C-C bond in single-walled carbon nanotube framework. [2]

Additionally, they produce topological defects such as pentagons and heptagons in the hexagonal network to form capped bent, toroidal, and helical nanotubes where electrons are localized in pentagons and heptagons because of redistribution of  $\pi$  electrons. [5] There can also be  $sp^3$  hybridized carbons, formed from the carbon framework due to oxidation, which can result in the formation of terminal esters, anhydrides and carboxylic acid groups at the open end of nanotubes, as illustrated in Fig. 2.3.

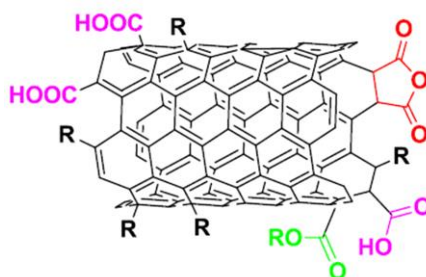


Fig. 2.3 - A schematic illustration of possible surface defects in a SWNT (R=alkyl). [2]

### 2.1.3 Structure and types of CNTs

It has been reported that the CNTs have extraordinary mechanical, thermal and electrical properties, and especially the electrical ones are highly related to the structure of CNTs. [6] With respect to the rolling angle of the graphene sheet, CNTs can have chiral and non-chiral configurations. For a unique definition of the structure of a particular nanotube, one needs to define a chirality vector, in terms of integer multiples of two primitive lattice parameters of graphene, that exactly maps the circumference of the nanotube. This chirality vector,  $C_h$ , is used to describe the chirality of the tube and it is defined as:

[2] [http://theses.dur.ac.uk/390/1/PhD\\_Thesis\\_MK\\_BAYAZIT\\_Chemistry\\_2010.pdf?DDD7+](http://theses.dur.ac.uk/390/1/PhD_Thesis_MK_BAYAZIT_Chemistry_2010.pdf?DDD7+)

$$\mathbf{C}_h = n\mathbf{a}_1 + m\mathbf{a}_2 \quad (2.1)$$

where  $\mathbf{a}_1$  and  $\mathbf{a}_2$  are the unite factors,  $n$  and  $m$  (integers) are the steps along the directions showed in Fig. 2.4 of the original graphene lattice. [7] If the graphene sheet is cut along the vertical direction of the vector  $\mathbf{C}$ , and rolled up into a cylinder, the tube can be defined as  $(n,m)$ . When  $n=m$  or  $m=0$ , the nanotube is symmetric and these nanotubes are named as armchair and zig-zag, respectively (Fig. 2.4). When  $n-m$  is a multiple of 3, the tube is metallic; otherwise, the tube is a semiconductor. [8] For the non-chiral configurations, two carbon-carbon atoms (C-C) on opposite sides of a hexagon may lie perpendicular to the tube axis (armchair) or parallel to the tube axis (zig-zag), while chiral configurations are defined as those that display any other angle. Illustrations are provided in Fig. 2.4.

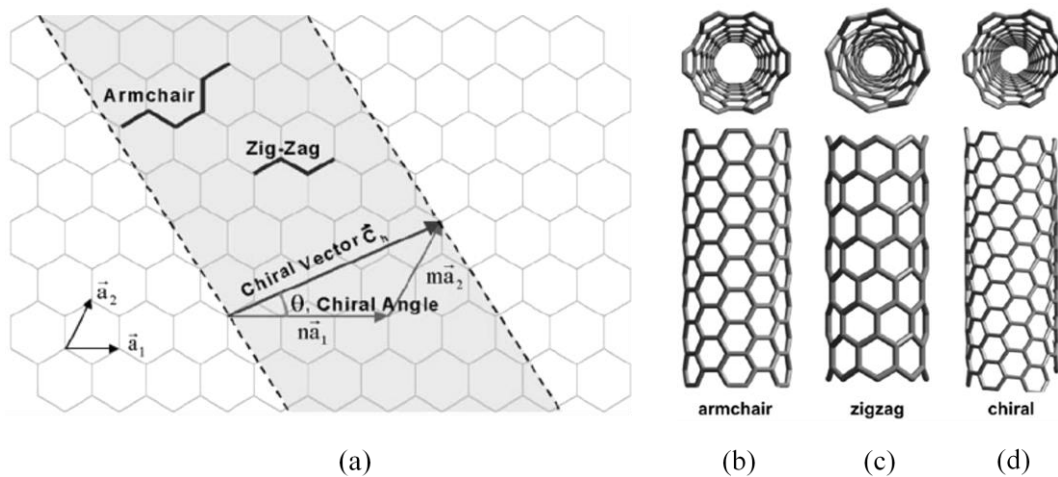


Fig. 2.4 - Schematic diagram showing the possible ways that an hexagonal graphene sheet can be rolled into a CNT along the chiral vector [7], and molecular models of SWNTs exhibiting different chiralities, (b) armchair  $(m, m)$  configuration, (c) zig-zag  $(n,0)$  arrangement and (d) chiral  $(n,m)$  conformation [9].

As reviewed by Terrones [9], the chiral vector may be used to determine the diameter of the tube according to the formula:  $d = \frac{a\sqrt{m^2+mn+n^2}}{\pi}$ , where  $a$  is the graphite sheet lattice constant ( $1.42 \times \sqrt{3}$  Å), and  $m$  and  $n$  are the lattice coordinates.

Carbon nanotubes can be divided into two groups depending on the number of their walls: single-walled carbon nanotubes (SWNTs) and multi-walled carbon nanotubes (MWNTs). The SWNTs have only one layer of graphene wall, and the MWNTs have two or several concentric

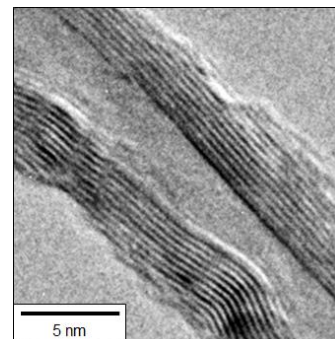
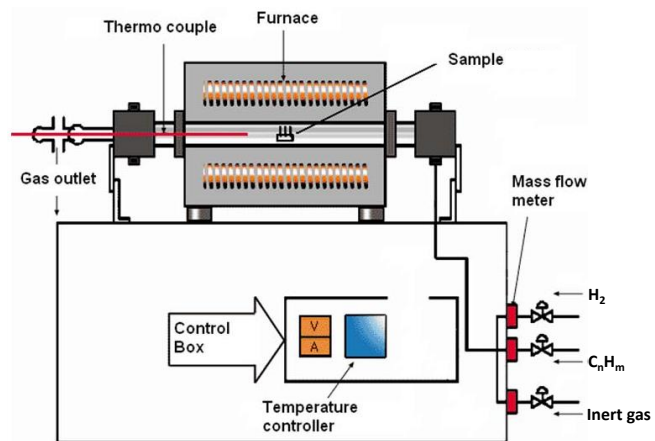


Fig. 2.5 – HR-TEM image of single MWNT showing the concentric walls.

cylinders of increasing diameter placed around a central axis (Fig. 2.5), binded together by the effect of Van der Waals forces. [4] The spacing between each shell is in the order of the spacing between two adjacent layers in graphite ( $3.4 \text{ \AA}$ ). [10] The typical diameter of SWNTs is in the range of 0.6-2 nm, while for MWNTs about 10-50 nm. The length of a CNT can range from 1 micron to tens of microns, depending on the type of CNTs or the production method.

CNTs can be produced by many different methods and each method has its own advantages and disadvantages in terms of cost and quality. Four major production methods have been widely used: arc discharge [11], laser ablation [12], high pressure CO conversion [13] and the chemical vapour deposition (CVD). [14] [1] Due to the simplicity of its production setup, the low costs and relatively high purity of the end product, the CVD technique (Fig. 2.6) has become the main technology for mass production of MWNTs.



**Fig. 2.6 – Schematic diagram for the CVD growth method. Hydrocarbon gas is decomposed in a quartz tube in a furnace over a transition metal catalyst (a CVD reactor) [1].**

#### 2.1.4 Electronic properties of CNTs

The electronic properties of CNTs have received a wide research interest for being utilised in specific applications. According to both experimental and theoretical results, SWNTs can be considered as either metallic or semiconducting depending on the wrapping angle of the graphene sheet with regards to the tube axis. [15] [16] [17] [18] [19] [20] Fig. 2.7 displays the chirality map which shows the various types of SWNTs that can be formed. The extraordinary and unique dependence of electronic structure on chirality vector arises from the fact that, in a single graphene sheet, the conduction and valence bands just touch each other at the six corner points, called as Fermi points which are one particular electron state, of the hexagonal first Brillouin zone. The Fermi point refers to an event chirality of electrons involved, and the diameter of a carbon nanotube for which the nanotube becomes metallic. This unusual band structure has a direct impact on the electronic properties of

graphene making it a zero band gap semiconductor. However, when a graphene sheet is rolled into a SWNT, periodic boundary conditions are imposed in the circumferential and as a result, each band of graphene splits into a number of 1-D sub bands. The allowed energy states of the tube are the cuts of the graphene band structure. When these cuts pass through a Fermi point, the tube is metallic whereas if no cuts pass through a Fermi point, the tube is semiconducting. [21]

Calculations [15] [16, 17] [18] [19] reveal that all armchair tubes ( $n=m$ ) are conducting, while the other tubes, which are zigzag and chiral, are either small band gap semiconductors (as a consequence of curvature-induced mixing of  $\pi$  and  $\sigma$  states) if  $n-m=3i$ , or otherwise truly semiconducting with larger band gaps if  $n-m \neq 3i$ , where ' $i$ ' is a non-zero integer. Theoretical calculations also predict that one third of the tubes are metallic and two thirds are semiconducting. [16] Scanning tunneling microscopy (STM) studies on SWNTs, by Wildöer [20] and Odom [22] confirm these predictions experimentally. However, CNTs are always produced as a mixture with a distribution of diameters and chirality and no method has so far been developed to synthesize individual nanotubes having the same chirality.

The electron transport property of MWNTs is more complicated than SWNTs. Each of its carbon shells can be metallic or semiconductive, depending on the chirality of the shell. At room temperature, the outer two shells will interact with each other and contribute to the conductance. [23] At low temperatures and low voltage bias, the current flows only through the outer shell. [24] Although the shells of the MWNT can be semiconductive, due to

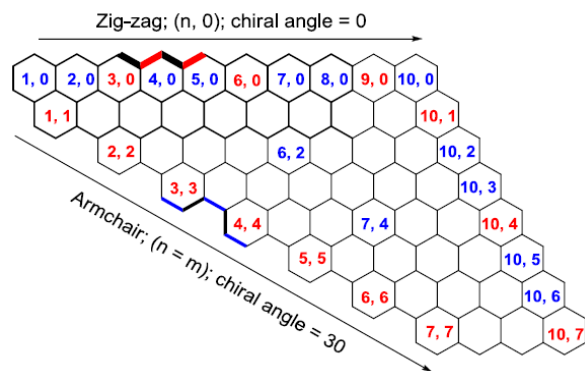


**Fig. 2.7 - Graphical representation of chirality map which displays the different types of SWNTs that can be formed via rolling a graphene sheet. SWNTs denoted by blue ( $n, m$ ) are semiconducting and red ( $n, m$ ) are metallic.**

the fact that the band gap of the nanotube is inversely proportional to the CNT diameter, the band gap for the outer two layers of the MWNT with a diameter about 10 nm is very small compared with semiconductive SWNTs. [23] Experimentally, both metallic and semiconductive behaviour have been observed for MWNTs, and tubes with more complex conduction behaviours have also been observed. [25] In conclusion, MWNT yarns or mats should behave as metallic at room temperature. The conductivity of a single MWNT has

been evaluated experimentally, ranging from  $10^5$ - $10^7$  S/m. [25] [26] Although it is still smaller than the conductivity of the gold or silver ( $10^8$  S/m), it is reaching the resistivity of the crystalline graphite,  $\sim 10^7$  S/m.

### 2.1.5 Applications of CNTs

Since their discovery, carbon nanotubes have attracted much interest due to their small dimensions, strength and their exceptional physical properties. Until now, they have been used in a wide range of scientific and industrial applications such as field-effect transistors, [27] [28] [29] nano-tweezers, [30] high resolution atomic probes, [31] chemical probes, [32] mechanical actuators, [33] hydrogen storage, [34] non-volatile random access memory, [35] field-emission displays, [36] data storage devices, [37] and chemical sensors. [38] Moreover, SWNTs are among the strongest materials known to exist in nature. Namely, SWNTs have a Young's modulus approximately 1 TPa and tensile strength nearly 50 GPa, which are greater than Young's modulus (200 GPa) and tensile strength (400 MPa) of stainless steel. [39] These values are in accordance with the in-plane values for graphite and with that of diamond, and also agree with theoretical calculations. [40] [41] Direct measurements performed by an AFM set-up in a scanning electron microscope also revealed similar values of tensile strengths of the order of 20 GPa. [42] Hence, nanotubes can tolerate large strain before mechanical failure [38] [43] [44] and in combination with their light weight, they are an ideal candidate for the reinforcement of polymer composites, [45-47] [48] [49] [50] [51] [52] in many applications such as the construction of aircraft, space-craft and building industry, [53] etc.

### 2.1.6 CNTs in polymer composites

The mechanical and electrical properties of CNTs render them as a very interesting material to reinforce polymer matrices as well as to obtain conductive polymer composites. When considering the potential applications of CNTs, important is to achieve a good dispersion of CNTs, or in other words obtaining individual CNTs instead of CNT aggregates. Depending on the production methods, the as produced CNTs have different aggregated morphologies. SWNTs produced by arc-discharge appear as yarns, while SWNTs or MWNTs produced by most of the CVD methods appear as random coils. These features result in difficulties in breaking down the CNT aggregates and obtaining individual CNTs. Apart from the intrinsic interaction between the adjacent CNTs in the yarns, or entanglements of the CNT in the coils, the poor compatibility between CNTs and many polymers or solvents is also found to be a big obstacle for obtaining individual CNTs in

solutions or composites. One of the solutions is to covalently or non-covalently attach small molecules or even polymer chains to the CNT sidewalls in order to improve their compatibility with polymer matrices. This method is called chemical functionalization of CNTs. Various kinds of molecules can be attached to the CNT side walls [54] [55] [56]. Banerjee *et al.* summarized various possibilities of covalent functionalization of SWNTs, which is shown in Fig. 2.8. [54] These treatments were proved to improve the dispersion of the CNTs in solutions. [57] Since the discovery of CNTs, the production volume of various kinds of CNTs has been dramatically increased. Several major producers have scaled up their CVD MWNT productions to the level of tons/year. This enables researchers to take CNT research to a semi-industrial scale. The price of the CVD MWNTs with a diameter of ~10 nm has dropped dramatically over the last couple of years, from ~50 €/g in 2005, to about ~100-150 €/kg in 2009, depending on the quantity of the orders. Except for the MWNTs, SWNTs are also widely available on the market. Although the price of SWNTs has also dropped, it is still very expensive compared to MWNTs. [58] Carboxyl (-COOH) and hydroxyl (-OH) functionalized MWNTs are available in large quantity also at reasonable prices; the price of 90 % purity functionalized MWNTs with diameters of 10-30 nm is ~900 \$/kg. [58]

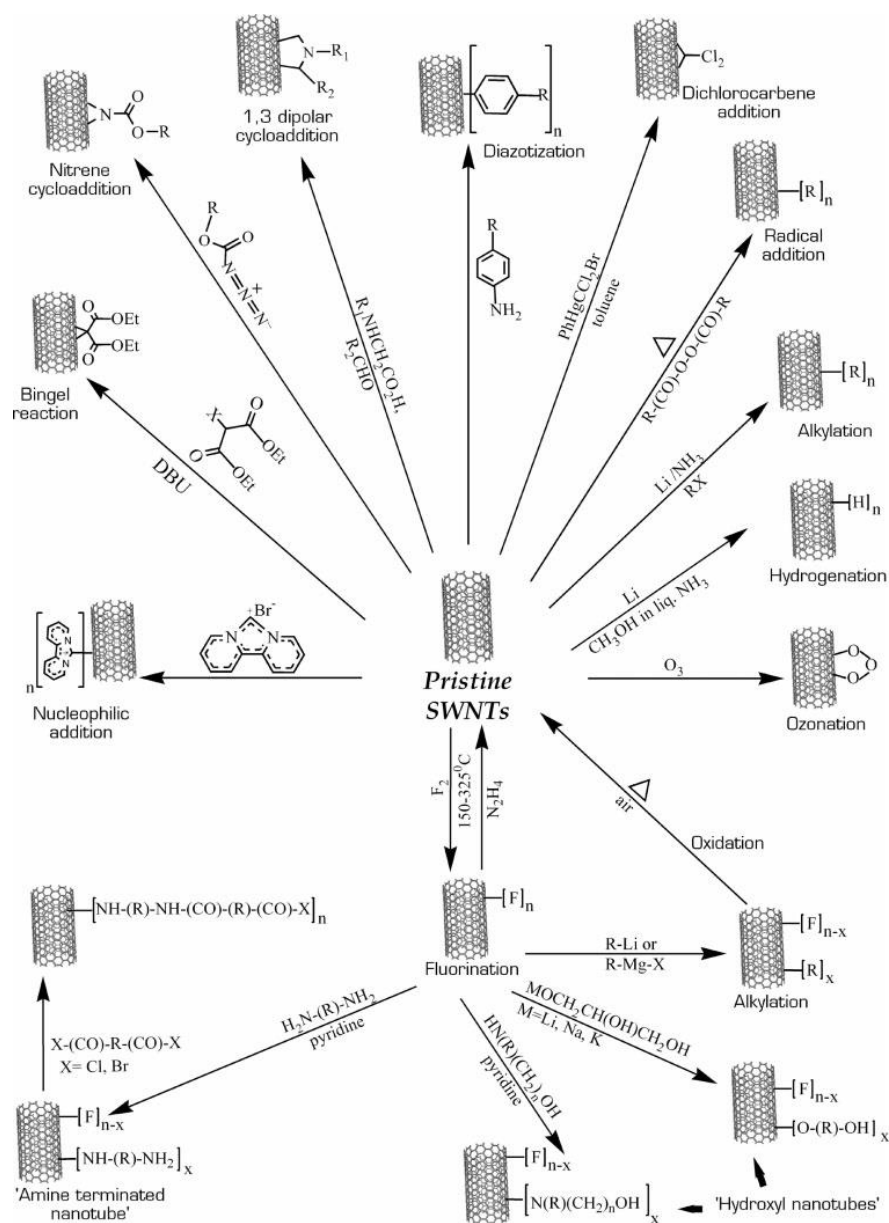


Fig. 2.8 – Diagram showing various covalent sidewall functionalisation reactions of SWNTs [54].

## 2.2 Nanoparticles and their physicochemical properties

### 2.2.1 Silica nanoparticles (SiO<sub>2</sub> NPs)

Colloidal silica (SiO<sub>2</sub>) can be defined as dispersed silica particles with a diameter in the range of  $1 \text{ nm} \leq d \leq 1000 \text{ nm}$ . In this size regime, the particles are large enough to display properties unique from true solutions and are small enough that Brownian motion has a large influence. [59] [60] Silica NPs are of particular interest due to the ease of synthesis and precise control of the size and distribution of the particles. [61] Silica finds various applications ranging from ceramics, industrial coatings, silicon wafer polishing, catalysis,



health care, etc. [60] Silica NPs have also been used as fillers in the manufacture of paints, rubber products, and plastic binders. [62] Moreover, silica particles coated with organic modifiers are used in applications that include stationary chromatography phases, [63] heterogeneous supported catalysts, [64] and in the automotive, electronics, appliance, consumer goods, [65] aerospace and sensor [66] industries.

The industrial development of colloidal silica started first at 1861 by acidifying a solution of sodium silicate. [60] Since that time, several variations of this aqueous process have been developed. An important factor in this method of colloid formation is the pH dependence of the rate of condensation/polymerization of the Si-O functionality. At high pHs, like those found in solutions of sodium silicate, polymerization is extremely slow. As the pH is lowered, polymerization of Si-O units occurs and particles begin to form. [67] It is also possible to form silica particles starting from tetraalkoxysilanes ( $\text{Si}(\text{OR})_4$ ). However, the alkoxy groups must first be hydrolyzed by acid or base catalysis before polymerization can occur, because hydrolysis is extremely slow at neutral pH. [68] [69] One of the most widely used base-catalyzed methods is the Stöber process.

Stöber and co-workers [70] reported a simple synthesis of monodisperse spherical silica particles. The synthesis proceeds with the hydrolysis of tetraethyl orthosilicate (TEOS) in a mixture of alcohol, water and ammonia (catalyst), and the subsequent condensation of the silanol groups. In

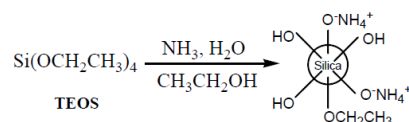
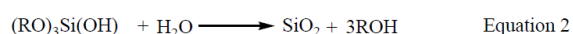
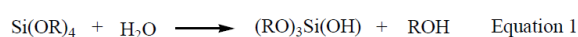


**Fig. 2.9 – (a) Synthesis of Stöber spherical silica particles and (b) stabilization of the silica particles.**

general, the hydrolysis reaction gives the slightly hydrolyzed TEOS monomer (Fig. 2.9, Equation 1). This hydrolyzed intermediate undergoes condensation to eventually form silica according to Fig. 2.9, Equation 2. The resultant particles are stabilized by electrostatic repulsion due to the ions in the ammonia solution (Fig. 2.9). By this method, monodisperse spherical particles of silica can be generated between 50 nm and 2  $\mu\text{m}$ , depending on which alcohol is used as solvent, concentration of water, concentration of ammonium hydroxide, concentration of alkoxy silane, and which alkoxy silane is used. The evolution of silica, formed in a sol gel process from alkoxy silanes, is well understood. At high pH, as in the Stöber process, [70] alkoxy silanes undergo efficient hydrolysis and less effective condensation. The primary particles that first appear after oligomerization are electrostatically stabilized by silanolate ( $\text{R}_3\text{SiO}^-$ ) groups on the surface. When properly

controlled, particles that subsequently form are captured by the primary particles, leading to a steady increase in the average diameter of relatively monodisperse particles.

### 2.2.2 Silver nanoparticles (Ag NPs)

During the last decades, the synthesis and characterization of noble metal nanoparticles (NPs), defined as particles with a diameter between 1 and 100 nm, have attracted an extensive research interest in the field of drug delivery, photonics, catalysis, biosensors, ultrasensitive molecular detection via SERS substrates [71-73], etc. Their characteristic colorful colloidal solutions [74] was the reason why Gold (Au) colloids were used as a pigment of ruby-colored stained glass dating at the 17<sup>th</sup> century. [75] Faraday first recognized that the red color was due to metallic gold in colloidal form. [76]

The use of noble metal NPs can be more precisely realized due to the fact that at this size level the properties of materials differ remarkably from that at the macroscopic scale or that of individual atoms or molecules. [77] These differences are, amongst others, caused by the well-known *localized surface plasmon resonance* (LSPR). [78, 79] This phenomenon is produced when an external electromagnetic field interacts with a metal nanoparticle resulting in the delocalization of the electron cloud. This electronic delocalization promotes two important consequences: *i*) an intense absorption band in the UV-vis spectrum, supplying interesting optical properties, [80] and *ii*) an increase in the local electromagnetic field near the nanoparticle surface that affect the local environment, which is exploited for surface-enhanced Raman spectroscopy (SERS) applications, [81-83] superlensing, [84] or light transmission through optically thick films. [85] Therefore, rough metallic surfaces or metal NPs under plasmonic excitation can act as antennae achieving scattering cross section enhancements of several orders of magnitude. [86] Amongst the three metals (Ag, Au, Cu) that display plasmon resonances in the visible spectrum, Ag exhibits the strongest plasmon band. [87] This is explained due to the higher energy of the interband transition (~3.2 eV), relative to the energy of the plasmon resonance, leading to a minimum damping of the plasmon. [88] Hence, silver NPs interact with light more efficiently than other particles of the same dimension composed of any known organic or inorganic chromophore. The light-interaction cross-section for Ag can be about ten times that of the geometric cross-section, which indicates that the particles absorb much more light than is physically incident on them. [89] Silver is also the only material whose plasmon resonance can be tuned to any wavelength in the visible spectrum. [90] It should be mentioned that the SPR characteristics of metal NPs are determined by a set of physical parameters that are particles size,

composition, structure (e.g., solid or hollow) and dielectric constant of the surrounding medium. To that end, anisotropic shaped NPs (i.e rods, wires, etc) have SPR intensity that is stronger compared to isotropic ones.

Noble metal NPs (Ag, Au, Cu) have been utilized also as catalysts for many electron-transfer chemical reactions acting as an electron-relay. Their high surface area relative to their volume enables an enormous amount of external atoms on the surface whose are accessible to react with the environment (atoms, molecules, etc). [91]

### 2.2.2.1 Origin of surface plasmon resonance (SPR)

*Plasmon resonance* is an optical phenomenon arising from the collective oscillation of the conduction band electrons in metals, when electrons are disturbed from their equilibrium positions. This can be induced by an electromagnetic wave (light), in which the free electrons of a metal are driven by the alternating electric field to coherently oscillate relative to the lattice of positive ions. For a bulk metal of infinite size, the frequency of oscillation  $\omega_p$  is defined as:  $\omega_p^2 = N_e e^2 / \epsilon_0 m_e$ , where  $N_e$  is the number density of conduction electrons,  $\epsilon_0$  is the dielectric constant of vacuum,  $e$  is the charge of an electron, and  $m_e$  is the effective mass of an electron. [92] Therefore, the bulk plasmon frequency of a particular material depends only on its free electron density and for most metals occurs in the UV range, while alkali and some transition metals such as Cu, Ag, and Au exhibit plasmon frequencies in the visible region.

Due to the fact that the penetration depth of an electromagnetic wave inside a metal is limited (typically less than 50 nm), only plasmons caused by surface electrons are significant and commonly referred to as surface plasmons. Additionally, if a surface plasmon is associated with an extended metal surface, it is called a propagating surface plasmon. The frequency of a propagating surface plasmon is lower than the bulk frequency, with the theoretical frequency value of  $\omega_p/\sqrt{2}$  for the metal-vacuum interface boundary conditions. [93] If the collective oscillation of free electrons is confined to a finite volume as with small metal particle, the corresponding plasmon is called a localized surface plasmon with the theoretical frequency of  $\omega_p/\sqrt{3}$  for a metal sphere placed in vacuum. [92]

Fig. 2.10 [94] depicts the interaction between the electric field of incident light and the free electrons of a metal sphere whose size is smaller than the wavelength of light. The electric field of incident light displaces particles electrons from equilibrium in one direction

creating dipoles that can switch direction with the change in electric field. A generated restoring force tend to recombine charges, resulting thus in oscillatory motion of electrons. When the frequency of the dipole oscillation approaches that of an incident light, a resonance condition is reached, leading to constructive interference and showing the strongest signal for the plasmon. Such a condition is referred to as *surface plasmon resonance* (SPR), or *localized surface plasmon resonance* (LSPR). [95]

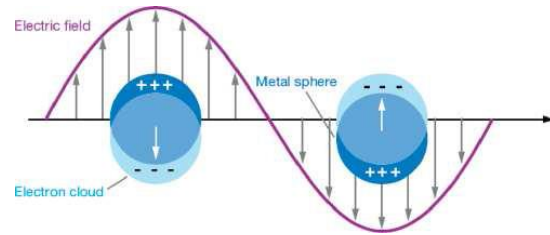


**Fig. 2.10 - Schematic illustration of a localized surface plasmon of a metal sphere. Reproduced from [95].**

Surface polarization (i.e. charge separation) is the most important factor that determines the frequency and intensity of plasmon peak for a given metal, because it provides the main restoring force for electron oscillation. Therefore, exact position and shape of SPR peak are mainly defined by the materials' properties, namely, materials' electron density and dielectric constant. Indeed, any variation in particle size, shape, or dielectric environment will change the surface polarization and, further the position of the resonance peak. Polarisation of the surrounding medium, which is induced by oscillation of metal electrons, reduces the restoring force for the electrons, and thereby shifting the SPR to a lower frequency. Thus, by controlling the dielectric constant of the surrounding medium, the wavelength of SPR can be fine-tuned to a desired position. With the increasing particle size, the plasmonic peak maximum shifts towards the red region of the visible spectrum. Furthermore, for larger particles, higher order peaks (e.g. quadrupole, octupole SPR) become noticeable, arising from the existence of two or more polarization directions (Fig. 2.11 [90]). [95]

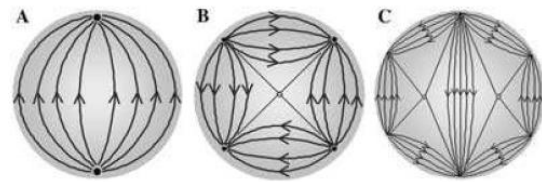


**Fig. 2.11 - Diagrams depicting the electric field lines for the (a) dipole, (b) quadrupole and (c) octupole resonances. Reproduced from [90].**

Gustav Mie [80] was the first who explained theoretically the localized surface plasmon resonance of metal colloids by solving the Maxwell's equation for an electromagnetic light wave interacting with small spheres having the same frequency dependent dielectric constant as the bulk metal. The solution of this electro-dynamic calculation with appropriate boundary conditions for a spherical object leads to a series of

multipole oscillations for the extinction cross-section of the particles ( $\sigma_{ext}$ ). For NPs with radius  $r$  much smaller than the wavelength of light ( $r \ll \lambda$ ), where only the dipole oscillation dominates (dipole approximation), the solution of Maxwell equations gives the following formula:

$$\sigma_{ext}(\omega) = \frac{12\pi\omega r^3}{c} \epsilon_m^{3/2} \frac{\epsilon_i(\omega)}{[\epsilon_r(\omega) + k\epsilon_m]^2 + \epsilon_i^2(\omega)} \quad (2.2)$$

where  $r$  is the particle radius,  $\omega$  is the angular frequency of the exciting light,  $c$  is the speed of light,  $\epsilon_m$  is dielectric constant of surrounding medium. While the  $\epsilon_m$  is assumed to be frequency independent, the dielectric function of material itself is complex and dependent on energy (i.e. frequency) of incident light:  $\epsilon(\omega) = \epsilon_r(\omega) + i \epsilon_i(\omega)$ , where  $\epsilon_r$  and  $\epsilon_i$  are the real and imaginary parts of dielectric function of material, respectively. The  $k$  factor is related to the particles shape anisotropy: it has a value of 2 for the case of a sphere, but increases to as large as 20 for the particle geometries with high aspect ratios. [96] For spherical particles, the resonance condition is fulfilled when  $\epsilon_r(\omega) = -2\epsilon_m$  and  $\epsilon_i$  is small or weakly dependent on  $\omega$ :

$$\sigma_{ext}^{res}(\omega) = \frac{12\pi\omega r^3 \epsilon_m^{3/2}}{c \epsilon_i} \quad (2.3)$$

#### 2.2.2.2 SERS effect and SERS substrates

The surface enhanced Raman scattering (SERS) effect was discovered by Martin Fleischman in 1974 as a large enhancement of the Raman signal of certain molecules adsorbed on roughened metallic surfaces. [97] Since then, SERS has been used as a powerful analytical tool for the sensitive and selective detection of molecules. The enhancement factors were calculated to be more than a million-fold in comparison with the normal Raman signals. Consequently, this means that the detection limits are considerably lower (down to  $10^{-9}$  M) compared to those for resonance Raman scattering. [98] In addition, the advantages of Raman scattering, i.e. molecularly specific vibrational spectra, simple versatile sampling and the ready determination of analytes in air and in water, are applicable to SERS spectroscopy.

More specific, a qualitative understanding of the SERS effect is provided by the classical theory of light scattering. [82] One can consider an incident light beam that induces an oscillation dipole  $P$  in a particle, which reemits or scatters light at the same frequency of

the dipole oscillation. For the particular case that the magnitude of the incident electric field  $E$  is not too large, the induced dipole moment,  $P$  can be approximated as follows:

$$P = \alpha E \quad (2.4)$$

where  $\alpha$  is the polarizability of the molecule.

The enhancement effect can influence either the molecular polarizability or the electric field experienced by the molecule. Surface selection rules are also available. [99] According to them, the most intense bands are those given by vibrations which induce a polarization of the adsorbate electron cloud perpendicular to the metal surface. [100] Hence, using the surface selection rules, the orientation of the adsorbed molecules relative to the metal surface can be predicted. [101]

Even if it is not yet fully understood the nature of mechanisms which are responsible for the SERS effect, nowadays, there considered two major types of contributions to the total enhancement of the Raman signal of different molecules: *i*) an *electromagnetic enhancement*, referred as the electric effect in which the molecule experiences large local fields caused by electromagnetic resonances occurring near the metallic surface, and *ii*) a *chemical or charge-transfer effect*, referred as the molecular effect in which the molecular polarizability is affected by the interaction between the molecule and the metallic surface. It is generally believed that the enhancement is mainly attributed to the electromagnetic mechanism; however, the contribution of the charge transfer mechanism to the overall SERS enhancement cannot be ignored. [102]

#### *i) Electromagnetic enhancement mechanism*

The electromagnetic enhancement is the result of two different factors. The first is the enhancement of the laser electromagnetic field due to the addition of the field induced by the polarization of the metal particle. The second is due to the molecule amplified Raman field which further polarizes the metal particle and acts as an antenna amplifying further the Raman signal. The concept of electromagnetic enhancement mechanism can be schematically illustrated as shown in Fig. 2.12. Considering a metal nanosphere with a diameter of  $2r$  (small compared to the wavelength  $\lambda$  of the incident light, with a complex dielectric function  $\epsilon$ ) embedded in a medium with a dielectric constant  $\epsilon_0$ , and a molecule located near the metallic surface at a distance  $d$ , it will be exposed to a field  $E_M$ , which is the

superposition of the incident field  $E_0$  and the induced dipole field on the metal sphere  $E_{sp}$ . [103]

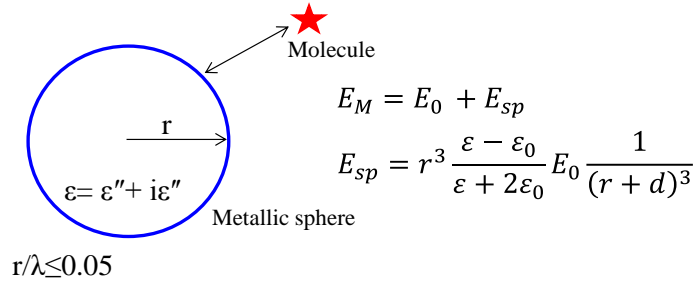


**Fig. 2.12 - Schematic illustration of the electromagnetic effect in SERS.**

The field enhancement factor  $A(\nu)$  is defined as the ratio of the field that the molecule experiences at a distance  $d$  from the particle surface, divided by the incident field.

$$A(\nu) = \frac{E_M(\nu)}{E_0(\nu)} \sim \frac{\epsilon - \epsilon_0}{\epsilon + 2\epsilon_0} \left(\frac{r}{r+d}\right)^3 \quad (2.5)$$

where  $A(\nu)$  is particularly intense when the real part of  $\epsilon(\nu)$  equals to  $-2\epsilon_0$ . Additionally, to get an increase in the electromagnetic field, the imaginary part of dielectric constant should be small. These are the conditions which describe the resonant excitation of surface plasmons in a metallic sphere.

In conventional Raman scattering, the Stokes scattering intensity ( $P^{RS}$ ) is proportional to the Raman cross section ( $\sigma^R$ ), the excitation laser intensity  $I(\nu_L)$  and the number of molecules in the irradiated volume ( $N$ ). [103]

$$P^{RS}(\nu_S) = N\sigma^R I(\nu_L) \quad (2.6)$$

To estimate the Stokes SERS intensity, equation (2.6) should be modified to describe the specific effects of metal nanostructures. According to the two mechanisms described previously, equation (2.6) gets the following form:

$$P^{SERS}(\nu_S) = N'\sigma^R |A(\nu_L)|^2 |A(\nu_S)|^2 I(\nu_L) \quad (2.7)$$

where  $A(\nu_L)$  and  $A(\nu_S)$  are the enhancement factors for the laser and for Raman Stokes respectively, and  $N'$  is the number of molecules involved in the SERS process. The enhancement of the electric field intensity close to the metallic surface is produced as consequence of the LSPR excitation. Therefore, the localized surface plasmon excitation is

the direct cause of the SERS electromagnetic mechanism, and any variation in the intensity or frequency of the plasmon has an impact on the SERS signal acquired. [103]

Taking into account the effects of the increase for the field of laser and Stokes, the electromagnetic enhancement factor for the Stokes signal intensity,  $G_{em}(v_s)$ , can be written as:

$$G_{em}(v_s) = |A(v_L)|^2 |A(v_S)|^2 \sim \left| \frac{\varepsilon(v_L) - \varepsilon_0}{\varepsilon(v_L) + 2\varepsilon_0} \right|^2 \left| \frac{\varepsilon(v_S) - \varepsilon_0}{\varepsilon(v_S) + 2\varepsilon_0} \right|^2 \left( \frac{r}{r+d} \right)^{12} \quad (2.7)$$

The electromagnetic mechanism does not require direct contact between the molecule and the metal, but decreases exponentially with the distance from the particle surface. This is because the dipole field decay with distance  $1/d^3$ , when it is raised to the fourth power, it results in the dependence  $1/d^{12}$ . [103]

Surface roughness is an important factor for SERS. On a smooth metallic surface, surface plasmons exist as waves of electrons bound to the metal surface and are capable of moving only in a direction parallel to the surface. On a roughened metal surface, the plasmons are no longer confined, and the resulting electric field can radiate both in a parallel as well as in perpendicular direction to the surface. When an incident photon falls on the roughened surface, excitation of the metallic particle plasmon resonance may occur and this allows scattering. Furthermore, due to the difference in dielectric constant between the roughened surface and the surrounding media, a concentration of electric field density occurs at sharp points on the surface. [104] Metal colloids and colloidal aggregates provide a particularly rich example of such local electromagnetic enhancement. Several authors [105] [106] have reported that protrusions on the surface of colloidal particles as well as cavities between adjacent particles in an aggregate can lead to a giant enhancement of the local field, up to a factor of  $10^{14}$ - $10^{15}$ .

### *ii) Charge Transfer Mechanism*

A lot of studies have been carried out to elucidate the existence of the charge transfer mechanism in SERS. [102] [107] The enhancement attributed to the charge transfer mechanism occurs when molecules physisorb or chemisorb on roughened metallic surfaces, forming an adsorbate-metal complex. In the case of chemisorption, the molecular orbitals are broadened by the interaction with the conduction bands of the metal surface. This results in a ready transfer of electrons and excitation from the metal to the adsorbate and vice versa (Fig. 2.13). Consequently, the SERS spectra of chemisorbed molecules are significantly different



from the Raman spectrum of the free species or even the physisorbed species. The charge transfer mechanism is restricted by its nature to molecules directly adsorbed on the metal surface, as opposed to the electromagnetic enhancement mechanism which requires a certain distance beyond the molecule and the metallic surface. Thus, it effectively operates only on the first layer of adsorbate. It was Campion *et al.* [108] who first reported the experimental evidence of the charge transfer mechanism linking new features in the electronic spectrum of an adsorbate to SERS, under conditions where electromagnetic enhancement were unimportant. It was mentioned that it was difficult to observe only the charge transfer because electromagnetic effects had to be accounted. However, this was restricted by measuring SERS enhancement on a flat, smooth single crystal surface where electromagnetic effects were small and well understood. The problem is even more complex due to the fact that electromagnetic enhancement decreases as the adsorbate-surface distance decreases, and only the additional enhancement can be classified as charge transfer. However, the degree of enhancement of the first layer is very large. Overall, the charge transfer mechanism is not yet completely understood and still there a big debate on its mechanism.

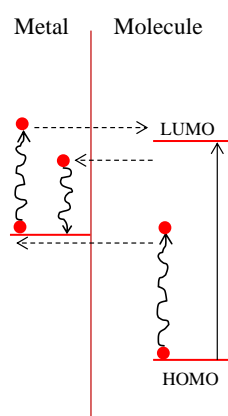


**Fig. 2.13 - Energy level scheme for a metal-molecule complex formed when an analyte chemisorbs on a metal surface.**

Colloidal suspensions of metallic nanoparticles are quite attractive for the fabrication of SERS substrates. The tendency of nanoparticles to coagulate upon casting on a surface leads to the formation of aggregates exhibiting roughness and fractal morphology, necessary for SERS. [109] [110] A lot of different metal colloids have been used, including gold and copper; however, silver is the most efficient since it has the most intense surface plasmon band due to the position of the interband transitions. It is also reported that SERS intensity increases with the size of silver particles (average diameter of 50 nm), however, further increase of the particle size (100-130 nm) has shown lower SERS signals. [111] The upper

dimension limit of the SERS-active system is determined by the laser wavelength. When nanoparticles with size of the order of the wavelength or larger are used, the optical fields excite progressively higher order multipoles that are non-radiative and thus not efficient in causing Raman excitations. [112]

The SERS substrates are very efficient when they are formed by plasmonic nanoparticles with fractal structures, like particle aggregates or thin films which form metallic islands. In these aggregates the oscillating surface plasmon is coupled between the particles being in close proximity. However, the field excitation is not uniformly distributed over all the aggregate; it is localized spatially in the so-called *hot spots*. The hot spot size is small, in the order of a few nanometers, and the localization depends on the fractal geometry, the excitation wavelength and the field's polarizations. When the optic excitation is located in small hot spots, the SERS electromagnetic enhancement is extremely high, because it is proportional to the forth power of the electric field. [103] For these areas a theoretical enhancement nearly to  $10^{12}$  has been predicted. [113] This order of magnitude has been confirmed by SERS experiments of one single molecule, in which the 'normal' Raman signal of  $10^{14}$  molecules of methanol possess the same SERS signal intensity of one single molecule. [114] One disadvantage of the aggregate formation is that the hot spots have a random distribution. Moreover, aggregate systems are difficult to be controlled, and their reproducibility is limited by the dependence on the particle size and the distance between particles. [115] These reasons prevent reproducible signal intensity, restricting the applications of this technique. Lithography techniques (i.e. electron-beam lithography) have been exploited to fabricate topographically engineered SERS substrates with desired shape, size and arrangement. The obtained substrates were used to explore how the magnitude of the enhancement factor is influenced, by the varied size, shape, and interparticle spacing. [116] [117] [118] It is still under investigation to develop SERS substrates with longer lifetime, with stable and optimized enhancement factors permitting SERS in different environments.

### 2.2.2.3 Synthetic routes for preparation of silver NPs

Several methods have been reported for the synthesis of Ag NPs, and they can be divided into 'traditional' and 'non-traditional' ones. [90] The term 'traditional' is used for solution-phase synthetic protocols that are based on the reduction of a silver salt. The most common methods were developed by Creighton and Lee who used  $\text{AgNO}_3$  as a metal source and  $\text{NaBH}_4$  as well as sodium citrate as a reducing agent, respectively. [119, 120] Resulting

colloids appear electrostatically stabilized due to the adsorption of citric ions to the particle surfaces during growth. A two-phase method, developed by Brust and co-workers, based on reduction of metal precursors, allows the preparation of metal organosols directly from water-soluble metal salts. [121] [122] By stirring aqueous solutions of metal salts (e.g.  $\text{HauCl}_4$ ,  $\text{AgNO}_3$ ,  $\text{AgClO}_4$ ) with toluene containing phase transfer agent, i.e. tetraoctylammonium bromide (TOAB), a two-phase system is formed initially, containing metal precursors on organic phase. Next, a measured quantity of capping agent, typically a long-chain alkanethiol, is added to the solution while stirring, and then a reducing agent (e.g.  $\text{NaBH}_4$  or hydrazine) is rapidly introduced to nucleate nanocrystals. The average particles size is coarsely tuneable by adjusting the ratio of the stabilizing agents to metal salt, whereas size-selective precipitation is employed to narrow the initial size distribution. The so-called 'non-traditional' methods, include Ag particle synthesis through high-temperature reduction in porous solid matrices, [123] vapor-phase condensation of metal onto a solid support, [124] laser ablation of a metal target into a suspending liquid, [125] photoreduction of silver ions [126] and electrolysis of a silver salt solution. [127] High temperature decomposition of metal precursors in the presence of stabilizing agents has been used to produce noble metal NPs. [128] In that case, preparation involves injection of metal precursors in high-boiling point inert solvents along with a combination of stabilizing ligands, such as alkanethiols, amines or carboxylic acids, at elevated temperature. Similar to other synthetic methods, NPs size can be coarsely tuned by the ratio of capping agent to metal salt, while size-selective precipitation yields particles with polydispersity of ~5%. Recently, Hiramatsu reported a simple and large-scale synthesis of gold and silver nanocrystals through mild reduction of metal precursors in the presence of oleylamine at elevated temperature. [129] This method can produce nearly monodisperse particles with no need of time- and solvent-consuming size selective precipitation steps. The oleylamine serves both as a reducing and stabilizing agent simplifying the optimisation of reaction conditions significantly if compared to more complex multicomponent systems. So far, different silver salts and reducing agents have been utilised to obtain stable and monodisperse Ag NPs in solution. [130, 131] Unfortunately, both of the two approaches have to face some inherent problems. Traditional methods, for instance, have a limited range in the final size of the particles producing in most of the cases particles below 10 nm, size not sufficient for optical and spectroscopic purposes. On the other hand, the disadvantages of the non-traditional methods are the wide size distribution, lack of crystallinity, high cost and up-scaling of the fabrication process.

Recently, some strategies have been exploited to overcome the previously mentioned problems of the traditional synthetic methods. Hybrid systems composed of polymer-

nanoparticle or inorganic material-nanoparticle arrangements have been developed where NPs can endow their unique properties to the resulting nanoassemblies. The structure and functionalities of the host material used as the support for the metal NPs can control the spatial distribution of NPs, avoiding thus the most prominent problem which is their tendency to agglomerate due to their high surface energy. [132] To that end, a great number of polymeric materials, such as dendrimers, [133] latex particles, [134] microgels, [135] polymers brushes, [136, 137] and inorganic materials like SiO<sub>2</sub> microspheres, [138] have been used as carriers for the immobilization of metal NPs. Liu *et al.* used poly(amidoamine) (PAMAM) dendrimers as carriers to incorporate Ag NPs after the reduction of Ag ions by NaBH<sub>4</sub>, previously interacted within the branched structure of PAMAM. [133] The disadvantage of this protocol is that the final size of the metal NPs is determined by the dimension of the dendrimer, limiting the method only for small Ag NPs. Chen *et al.* synthesized poly(N-isopropylacrylamide)-coated latex microgels to facilitate the deposition of Ag nanospheres on the microgel surface in ethanol/water media. [134] These Ag NPs were produced via in situ reduction of Ag<sup>+</sup> by radicals generated from the polymerization initiator. Ballauff *et al.* used also the same core-shell system to immobilize Ag NPs via chemical reduction of Ag<sup>+</sup> with sodium borohydride, and proposed the hybrid system for catalytic applications tunable with temperature variations. [135] For both cases, non-biocompatible polymers were used preventing from bio-medical applications. In order to overcome this obstacle, metal coated SiO<sub>2</sub> particles have gained tremendous interest and many synthetic approaches have been reported. [138, 139] Core-shell Ag@SiO<sub>2</sub> particles have been also fabricated with a homogeneous SiO<sub>2</sub> shell surrounding the silver surface used as nanoreactors for redox catalysis. [140] Moreover, Deng *et al.* used polyvinylpyrrolidone (PVP) as reducing and stabilizing agent for the fabrication of SiO<sub>2</sub>@Ag nanocomposites. [141] Although no additional reducing agent was needed, the synthesis is unfeasible in aqueous media and limited for particles dispersed finally in an organic solvent. Zhu *et al.* used an electroless process to obtain core-shell SiO<sub>2</sub>@Ag submicrometer spheres. In that case, the silica surface was modified through the adsorption of Sn<sup>2+</sup> ions in a first step, and then reduced by an ammoniacal silver nitrate solution at low concentration, using a mixture of ethanol/formaldehyde to obtain a dense silver coating. [142] However, an important drawback of this protocol is the use of toxic formaldehyde. Kobayashi *et al.* used as well an electroless plating process to deposit Ag NPs on silica spheres. Initially, they modified the silica surface with SnCl<sub>2</sub>, and then Ag<sup>+</sup> where reduced to Ag<sup>0</sup>, while Sn<sup>2+</sup> oxidizes to Sn<sup>4+</sup>, leading to a homogeneous deposition of Ag NPs. [143] Nevertheless, in order to obtain a relatively dense Ag coating, the two step process had to be repeated several times.

### 2.3 Block copolymer (BCP) nanostructures

Nanostructured Epoxy/BCP blends have been fabricated in this thesis using diblock copolymers. Diblock copolymers represent a sort of block copolymers, consisting of two covalently bonded and chemically dissimilar polymer subunits (blocks) (Fig. 2.14). [144] Block copolymers (BCPs) are considered also other sorts of macromolecules like triblock copolymers, star-block copolymers, cyclic block copolymers, etc. [145] [146]

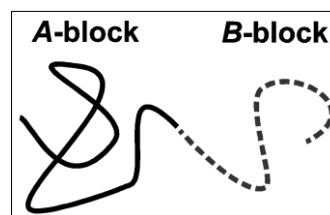


Fig. 2.14 - A diblock copolymer.

The most used macromolecular components in diblock copolymers are polystyrene (PS), poly(methyl methacrylate) (PMMA), polyvinylpyridine (PVP), polyisoprene (PI), polybutadiene (PB), polydimethylsiloxane (PDMS), and poly(ethylene oxide) (PEO). Although the first block copolymers were synthesized in 1950s, the extensive research emerged upon advanced polymerization methods at the end of 1980s. [147] Their synthesis utilizes the well-known living polymerisation techniques; 1) Living Anionic or Cationic Polymerization, 2) Atom Transfer Free Radical Polymerization (ATRP), 3) Reversible Addition Fragmentation Chain Transfer (RAFT) and 4) Group Transfer Polymerization (GTP) which efficiently enable a control over the chain polydispersity (PDI) [146] [148].

Block copolymers have obtained a significant interest due to their inherent microphase separation of the chemically distinct blocks in microdomains, at the nanometer scale. This characteristic arises from the covalent coupling of the blocks, unlike polymer blends which provide microdomains of a micrometer scale. Therefore, the term ‘microphase separation’ seems obsolete; however, it is steadily used in place of ‘nanophase separation’ because of similar thermodynamic processes, which describe the origin of microdomains. The nanometer scale of the BCP morphologies is considered as a very attractive structural asset for many physico-chemical devices, since it is of the same order as the exciton diffusion length or the thickness of tunneling barriers. Also the surface to volume ratio, in comparison for instance with a polymer blend, is much higher in BC microdomains (around two orders of magnitude). This is very challenging for surface dependent processes like photovoltaics, electroluminescence, catalysis, etc.

There are three principal factors which can determine the morphology of a BCP; the total degree of polymerisation  $N (= N_A + N_B)$ , the Flory-Huggins segment-segment interaction parameter  $\chi$ , and the volume fractions of the blocks  $f (f_A, f_B)$ . [149] Degree of polymerization predestinates the radius of gyration  $R_g$  of the polymer, and therefore the

size of the microdomains. Growing of polymer chains is associated with characteristic stretching in order to fill space, thus,  $N$  specifies the entropic contribution to the overall Gibbs energy of the BCP. On the other hand, chemical incompatibility of the blocks results in their repulsion, and so it leads to penetration of the phase  $A$  into the phase  $B$ .

The incompatibility is expressed with the  $\chi$  parameter, which is a rational function of temperature <sup>[3]</sup> so that it specifies the enthalpic contribution to the overall Gibbs energy. Plot of the product  $\chi N$  vs. the volume fraction  $f$  of one of the blocks, expresses the phase balance between entropy and enthalpy of the block, and it is called as phase diagram. Using the full

self-consistent field theory (SCFT), Matsen and Bates calculated the complete phase diagram of diblock copolymer melt (Fig. 2.15). [150] [151] Accordingly, they found that diblock copolymer at  $\chi N$  less than ca. 10.5 is always in disordered state irrespective of the volume fraction. This may occur at higher temperature and lower degree of polymerization. The diblock copolymers used in this thesis have  $N$  around 400 and such degree of polymerization is usually high enough to overcome the order-disorder transition (ODT) at room

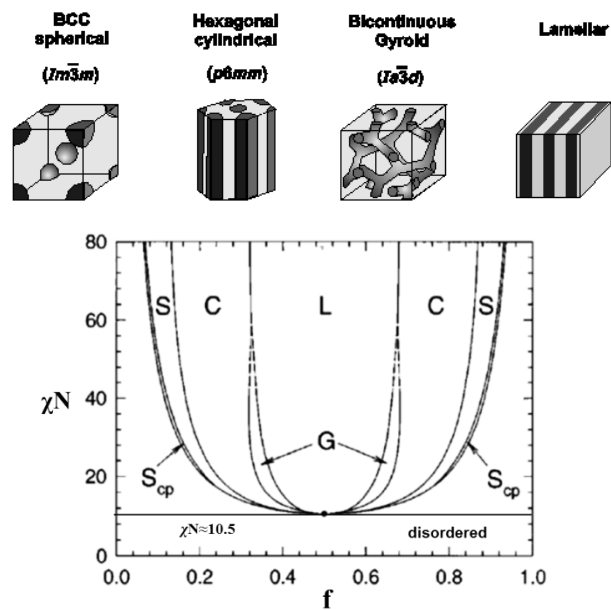


Fig. 2.15 - Diblock copolymer morphologies with the corresponding phase diagram. [150]

temperature. Typical value of  $\chi$  parameter in copolymer melts is around 0.1 (e.g. PS-P2VP);  $\chi$  parameter of PS-P4VP several times is higher due to ionic nature of P4VP. [152] [153] It is also worthwhile to mention the experimental work of F. S. Bates *et al.* [154] who estimated the thermal dependence of  $\chi$  as  $\chi(T)=91.6/T-0.095$  for symmetric PS-*b*-P2VP via rheological measurements. Dai and Kramer [155] came to similar result using forward recoil spectrometry:  $\chi(T)=66/T-0.033$ . PS-P4VP copolymers have also higher ODT temperature than PS-P2VP due to greater dipole polarization as was found using thermally stimulated currents and dielectric relaxation spectroscopy. [156] Over ODT, the copolymer blocks are segregated in microdomains according to the phase diagram (Fig. 2.15). However, if  $\chi N$  is

<sup>[3]</sup>  $\chi = \frac{C_1}{T} - C_2$ , where  $C_1$  and  $C_2$  are constants.

less than ca. 50 the phases are only moderately segregated, i.e. the phases fluctuate at the interfaces. In the strong segregation regime ( $\chi N > 50$ ), the interfaces among the microdomains are very sharp and so the microdomains are well defined. In strongly segregated diblock copolymer, the disordered state is observed only at high asymmetry, with volume fraction of the minor block less than ca. 5 %.

With increasing volume fraction, strongly segregated diblock copolymer forms body-centered cubic (BCC) arranged spheres (S) of *A*-phase for  $f_A \approx 5-15$  %, hexagonally arranged cylinders (C) for  $f_A \approx 15-30$  %, and stacking lamellae (L) for  $f_A \approx 30-50$  %. For  $f_A > 50$  %, *A*-phase becomes a matrix for *B*-phase morphologies as is evident from the axial symmetry of the phase diagram at  $f = 0.5$  (Fig. 2.15). Weak segregated regime provides also intermediate morphologies as closed-packed ( $S_{cp}$ ) or bicontinuous gyroids (G). Emergence of these morphologies in diblock copolymers is strongly dependent on both  $\chi N$ , and  $f$ , respectively. Several further metastable morphologies, like hexagonal modulated lamellae (HML), hexagonal perforated lamellae (HPL), and double-diamond (D), have been observed in diblock copolymer melts. [157]

## 2.4 Fiber Reinforced Polymer Composites (FRPCs)

Composites are the materials which are composed of a mixture of two or more immiscible phases, and their performance is highly dependent on the properties and interactions of the constituent phases. The classification of fiber reinforced polymer composites (FRPCs) is in general contradictory and arbitrary. Composites are often classified according to the matrix or the fiber used, the length of the fiber, the goal of the application, etc. The most used composite materials are consisted of long fiber reinforced thermoset composites, and the fibers are usually glass, carbon or aramid. These materials possess exceptional stiffness and strength; they are light-weight, however, usually very expensive. The amount of long fiber reinforced thermoplastic composites is much smaller because of the processing difficulties. Extruded profiles and glass mat or woven textile reinforced polymers represent this class. Moreover, both thermosets and thermoplastics are reinforced by short fibers. Short fiber reinforced composites are extensively used by the automotive and machine industry. These materials are usually supplied in the form of granules and they are processed by injection molding.

The properties of FRPCs are determined by four factors: *i*) component properties, *ii*) structure and *iii*) interphase between fiber and matrix. All four are equally essential and they must be adjusted to achieve optimum performance of the final composite. The materials

studied in this thesis fall into two categories. The first chapter discusses Epoxy/GF model composites. Single GFs covalently and non-covalently bonded with MWCNTs were embedded in an epoxy matrix, and investigations of the interphasial adhesion strength as well as the electrical properties of the interphase for specific applications, have been studied. The other chapter deals with CNT-modified short JFs and their use for reinforcing natural rubber. In that case, the use of CNTs functions as a macromolecular coupling agent improving the interfacial interaction, and together with the interfacial toughening mechanisms are discussed in detail to explain the remarkable enhancement of the mechanical properties of the natural rubber matrix. If we consider that the factors determining the properties of polymer composites are the same, on the one hand, and that the thesis focuses mostly on interfacial interactions and their modification, on the other hand, the variation of composite components becomes of much less significance.

Some applications of the materials used in this study, which our results can be of great interest for the fabrication of final products in the future, are depicted in Fig. 2.16. In the upper side, products made out of Epoxy/GF composites are illustrated, while in the lower left side; epoxy/natural fiber composite parts of a car are depicted, while in the lower right side, natural rubber/natural fiber based composite material for shoe application is illustrated.



**Fig. 2.16 – Applications of Epoxy/GF composites (upper side), as well as natural fiber reinforced epoxy (lower left side) and natural rubber (lower right side) composites.**

#### 2.4.1 Fibers used to reinforce a polymer matrix

Due to the high tensile modulus and strength, the *fibers* carry the most of the load in a FRPC. The fibers also toughen the brittle matrix by blocking or deflecting any cracks that may propagate through the polymer matrix. In addition, the fibers can be selectively aligned in specific directions and locations where the maximum stresses are likely to occur. [158] [159] The fiber content of polymer composites may change in a wide range and the ulterior aim to improve stiffness and strength. These goals require the introduction of the largest possible amount of fibers in a polymer matrix, but the improvement of the targeted property



may be accompanied by the deterioration of some others. Numerous fiber characteristics such as chemical composition and purity, fiber surface morphology and chemistry, surface free energy, hardness and other properties can influence the properties of FRPCs. [160]

*Glass fibers* (GFs) are the most used reinforcing fibers in modern composites, and their products are found in various market areas such as transportation, construction, marine, electric and consumer products. Fig. 2.16 shows some examples of GFRPs applications. Many of these industrial composites are cost-competitive with metals, and in many cases are able to substitute metals due to their unique and inherent properties (low corrosion and better fatigue resistance), lower tooling costs and ease of fabrication. [161] The chemical composition and properties of different types of GFs commercially available in the market, are given in Table 2.1. [162] As it can be observed, GFs exhibit in general high strength-to-weight ratio and this justifies their use as reinforcement where high strength and minimum weight are required. As a textile, GFs can be in the form of unidirectional or bidirectional and they are known for their electrical and thermal insulating properties. E-Glass fibers are mostly used nowadays, and they have been employed within this thesis throughout all the experiments.

**Table 2.1 Different types of GFs with their composition and their physical properties [162]**

	A Glass	C Glass	D Glass	E Glass	AR Glass	R Glass
	High alkali	Chemical resistance	Hi-dielectric	'Electric' glass	Alkali-resistance	High-dielectric
SiO <sub>2</sub>	63-72	64-68	72-75	52-56	55-75	55-60
Al <sub>2</sub> O <sub>3</sub>	0-6	3-5	0-1	12-16	0-5	23-28
B <sub>2</sub> O <sub>3</sub>	0-6	4-6	21-24	5-10	0-8	0-0.35
CaO	6-10	11-15	0-1	16-25	1-10	8-15
MgO	0-4	2-4		0-5		4-7
ZnO						
BaO		0-1				
Li <sub>2</sub> O					0-1.5	
Na <sub>2</sub> O+K <sub>2</sub> O	14-16	7-10	0-4	0-2	11-21	0-1
TiO <sub>2</sub>	0-0.6			0-1.5	0-12	
ZrO <sub>2</sub>					1-18	
Fe <sub>2</sub> O <sub>3</sub>	0-0.5	0-0.8	0-0.3	0-0.8	0-5	0-0.5
F <sub>2</sub>	0-0.4			0-1	0-5	0-0.3
Density(g/cm <sup>3</sup> )	2.44	2.52		2.58	2.70	2.54
Tensile str. (MPa)	3310	3310		3445	3241	4135

Young's Mod. (GPa)	68.9	68.	72.3	73.1	85.5
Elongation %	4.8	4.8	4.8	4.4	4.8
Durability (% wt loss)					
H <sub>2</sub> O: 24 hr	0-6	3-5	12-16	0-5	23-28
10% HCl: 24 hr	0-6	3-5	12-16	0-5	23-28
Vol. res. (Ohm×cm)	1.0E+10		4.02E+14		2.03E+14
Surf. resistivity (Ohms)			4.20E+15		6.74E+13

Among others, *natural fibers* are used as reinforcement of polymer matrices because of their good strength and stiffness, as well as their low density. Another important factor is their low price, since these raw materials obtained from natural, renewable resources and usually are much cheaper than synthetic fibers. Natural fibers can be derived from plants, animals (wool) or minerals (asbestos, basalt) [163] [164] and mostly composites are prepared from plant fibers. Plant fibers can be classified according to their origin, the part of the plant supplying the fiber, thus we talk about seed fibers (cotton, coconut), bast fibers (flax, hemp, jute) and leaf or hard fibers (sisal, pineapple, abaca or Manila hemp). [164] All of these fibers are based on cellulose, which is the building element of the long fiber-like plant cells. The chemical composition of different types of natural fibers is given in Table 1.2. [164] Depending on the climatic conditions of the crop area and the technology of the treatment, it can be clearly observed that they differ remarkably in their chemical composition from each other (Table 1.2). [164] The physical and chemical characteristics (biological degradation, flammability, sensitivity to moisture, thermal/UV stability) are strongly influenced by the additional components of the fiber, the amorphous hemicellulose and the lignin contents.

**Table 2.2 Chemical composition of plant fibers [164]**

Component	Composition of fiber (wt%)				
	Cotton	Jute	Flax	Ramie	Sisal
Cellulose	82.7	64.4	64.1	68.6	65.8
Hemicellulose	5.7	12.0	16.7	13.1	12.0
Pectin	5.7	0.2	1.8	1.9	0.8
Lignin	-	11.8	2.0	0.6	9.9
Water soluble	1.0	1.1	3.9	5.5	1.2
Wax	0.6	0.5	1.5	0.3	0.3
Water	10.0	10.0	10.0	10.0	10.0

The main characteristics of different natural fibers compared to synthetic ones are listed in Table 1.3. [164] The data clearly indicate that the properties of natural fibers vary in wide range. As mentioned above, these differences can be explained by the dissimilar structure of fibers coming from crop areas with different climatic conditions, and besides the climatic differences, the technology and treatment applied to obtain the fibers influences significantly their properties as well.

**Table 2.3 Selected properties of natural and synthetic fibers [164]**

<b>Fiber</b>	Density(g/cm <sup>3</sup> )	Tensile strength (Mpa)	Elongation	Young's modulus (GPa)
Cotton	1.5-1.6	290-600	7.0-8.0	5.5-12.6
Jute	1.3	390-780	1.5-1.8	26.5
Flax	1.5	350-1040	2.7-3.2	27.6
Hemp	-	690	1.6	-
Ramie	-	400-940	3.6-3.8	61-128
Sisal	1.5	510-640	2.0-2.5	9-22
Coir	1.2	175	30.0	4-6
Soft wood	1.5	1000	-	40
E glass	2.5	2000-3500	2.5	70
S Glass	2.5	4570	2.8	86
Aramide	1.4	3000-3150	3.3-3.7	63-67
Carbon	1.4	4000	1.4-1.8	230-240

The preparation and use of polymers containing natural fillers or reinforcements is not new in the plastic industry, however, these materials went through a revival in recent years all over the world. Composites containing lignocellulosic components are known since the 1900-ies, especially in the building and furniture industry. [165] Already in 1916 Rolls Royce used a phenol-formaldehyde resin/wood composite for the production of the knob of its gear lever. [166] The various wood-fiber, laminated and MDF boards are prepared from phenol-formaldehyde, urea-formaldehyde and melamine formaldehyde resins [165]. After recognizing the advantages of natural fillers and fibers, more and more research groups started to work on the replacement of glass and carbon fibers in composites and to study natural fiber reinforced unsaturated polyester [167], epoxy [168] and novolac [169] composites. In recent years, increasing quantities of thermoplastic polymers were used as matrix materials in wood/plastic composites (WPC). Due to geographical conditions, i.e. large quantities of primary wood raw material as well as byproducts, wood composites are

used in the building industry as decking mainly in North America. [170] Europe is behind the US and Canada in the application of natural fiber reinforced plastics. Hemp, flax and jute are more often used here as natural reinforcements mostly in the automotive industry [171], since wood based raw materials, as well as wood waste are available in smaller quantities. [170] [171] Commodity polymers are used the most often as matrices for the production of composites. [172] Internal panels in cars are produced from polypropylene or polyurethane reinforced with natural fiber. [173] Apart from the advantages listed above, natural fibers have also some drawbacks. Their hydrophilic nature may create problems when introduced in polymer composites. Moisture content can reach as high as 10 wt% depending on their chemical composition and the amount of voids in the non-crystalline regions. The mechanical properties of composites are strongly affected by the moisture content of the fibers. [164] In addition, the transverse strength of the fibers is small and they can easily break or split at this direction of the load.

#### 2.4.2 Polymer matrices

The characteristics of the *polymer matrix* strongly influence the effect of fiber on composite properties. The role of the polymer matrix is to determine and maintain the shape of the composite, to keep the fibers in position, to prevent the fibers from buckling, and to protect the fiber surfaces from chemical and mechanical damage. Apart from the fiber characteristics, the matrix properties influence also the performance of the composite, and the selection of the polymer depends on the intended application.

Based on the chain structure, polymers can be classified as linear, branched or cross-linked. In linear polymers, the mer units are from single continuous chain and the mer units in the chain are bonded together by weak Van der Waals forces. In the case of branched polymers, additional side branches result from further reaction that occurs during synthesis. In cross-linked polymers, the side branches join up with adjacent branches chains. These bonds are covalent bonds formed during the synthesis of the polymer or at elevated temperature, resulting in a cross-linked polymer chain network. [174] Polymers can also be classified as either thermosets or thermoplastics. Thermoplastic polymers melt upon heating and return in their original chemical state upon cooling, whereas, thermoset polymers become infusible and insoluble upon heating and do not return in the original chemical state upon cooling. Thermoplastics can be further classified as amorphous, semi-crystalline or highly-crystalline. Amorphous thermoplastics have no long range order on supramolecular level. Semi-crystalline and highly-crystalline thermoplastics have at least some portion of

their bulk with a long range order. Thermoset polymers can be amorphous or semicrystalline. [175]

Epoxy resin is one of the most resistant thermosetting polymers and contains more than one ethoxyline group in its molecular structure. The epoxy monomer contains epoxide groups which can polymerize in the presence of a ‘hardener’. The polymerisation process is known as ‘curing’, and it can be controlled by temperature, choice of resin/hardener and the ration of the reactive components. There are two main categories of epoxy resins, the glycidyl and the non-glycidyl epoxies. Diglycidyl ether of bisphenol-A (DGEBA) is a typical commercial epoxy resin and it is synthesized by reacting bisphenol-A with epichlorohydrin in the presence of a basic catalyst. [176] Fig. 2.17 shows the structure of DGEBA resin. [177] The properties of the resins depend on the value of  $n$ , which is the number of repeating units commonly known as degree of polymerisation. Typically,  $n$  ranges from 0 to 25 in many commercial products.

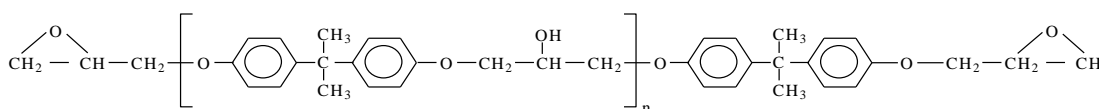


**Fig. 2.17 – Generalised structure of bisphenol-A epichlorohydrin resin (or DGEBA).**

The curing agents usually include amine, polyamides, phenolic resins, anhydrides, isocyanates and polymercaptans compounds or a mixture of them. The stoichiometry of the epoxy/hardener system affects the properties of the cured material. By employing different types and amounts of hardener, one can control the cross-linking density which can affect further the structure and the final properties. Amines and amine-functional amides are the most commonly used hardeners for high-performance, ambient-cured industrial maintenance epoxy resins. The typical reactions between epoxy and amine hardener are shown in Fig. 2.18. [177]

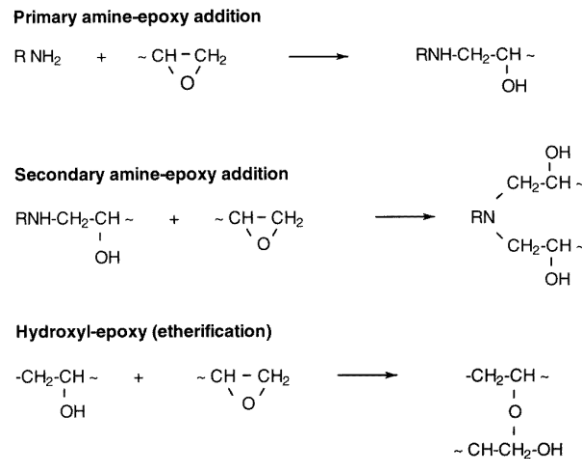


Fig. 2.18 – Epoxy reaction mechanisms. [177]

Primary and secondary amines are highly reactive with epoxide groups and nucleophilic ring-opening addition reactions occur. At the same time, an etherification reaction can also occur between the reacted epoxy groups which carry a terminal –OH group, with the non-reacted epoxide groups. [177] These epoxy polymers are commonly used as adhesives, high-performance coatings and potting, and encapsulating materials, owing to their excellent electrical insulating properties low shrinkage, good adhesion to many metals and resistance to moisture, thermal and mechanical shock.

### 2.4.3 Interphase between fiber and matrix and interfacial interactions

The *interphase* is considered as a crucial parameter in controlling the overall composite performance. The load is transferred from the matrix to the fiber through the interphase, and deformation of the interphase region upon loading is critical in absorbing energy during failure. [158] [159] The interphase joins the composite constituents, and it serves as an important determinant for the composite properties such as interlaminar shear strength (ILSS), stiffness, delamination resistance, fatigue and corrosion resistance. Therefore, it is imperative that the interphase should be ‘engineered’ to enhance the component interaction. [178]

As noted by Hoecker and Karger-Kocsis, [179] the inherent three dimensional stresses that arise within laminate composite samples are quite complicated; thus, single fiber testing has been adopted to simplify analysis. Currently, the test of single fiber microcomposites is a widely used method to analyze the fiber/matrix interphase, in which single fibers are embedded in special geometries of matrix blocks. Micromechanical test methods include: a) *the single fiber pull-out test*, b) *the single fiber micro-debond test*, c) *the*

single fiber fragmentation test and d) the single fiber push-out test (or indentation) which are illustrated schematically in Fig. 2.19.

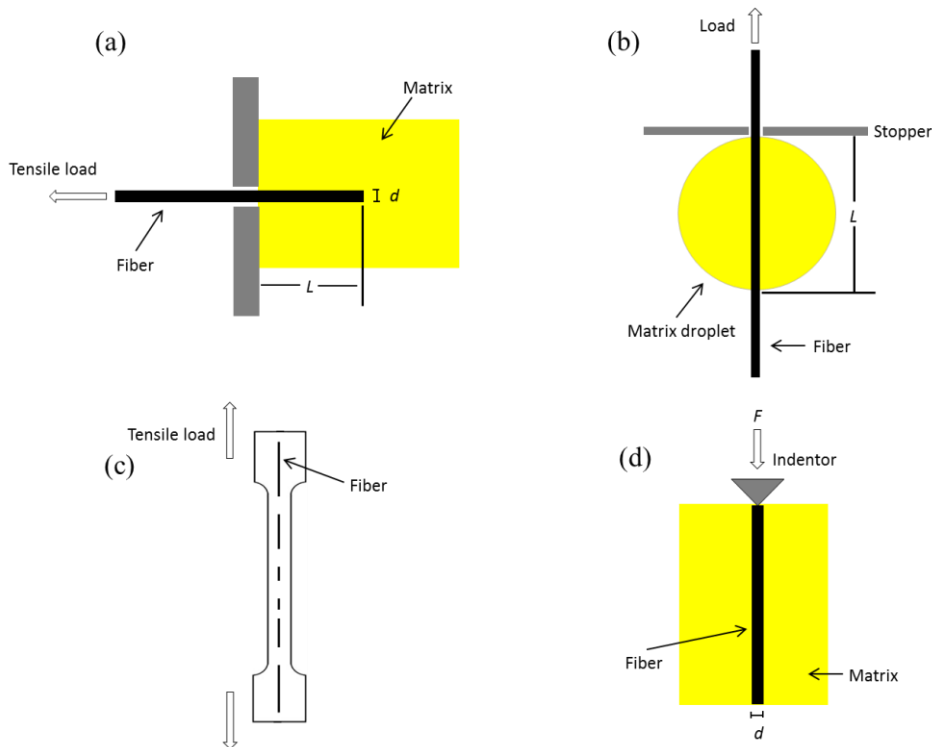


**Fig. 2.19 – Schematic illustration of the different micromechanical tests used to determine the interfacial adhesion strength of single fiber model composites. a) single fiber pull-out test, b) single fiber micro-debond test, c) single fiber fragmentation test and d) single fiber push-out test (or indentation).**

Matrix/fiber interactions lead to the development of an interphase with properties different from those of both components. Strong interaction is needed that is usually achieved by the creation of covalent bonds between the fiber and the matrix. Other types of interactions discussed sometimes are, Van der Waals forces, electrostatic interactions, interdiffusion, mechanical interlocking, and they usually depend on the fiber surface chemistry or the matrix functionality.

In fiber reinforced polymers, strong interaction is usually achieved by coupling. This assumes the chemical, covalent bonding of the components. However, either the fibers or the polymers rarely contain reactive groups, which can react with each other. As a consequence, *coupling agents* are used, which can react both with the polymer and the fiber. A typical example is the use of organofunctional silane coupling agents in glass fiber reinforced thermoset composites. The properly selected organofunctional group reacts with the matrix polymer, while silanols formed by hydrolysis from trimethoxy groups react by condensation

with the active –OH functionalities of the GF surface. The success of silanols in such composites led to their application in other material combinations. The principle of coupling and the example presented above clearly indicates that coupling agents are system specific, so they must be selected according to the chemical structure of the component.



## Chapter 3

### Experimental Techniques

#### 3.1 Analytical methods

##### 3.1.1 Fourier transform infrared spectroscopy (FT-IR)

Infrared (IR) spectroscopy is a useful analytical technique for studying pure rotational, pure vibrational, and rotation-vibration energy changes in the ground state of molecules. [180] Especially, it deals with the interaction between a molecule and photon energy from the IR region (IR region =  $4000 - 400 \text{ cm}^{-1}$ ) of the electromagnetic spectrum, which is translated as energy of molecular vibration, either stretching or bending. The appearance of a vibrational transition in the IR region depends on an overall change of the electric dipole moment during the vibration, and the intensity of the bands is dependent on the magnitude of the dipole moment change. [180] IR gives information on vibrational frequencies which have been extensively used to fingerprint certain groups in different molecules. In FT-IR spectroscopy, there are three frequency regions, which are attributed to different vibration modes: near-infrared ( $10000-4000 \text{ cm}^{-1}$ ), middle ( $4000-200 \text{ cm}^{-1}$ ) and far infrared ( $200-10 \text{ cm}^{-1}$ ). FT-IR spectrum is plotted as transmittance (or absorbance) versus wavenumber. Liquids are examined as thin films sandwiched between two polished NaCl plates that display no absorbance in IR region. Solids usually are incorporated into thin KBr disk, prepared under high pressure, or mixed with non-volatile liquid and ground to a paste that is smeared between salt plates.

##### 3.1.2 Raman and Surface-enhanced Raman spectroscopy

Raman spectroscopy belongs to the family of vibrational spectroscopy, and it is commonly used as a fingerprint of chemical bonds in molecules. The Raman effect allows the observation of vibrational spectra giving complementary information to those of infrared spectroscopy. The most important stimulus to the development of Raman spectroscopy has been the laser, invented by Maiman in 1960. [181] Due to its non-destructive character; Raman spectroscopy represents one of the most useful tools to obtain information about the structure and properties of molecules from their vibrational transitions. However, the direct assignment of Raman bands of relatively complex species is rather complicated. [182]

The Raman instrument consists of 3 components: a laser source, a sample illumination system and a spectrophotometer. When electromagnetic radiation falls on an atomic or molecular sample, it may be absorbed if the energy of the radiation corresponds to the separation of two energy levels of the atoms or molecules. If not, the radiation will be either transmitted or scattered. The scattered light consists of two types: *i*) one called Rayleigh scattering which is strong and has the same frequency as the incident beam ( $\nu_0$ ); it was Lord Rayleigh in 1871 who showed that the intensity  $I_s$  of scattered light is related to  $\lambda$  by

$$I_s \propto \lambda^{-4} \quad (3.1)$$

and *ii*) the other called Raman scattering which is very weak ( $\sim 10^{-5}$  of the incident beam), and has frequency  $\nu_0 \pm \nu_m$ , where  $\nu_m$  is a vibrational frequency of a molecule. The  $\nu_0 - \nu_m$  and  $\nu_0 + \nu_m$  lines are called Stokes and anti-Stokes lines, respectively. In fact, in Raman spectroscopy it is measured the vibrational frequency ( $\nu_m$ ) as a shift from the incident beam frequency ( $\nu_0$ ). In contrast to IR spectra, Raman spectra are measured in the UV-vis region where the excitation as well as Raman lines appear. The incident radiation should be highly monochromatic so as the Raman effect can be observed, and because Raman scattering is so weak should be also very intense. According to classical theory, Raman scattering can be explained as follows: The electric field strength ( $E$ ) of the electromagnetic wave (laser beam) fluctuates with time ( $t$ ) as described by

$$E = E_0 \cos 2\pi\nu_0 t \quad (3.2)$$

where  $E_0$  is the vibrational amplitude and  $\nu_0$  is the frequency of the laser. If a diatomic molecule is irradiated by this light, an electric dipole moment  $P$  is induced

$$P = \alpha E = \alpha E_0 \cos 2\pi\nu_0 t \quad (3.3)$$

Here,  $\alpha$  is a proportionality constant called polarizability. Accordingly, if the molecule is vibrating with a frequency  $\nu_m$ , the nuclear displacement  $q$  is written as

$$q = q_0 \cos 2\pi\nu_m t \quad (3.4)$$

where  $q_0$  is the vibrational amplitude. For small amplitude of vibration,  $\alpha$  is a linear function of  $q$ . Thus, it can be written

$$\alpha = \alpha_0 + (\delta\alpha/\delta q) q_0 + \dots \quad (3.5)$$

The combination of [3.3], [3.4] and [3.5] equations results in the formula:

$$\begin{aligned}
 P &= a E_0 \cos 2\pi\nu_0 t = a_0 E_0 \cos 2\pi\nu_0 t + \left(\frac{\delta a}{\delta q}\right) q E_0 \cos 2\pi\nu_0 t = a_0 E_0 \cos 2\pi\nu_0 t + \\
 &\left(\frac{\delta a}{\delta q}\right) q_0 E_0 \cos 2\pi\nu_0 t \cos 2\pi\nu_m t = a_0 E_0 \cos 2\pi\nu_0 t + \frac{1}{2} \left(\frac{\delta a}{\delta q}\right) q_0 E_0 \{ \cos [2\pi(\nu_0 + \nu_m)t] + \\
 &\cos [2\pi(\nu_0 - \nu_m)t] \} \quad (3.6)
 \end{aligned}$$

According to classical theory, the first term represents an oscillating dipole that radiates light of frequency  $\nu_0$  (Rayleigh scattering), while the second term corresponds to the Raman scattering of frequency  $\nu_0 + \nu_m$  (anti-Stokes) and  $\nu_0 - \nu_m$  (Stokes). If  $(\delta\alpha/\delta q)_0$  is zero, the vibration is not Raman-active, therefore, the rate of change of polarizability ( $\alpha$ ) with the vibration must not be zero. Accordingly, Fig. 3.1 illustrates the Raman scattering in terms of a simple diatomic energy level. In normal Raman spectroscopy, the exciting line ( $\nu_0$ ) is chosen so that its energy is far below the first electronic excited state. The dotted lines indicate a ‘virtual energy state’ to distinguish from the ‘vibrational energy state’. The population of molecules at  $v=0$  is much larger than that at  $v=1$  (Maxwell-Boltzmann distribution law). Hence, the Stokes lines are stronger than the anti-Stokes lines under normal conditions. Since both give the same information, it is necessary to measure only the Stokes side of the spectrum. Resonance Raman (RR) scattering occurs when the exciting frequency coincides with the electronic transitions, so that its energy intercepts the manifold of an electronic excited state. Excitation then produces RR spectra that show extremely strong enhancement of Raman bands originating in this particular electronic transition.

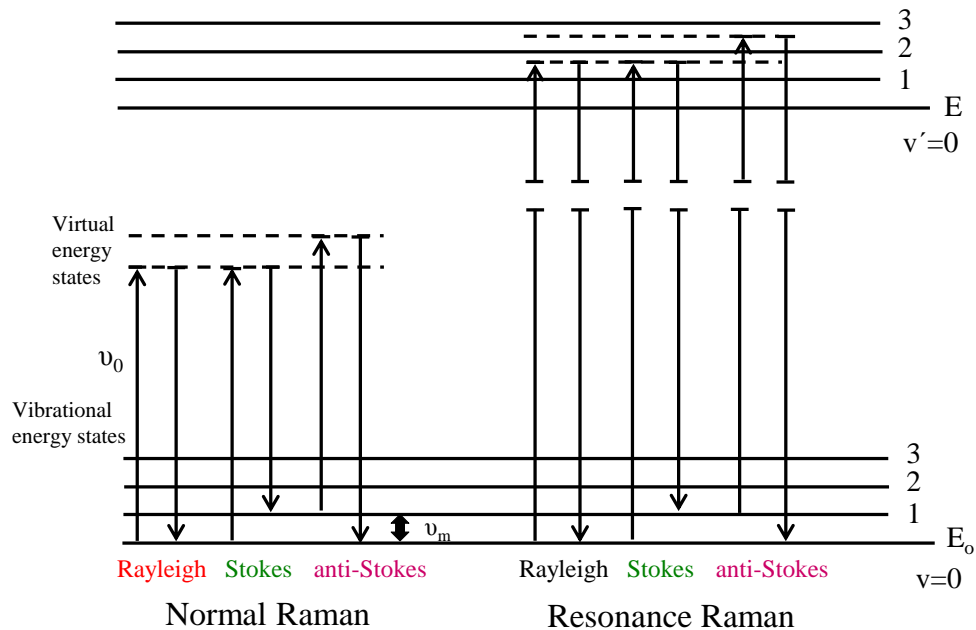


**Fig. 3.1 - Mechanism of various light-scattering processes: Rayleigh, Stokes and anti-Stokes Raman, for non-resonance and resonance Raman.**

In this study, Raman is a facile tool for the characterization of CNTs as well as jute cellulose based natural fibers. Raman spectra were measured with an alpha300R Raman spectrometer system (WITEC GmbH, Germany), and the same instrument was used for SERS ultradetection of Rhodamine molecules. The spectra were acquired in the back-scattering geometry and the excitation wavelength was 532 nm from an Nd:YAG laser in various powers. In most of the cases, the 20× magnifying objective of the microscope focused the beam into a spot of about 1 μm in diameter was used. In general, when higher sensitivity is required, Argon-ions lasers with line at 488 and 514 nm can be utilized.

The Raman spectra of CNTs are rich in information about the structure and properties of nanotubes. Normally, within the spectrum, the radial breathing mode (RBM), the disorder-induced mode (*D* mode) and the tangential modes (G mode), can be used to access different properties. Radial breathing band (RBM) appears in a range of 120-250 cm<sup>-1</sup>, and it corresponds to the atomic vibration of C atoms in the radial direction, as if the tube was breathing. (Fig. 3.2<sup>[4]</sup>). The frequency of the radial breathing mode can be used to determine the diameter of the nanotube. RBM mode, in fact, is proportional to the inverse of the nanotube diameter. For large diameter tubes ( $d > 2$  nm), the intensity of the RBM is weak and hardly detectable. The observation of characteristic multi-peak features around 1580 cm<sup>-1</sup> (G-band) provides also a signature of CNTs. Spectra in this frequency range can be used for SWNT characterization, independent of the RBM observation. This multi-peak feature can also be used for diameter characterization, although the information obtained is less accurate than the RBM feature. G-band also provides information about the metallic character of the SWNTs in resonance with a given laser line. Thus, Raman scattering can distinguish between metallic and semiconducting nanotubes. In metallic CNTs the lower high-energy mode is strongly broadened and shifted to smaller energies (1540 cm<sup>-1</sup>). This so-called metallic spectrum appears only in metallic tubes. Finally the observation of a peak around 1450 cm<sup>-1</sup> (D-band) is also common. The intensity of the disorder-induced D-band

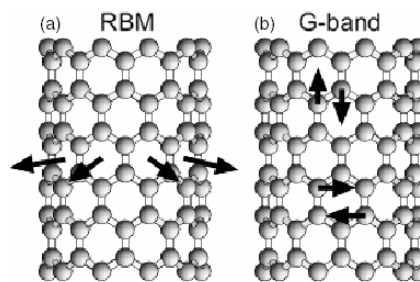


**Fig. 3.2 - Schematic showing the atomic vibrations for (a) the RBM and (b) the G-band modes.**<sup>[4]</sup>

<sup>[4]</sup>[http://www.scielo.br/scielo.php?pid=S0001-37652006000300004&script=sci\\_arttext](http://www.scielo.br/scielo.php?pid=S0001-37652006000300004&script=sci_arttext)

can be used to determine the defects in the structure. Furthermore it can be used to monitor the process of functionalization, which transforms the carbon from  $sp^2$  to  $sp^3$  hybridization.

Nevertheless, the application of conventional Raman spectroscopy for a lot of molecules is limited by the weak intensity of the Raman scattered light. One way to overcome this is the so-called surface-enhanced Raman spectroscopy (SERS). [81] The SERS effect is known as a large enhancement of the Raman signal of certain molecules adsorbed on roughened metallic surfaces. The first period of SERS started after its discovery and lasted until the mid-1980s. The research activity was focused on getting a mechanistic comprehension of the  $10^6$  fold intensity enhancement observed for normal Raman scattering. It was stated [81] [99] [101] that the enhancement of the Raman signal can be considered as the product of two main contributions: i) *an electromagnetic enhancement mechanism* and ii) *a chemical or charge-transfer enhancement mechanism*, while the contribution of the electromagnetic mechanism to the total enhancement is of the order of  $10^4$ , and the chemical mechanism participation is in the range of  $10^2$ . Surface selection rules were also presented in this time. In their simplest form, and assuming no specific symmetry selection rules, the most intense bands are predicted as those from vibrations, which induce a polarization of the adsorbate electron cloud perpendicular to the metal surface. [100] This information can be used qualitatively to find out details about the angle formed between the adsorbed molecule and the metal surface. It should be also mentioned the case of surface-enhanced resonance Raman scattering (SERRS) with combined SERS and resonant Raman scattering (RRS) enhancement factors in the range of  $10^9$ - $10^{10}$ . [98] In the next decade, the attention of researchers of the condensed matter physics was turned from SERS to other subjects, and other researchers started working in SERS spectroscopy as a potential analytical tool in the field of electrochemistry, heterogeneous catalysis, polymer science, biochemistry of surface immobilized proteins, etc. [183] In the last years the interest in SERS has been extended mainly because of the discovery of a single molecules by SERS. [184] Moreover, there is an huge research interest concerning how to control, manipulate and amplify light on the nanometer length scale using the properties of the collective electronic excitations in noble metal films or nanoparticles. Although the theoretical understanding of the mechanism of SERS is not definite and still evolving, the experimental data have demonstrated SERS to be a sufficiently sensitive spectroscopic method for possible use in surface science, analytical and environmental applications, biomedicine and biochemistry, etc. [185] [186] [187]

### 3.1.3 Ultraviolet-visible spectroscopy (UV-vis)

UV-vis spectroscopy is suitable for characterization of many compounds due to their absorption of the light. [188] In UV-vis, absorbance  $A$ , as a measure of ratio between the source intensity  $I_0$  and the transmitted intensity  $I$ , is measured as function of the wavelength and it obeys the Beer-Lambert law:

$$A = -\log \frac{I}{I_0} = \varepsilon \cdot c \cdot b, \quad (3.7)$$

where  $\varepsilon$  is the molar absorptivity,  $c$  is the concentration of solution and  $b$  is thickness of the cuvette. In thin film geometry, the absorbance is usually expressed as:

$$A = -\ln \frac{I}{I_0} = \alpha \cdot d \cdot \log(e), \quad (3.8)$$

where  $\alpha$  is the absorption coefficient of the film material and  $d$  is the film thickness. Absorption spectra reflect electronic structure of molecules and therefore, their shape depends on bonding and polarization of the molecules (the Franck-Condon principle). [189]

### 3.1.4 Electrokinetic analysis

The zeta potential (ZP) and the size distribution of colloidal NPs were measured with the Zetasizer nano ZS, Model Zen 3600 (from Malvern Instruments Ltd., UK), which works in the particle size range from 0.6 nm to 6  $\mu\text{m}$  and uses a 4 mW He-Ne (633 nm) laser. The size measurements employed the NIBS (non-invasive back scatter technology). The Zetasizer measures zeta potential by measuring the velocity of the charged particles moving toward the electrode of the opposite sign under the applied potential. The ZP is proportional to the velocity of the particles. All measurements were made using disposable cells.

### 3.1.5 Thermogravimetric analysis (TGA)

TGA is an analytical method used to determine the thermal stability of a compound, by monitoring the weight change that occurs upon heating. The analyzer usually consists of a high-precision balance with a pan loaded and a furnace. The measurement is normally performed in air or in an inert atmosphere, such as  $\text{N}_2$  or Argon and the weight loss of a sample is recorded as a function of temperature. A computer is used to control the instrument. TGA is commonly employed to determine characteristics of materials such as polymers, to determine degradation temperatures, absorbed moisture content of materials,

the level of inorganic and organic components in materials, decomposition points, and solvent residues.

### 3.1.6 X-ray Photoelectron Spectroscopy (XPS)

XPS is a very informative surface chemical analysis technique that involves analysis of kinetic energy distribution of electrons knocked out from inner electron shells of atoms by a monochromatic beam of soft X-rays. [190] Due to the softness of X-rays, free electrons pass small distances in a material without scattering, therefore, only electrons ionized close to the sample surface (max 10 nm) could be detected. The kinetic energy of the emitted electrons,  $E_k$ , is equal to the difference between the energy of X-ray photons ( $E_p = hc$ ) and the electron binding energy,  $E_b$ :

$$E_k = hc / \lambda - E_b \quad (3.9)$$

The core electrons of each element have unique binding energy, thus by its measuring the elemental composition could be determined. The electron binding energy also depends on the chemical environment of the element. This variation of the binding energy assists to study the chemical status of the element (oxidation state, functional groups, etc.). After all, XPS provides a wealth of information related to elemental composition, empirical formula, chemical state and electronic state of the elements present in sample.

### 3.2 Atomic force microscopy (AFM)

AFM belongs to a family of Scanning Probe Microscopy (SPM) instruments, and it is widely used for the investigation of materials' surface properties at the nanometer scale. The development of the AFM was preceded by the development of the Scanning Tunneling Microscope (STM) in 1982 at IBM Zurich Research Laboratory by G. Binnig and H. Rohrer. [191] AFM is used to solve processing and materials problems for a lot of technological issues related to electronics, telecommunications, biological, chemical, automotive, aerospace and energy industries. AFM offers a wide range of new contrast mechanisms which provide information about

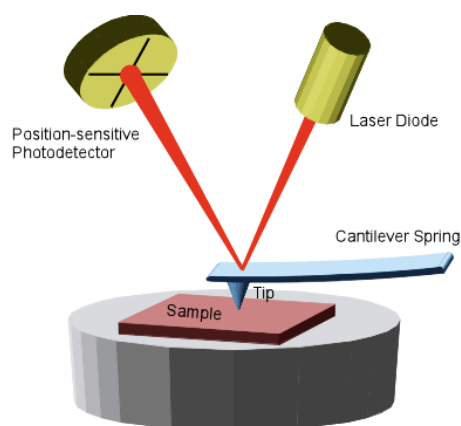


**Fig. 3.3 - Schematic illustration of the AFM working principle.** [5]

friction, adhesion, elasticity, hardness, electric fields, magnetic fields, carrier concentration, temperature distribution, spreading resistance and conductivity.

During the scanning process, a sharp tip at the end of a flexible cantilever interacts with the specimen to form three-dimensional surface topography image of nanometer lateral and subangstrom vertical resolution. The tip-sample interaction is monitored by reflecting a laser off the back of the cantilever into a split photodiode detector. A principal schematic of AFM is shown in Fig. 3.3. [5] In general, physical nature and character of tip-sample interaction are quite complicated, since they are defined by tip characteristics, surface properties and surrounding medium. The main forces which contribute to exert the tip are:

force, coming from mechanical contact of tip end atoms with sample, van der Waals force and capillary force, arising from condensation of water vapour in the contact area. The forces between them are not measured directly, but calculated by measuring the deflection of cantilever. The tip-sample interaction force  $F$  is proportional to the tip deflection  $x$  (according to Hook's law  $F = -kx$ , where  $k$  is the stiffness of the cantilever). The interaction force between the surface and the tip could be either attractive, reaching maximum value at

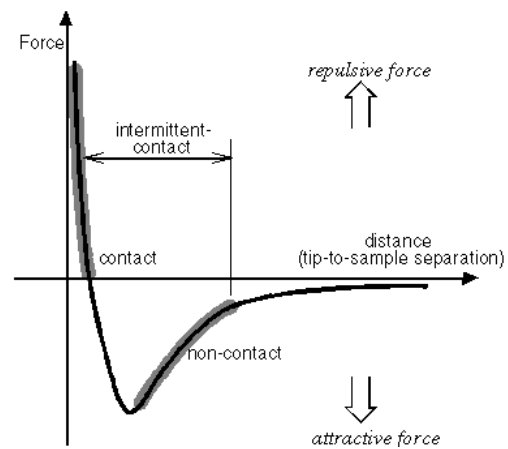


**Fig. 3.4 - Force versus distance curve and AFM operating modes.** [6]

either attractive, reaching maximum value at certain sample-to-tip distance, or repulsive, reaching infinity when this distance approaches zero. The dependence of force versus sample-to-tip distance is illustrated in Fig. 3.4. [6]

AFM can be operated in many ways measuring different interactions between the probe tip and sample and using different types of detection schemes. The two most commonly used modes of operation are contact mode AFM and TappingMode™ (or intermittent mode). In TappingMode (TM-AFM), a probe cantilever is driven to vibrate with high amplitude (10–100nm) near its resonant frequency by a piezoelectric element. Since the contact time between the tip and the sample is two orders shorter as compared to *contact mode*, the TM-AFM is less damaging and typically used for imaging topography of soft materials. Because of the high amplitude of oscillation, the tip propagates through regions of

[5] [http://www3.physik.uni-greifswald.de/method/afm/AFM\\_laser.gif](http://www3.physik.uni-greifswald.de/method/afm/AFM_laser.gif) ml

[6] [www.nanoscience.com/education/AFM.html](http://www.nanoscience.com/education/AFM.html)



attractive (Van der Waals, electrostatic) and repulsive forces in a single oscillation cycle (Fig. 3.4). The amplitude and the frequency of the cantilever decrease while approaching the sample surface. Upon scanning, these parameters (and, hence, the force gradient) are maintained constant at a set-point level, by adjusting the tip-sample distance. This is controlled by feedback loop. The feedback signal and the phase lag of the cantilever oscillation relative to the driving oscillation are displayed yielding height and phase images, respectively.

### 3.3 Scanning electron microscopy (SEM)

The electron microscopy images were collected using a Zeiss NEON 40 (from Carl Zeiss SMT AG, Germany) field emission microscope, operated at 1 kV, with a nominal resolution of 0.23 nm.<sup>[7]</sup>



**Fig. 3.5 – FIB/FE-SEM CrossBeam  
Carl Zeiss NEON 40 EsB.<sup>[7]</sup>**

### 3.4 Transmission electron microscopy (TEM)

The transmission electron microscopy (TEM) is an imaging technique based on the irradiation of a sample by a beam of electrons. The image is formed, magnified and detected by a sensor such as CCD camera. Contrary to the normal light microscope where photons are employed, TEM uses electrons as light source. In this way it is possible to get a resolution a thousand times better than with a light microscope thanks to their much lower wavelength. The filament on the top of the microscope emits electrons that go through vacuum in the column of the microscope. Electromagnetic lenses are used to focus the electrons into a very thin beam. This beam travels through the sample to study.

<sup>[7]</sup><http://www.semtechsolutions.com/node/138/zeiss-neon-40-esb-crossbeam> (SEM)

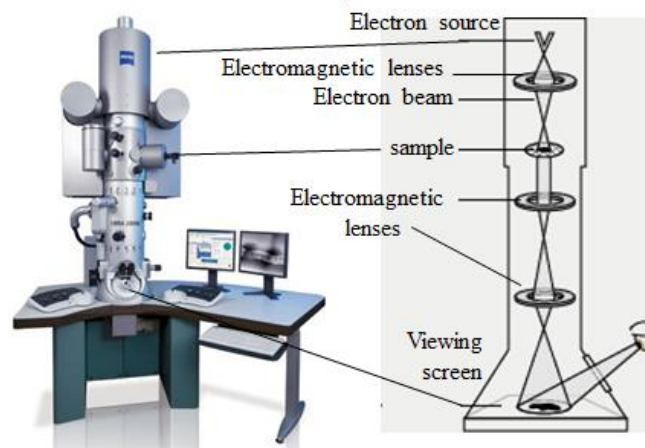


**Fig. 3.6 - Transmission Electron Microscope (TEM), Zeiss Libra 200 MC, U = 200. Picture (left side) and scheme of TEM (right side).** <sup>[8]</sup>

Depending on the density of the material, some of the electrons are scattered away from the beam. At the bottom of the microscope the unscattered electrons hit the fluorescent screen and an image of the sample is obtained. The image can be photographed with a camera. The TEM micrographs were recorded on a high-resolution CCD camera using Digital Micrograph software.

### 3.5 Electrical resistance measurements

DC-electrical resistance measurements were performed using the Keithley 2400 Source-Measure Unit. The Keithley model 2400 SourceMeter solution is a 20W instrument that allows sourcing and measuring voltage from  $\pm 5\mu\text{V}$  (sourcing) and  $\pm 1\mu\text{V}$  (measuring) to  $\pm 200\text{V}$  DC and current from  $\pm 10\text{pA}$  to  $\pm 1\text{A}$ . All data were automatically transferred to computer and treated with an interfaced LabVIEW™ program.



**Fig. 3.7 - Photo of the Keithley 2400 source-measure unit used for the DC-electrical resistance measurements.**

<sup>[8]</sup> <http://ibme.utk.edu/wp-content/uploads/2013/04/Zeiss-Libra200MC.jpg>

## Chapter 4

### Synthesis and properties of nano-sized colloidal systems

#### 4.1 Chemical modifications of carbon nanotubes (CNTs)

##### 4.1.1 Acid treatment of MWCNTs

Throughout the whole experimental work, commercially available MWCNTs (Nanocyl, NC 7000) with a carbon purity of >90%, average length 1.5  $\mu\text{m}$  and diameters around 10 nm were received from Nanocyl S.A. (Sambreville, Belgium). As received MWCNTs, were treated first with hydrochloric acid (HCl) to remove impurities arising from the catalytic process. [192] In brief, one gram of MWCNT was placed in a 500 ml round bottom flask, and 200 ml of HCl was added. The mixture was stirred for 2 h, then diluted in water, filtered and washed several times with deionized water until the neutral pH value. The TEM images in Fig. 4.1 show the structure of as received MWCNTs where catalytic residue particles could be observed, as well as after the HCl treatment that all the impurities have been removed.

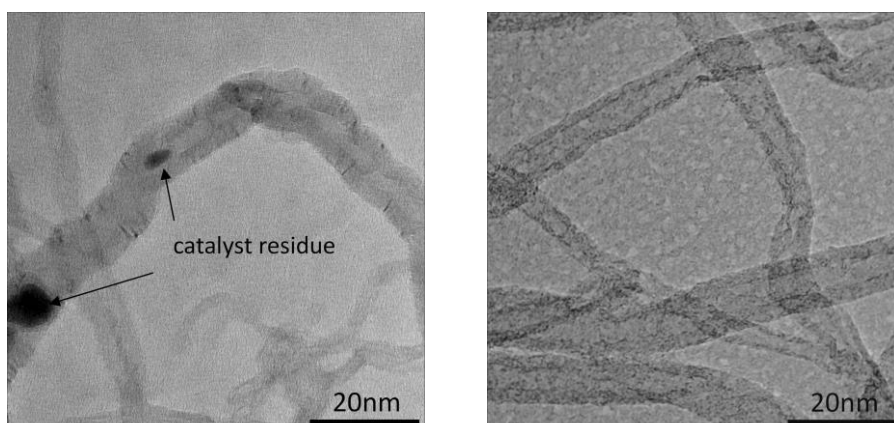


Fig. 4.1 – TEM images of as received (left side) and HCl treated (right side) MWCNTs.

In the next step, MWCNTs were treated with a mixture of concentrated  $\text{H}_2\text{SO}_4$  (98%) /  $\text{HNO}_3$  (67%) to introduce carboxylic acid groups (MWCNT-COOH). [193] Briefly, 1 g of MWCNTs was added in a round bottom flask containing 120 ml of the acidic mixture, and stirred for 6 h at 60  $^\circ\text{C}$  under reflux. The mixture was left to cool down and diluted with distilled water followed by filtering through a polycarbonate membrane (47 mm diameter and 0.4  $\mu\text{m}$  pore size). Several steps of cleaning with distilled water were acquired to reach a

neutral pH value. The MWCNTs were collected and dried overnight under vacuum at 60 °C. The carboxyl groups were converted further to carbonyl chloride groups. In that case MWCNT-COOH (70 mg) were treated with 50 ml of  $\text{SOCl}_2$  / 2.5ml DMF (20:1 v/v) at 70 °C for 24 h under argon atmosphere. Thionyl chloride was removed by vacuum filtration using a PTFE membrane (47 mm diameter and 0.2  $\mu\text{m}$  pore size) and the MWCNT-COCl filtrate was washed several times with extra dry THF and finally dried in a vacuum oven at 50 °C for 6 h. The carboxylation and acyl chlorination treatment of MWCNTs were carried out to attach them via covalent and non-covalent bonds to amine terminated glass fiber which will be described in detail in Chapter 6. The morphology of MWCNTs after the acid oxidation is depicted by the TEM image in Fig. 4.2, and as it can be observed the outer wall of CNTs seems to expose some defects.

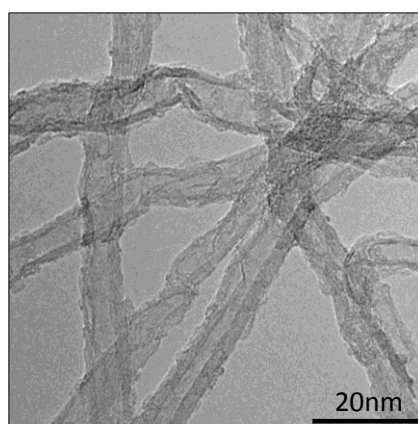


Fig. 4.2 – TEM images of as received (left side) and HCl treated (right side) MWCNTs.

Besides, the Raman spectra in Fig. 4.3 reveal that the amount of defects after the harsh acidic treatment has not been significantly increased and this is a good hint for keeping the electronic properties of the starting material unaltered.

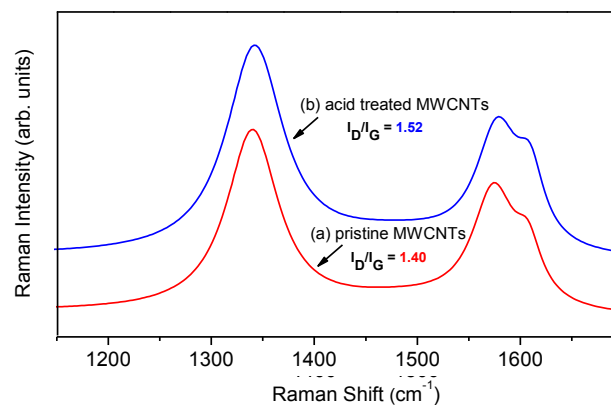


Fig. 4.3 – Raman spectra of (a) pristine (red line) and (b) acid treated (blue line) MWCNTs.

#### 4.1.2 Grafting of MWCNTs with Polystyrene (PS) chains

In this thesis, hydrochloric acid purified MWCNTs have been grafted with polymeric chains for their application in polymer composites. For this purpose, nitroxide mediated radical polymerization (NMP) was performed with 2,2,6,6-tetramethylpiperidinyl-1-oxyl (TEMPO) following the method of Lou *et al.*, [194, 195] and polystyrene homopolymer with TEMPO terminal groups has been synthesised. The PS-TEMPO precursor was grafted afterwards (“grafting to” approach) onto the MWCNT surface via radical addition as described in the work of Wode *et al.* [196] The average molecular weight per number of the precursor was determined from GPC to be 55.600 g/mol (PDI=2.4). The TEM images in Fig. 4.4 show the PS brushes grafted on the outer wall of CNTs (left image), and the successful grafting was proven by the selective localisation of MWCNT-g-PS in the PS phase of a PS/P2VP blend (right image).

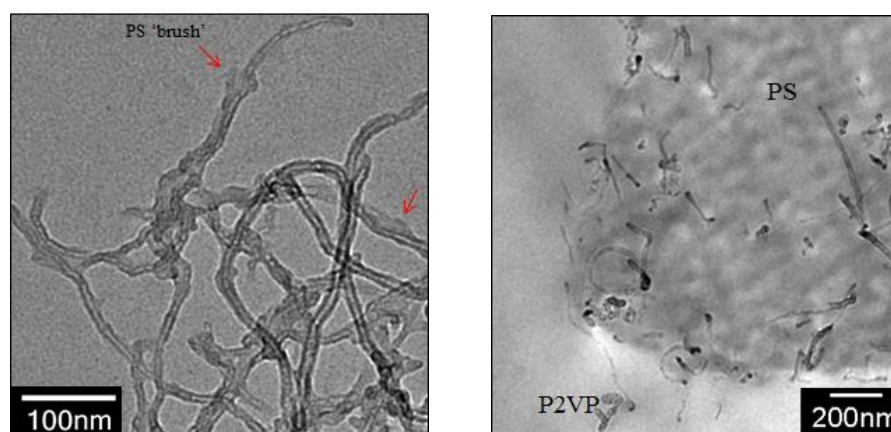


Fig. 4.4 – TEM images showing the PS brushed grafted to the MWCNT surface (left image), and the selective localization of MWCNT-g-PS in the PS phase of a blend (left image).

#### 4.2 Synthesis of silica spheres (~120 nm)

Prior to use, all glassware were cleaned with a 3:1 v/v acidic solution consisting of hydrochloric/nitric acid (36% and 68%, respectively) and then rinsed copiously with MilliQ water. Monodisperse SiO<sub>2</sub> spheres were synthesized through base-catalyzed hydrolysis of TEOS following the protocol of An *et al.* with some slight modifications. [197] In brief, a round bottom flask was charged with 3.3 mL of saturated ammonia solution (28%) and 47 mL of ethanol under magnetic stirring to form a homogeneous solution. In this mixture, 4 mL of TEOS were injected and kept under stirring at 750 rpm for 24 h. The resulting SiO<sub>2</sub> spheres were centrifuged, washed with ethanol and dried under vacuum at 50 °C for 24 h. The washing steps with centrifugation and redispersion in ethanol were repeated at least five

times in order to fully purify the particles. Fig. 4.5 depicts the SEM (left) and TEM (right) images of bare silica spheres, respectively, with an average diameter of 120 nm.

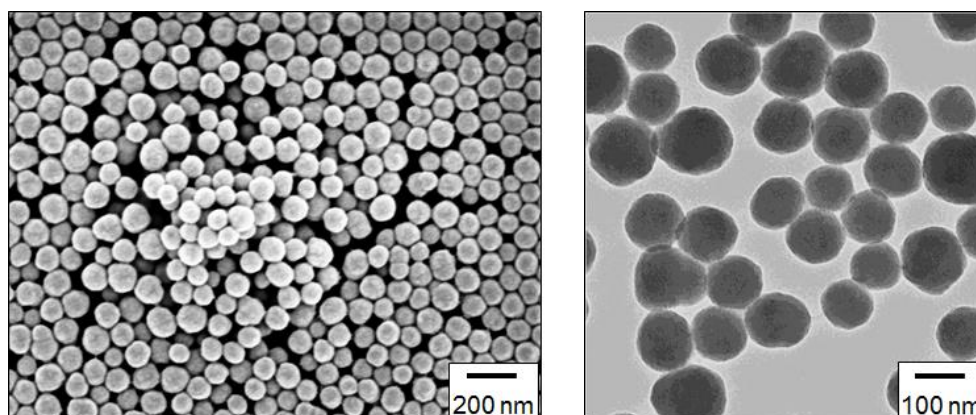


Fig. 4.5 – SEM (left) and TEM (right) images of bare silica spheres.

### 4.3 Synthesis of silica@silver hybrid particles for SERS and catalytic applications

A facile water-based method for the synthesis of silica ( $\text{SiO}_2$ ) spheres decorated with silver nanoparticles (Ag NPs) of controllable and uniform metal size has been developed. The hybrid particles exhibited a raspberry-like morphology, and their potential for SERS and catalytic applications has been demonstrated.  $\text{SiO}_2$  spheres with an average diameter of 120 nm were synthesized and modified with polyethyleneimine (PEI) to introduce amine surface functionalities. The amine groups were coordinated with silver ions ( $\text{Ag}^+$ ) and reduced to Ag seeds using sodium borohydride ( $\text{NaBH}_4$ ). The Ag seeds with an average diameter of 4 nm were uniformly distributed onto the  $\text{SiO}_2$  surface ( $\text{SiO}_2@$ Ag-seed), as revealed by the TEM investigations. Two subsequent silver growth steps were performed over the  $\text{SiO}_2@$ Ag-seed system to improve the optical and spectroscopic responses as well as the catalytic activity. The diameter of Ag seeds was increased to 12 and 19 nm, respectively, hereafter denoted as  $\text{SiO}_2@$ Ag-1 and  $\text{SiO}_2@$ Ag-2. The immobilization and controlled growth of Ag NPs on the  $\text{SiO}_2$  spheres was confirmed by UV-vis spectroscopy, scanning and transmission electron microscopy (SEM, TEM). All specimens displayed remarkable SERS activity increasing with the Ag NP size, showing clear Raman peaks of Rhodamine 6G (R6G). The  $\text{SiO}_2@$ Ag particles were also tested and compared for their catalytic efficiency towards the reduction of 4-nitrophenol (4-Nip) by  $\text{NaBH}_4$ . The principal advantages of this protocol lie on the ability to tune the Ag NP size, the long-term colloidal stability of all fabricated  $\text{SiO}_2@$ Ag systems in aqueous media, and the limited use of hazardous chemicals and pollutant organic solvents during the synthetic process.

### 4.3.1 Decoration of SiO<sub>2</sub> spheres with Ag seeds (SiO<sub>2</sub>@Ag-seed)

Initially, 100 mg of dried SiO<sub>2</sub> spheres were dispersed in 100 mL of MilliQ water and sonicated for 30 min to fully disperse them. To this colloidal solution, 5 mL of PEI aqueous solution (2 mg/mL) were added under gentle magnetic stirring. The mixture was kept for 30 minutes to achieve the adsorption of positively charged PEI chains onto the negatively charged SiO<sub>2</sub> surface followed by centrifugation at 8000 rpm for 30 min to remove excess of PEI. After centrifugation, the supernatant was discarded and the pellet was annealed at 100 °C for 30 min. Afterwards, the PEI modified particles were redispersed in 40 mL of MilliQ water. To this suspension, 1.75 mL of AgNO<sub>3</sub> (10 mM) were added dropwise under magnetic stirring and maintained for 30 min in order to allow a homogeneous coordination of the silver ions with the amine surface moieties. It should be noted that the amine groups of the silica surface are capable of forming complexes with metal ions via coordination.[198] The resulting mixture was centrifuged at 8000 rpm for 30 min, the supernatant was removed and the precipitate was redispersed in 40 mL of MilliQ water. Finally, 1.75 mL of ice-cold freshly prepared NaBH<sub>4</sub> solution (50 mM) was added under vigorous stirring to promote the Ag NP growth. Simultaneously, a rapid color change to slight yellow was observed indicating the formation of Ag NPs (seeds) and the stirring was slowed down after 30 min to ensure that complete reduction has occurred. The solution was centrifuged at 8000 rpm for 45 min, followed by the removal of the supernatant and redispersion in 40 mL of MilliQ water. Subsequent centrifugation-redispersion steps were conducted to remove traces of NaBH<sub>4</sub> as well as Ag NPs not strongly bound to the SiO<sub>2</sub> surface. Finally, the SiO<sub>2</sub>@Ag-seed particles were dispersed and remained in 100 mL of MilliQ water. The average size of silver NPs formed was statistically extracted from the TEM images and found to be (4.2 ± 1.1) nm. The described protocol is illustrated in Fig. 4.6 A, and the fabricated SiO<sub>2</sub>@Ag-seed colloids with a raspberry-like morphology were used further for the subsequent Ag growth steps.

### 4.3.2 Silver growth using SiO<sub>2</sub>@Ag-seed as templates

Two different silver growth steps were performed over the SiO<sub>2</sub>@Ag-seed system using a slightly modified protocol of Yang *et al.* [199] In detail, for the preparation of the SiO<sub>2</sub>@Ag-1 system, 5 mL of a solution composed by 0.4 M glycine buffer solution with pH 8.5 (adjusted by addition of NaOH, 1 M) and CTAB (200 mM) were mixed with 5 mL of the previously synthesized SiO<sub>2</sub>@Ag-seed particles. Then, 100 μL of AgNO<sub>3</sub> (10 mM) were added under medium magnetic stirring. After 30 min, 50 μL of ascorbic acid (50 mM) were

added under vigorous magnetic stirring and the mixture was maintained for 30 min, followed by centrifugation (8000 rpm, 30 min). The supernatant was removed and the precipitant was redispersed in 10 mL of MilliQ water. The average dimension of Ag NPs after this step was measured by TEM and it was  $(12.8 \pm 3.4)$  nm. Further, a second silver growth step was performed using the previously grown  $\text{SiO}_2@Ag-1$  particles as seed system. Briefly, 5 mL of a buffer solution composed by 0.4 M glycine at pH 8.5 and CTAB (200 mM) as stabilizer were mixed with 5 mL of  $\text{SiO}_2@Ag-1$  particles. Afterwards, 100  $\mu\text{L}$  of  $\text{AgNO}_3$  (10 mM) were added under medium magnetic stirring. After 30 min, the silver reduction was carried out adding 50  $\mu\text{L}$  of ascorbic acid (50 mM) under vigorous magnetic stirring and the mixture was allowed to react for 30 min. In order to remove excess of ascorbic acid, the solution was centrifuged at 8000 rpm for 30 min, the supernatant was discarded and the precipitant was redispersed in 10 mL of MilliQ water. TEM analysis of the  $\text{SiO}_2@Ag-2$  particles revealed an average diameter of Ag NPs in the range of  $(19.6 \pm 3.9)$  nm. The subsequent silver growth steps yielding  $\text{SiO}_2@Ag-1$  and  $\text{SiO}_2@Ag-2$  with a raspberry-like morphology are highlighted in Fig. 4.6 B and 4.6 C, respectively.

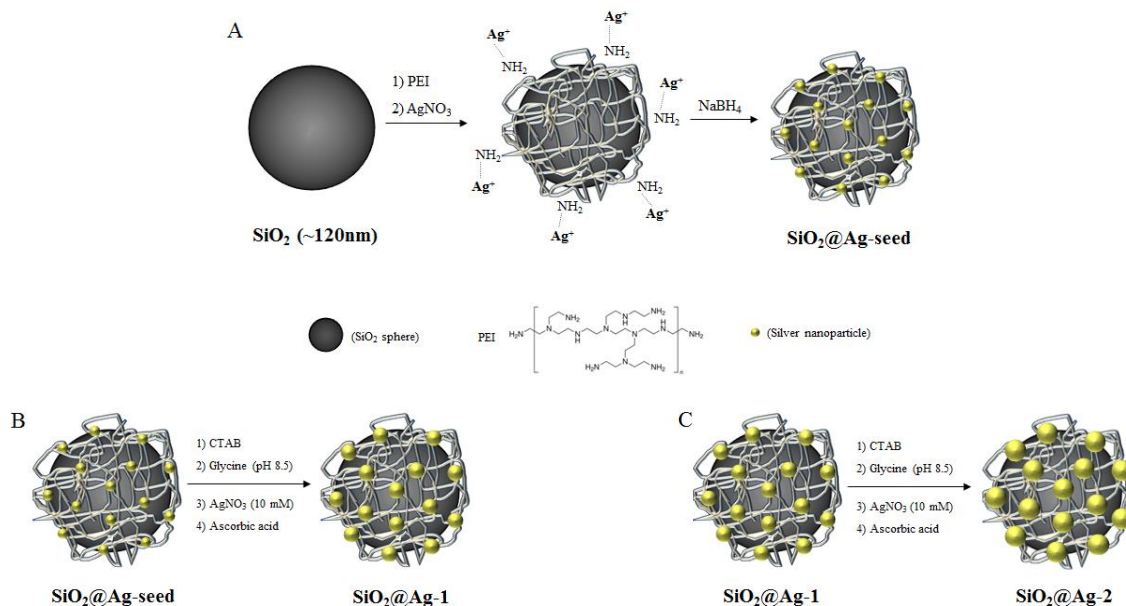


**Fig. 4.6 - A)** Schematic illustration for the decoration of silica particles with silver seeds using PEI as ligand of silver ions and further silver growth on the preformed silver seeds using two subsequent growth steps (B and C).

### 4.3.3 Characterization techniques

Fourier-transformed infrared (FT-IR) spectra were recorded using a Vertex 80v FT-IR spectrometer (Bruker Germany) equipped with a DTGS detector by signal averaging of



256 scans. Approximately 1.0 mg of neat or PEI modified SiO<sub>2</sub> particles were pressed together with 100 mg of crystalline KBr to form pellets. The zeta-potential of SiO<sub>2</sub> particles as a function of pH was investigated by electrokinetic analysis (EKA) at 25.0 ± 0.2 °C using a zeta potential analyser (Zetasizer Nano-ZS, Malvern Instruments Ltd, UK). Aqueous suspensions with 1.0×10<sup>-3</sup> M KCl at different pH values were used for the zeta potential determination and the relation between zeta potential and pH was used to determine the isoelectric point (IEP). X-ray diffractometry (XRD) was performed with an X-ray diffractometer XRD T/T (GE Inspection Technologies Ahrensburg, Germany) in symmetric step-scan mode with  $\Delta 2\Theta = 0.05^\circ$  in transmission operating at 40 kV and 30 mA with Cu K $\alpha$  radiation. All UV-vis spectra were recorded using a Cary 50 scanning spectrophotometer (Varian, USA) with an incorporated xenon flash lamp at room temperature by using 1-cm quartz cell. Scanning electron microscopy (SEM) was performed using the NEON 40 (Carl Zeiss AG, Germany) scanning electron microscope under an accelerating voltage of 1.0 kV. Samples were prepared by drop casting 100  $\mu$ L of each aqueous suspension on a 2×1 cm<sup>2</sup> silicon substrate followed by drying at room temperature in a fume hood. TEM investigations were performed with the Libra 200 transmission electron microscope (Carl Zeiss AG, Germany) operating at 200 kV. Samples for TEM were prepared by dispensing 10  $\mu$ L of each suspension on a Cu grid with a carbon support membrane, followed by drying.

Raman and surface enhanced Raman scattering spectra were measured using the confocal Raman Microscope (CRM) alpha 300R, (WITec GmbH, Germany). The spectrograph uses high resolution gratings with additional band-pass filter optics and a 2D-CCD camera. Raman and SERS signals were recorded by exciting the samples with a laser power of 5 mW using a laser line (Nd:YAG) at 532 nm. All measurements were obtained in backscattering geometry using a 20× microscope objective with NA values of 0.46 which provided scattering areas of 1.0  $\mu$ m<sup>2</sup>. For one measurement, between 50 and 200 single Raman spectra with a measuring time of 0.5 s were accumulated and the corresponding Raman spectra were recorded within the spectral range of 150-3500 cm<sup>-1</sup> for Raman shift. For SERS experiments, 1.5 mg of SiO<sub>2</sub>@Ag-seed, SiO<sub>2</sub>@Ag-1 and SiO<sub>2</sub>@Ag-2 particles, respectively, were added into 1.5 mL of Rhodamine (R6G) aqueous solution at a concentration of 10<sup>-5</sup> M. The solutions were sonicated for 5 min. to fully disperse the particles and kept in the dark for 30 min, time enough to reach a thermodynamic equilibrium. A homogenous film of each of the as-prepared SiO<sub>2</sub>@Ag/R6G solutions was formed onto the surface of cleaned glass slides by dip coating. Then, the substrates were air-dried and used for SERS investigations.

The catalytic activity was proven quantitatively using a model reaction, the reduction of 4-nitrophenol (4-Nip) to 4-aminophenol (4-Amp) in excess of  $\text{NaBH}_4$ . In a typical experiment, 0.5 mL of freshly prepared aqueous solution of  $\text{NaBH}_4$  (60 mM) was mixed with 2.0 mL of 4-nitrophenol aqueous solution (0.1 mM) in a standard quartz cuvette (path length 1 cm). To this mixture, a constant amount (2 mg) of each of the  $\text{SiO}_2@Ag$  particles dispersed in 0.2 mL of MilliQ water was added and the reaction mixture was monitored immediately by successive UV-vis spectra taken every 50 s in the range of 250-550 nm. All experiments were performed at room temperature (20 °C). The rate constants of the catalytically activated reactions using each of the  $\text{SiO}_2@Ag$  systems were determined by measuring the change in intensity of the peak at 400 nm with time.

#### 4.3.4 Results and discussion

##### 4.3.4.1 Fourier transformed infrared spectroscopy (FT-IR)

The surface modification of silica spheres with PEI chains was proven in a first instance by FT-IR spectroscopy. Fig. 4.7 A shows the FT-IR spectra of  $\text{SiO}_2$  particles in the spectra range of 4000-1400  $\text{cm}^{-1}$ . For the bare  $\text{SiO}_2$  (black solid line), the broad band at around 3325  $\text{cm}^{-1}$  is assigned to the asymmetric stretching vibrations of silanol groups (Si-OH) and adsorbed water molecules on the silica surface, while that at 1631  $\text{cm}^{-1}$  belongs to H-O-H bending. [200] In the case of PEI modified particles (red solid line), the band in the range of 3325  $\text{cm}^{-1}$  is slightly weakened and new bands appear at 2982 and 2906  $\text{cm}^{-1}$  corresponding to the symmetric and asymmetric stretching vibrations of C-H bond, confirming the existence of  $-\text{CH}_2$  groups. Fig. 4.7 B depicts the selected FT-IR spectra region from 1500 to 1350  $\text{cm}^{-1}$  where the peaks located at 1485, 1451 and 1398  $\text{cm}^{-1}$  belong to the C-H bending vibrations of the  $-\text{CH}_2$  groups, arising from the adsorbed PEI molecules. [201] Unfortunately, N-H peaks of the PEI amine groups were overlapped from the band of silanol groups of the  $\text{SiO}_2$  surface. However, we can confirm the presence of amine groups with the peak located at 1360  $\text{cm}^{-1}$ , corresponding to the C-N stretching vibration. [202]

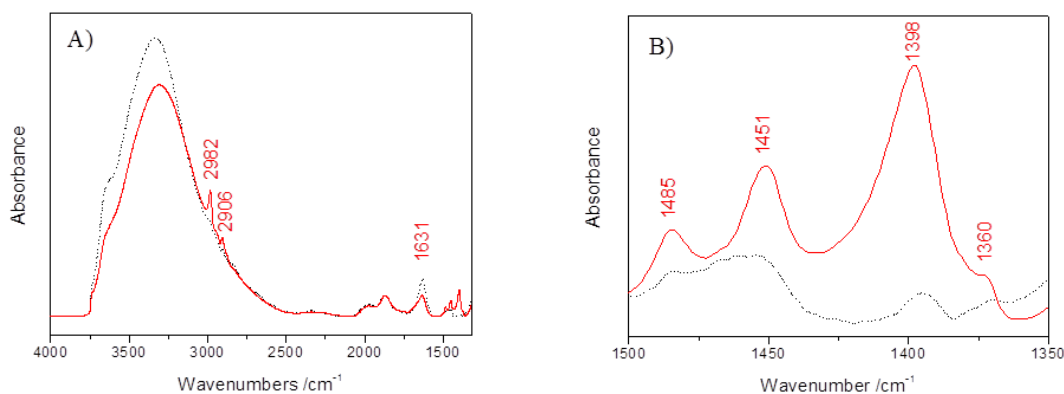


**Fig. 4.7 - FT-IR spectra of bare SiO<sub>2</sub> (black line) and PEI functionalized SiO<sub>2</sub> particles (red line) for A) the spectral region between 4000-1400 cm<sup>-1</sup> and B) from 1500 to 1350 cm<sup>-1</sup>.**

#### 4.3.4.2 Zeta potential measurements

Fig. 4.8 represents the zeta potential as a function of pH for bare and PEI functionalized SiO<sub>2</sub> particles at constant ionic strength (10<sup>-3</sup> M KCl). For the neat SiO<sub>2</sub> particles, the mean zeta potential values are negative in the pH range between 3.0 and 10.0, while the isoelectric point (IEP) was found to be slightly below pH 3.0, suggesting a negative surface charge. This could be attributed to the acidic behavior of the surface silanol groups. On the other hand, for PEI modified particles, the effect of basic amine groups can explain the positive zeta potential values throughout the pH range between 3.0 and 8.0, with the IEP slightly below pH 9.0. [203] The results demonstrate the change of the surface charge upon adsorption of the PEI molecules, confirming a successful surface modification.

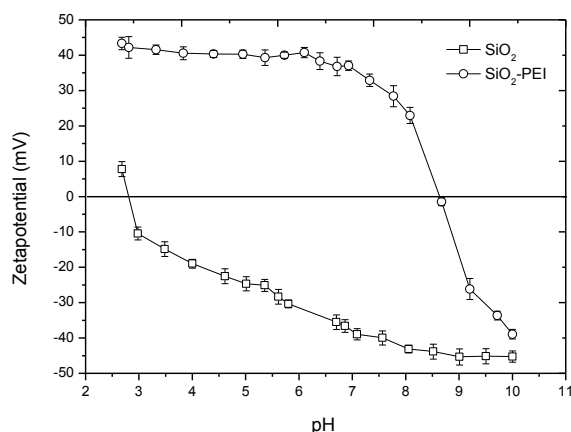


**Fig. 4.8 - Mean zeta potential as a function of pH for bare and PEI functionalized SiO<sub>2</sub> particles.**

4.3.4.3 UV-vis spectroscopy of SiO<sub>2</sub> and SiO<sub>2</sub>@Ag particles

Fig. 4.9 shows the UV-vis spectra of the three different SiO<sub>2</sub>@Ag colloidal systems in aqueous media, as well as for the bare SiO<sub>2</sub> particles at a concentration of 1 mg/mL. The optical image given as an inset demonstrates the high colloidal stability of the suspensions at a concentration of 1 mg/mL, while the images were recorded one week after the dispersions have been prepared. It can be observed that the color changes after immobilization of Ag NPs onto the SiO<sub>2</sub> spheres, and especially becomes more intense yellow with the increased Ag NP size. As it was expected, no distinct plasmon band was detected for the SiO<sub>2</sub> spheres. However, after decoration of the Ag NPs, each corresponding spectrum depicted a localized surface plasmon resonance (LSPR) band with a maximum centered at ca. 400 nm. The presence of a minimum at ca. 320 nm can be also observed, characteristic of the interband transition in the metal that damps the plasmon oscillation in this spectral region. [78] With the increased silver size, the position of the absorption peak is slightly shifted to higher wavelengths. This red-shift is accompanied also by a strong increase in the peak intensity. This behavior can be explained with two different factors, *i*) the higher excitation cross-section of the metal nanoparticle in each growth step, and *ii*) the increase of the particle volume. [204] This evolution confirms not only the presence of Ag NPs onto the SiO<sub>2</sub> spheres, but also the increase of the particle size during the silver growth steps.

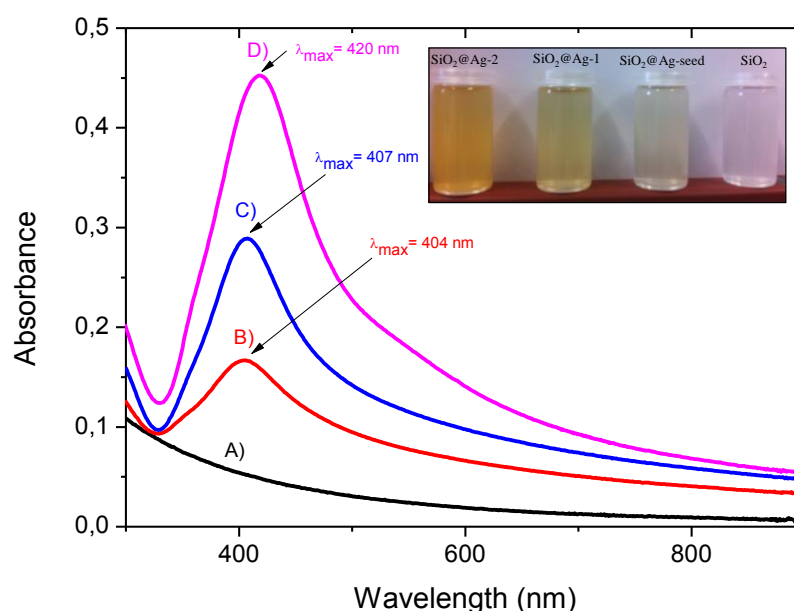


**Fig. 4.9** - UV-vis spectra of the different colloidal systems in aqueous media: A) bare silica (black solid line), B) SiO<sub>2</sub>@Ag-seed (red solid line), C) SiO<sub>2</sub>@Ag-1 (blue solid line) and D) SiO<sub>2</sub>@Ag-2 (pink solid line). The optical image given as an inset depicts the high colloidal stability of SiO<sub>2</sub> and SiO<sub>2</sub>@Ag systems as well as the changes in color upon deposition of Ag NPs.

#### 4.3.4.4 XRD of SiO<sub>2</sub>@Ag nanohybrids

Fig. 4.10 represents a typical X-ray diffraction pattern of the nanohybrid SiO<sub>2</sub>@Ag system (pattern of the SiO<sub>2</sub>@Ag-2 sample). Sharp diffraction peaks were observed which can be indexed to the face-centered cubic (fcc) structure of metallic Ag (blue lines in Fig. 4.10), with the diffraction peaks corresponding to the (1 1 1), (2 0 0), (2 2 0) and (3 1 1) planes indicating the formation of pure silver of high crystallinity (JCPDS file, No. 4-783). We can also observe the X-ray diffraction of the silica particles with a broad scattering maximum centered at 22.5°, typical for amorphous SiO<sub>2</sub>. [205]

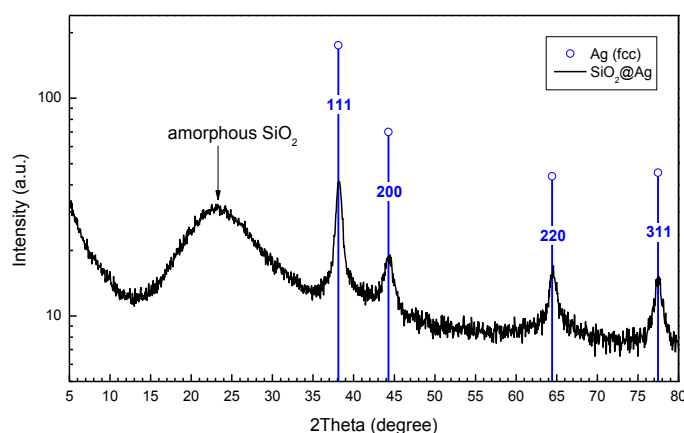


Fig. 4.10 - Typical X-ray diffraction pattern of the SiO<sub>2</sub>@Ag particles. The blue lines correspond to the pure crystalline Ag diffraction peaks.

#### 4.3.4.5 Electron microscopy investigations

The presence of Ag seeds onto the SiO<sub>2</sub> surface as well as the increase of the Ag seed size during the different growth steps were visualized by SEM and TEM images. Representative SEM (left side) and TEM (right side) micrographs of SiO<sub>2</sub> and the different SiO<sub>2</sub>@Ag particles, exhibiting a raspberry-like morphology, are depicted in Fig. 4.11. Bare SiO<sub>2</sub> particles with uniform size are shown in Fig. 4.11 A. Fig. 4.11 B demonstrates the morphology of SiO<sub>2</sub>@Ag-seed particles, while 4.11 C and 4.11 D correspond to the SiO<sub>2</sub>@Ag-1 and SiO<sub>2</sub>@Ag-2 system, respectively. It is important to note that from the SEM and TEM investigations, no residual silver dots were detected after the silver growth steps, confirming a homogeneous nucleation and increase of the Ag NP size.

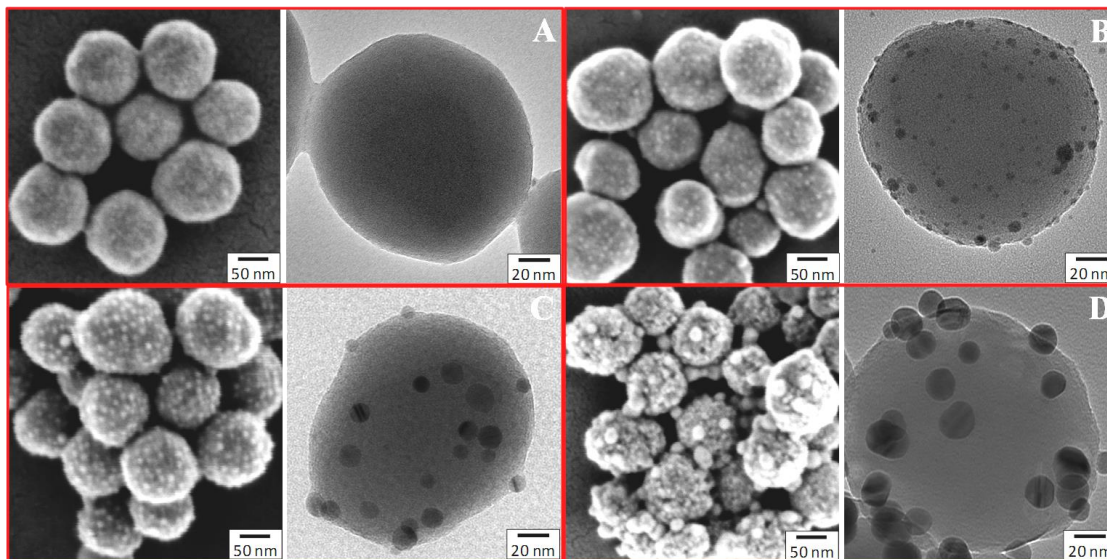


Fig. 4.11 - SEM (left side) and TEM (right side) images of A) bare silica spheres, B) SiO<sub>2</sub>@Ag-seed, C) SiO<sub>2</sub>@Ag-1 and D) SiO<sub>2</sub>@Ag-2 hybrid particles with a raspberry-like morphology.

The size of Ag NPs for each of the SiO<sub>2</sub>@Ag systems was determined from the corresponding TEM images, and the resulting histograms are plotted in Fig. 4.12. Fig. 4.12 A displays the histograms of around 100 NPs analyzed from the TEM images of SiO<sub>2</sub>@Ag-seed system, showing an average diameter of  $(4.2 \pm 1.1)$  nm. The histograms corresponding to the SiO<sub>2</sub>@Ag-1 and SiO<sub>2</sub>@Ag-2 system are depicted in Fig. 4.12 B and 4.12 C, exposing a clear increase of the Ag NP size with  $(12.8 \pm 3.4)$  and  $(19.6 \pm 3.9)$  nm, respectively.

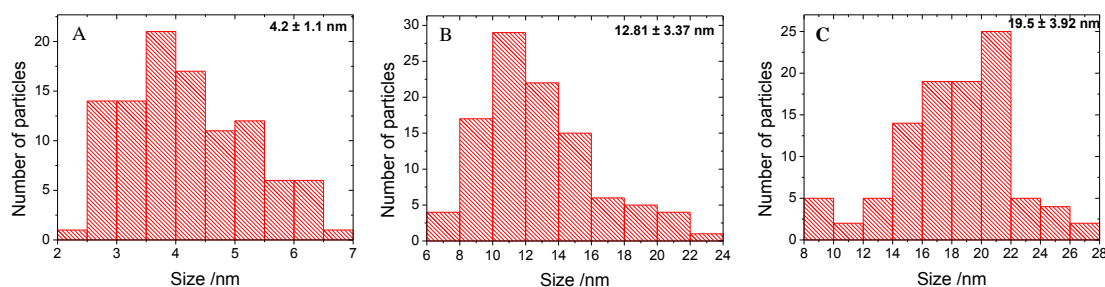


Fig. 4.12 - Histogram of 100 Ag NPs measured by TEM images of A) SiO<sub>2</sub>@Ag-seed, B) SiO<sub>2</sub>@Ag-1 and C) SiO<sub>2</sub>@Ag-2 systems, showing the corresponding average size and size distribution of Ag NPs.

#### 4.3.4.6 SERS experiments

In order to exploit the excellent SERS capabilities of Ag NPs, Rhodamine 6G (R6G) was used as a model analyte to demonstrate the potential of our nanohybrid systems for SERS ultradetection. Fig. 4.13 illustrates the 532 nm excitation SERS spectra of R6G

( $1.0 \times 10^{-5}$  M), previously mixed with the three different colloidal suspensions and deposited onto glass slides, as described in the experimental section. It is obvious that all specimens exposed SERS activity as revealed by the characteristic peaks of R6G at 615, 779, 1189, 1316, 1365, 1510, 1577 and  $1652 \text{ cm}^{-1}$  within the spectral region of 600 to  $1800 \text{ cm}^{-1}$ , perfectly matching with those found in literature. [206] In addition, the Raman peak located at  $1365 \text{ cm}^{-1}$  confirms that the enhancement of the SERS signal increases with the Ag NP size, being in a good agreement with previously reported results. [207, 208] It is important to note that the improvement of the SERS intensity for the  $\text{SiO}_2@\text{Ag-1}$  and  $\text{SiO}_2@\text{Ag-2}$  systems is not only attributed to the increased Ag NP size. It is a well-known fact that the SERS property remarkably increases when NPs are close enough to induce coupling between their oscillating surface plasmon. This plasmon coupling is expected only for core-core distances below one particle diameter and produces high local excitation fields. [209] Within these areas, the so-called hot spots, the SERS electromagnetic enhancement is extremely high [136, 210] and a theoretical enhancement factor nearly to  $10^{12}$  has been calculated in some cases. [113] The TEM images in Fig. 4.11C and 4.11D indicate that some Ag NPs are in close proximity to allow plasmon coupling, and consequently the generation of hot spots increasing the SERS signal. [52] On the contrary, the smaller size of Ag seeds for the  $\text{SiO}_2@\text{Ag-seed}$  system (Fig. 4.11B) is not suitable for the generation of hot spots, resulting in the lowest SERS response. In order to quantitatively compare the SERS activity of the three fabricated systems, surface enhanced factors (SEFs) were calculated according to the expression  $\text{SEF} = (I_{\text{surf}}/C_{\text{surf}})/(I_{\text{bulk}}/C_{\text{bulk}})$ , [30] where  $I_{\text{surf}}$  and  $I_{\text{bulk}}$  denote the intensities of the R6G at  $1365 \text{ cm}^{-1}$  adsorbed to the  $\text{SiO}_2@\text{Ag}$  systems and those of dissolved as bulk in solution ( $10^{-1}\text{M}$ ), respectively. The  $C_{\text{surf}}$  and  $C_{\text{bulk}}$  represent the concentrations of R6G used for the Raman and the SERS experiments, respectively. The  $I_{\text{surf}}$  values at  $1365 \text{ cm}^{-1}$  (vibration of aromatic C-C stretching band) for the three different systems are provided by the SERS spectra in Fig. 4.13 which correspond to 7211, 14393 and 21897 counts for the  $\text{SiO}_2@\text{Ag-seed}$ ,  $\text{SiO}_2@\text{Ag-1}$  and  $\text{SiO}_2@\text{Ag-2}$  systems, respectively. Unfortunately, due to the fact that R6G is a fluorescent molecule which absorbs strongly with a maximum at 528 nm, close to the laser measurements (532 nm), no proper value can be assigned to the Raman signal  $I_{\text{bulk}}$ . Therefore, we assume a maximum value of  $I_{\text{bulk}}$  in the range of the detector noise of 200 counts. [30] For the  $C_{\text{bulk}}$  and  $C_{\text{surf}}$  values representing the concentrations of R6G solutions used for the Raman and SERS experiments, we used  $1.0 \times 10^{-1}$  M and  $1.0 \times 10^{-5}$  M, respectively. Consequently, the calculated SEFs for the  $\text{SiO}_2@\text{Ag-seed}$ ,  $\text{SiO}_2@\text{Ag-1}$  and  $\text{SiO}_2@\text{Ag-2}$  are  $3.61 \times 10^5$ ,  $7.19 \times 10^5$  and  $1.09 \times 10^6$ , confirming the relationship between the SERS intensity and the Ag NP size deposited to the  $\text{SiO}_2$  surface. The excellent SERS

performance of all fabricated systems in combination with their high colloidal stability could be an important parameter for the detection of various water-soluble contaminants by means of SERS spectroscopy.

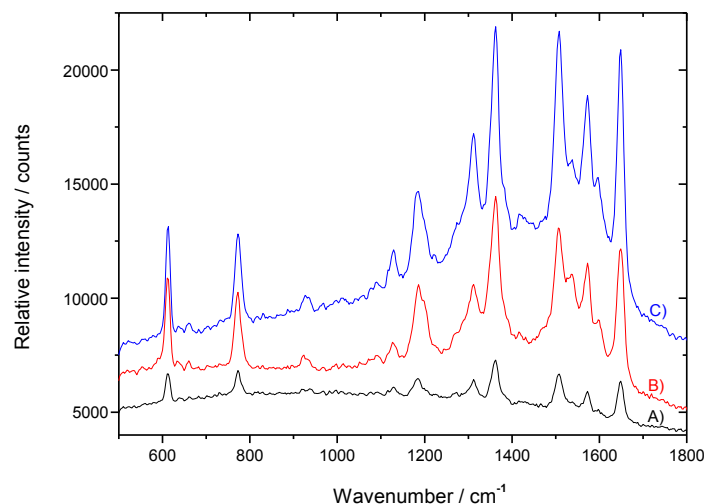


**Fig. 4.13** - SERS spectra of R6G ( $10^{-5}$  M) adsorbed from aqueous solution at the three different samples tested; A) SiO<sub>2</sub>@Ag-seed (black line), B) SiO<sub>2</sub>@Ag-1 (red line) and C) SiO<sub>2</sub>@Ag-2 (blue line).

#### 4.3.4.7 Catalytic reduction of 4-nitrophenol to 4-aminophenol

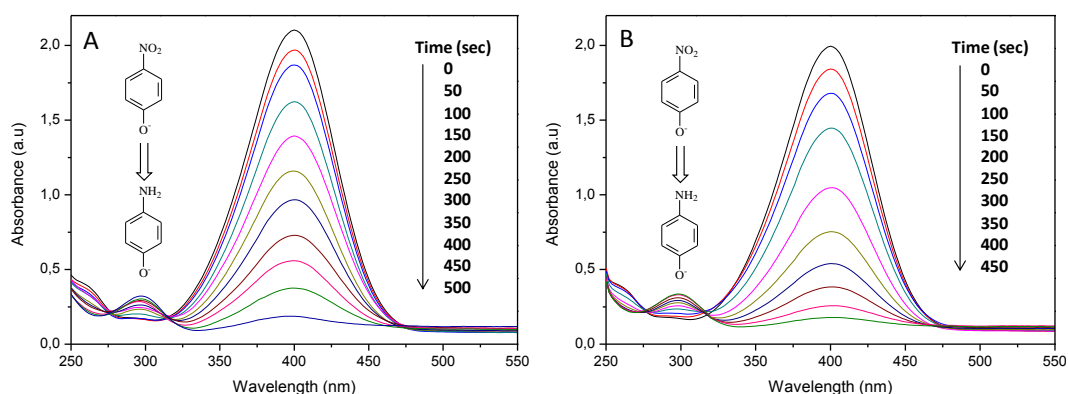
In order to test quantitatively the catalytic efficiency of SiO<sub>2</sub>@Ag systems, the reduction of 4-nitrophenol (4-Nip) to 4-aminophenol (4-Amp) with an excess of NaBH<sub>4</sub> was employed as a reliable model reaction. [211] Although the reduction of 4-Nip to 4-Amp using aqueous NaBH<sub>4</sub> is thermodynamically favorable ( $E_0$  for 4-Nip/4-Amp =  $-0.76$  V and  $H_3BO_3/BH_4^- = -1.33$  V versus NHE: normal hydrogen electrode), the presence of a kinetic barrier due to the large potential difference between donor and acceptor molecules decreases the feasibility of this reaction. Metal NPs can serve as electron relay from electron donor BH<sub>4</sub><sup>-</sup> ions (reductant) to the acceptor 4-nitrophenolate (oxidant) ions, overcoming the kinetic barrier and efficiently catalyze the reduction of 4-Nip to 4-Amp. [212] A typical UV-vis spectrum of 4-Nip aqueous solution shows a distinct absorption maximum peak at  $\sim 317$  nm. Upon the addition of NaBH<sub>4</sub>, the light yellow color of 4-Nip changes to yellow-green and the 4-Nip peak at  $\sim 317$  nm is immediately red-shifted to 400 nm due to the formation of 4-nitrophenolate ions in the alkaline medium caused by NaBH<sub>4</sub>. The progress of the catalytic reaction was evaluated quantitatively by monitoring the changes of the absorption spectra of 4-nitrophenolate ions as a function of time after adding each of the SiO<sub>2</sub>@Ag colloidal



catalytic systems into the 4-Nip/ $\text{NaBH}_4$  reaction mixture. [211] As a control experiment, the catalytic activity of bare  $\text{SiO}_2$  particles instead of  $\text{SiO}_2@Ag$  was evaluated. After a time period of six hours, no change of the nitrophenolate anions peak intensity was observed confirming the catalytic role of Ag NPs. After the addition of  $\text{SiO}_2@Ag$  nanocolloids in the reaction mixture, the reduction of 4-Nip by  $\text{NaBH}_4$  and its conversion to 4-Amp was observed. The intensity of the peak at 400 nm gradually dropped with time accompanied by a concomitant appearance of a new peak at 295 nm indicating the formation 4-Amp. The UV-vis spectra were recorded at regular intervals of 50 seconds and they are depicted in Fig. 4.14. Fig. 4.14 A represents the time dependent UV-vis spectra during the reduction of 4-Nip using  $\text{SiO}_2@Ag$ -seed as the reaction catalyst. The data in imply that the reaction terminates within a time frame of 500 s consistent with the disappearance of the yellow color of 4-Nip at the end of the reaction. Fig. 4.14 B and 4.14 C display the time dependent reduction of 4-Nip using  $\text{SiO}_2@Ag$ -1 and  $\text{SiO}_2@Ag$ -2, respectively. The results indicate that  $\text{SiO}_2@Ag$ -1 and  $\text{SiO}_2@Ag$ -2 particles effectively catalyze the reaction as well, however, at different reaction times. From the spectra presented in Fig. 4.14 A, 4.14 B and 4.14 C, it can be concluded that the intensity of the peak at 400 nm decreases gradually during the catalytic reaction but with a different reaction rate. Fig. 4.14 C demonstrates that,  $\text{SiO}_2@Ag$ -2 system shows the shortest time needed for the complete conversion of 4-Nip to 4-Amp. Consequently, the order of catalytic activity for the three samples is  $\text{SiO}_2@Ag$ -2 >  $\text{SiO}_2@Ag$ -1 >  $\text{SiO}_2@Ag$ -seed and this trend is in accordance with the size of Ag NPs. Since the concentration of  $\text{NaBH}_4$  greatly exceeds that of 4-Nip and  $\text{SiO}_2@Ag$ , the reduction rates can be assumed to be dependent only on the concentration of 4-Nip and independent of the  $\text{NaBH}_4$  concentration. Taking into account the aforementioned assumption, the catalytic reaction rate constants ( $K$ ) can be evaluated by studying the pseudo-first-order kinetics with respect to 4-Nip concentration. [213] As a result, the reaction rate constants ( $K$ ) were calculated from the corresponding slopes, which can be determined from the linear fits of the  $\ln(A_t/A_0)$  versus  $t$  plots. This allows the qualitative comparison of the catalytic activity of the three different hybrid nanocolloids as well as with other systems reported in literature, in which Ag-based systems were used as nanocatalysts for the reduction of 4-Nip. Specifically,  $A_t$  stands for absorbance at time  $t$  and  $A_0$  for absorbance at time 0 which was taken as the time at 50 s corresponding to the second absorbance peak at 400 nm, because of the relatively small ‘induction times’ (will be discussed in the next paragraph), observed at the beginning of each reaction. [211] Fig. 4.14 D demonstrates the differences of the reaction rate constants for the three different  $\text{SiO}_2@Ag$  catalysts which can be attributed to the increased Ag NP size. All the plots shown in Fig. 4.14 D, present a good linear relation

between  $\ln(A_t/A_0)$  and time  $t$ , for almost 90% of the reactions for each catalytic system.  $K$  exhibits the highest value for the  $\text{SiO}_2@\text{Ag-2}$  particles ( $K = 9.32 \times 10^{-3} \text{ s}^{-1}$ ), whereas the lowest value was found for the  $\text{SiO}_2@\text{Ag-seed}$  with a reaction rate constant of  $2.9 \times 10^{-3} \text{ s}^{-1}$ . The same conditions in all the experiments were used and the results of rate constants ( $K$ ) are summarized in Table 1. The rate constant of the  $\text{SiO}_2@\text{Ag-2}$  system which was found to be  $9.32 \times 10^{-3} \text{ s}^{-1}$  is higher than values reported by Zhang ( $5.63 \times 10^{-3} \text{ s}^{-1}$ ), Gangula ( $9.19 \times 10^{-3} \text{ s}^{-1}$ ) and Huang ( $4.73 \times 10^{-4} \text{ s}^{-1}$ ) *et al.* [211, 212, 214]

The induction time which was previously mentioned is a typical phenomenon for the heterogeneous catalysis, and related to the time required for the catalyst activation. In the reactions performed in our study, after addition of all the reactants, within the second spectrum run at a time interval of 50 s the absorbance intensity was already decreased revealing the initiation of the catalytic reaction. This observation can prove that the induction time in our systems was very small because the Ag NPs are directly in contact with the reaction components and no time for the diffusion of 4-Nip to reach the surface of metal particles was needed like in previously reported studies. [213, 215] Normally, bigger induction times are attributed to many factors: (i) the diffusion-controlled adsorption of reactants onto the nanoparticle surface as already mentioned, (ii) the presence of dissolved oxygen in water reacting at a faster rate with  $\text{NaBH}_4$  than with 4-Nip, (iii) the coating of a metal oxide layer onto the metal surface upon the addition of  $\text{BH}_4^-$ , poisoning the catalyst surface and (iv) a slow surface restructuring of the nanoparticles. [171] However, in our work the aqueous reaction medium containing the 4-Nip was degassed before adding the  $\text{NaBH}_4$ , therefore, we avoided the formation of an oxide layer at the Ag NP surface as well as the reaction of  $\text{NaBH}_4$  with dissolved oxygen.



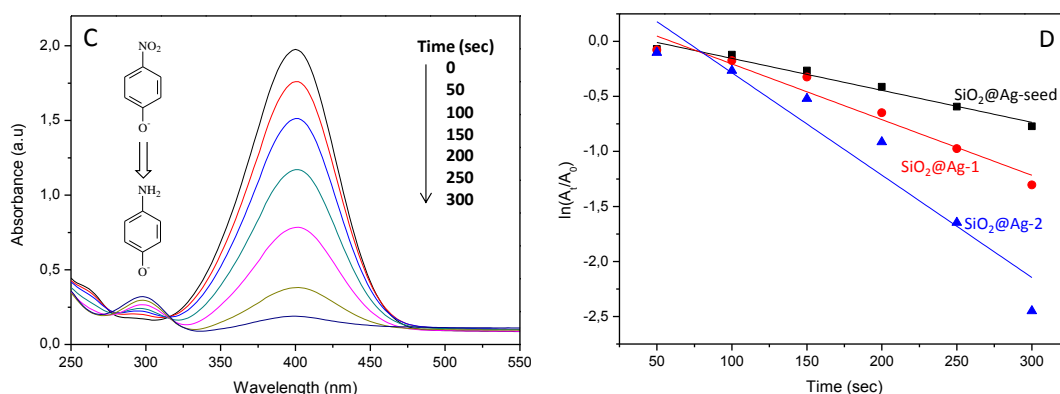


**Fig. 4.14** - Time dependent UV-vis spectra (A, B and C) for the catalytic reduction of 4-Nip by  $\text{NaBH}_4$  in the presence of  $\text{SiO}_2\text{@Ag-seed}$ ,  $\text{SiO}_2\text{@Ag-1}$  and  $\text{SiO}_2\text{@Ag-2}$ , respectively. D) Comparative plots of  $\ln(A_t/A_0)$  versus time  $t$  towards the reduction reaction using  $\text{SiO}_2\text{@Ag}$  catalytic systems.

**Table 1** Summary of the catalytic activity of the three different  $\text{SiO}_2\text{@Ag}$  systems towards the reduction of 4-Nip to 4-Amp by  $\text{NaBH}_4$  at room temperature ( $20^\circ\text{C}$ ).

Sample ID	Amount of $\text{SiO}_2\text{@Ag}$ used (mg)	Aver. size of Ag NPs decorated to the $\text{SiO}_2$ spheres (nm)	Time of completion the reaction (s)	Calculated rate constant, $K$ ( $\text{s}^{-1}$ )
$\text{SiO}_2\text{@Ag-seed}$	0.5	$4.2 \pm 1.1$	500	$2.91 \times 10^{-3}$
$\text{SiO}_2\text{@Ag-1}$	0.5	$12.8 \pm 3.4$	450	$5.06 \times 10^{-3}$
$\text{SiO}_2\text{@Ag-2}$	0.5	$18.6 \pm 3.9$	300	$9.32 \times 10^{-3}$

In summary, a relatively simple and facile method for the decoration of  $\text{SiO}_2$  spheres with Ag NPs of tunable and uniform metal size has been developed. The general process involves the functionalization of  $\text{SiO}_2$  particles with terminal amine groups and the coordination of silver ions which were reduced to Ag seeds. By using the  $\text{SiO}_2\text{@Ag-seed}$  system as a template, subsequent Ag growth steps were performed and the size of Ag seeds was remarkably increased, facilitating enhanced SERS and catalytic properties. The SERS ability can be exploited for the detection of conventional SERS analytes in water due to the long-term colloidal stability of all fabricated systems in aqueous media. It should be also emphasized that due to the limited use of organic solvents and toxic substances during the synthetic process, this protocol can be defined in general as an environmentally ‘green’ synthetic approach, feasible to be scaled up for the production of bigger amounts of the hybrid particles.

#### 4.4 Synthesis of superparamagnetic Fe<sub>3</sub>O<sub>4</sub> nanoparticles

Magnetite nanoparticles (Fe<sub>3</sub>O<sub>4</sub> NPs) have been synthesized via a solvent-free thermal decomposition method according to the protocol of Maity *et. al.* [216] In brief, 2 mmol of iron(III) acetylacetonate, Fe(acac)<sub>3</sub>, were dissolved in 20 ml of oleic acid/oleylamine surfactant mixture, and magnetically stirred under argon atmosphere. The mixture was kept at 120 °C for one hour to achieve dehydration, and then quickly heated to 300 °C and kept for 2 h. The black solution was cooled down then and 20 ml of ethanol were added to achieve the precipitation of the particles. The Fe<sub>3</sub>O<sub>4</sub> NPs were dispersed then in hexane for size analysis and further use. The TEM images at two different magnifications in Fig. 4.15 (left and central image) demonstrate the excellent stabilized particles with a relatively narrow size distribution (12.3±3.8 nm) while in the right side, the digital photograph depicts the response of Fe<sub>3</sub>O<sub>4</sub> NPs to an external magnetic field.

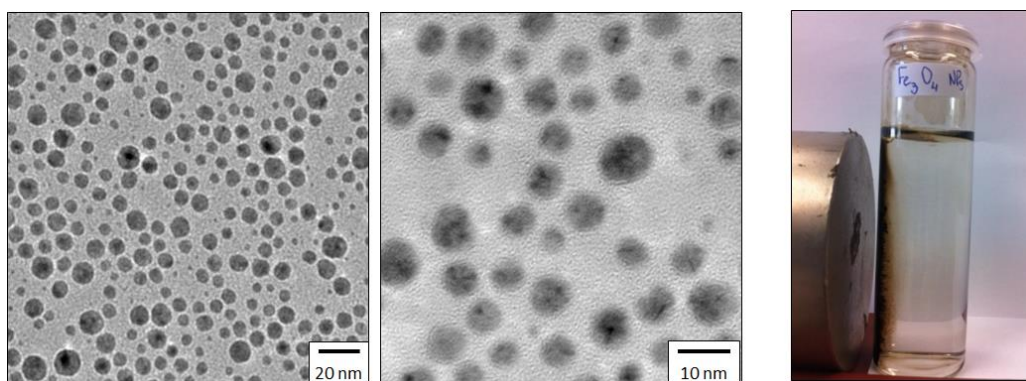
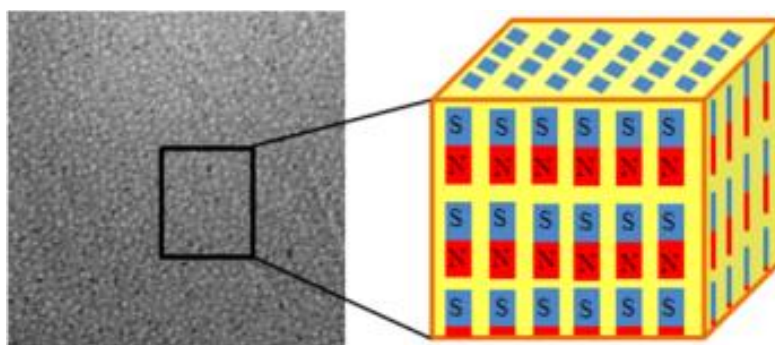


**Fig. 4.15 – TEM images at two different magnifications (left and central image) showing the excellent stabilized particles with a relatively narrow size distribution (8.3±3.8 nm). In the right side, the particles very fast respond to the external magnetic field.**

## Chapter 5

### Epoxy/BCP nanostructured thermosetting materials

#### Thermoset Magnetic Materials Based on Poly(ionic liquid)s Block Copolymers



#### Abstract

The preparation of nanostructured magnetic thermoset materials without any kind of metal oxide or metal magnetic nanoparticles has been developed. The present protocol describes the nanostructuring of thermoset materials based on poly(ionic liquid)s block copolymer, and the subsequent production of magnetic nanostructured thermoset. Judicious selection of block copolymer, such as P2VP-b-PMMA, soluble in epoxy and its subsequent quaternization leads to a phase modification of the system, from totally soluble to a nanostructured system. Different degree of quaternization of the pyridine groups showed the range of quaternization values which allowed the nanostructuring of the thermoset. Magnetic material was obtained by anion exchange of the quaternized poly(ionic liquid) block copolymer without using any kind of metal oxide or metal magnetic nanoparticles. The different materials obtained by quaternization of the block copolymers, the anion exchange of the polymeric ionic liquid and thermoset materials were characterized by  $^1\text{H}$  nuclear magnetic resonance ( $^1\text{H-NMR}$ ), thermogravimetric analysis (TGA), differential scanning calorimetry (DSC), transmission electron microscopy (TEM), and magnetic properties were measured by Superconducting Quantum Interference Device (SQUID).

#### 5.1 Introduction

Conventional plastics form a wide variety of durable and light-weight materials that are easy and inexpensive to process, but they often lack properties such as electrical conductivity, mechanical strength, heat resistance, magnetism or high dielectric constants.

[217] For this reason, in the past few years, research in the field of advanced materials with novel properties has targeted combining materials with different properties. The term ‘nanocomposites’ relates to composite materials whose characteristic length scale of the reinforcing agent is in the nanometer range. When different materials are combined to form a heterogeneous structure, the properties of the resulting nanocomposites depend closely on the properties of the constituent materials, i.e. the length scale, as well as the chemical and morphological details of the dispersion. In the field of nanocomposites, recent studies have shown that magnetic polymer nanocomposites prepared with magnetic nanoparticles are one promising material [218] with high-valued potential applications in high density magnetic recording, magnetic sensors, magnetic carriers, color imaging, biomedical, magnetic storage, and electronics. [219-222] So far, most of the works reported on magnetic nanocomposites have been based on metal oxide or metal magnetic nanoparticles in various polymers, such as vinyl-ester resin, polyurethane, parylene, polymethyl methacrylate, epoxy resin, and block copolymers. [223-229] Herein, a novel route to obtain nanostructured magnetic thermoset materials without use of any kind of metal oxide or metal magnetic nanoparticles, but simply introducing magnetic poly(ionic liquid) block copolymer is proposed. The resulting material exhibits well defined ferromagnetic interactions, remanence and coercivity at room temperature.

Ionic liquids (ILs) are organic salts with low melting point. Like salts, ionic liquids are composed of cations and anions responsible of the material properties. [230] Moreover, the ILs properties can be tuned by simple anion exchange. [231] Ionic liquids have been combined with polymer networks which offer great value practical applications like specialty polymer additives and for the development of functional polymers. [232-235] However, ionic liquids present one main disadvantage by exuding easily from the polymer network. To tackle this problem poly(ionic liquid)s (PILs) may be used. PILs are described as a new class of polymeric materials with unique properties combining those of ILs (ionic conductivity, thermal stability, tuneable solution properties and chemical stability) and specific properties of polymers. Although several studies have been devoted to magnetic ILs, [236-238] the synthesis, characterization and application of paramagnetic PILs are still at their infancy. For example, Tang *et al.* investigated the properties and application of PILs as optically transparent micro-wave absorbing materials [239] since PILs contain anion-cation pairs. Therefore, PILs have a relatively high density of strong dipoles, which makes them promising candidates for microwave absorption. That is the reason why the development of a magnetic structural material, such as magnetic epoxy, should be of great interest as a

microwave absorption material and could open new fields of application to structural materials.

In order to develop the nanostructured epoxy material, we make use of (i) the anionic synthesis of poly(2-vinylpyridine)-b-poly(methyl methacrylate), (ii) the production of a microphase separated thermoset system which consists of an epoxy resin containing a diblock copolymer, like poly(2-vinylpyridine)-b-poly(methyl methacrylate) [where the two blocks are selected in order to be completely miscible with the epoxy], (iii) the influence of the degree of quaternization of the poly(2-vinylpyridine) block on the morphology of the final nanostructured thermoset materials and (iv) the development of a novel magnetic nanostructured thermoset material based on a magnetic PIL block copolymer obtained by anion exchange.

## 5.2 Experimental part

### 5.2.1 Materials

Calcium hydride ( $\text{CaH}_2$  purity 95%, Acros), 1,1 diphenylethylene (DPE) (purity 97%), n-butyl lithium (1.6 M in hexanes), butyllithium (*sec*-BuLi) (1.4 M in cyclohexane), 1,1 diphenylethylene (98%, Acros), methyl methacrylate (99%, MMA), triethyl aluminum (TEA) (25% in toluene), 2-vinylpyridine (95%, 2-VP, Aldrich), bromoethane, diethyl ether, iron (III) bromide ( $\text{FeBr}_3$ ) were purchased from SigmaAldrich. Tetrahydrofuran (THF) (99.99%), hexane (99.7%) methanol (99.9%), were obtained by Fisher Scientific, Riedel de Haen and Fluka respectively. The epoxy system was composed by an epoxy resin (Araldite LY556), an anhydride hardener (Aradur 917) and an imidazole accelerator (DY 070).

### 5.2.2 Synthesis of P2VP-b-PMMA

The synthesis of poly(2-vinylpyridine)-b-poly(methyl methacrylate) (poly(**0**)) was carried out according to the protocol: The solvent for the polymerization was THF purified via freezing-degassing cycles in the presence of calcium hydride, distillation from sodium/potassium alloy (Na/K), and finally stored under high vacuum in diphenylhexylithium (DPHLi), which was prepared through the reaction of 1,1-diphenylethylene and n-butyl lithium. The initiator used was *sec*-BuLi and was diluted in hexane to a more convenient concentration (0.2 M) in a custom made Pyrex glass apparatus through scientific glassblowing. 1,1 diphenylethylene was purified by reaction with n-BuLi, distilled under vacuum, diluted with hexane and stored in a custom made Pyrex glass

apparatus through scientific glassblowing into precalibrated ampoules. A Pyrex glass ampoule was calibrated at ambient conditions with distilled water according to a well-established procedure thoroughly described in the literature. [240] In all cases the amount of solvent used for dilution was adjusted according to the concentration required to achieve the desired molecular weight of each block.

2-Vinylpyridine was purified twice with calcium hydride to remove water traces, distilled over at least two sodium mirrors in order to be completely dried and finally distilled from triethylaluminum for final purification under stirring for twenty minutes. 2VP was finally distilled in an evacuated calibrated glass ampoule, stored at  $-27\text{ }^{\circ}\text{C}$  and was freshly distilled prior to use and was continuously kept frozen. The second monomer, methyl methacrylate, was purified as well through freeze drying via  $\text{CaH}_2$ , TEA and then distilled in a custom made Pyrex precalibrated ampoule through scientific glassblowing. During the anionic polymerization procedure, 2VP as well as MMA were kept frozen at  $-196\text{ }^{\circ}\text{C}$  (liquid nitrogen temperature) prior to their use. The living chains were terminated with methanol, which was purified after freeze-drying cycles and finally distilled into Pyrex glass precalibrated ampoules through calcium hydride.

The polymerization was carried out according to the literature and methods usually adopted for anionic polymerization, [241-243] and a brief description is given. The diblock copolymer of the poly(**0**) type was synthesized through sequential anionic polymerization and high vacuum techniques. [244] A specific Pyrex glass apparatus was built up via scientific glassblowing. After the purification of the Pyrex custom made glass apparatus with DPHLi through continuous rinsing of THF until no red colour appears throughout the main reactor, the appropriate amount of 2VP (0.030 mol or 3.15 g) was distilled in the reactor followed by the addition of the initiator (0.141 mmol). An intense red colour appeared due to the living ends of  $\text{P2VP}^{(-)}\text{Li}^{(+)}$  and the mixture was left to react for approximately one hour. All procedures were performed at  $-78\text{ }^{\circ}\text{C}$ , using a 2-propanol / liquid nitrogen bath. Then, 1,1-DPE (0.155 mmol, ratio 1:1.1, excess of DPE when compared with the initial  $\text{sec-BuLi}$  concentration) was added in order to avoid the competitive reaction of the carbonyl bond from the MMA monomeric units leading eventually to side products. Following the addition of the protective agent, the second monomer (MMA, 0.070 mol or 7 g) was added via distillation and almost immediately the dark red colour disappeared due to the fast initiation and propagation of the MMA quantity through the macroinitiator  $[\text{P2VP}^{(-)}\text{Li}^{(+)}]$ . The mixture was left to react for approximately 1 hour again at  $-78\text{ }^{\circ}\text{C}$ . The synthesis procedure was accomplished in approximately 200 mL of THF as solvent. Finally, a small quantity of



methanol was added for the termination of the living ends. The diblock copolymer was precipitated into a large excess of hexane, dried from the solvents and stored under vacuum in sealed ampoules. The synthetic procedure is shown in Fig. 5.1.

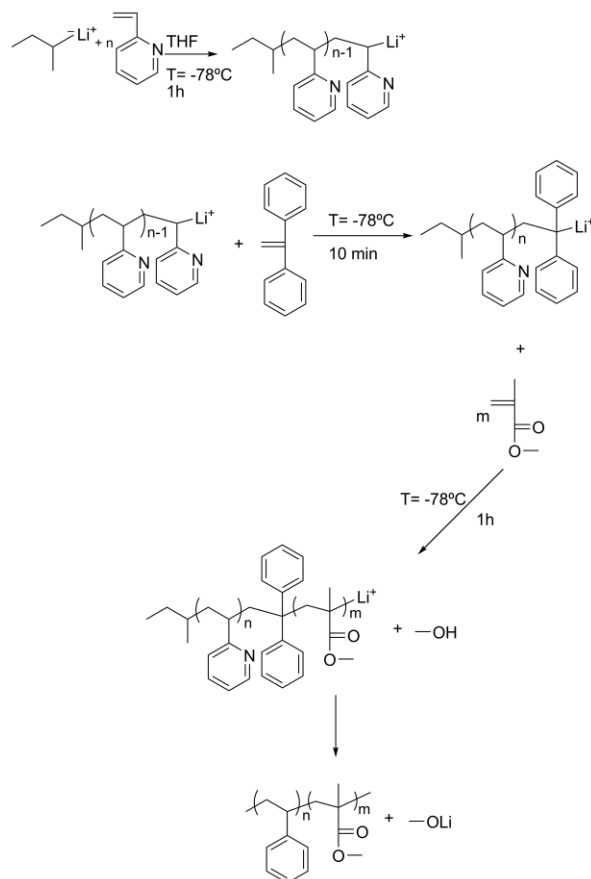


Fig. 5.1 – Synthetic procedure of the poly(0) diblock copolymer through anionic polymerization.

### 5.2.3 Synthesis of the Ionic Liquid Block Copolymer

[P2VP-r-poly(1-ethyl-2-vinylpyridinium bromide)]-b-Poly(methyl methacrylate) block copolymer were prepared (poly(1), poly(2) and poly(3)) following a similar procedure to the one described in literature. [245] Under vigorous stirring, 40 mL of bromoethane was added to 0.4 g of poly(0) in a round-bottom flask. The mixture was refluxed for 168 h. At specific time intervals, aliquots were taken from the flask using syringes. The resulting white-yellow solid was allowed to cool down at room temperature, and then washed several times with diethyl ether. The product was isolated and dried in a vacuum oven at  $50^\circ\text{C}$ .

### 5.2.4 Synthesis of paramagnetic ionic liquid block copolymer

[P2VP-r-poly(1-ethyl-2-vinylpyridinium  $\text{Fe}_3\text{Br}_{10}$ )]-b-Poly(methyl methacrylate) (poly (4)) was prepared following a similar procedure to the one described in the literature. [246] For the synthesis of paramagnetic ionic liquid block copolymer, three equivalents (with respect to monomer units) of  $\text{FeBr}_3$  were dissolved in methanol and added drop-wise under stirring to poly(1), previously dissolved in methanol. After addition of the iron halogenide, the final solution was stirred for 24 h. Finally, poly (4) was obtained by removing the solvents using a rotary evaporator followed by freeze-drying up to a constant weight. Reactions for the synthesis of poly(ionic liquid)s and magnetic poly(ionic liquid) are given in Fig. 5.2.

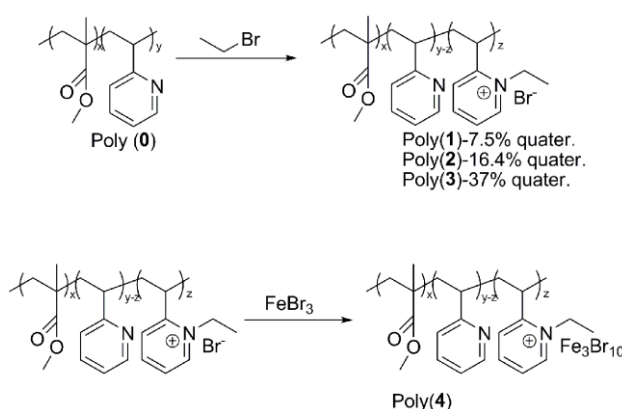


Fig. 5.2 - Synthesis reactions of the poly(ionic liquid)s and magnetic poly(ionic liquid).

### 5.2.5 Protocol for blending epoxy and PIL block copolymer

The protocol to prepare the thermoset samples of block copolymer and epoxy system was already described [247], and typically all block copolymers were dissolved in THF in all cases (except poly(4), which was dissolved in dichloromethane), Araldite LY556 was added to the block copolymer (all samples contain 30 wt.% of the diblock copolymer). Then, the solvent was partially evaporated at room temperature. Aradur 917 and DY 070 were added and blended with the concentrated mixture. A small amount of this mixture was introduced and degassed in a mold at room temperature and heated up to 80 °C for 2 h. Finally, the sample was post-cured at 100 °C for 2 h.

### 5.2.6 Experimental techniques

<sup>1</sup>H NMR experiments were performed on a Bruker AVANCE III spectrometer at 500 MHz. Measurements were performed at room temperature in deuterated chloroform ( $\text{CDCl}_3$ ) and  $\text{DMSO-d}_6$ . Transmission electron microscopy (TEM) was performed using a ZEISS

Libra 120 TEM with an acceleration voltage of 120 kV. Samples for TEM were prepared by ultramicrotomy, using an Ultramicrotome Reichert Ultracut S (Leica) to obtain thin slices (ca. 70 nm thick). Diamond knives for cryo-temperatures (Diatome) were used for both the trimming (model cryotrim 45) and cutting process (model cryo 35°). The slices were placed on copper grids (400 mesh Cu, Agar), and stained for 8-13 h with iodine. Thermal analysis was performed by Differential Scanning Calorimetry (DSC) using a DSC instrument from Perkin Elmer (Pyris Diamond DSC) in a temperature range from 50 to 220 °C, under nitrogen. The glass transition temperature ( $T_g$ ) was obtained as the onset point of the heat flow step recorded at a scan rate of 40 °C min<sup>-1</sup> in case of thermoset materials and 20 °C min<sup>-1</sup> for the block copolymers. Thermal Gravimetry Analysis (TGA) measurements were carried out with a TA-Instrument Q500 TGA using a temperature range of 30 - 800 °C at a heating rate of 10 °C min<sup>-1</sup> under nitrogen. Fourier-Transform Infra-Red (FTIR) spectra were recorded at room temperature using a Nicolet Avatar 360 spectrophotometer. All samples were cast directly onto KBr pellets. A 4 cm<sup>-1</sup> resolution in a wavenumber range from 4000 to 600 cm<sup>-1</sup> was used. The synthesized copolymers were characterized by high temperature size exclusion chromatography (HT-SEC) to confirm the molecular weight distributions and the corresponding number average molecular weight ( $M_n$ ) values. Additionally, membrane osmometry (MO) technique was carried out to confirm the results obtained by HT-SEC. Moreover, proton nuclear magnetic resonance spectroscopy (<sup>1</sup>H NMR) and infrared spectroscopy (IR) were used to calculate the weight fraction of each block and to certify the chemical structure of the final diblock copolymers respectively. The equipment used for the characterization was a HT-GPC from Polymer Laboratories (PL-GPC-120) equipped with one pre-column for organic solutions, three PLgel 5µm MIXED-C columns and a refractive index (RI) detector. The solvent used was THF containing 0.5% pyridine at 35 °C with a flow rate of 1ml/min. Size exclusion chromatography (SEC) was calibrated with eight PS standards (Mp: 4,300 g/mol to 3,000,000 g/mol) and PS standard were regularly tested to ensure the accuracy of the SEC instrument. The number-average molecular weights ( $M_n$ ) (higher than 15,000 g/mol) of the precursors and the final products were measured with a membrane osmometer (MO) Gonotec-Osmomat 090 at 35 °C. Toluene, distilled over CaH<sub>2</sub>, was used as the measuring solvent. For the magnetic characterization a “Superconducting Quantum Interference Device” (SQUID) from Quantum Design Magnetic Property Measurement System (MPMS) 5T was used. Isothermal hysteresis cycles were measured at 300K with applied magnetic field ranging between -50,000 Oe and 50,000 Oe.

### 5.3 Results and discussion

Production of the magnetic thermoset involved several steps. Firstly, a copolymer poly(0) was synthesized by anionic polymerization as described in the experimental section. After purification, the resulting poly(0) block copolymer had a number average molecular weight roughly equal to 71,000 g/mol. The molecular characteristics are summarized in Table 1 as determined with the aforementioned instrumentation. It is important to mention that the final diblock copolymer can be considered a model material, according to molecular characterization results since it exhibits molecular and compositional homogeneity.

**Table 1** Molecular characterization results for the initial P2VP segments and the final diblock copolymer poly(0) as calculated from HT-SEC and <sup>1</sup>H NMR spectroscopy.

	$\overline{M}_n^{P2VP}$ (g/mol) <sup>a,b</sup>	PDI <sup>a</sup> P2VP	$\overline{M}_n^{PMMA}$ (g/mol) <sup>c</sup>	$\overline{M}_n^{total}$ (g/mol) <sup>b</sup>	$\overline{M}_w^{total}$ (g/mol) <sup>a</sup>	PDI <sup>a</sup>	% wt P2VP <sup>d</sup>
Poly(0)	22,000	1.08	49,000	71,000	80,200	1.13	30

a. Calculated from size exclusion chromatography (HT-SEC).

b. Calculated from membrane osmometry (MO).

c. Calculated from the equation:

$$\overline{M}_n^{total} = \overline{M}_n^{P2VP} + \overline{M}_n^{PMMA}$$

d. Calculated from <sup>1</sup>H NMR spectroscopy (<sup>1</sup>H NMR).

Fig. 5.3 shows the <sup>1</sup>H NMR spectrum obtained for poly(0) in CDCl<sub>3</sub>. The weight fraction of P2VP was estimated to be 30 %. This value was determined by taking into account the relative peak integration values at  $\delta \approx 8.3$  ppm corresponding to the proton (N-CH-) of P2VP compare to the signal at  $\delta \approx 3.6$  ppm was attributed to the methyl group of PMMA.

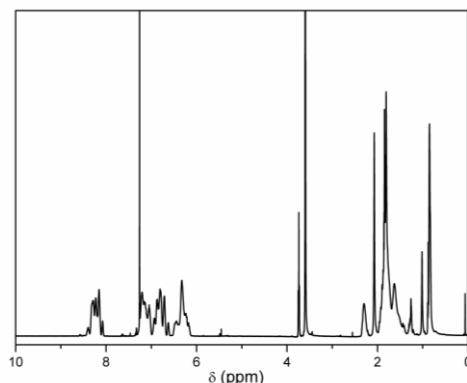
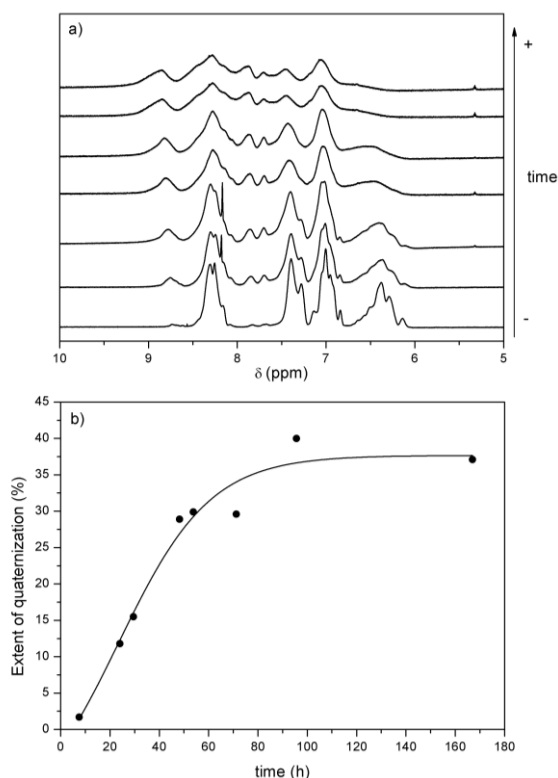


Fig. 5.3 -  $^1\text{H}$  NMR spectra in  $\text{CDCl}_3$  of poly(0).

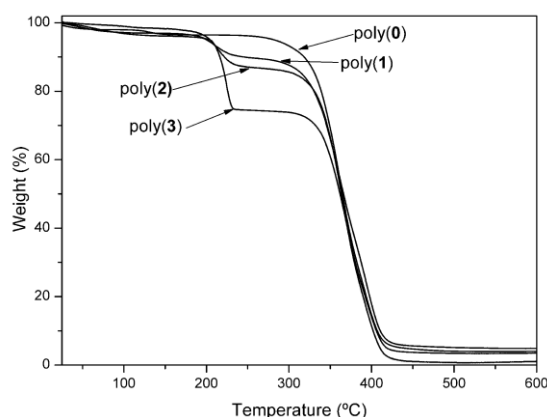
Poly(1), poly(2) and poly(3) were prepared following a similar procedure to the one described in the literature. [245] In order to calculate the extent of quaternization of poly(0), the initial diblock and the intermediate PILs were characterized by  $^1\text{H}$  NMR in  $\text{DMSO-d}_6$  (Fig. 5.4a). The decrease of the signals characteristic of the pyridine protons ( $\delta \approx 8.27\text{-}6.10$  ppm) as well as the appearance of the ( $\text{N}^+\text{-CH}$ ) peak ( $\delta \approx 8.85$  ppm) of the pyridine group after quaternization confirmed the successful quaternization of the nitrogen from the P2VP chains. Furthermore, the doublet observed at  $\delta = 8.3$  ppm corresponding to the proton ( $\text{N-CH-}$ ) of P2VP at short reaction time (or low conversion) became a singlet at longer reaction time (or higher conversion). Ruiz de Luzuriaga *et al.* [248] reported similar behaviour during the quaternization of poly(4-vinylpyridine) which was attributed to the mobility reduction of monomeric units after quaternization.  $^1\text{H}$  NMR was used to monitor the kinetics of quaternization of poly(0). The degree of quaternization P2VP increased linearly until 90 h reaching a plateau at 37%. The steric hindrance induced by the neighbouring 2-vinylpyridine units could explain the low conversion obtained for the quaternization reaction.



**Fig. 5.4 - a)  $^1\text{H}$  NMR spectra in DMSO- $d_6$  spectra for quaternization degree and b) extent of quaternization versus time of reaction of neat poly(0).**

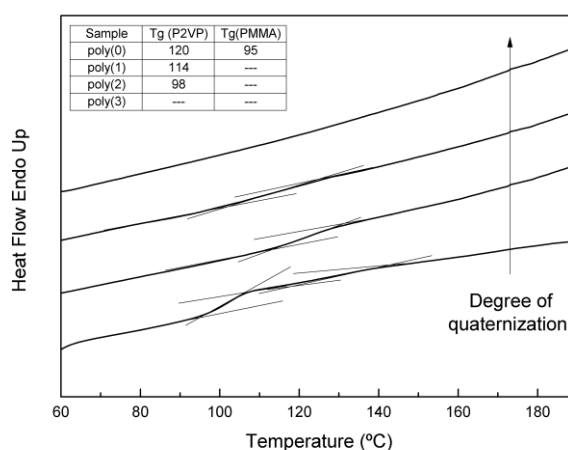
The influence of the quaternization degree of 2-vinylpyridine in the nanostructuring of the thermoset materials was carried out using three PILs with different degrees of quaternization (poly(1)=7.5, poly(2)=16.4 and poly(3)=37). Poly(1), poly(2) and poly(3) were characterized by DSC and TGA prior to blending with epoxy resin.

Fig. 5.5 shows the TGA curves of poly(0), poly(1), poly(2) and poly(3). It can be seen that poly(0) shows only one weight loss that starts at 275 °C. This weight loss is attributed to backbone degradation. However, in the case of poly(1), poly(2) and poly(3), quaternized block copolymers, two weight losses were observed. The first one, in the range 175-250 °C which could correspond to the loss of the bromide anion as alkyl bromide after dealkylation of pyridinium salt. [249] Likewise, these block copolymers show the same weight loss that starts at 275 °C as poly(0). From the first weight drop quaternization degree could be estimated. As expected, the weight decreased in the range of 175-250 °C increased as the quaternization degree increased. Degree of quaternization determined by TGA confirmed the value obtained by  $^1\text{H}$  NMR. Nevertheless, it is worth pointing out that the values determined by  $^1\text{H}$  NMR are more accurate.



**Fig. 5.5 - TGA curves of poly(0), poly(1), poly(2) and poly(3).**

DSC curves of the poly(0) and the three PILs with different degree of quaternization are shown in Fig. 5.6. The table inserted in Fig. 5.6 shows  $T_g$  values for PMMA block and P2VP block of each block copolymer. The  $T_g$  of pure PMMA and P2VP blocks in the poly(0) copolymers were measured to be 95 °C and 120 °C, respectively. In the case of PILs, on one hand the disappearance of the  $T_g$  of PMMA block was observed in all cases. On the other hand, a decrease of the  $T_g$  of P2VP block was noticed with increasing the degree of quaternization. The  $T_g$  value of P2VP block of poly(1) and poly(2) was measured to be 114 and 98 °C, respectively. Surprisingly, no transition could be detected for the poly(3). The decrease of  $T_g$  observed for the PILs is influenced by the increasing number of ethyl groups after quaternization inducing higher mobility of the polymer chains which results in a decrease of the glass transition temperature.



**Fig. 5.6 - DSC curves of poly(0), poly(1), poly(2), and poly(3).**

After characterization of poly(0), poly(1), poly(2) and poly(3), several thermoset materials were prepared at 30 wt.% in epoxy resin as already reported. [247] All samples were found to be transparent indicating the absence of macroscopic phase separation, except for the sample prepared with poly(3) that was opaque (Fig. 5.7).



**Fig. 5.7 - From left to right sequence of photographs for the obtained thermosets with poly(0), poly(1), poly(2) and poly(3).**

Fig. 5.8 shows the DSC curves of the neat epoxy system and their thermoset blends. The inserted table in Fig. 5.8 shows  $T_g$  values for each of the samples. On one hand the  $T_g$  measured for the neat epoxy system was 138 °C. On the other hand, the  $T_g$  for the epoxy-rich phase in modified systems with 30 wt.% poly(1), poly(2) and poly(3) decreased with increasing degree of quaternization, ranging from 88 to 77 °C. Several factors can explain the decrease of  $T_g$  for cured blends modified with the same amount of block copolymer with different degree of quaternization, such as dilution of epoxy groups and an increment of the system viscosity, leading to a decrease in the curing rate. Moreover, the solubility of PMMA block with the epoxy system could explain the decrease of  $T_g$  observed. The miscibility of PMMA in an epoxy system was evidenced by the depletion of  $T_g$  of the epoxy-rich phase as a result of its miscibility in the matrix. [250, 251]

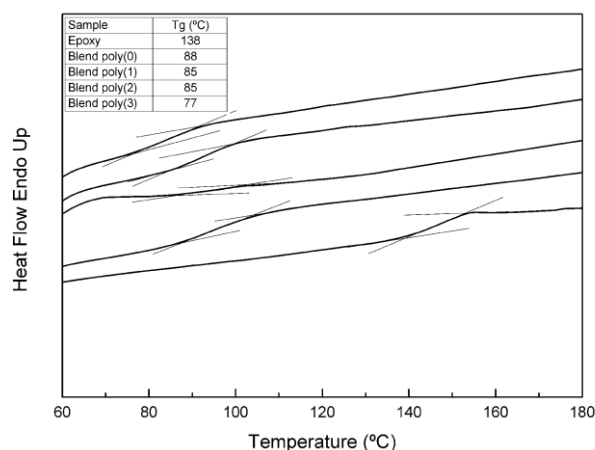


**Fig. 5.8 - DSC curves of neat epoxy system and its blends with poly(0) and poly(1), poly(2) and poly(3). Table inset shows the glass transition temperatures of neat and poly(ionic liquid) cured blends.**



The evolution of self-assembly of the P2VP block at different degrees of quaternization is shown in Fig. 5.9. TEM image of the poly(0)/epoxy blend (Fig. 5.9a) did not show any nanostructure since both blocks are fully miscible with the epoxy. For cured blends containing poly(1), a well-defined nanostructure was observed with the presence of round spheres corresponding to the coaxial (Fig. 5.9b) and the parallel (Fig. 5.9c) view to the main axis, at which cross-sections have been prepared. The average diameters of P2VP-r-poly(1-ethyl-2-vinylpyridinium bromide) domains were approximately 38 nm. Similar behaviour was found in cured systems containing poly(2), where spherical nanostructures could be clearly seen (Fig. 5.9d, coaxial view and Fig. 5.9e, parallel to the main axis) with a diameter of the pattern  $\sim 27$  nm. The cured blends containing poly(3) were opaque, thus indicating the presence of macroscopic phase separation. The TEM images of poly(3)/epoxy cured blend (Fig. 5.9f and 5.9g) showed the absence of nanodomains. TEM images reveal that degree of quaternization of poly(2-vinylpyridine) block between 7.5% and 16.4%, allows nanostructuring of the thermoset material with the P2VP-r-poly(1-ethyl-2-vinylpyridinium bromide) chains being in the form spheres within the epoxy cured system containing the PMMA block. It should be noted that for degrees of quaternization of 37% or more, macrophase separation of PIL in epoxy occurs.

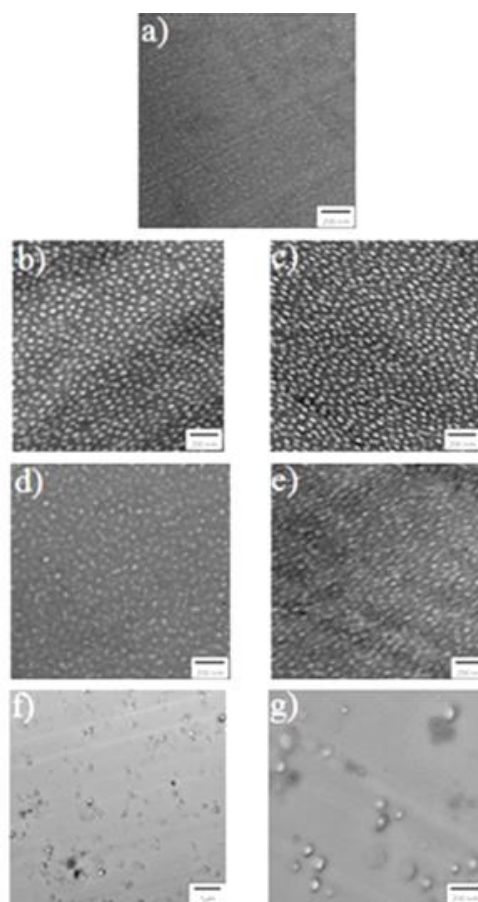


**Fig. 5.9 - TEM micrographs for the blends with 30 wt% poly(0) (a), 30 wt% poly(1) (b and c), 30 wt% poly(2) (d and e) and 30 wt% poly(3) (f and g). Scale bar: 200 nm except f which is 1  $\mu\text{m}$ .**

Before producing thermoset with poly(4) FTIR characterization of poly(0) and poly(4) was carried out in order to study the coordination of iron with pyridine units. Ramos *et al.* [252] studied the complexes formation of poly(4-vinylpyridine) with different transition metals such as cobalt, nickel and iron using FTIR spectroscopy to assess the nitrogen-metal coordination bonds. They found that pyridine stretching band at  $1600\text{ cm}^{-1}$  was displaced to higher wavenumber when coordination occurred. Fig. 5.10 shows the infrared spectra for poly(0) and poly(4). In the presence of iron metal, a new absorption band at  $1623\text{ cm}^{-1}$  attributed to the new nitrogen-metal coordination bonds was observed. The presence of this band indicates the coordination of the iron salt with P2VP after  $[\text{Fe}_3\text{Br}_{10}]^-$  anion exchange.

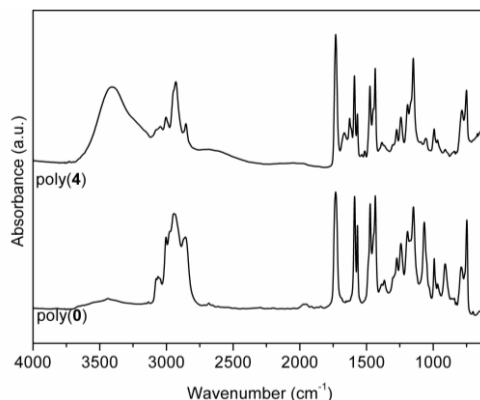


**Fig. 5.10 - FTIR spectra of poly(0) and poly(4).**

Poly(4) was blended with the epoxy resin and cured. Afterwards, it was characterized by carrying out both TEM and SQUID investigations. Fig. 5.11 shows the TEM micrographs of 30 wt% poly(4)/epoxy cured blend (Fig. 5.11a, coaxial view and Fig. 5.11b, parallel to the main axis). TEM images revealed a well-defined spherical nanostructure of the thermoset material. The size of spheres in this case was approximately 16 nm. It should be noted that despite having the same diblock copolymer content, the domain size was significantly different. It is well known that, the physical and chemical properties of PILs can be modified by anion exchange without altering the main structure of the polymer. [253] As a consequence, the miscibility of PILs with organic solvents or water becomes mostly dependent on the anions. This variation of block copolymers solubility influences strongly the morphology and the orientation of nanostructures. [245]

Fig. 5.11c shows the corrected long moment ( $M$ ) vs. magnetic field ( $H$ ) behaviour of samples poly(**4**) and 30 wt% poly(**4**)/epoxy cured blend, after careful subtraction of the diamagnetic background stemming from the organic fraction of the polymer. For such purpose the high field data of the cyclates were fitted to a straight line with negative slope and this contribution was subsequently subtracted from the data. The resulting hysteresis cycles revealed the presence of well conformed ferromagnetic interactions exhibiting remanence and coercivity. As expected, the reference compound, poly(**4**), showed one order of magnitude higher saturated values of the magnetization ( $M_s = 1.04 \times 10^{-02} \text{ emu g}^{-1}$ ) when compared to the cured blend 30 wt% poly(**4**)/epoxy ( $M_s = 1.68 \times 10^{-03} \text{ emu g}^{-1}$ ). The same trend was observed for the remanence,  $M_r = 9.40 \times 10^{-04} \text{ emu g}^{-1}$  and  $M_r = 1.37 \times 10^{-04} \text{ emu g}^{-1}$ , for poly(**4**) and 30 wt% poly(**4**)/epoxy cured blend respectively. These discrepancies were not observed in the coercive fields,  $H_c = 72 \text{ Oe}$  and  $H_c = 83 \text{ Oe}$  for 30 wt% poly(**4**) and 30 wt% poly(**4**)/epoxy respectively, pointing out towards similar levels of magnetic disorder and number of pinning centres in both samples. Differences in the saturated and remanence values of the magnetization of poly(**4**) and 30 wt% poly(**4**)/epoxy are probably due to the dilution of the magnetic entities per mass unit in the blend rather than to a real change in the basics of the ferromagnetic interactions. It is noteworthy that Döbbelin *et al.* [246] reported the synthesis of novel homopolymeric paramagnetic PIL. In their work, they did not observe a qualitative dependence of the magnetic behaviour on the nature of the polymer (imidazolium or diallyldimethylammonium-monomers, or the anion, chloride or bromine) used for building up magnetic interactions in their homopolymers. Also, the homopolymers used for their studies did not exhibit any kind of structure related to the assembly of the polymeric chains. As a result, the observed paramagnetic behaviour was consistent with a single ion picture of isolated, non interacting magnetic entities (i.e. the anions lying far apart in the proximity of the linear polymer chains). In contrast, our materials, poly(**4**) and poly(**4**)/epoxy cured blend, showed a clear ferromagnetic ordering related to the material composition. Nanostructures in block copolymers are generated by the self-assembly of less miscible blocks. As inferred from the TEM micrographs, our polymeric chains undergo an ordering process that makes the P2VP-r-poly(1-ethyl-2-vinylpyridinium  $\text{Fe}_3\text{Br}_{10}^-$ ) block to induce spherical nanostructuration (or assembly). This nanostructuration, in turn, allows the confinement of several magnetic anions within these spherical nanostructures, as inferred from the bright spots in Fig. 5.11, which translates into the promotion of strong dipolar interactions between the magnetic entities and the observed ferromagnetic ordering.

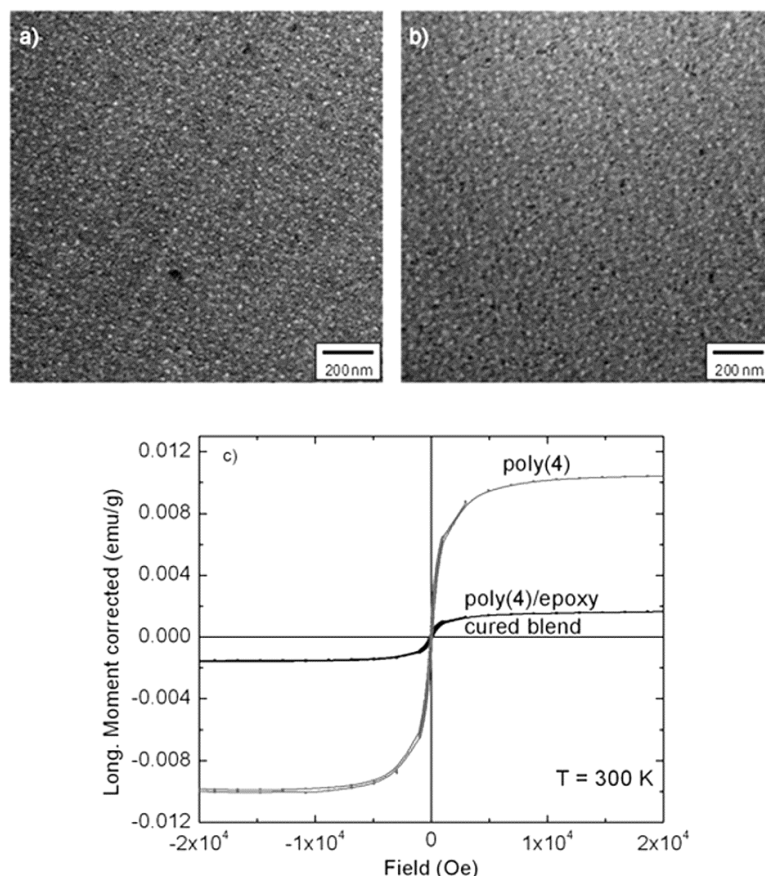


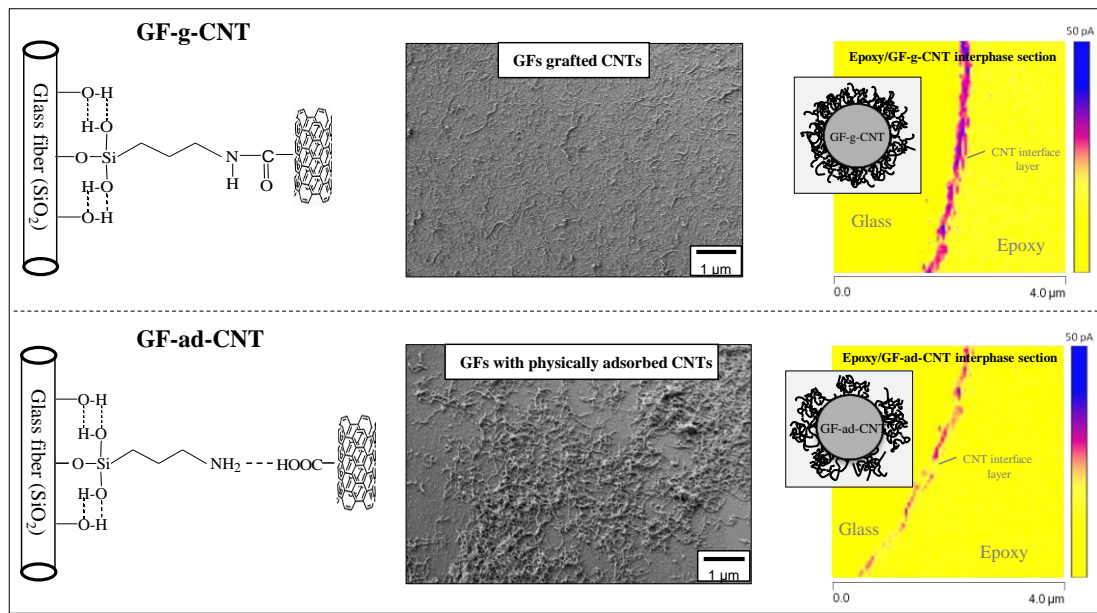
**Fig. 5.11** - TEM micrographs for 30 wt% poly(4)/epoxy cured blend (a and b) and magnetization curve of poly(4) and 30 wt% poly(4)/epoxy cured blend (c).

In conclusion, a new methodology for the production of nanostructured magnetic thermoset materials without any kind of metal oxide or metal magnetic nanoparticles has been proposed. We have demonstrated that the degree of quaternization of the pyridine block can induce microphase separation through self-assembly of the quaternized pyridine block in the epoxy matrix. When the quaternization degree is higher than the maximum threshold, macrophase separation occurred. Furthermore, anion exchange of corresponding selected poly(ionic liquid)s block copolymer, led to the formation of a new magnetic nanostructured thermoset material which revealed the presence of well conformed ferromagnetic interactions by exhibiting remanence and coercivity at room-temperature.

## Chapter 6

### Epoxy/Glass fiber nanostructured interphases

**6.1 The interphase microstructure and electrical properties of glass fibers covalently (GF-g-CNT) and non-covalently (GF-ad-CNT) bonded with multiwall carbon nanotubes**



#### Abstract

A solution-based method for the chemical grafting of multiwall carbon nanotubes (MWCNTs) onto the surface of glass fibers (GFs) is reported. MWCNTs and GFs were modified to expose the functional moieties for the formation of an ‘amide’ chemical bond. Treatment with strong acids introduces carboxylic groups to the MWCNT walls, which are converted to carbonyl chloride groups. The GFs are coupled with gamma-aminopropyltriethoxysilane ( $\gamma$ -APS) yielding amine surface functionalities (GF-APS), and acyl chloride modified MWCNTs (MWCNT-COCl) are covalently bonded in a dip-coating deposition process. The surface morphology and electrical properties of single fibers grafted with CNTs (GF-g-CNT) are studied and compared to physically adsorbed ones (GF-ad-CNT). The GF-g-CNT exhibited a fully CNT surface coverage and ten times higher electrical conductivity compared to GF-ad-CNT. X-ray photoelectron spectroscopy (XPS), scanning electron and atomic force microscopy (SEM, AFM) were used to characterize the fibers after each step of treatment. Single filaments were embedded in an epoxy to

investigate the interphase microstructures, through transmission electron microscopy (TEM). Single-fiber pull out (SFPO) tests accompanied with fractographic analysis of the pulled-out fibers were performed to study the interfacial adhesion strength. The results suggest that GFs with chemically grafted MWCNTs are promising multi-functional reinforcements.

### 6.1.1 Introduction

Carbon nanotubes have been widely used for advanced applications in the field of nanotechnology due to their unique electrical, mechanical and thermal properties. [6] [254] The combination of their extraordinary intrinsic properties, as well as their nanoscale size, low density and extremely high aspect ratio makes them an ideal candidate for fabricating functional polymer nanocomposites. [255] [256] [257] [258] [196] Recently, the deposition of MWCNTs onto micro-scaled reinforcements has attracted the interest of various research groups working in the area of high-performance polymer composites. [259] Several studies exist in which conventional fibers have been modified with CNTs creating 'hierarchical' structures, and incorporated further into polymer matrices. [260] [261] [262] [263] A review could be found where carbon nanotube-based hierarchical composites and the advantages of fabricating hybrid fiber/CNT multi-scale reinforcements were elaborately discussed. [264]

The mechanical behavior of polymer composites depends strongly on the interphase between fibers and the host matrix. The interphase acts as the intermediate bridge, which transfers the mechanical stresses from the matrix to the reinforcement upon loading through the shear flow. Therefore, an appropriately designed/engineered interphase is a critical parameter to control the strength and toughness of polymer composites. [265] [266] By definition, the interphase exists from some area around the fiber surface where the local properties including *i*) morphological characteristics, *ii*) chemical composition and *iii*) thermo-mechanical properties begin to alter from the bulk matrix properties. [267] [178] Normally, fibers used to reinforce a polymer matrix are modified to introduce functional groups, and increase the chemical interaction and wettability with the polymeric resin. In addition, the fiber surface modification can increase the surface nanoscale roughness which can impart mechanical interlocking with the polymer matrix. In such a way, optimal interphases with high interfacial adhesion strength can be developed facilitating an efficient stress transfer from the continuous matrix phase to the reinforcing fibers, whereby the fibers act as the main load-bearing constituent. [268] [269] Modification of fibers by CNTs has also been proposed as an efficient method to increase the interfacial adhesion strength as well as to introduce functionality at the interphase of the final composites. [270] [271] [272] By this approach, high loadings of CNTs can be achieved in the final composites alleviating the

critical problems encountered during the composite fabrication process related to the high viscosity of the polymer melts as well as the CNT agglomeration. [13] [273] Grafting of CNTs to the surface of glass or carbon fibers was found to enhance the interfacial strength via increased chemical bonding, mechanical interlocking and/or local stiffening of the polymer chains at the fiber/matrix interface, all of which can improve the stress transfer efficiencies, as outlined before. Composites reinforced with hierarchical multi-scale CNT-modified fibers leading to enhanced interfacial shear strength (IFSS) have already been reported. [274] [275] [276] Several approaches have been followed to deposit CNTs onto the surface of either glass or carbon fibers. In particular, in-situ growth of CNTs by chemical vapor deposition (CVD) directly to the surface of carbon [277] [278] [279] [280] or silica [281] fibers has been extensively used. An important finding was that controlling the experimental parameters, different lengths, density and orientation of the grown CNTs can be achieved and the structural characteristics of the CNT-networks could affect the composite's interfacial strength as revealed by model composite investigations. [24] [31] [282] However, there are some drawbacks of the CVD technique itself. The fibers must be modified with a catalyst before performing the CVD process, which can result in contamination of the fibers. In addition, the growth of CNTs requires the use of high temperatures, which can deteriorate the inherent strength of the fibers. Other methods that have been proposed to deposit CNTs onto conventional fibers include dip coating and electrophoretic deposition processes based on physical interactions between modified CNTs and functionalities of the fiber surface. [20] [283] [284] Fibers have been also modified after the spinning process with multi-component nanocomposite sizing systems containing specific amount of CNTs in the sizing mixture. [285] In general, CNT-coatings convert glass fibers from insulators to semi-conductive reinforcements with increased composite interfacial strength and multifunctional interfacial properties. [34] The resulting composite materials can be used for a wide range of applications such as electrostatic dissipation, interfacial damage sensing and electric field shielding. Recently, it has been reported by Gao *et al.*, [283] the use of CNT-coated GFs as interfacial damage, humidity and temperature sensors. Until now, the enhancement of interfacial strength and the functionality of hierarchical CNT/fiber structures have been discussed in several studies. [9-12, 20-27] Chemical methods for the deposition of MWCNTs onto the surface of carbon fibers via chemical bonding have also been reported, and their surface morphology as well as the interfacial strength enhancement have been discussed. [286] [287] [288] [289] [290]

Herein, a chemical method for grafting MWCNTs onto the surface of GFs is proposed. Single GFs with amine surface functionalities ( $\gamma$ -APS treated) were dipped in a

solution of acyl chloride modified MWCNTs (MWCNT-COCl), and amide chemical bonds were formed (GF-g-CNT). In comparison, and in order to elucidate the importance of activating MWCNTs with –COCl groups, silanized GFs were dipped in a solution of carboxylated MWCNTs (MWCNT-COOH). In that case, CNTs were physically adsorbed to the GF surface (GF-ad-CNT) via hydrogen bonds or zwitterionic interactions (MWCNT-COO<sup>⊖</sup>...<sup>⊕</sup>H<sub>3</sub>N-GF), as revealed by the XPS analysis. In both cases, electrically conductive GFs were achieved due to the MWCNT deposited networks. Our approach differs from the protocol of Zhang *et al.* [270, 283] where commercial carboxyl functionalised MWCNTs were dispersed with the help of an anionic surfactant (SDS), and a dip coating and/or electrophoretic deposition was utilized to deposit them onto silanized GFs with a positive charge (non-covalent bond formation). Fourier-transform infrared spectroscopy (FT-IR), Raman spectroscopy, thermogravimetric analysis (TGA) and electrokinetic investigations proved the successful modification of MWCNTs with carboxyl groups. The surface morphology of single filaments was characterized by scanning electron microscopy (SEM) and tapping mode atomic force microscopy (TM-AFM). The fiber and MWCNT surface element concentrations, functional groups, as well as the chemical grafting reaction of MWCNTs to the GFs were detected by X-ray photoelectron spectroscopy (XPS). GF-g-CNT and GF-ad-CNT were characterized electrically by ‘two probe’ electrical resistance measurements. The interphase microstructures of single GF-g-CNT and GF-ad-CNT epoxy composites were studied by transmission electron microscopy (TEM) of interphase-sections prepared by focused ion beam (FIB). High durability of the grafted MWCNT-network to remain attached to the GF surface was observed and further correlated to the interfacial mechanical properties studied by single-fiber pull out tests. The TEM images reveal that the microstructure of the CNT-network along the GF/epoxy interphase is affected by the polymerization and cross-linking of epoxy resin during the hardening process. The nature of bonding between GF and MWCNTs with respect to the electrical properties, interfacial microstructure and interfacial adhesion strength will be discussed further more in detail.

## 6.1.2 Experimental

### 6.1.2.1 Materials

E-glass fibers (GFs) without sizing with an average diameter of 18 μm and yarns’ fineness of 120 tex having 204 filaments were used in this study. The GFs were manufactured by a continuous melt-spinning process at the Leibniz Institute of Polymer Research Dresden. Commercially available MWCNTs (Nanocyl, NC 7000) with a carbon



purity of >90%, average length 1.5  $\mu\text{m}$  and diameters around 10 nm were received from Nanocyl S.A. (Sambreville, Belgium). The silane coupling agent, 3-aminopropyltriethoxysilane ( $\gamma$ -APS, 98%) was supplied by ABCR (Karlsruhe, Germany) and used for the GF surface modification. Ammonium hydroxide (28 wt% ammonia), hydrogen peroxide, absolute ethanol, acetone, sulfuric-nitric acid, thionyl chloride ( $\text{SOCl}_2$ ), dichloromethane, extra dry toluene, dimethylformamide (DMF) and tetrahydrofuran (THF) were purchased from Sigma-Aldrich (Steinheim, Germany). As commercial DGEBA-based epoxy resin and amine-based hardener (resin EPR L20 and hardener EPH 960) were obtained from Hexion Specialty Chemicals (Stuttgart GmbH) and used as the polymer matrix with a resin to hardener weight ratio of 100:34. The curing of the resin was carried out at 60  $^\circ\text{C}$  for 4 h, followed by high temperature post curing at 120  $^\circ\text{C}$  for 3 h. All the chemical reagents were analytical grade and used as received without further purification.

#### 6.1.2.2 Glass fiber cleaning - silanisation treatment

10 cm long tow of GFs was cut from the spin cake and cleaned with dichloromethane for half an hour. The fibers were collected and treated with a basic piranha solution consisting of  $\text{NH}_4\text{OH}/\text{H}_2\text{O}_2/\text{H}_2\text{O}$  (1:1:1 in volume, respectively) for 2 h at 65  $^\circ\text{C}$ . This step was performed in order to fully purify the fibers and increase the number of surface silanol groups (Si-OH) by hydrolysis of the fiber surface siloxane network. Therefore, it is defined onwards as ‘cleaning-activation’ treatment. Afterwards, the GFs were dried for 6 h at 80  $^\circ\text{C}$  under vacuum, and subjected further to a silanisation treatment by immersing into a  $\gamma$ -APS (1%) solution in extra dry toluene. The reaction left for 24 h at 80  $^\circ\text{C}$  in  $\text{N}_2$  atmosphere. Then, the fibers were removed and cleaned several times with toluene followed by ethanol and water to remove any trace of physically adsorbed silane. Silanised fibers were kept for 6 h at 80  $^\circ\text{C}$  under vacuum to complete the condensation of surface silanol groups and remove traces of ethanol molecules from the hydrolysis of  $\gamma$ -APS. [291] Then, they were stored in a desiccator until the MWCNT deposition process and other analytic investigations.

#### 6.1.2.3 MWCNT functionalisation

MWCNTs were treated with a mixture of  $\text{H}_2\text{SO}_4$  (98%) /  $\text{HNO}_3$  (67%) to introduce carboxylic acid groups (MWCNT-COOH) [193]. 1 g of HCl treated MWCNTs was added in a flask containing 120 ml of the acidic mixture, and stirred for 6 h at 60  $^\circ\text{C}$  under reflux. The mixture was left to cool down and diluted with distilled water followed by filtering through a polycarbonate membrane (47 mm diameter / 0.4  $\mu\text{m}$  pore size). Several steps of cleaning with distilled water were acquired to reach a neutral pH. MWCNTs were collected then and

dried overnight at 60 °C under vacuum. The carboxyl groups were converted further to carbonyl chloride groups in order to facilitate the chemical grafting reaction with the terminal amine groups of the GF surface. Particularly, MWCNT-COOH (70 mg) were mixed with 50 ml SOCl<sub>2</sub> / 2.5ml DMF (20:1 v/v) at 70 °C for 24 h under argon atmosphere, and thionyl chloride was removed by filtration using a PTFE membrane. The MWCNT-COCl filtrate was washed several times with THF and dried at 50 °C for 6 h in a vacuum oven.

#### 6.1.2.4 Deposition of MWCNTs onto single glass fibers via chemical or physical bonds

MWCNTs containing carbonyl chloride groups (10 mg) were dispersed by ultrasonication in 100 ml of extra dry THF (0.1 mg/ml). GFs modified with  $\gamma$ -APS were carefully de-yarned the previous day and individual fibers were attached lengthwise on a glass frame using a quick-dry adhesive. The fibers were kept then in a vacuum oven at 60 °C overnight. Once the MWCNT-COCl suspension was ready, a conventional dip coating apparatus was used and the glass frame was immersed into the CNT solution for 30 min. This time was sufficient to complete the MWCNT chemical grafting onto the GF surfaces through nucleophilic substitution reaction between the GF amine groups and the CNT acyl chloride groups. Afterwards, the frame was removed and GF-g-CNT kept for drying with their axes perpendicular at 80 °C for 24 h. It should be mentioned that all the reaction steps were carried out under argon (Ar) atmosphere. Following the same deposition process, GFs were coated also with MWCNT-COOH (GF-ad-CNT) via hydrogen bonds and/or zwitterionic interactions between the GF amine groups and MWCNT carboxyl groups (MWCNT-COO<sup>⊖</sup>...<sup>⊕</sup>H<sub>3</sub>N-GF). The two different approaches used to attach MWCNTs to the GF surfaces, based either on chemical or physical bonds are illustrated in Fig. 6.1.

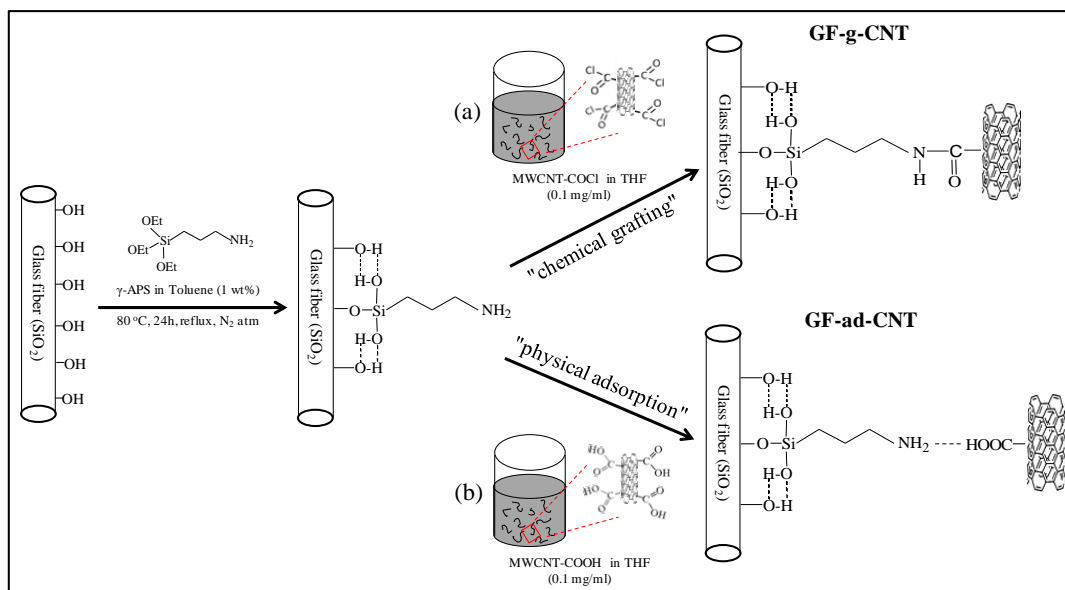


**Fig. 6.1 - Schematic illustration of (a) MWCNTs chemically grafted (GF-g-CNT) and (b) physically adsorbed (GF-ad-CNT) to the GF surface. Dip coating was used in both cases.**

#### 6.1.2.5 Characterization techniques

Fourier-transform infrared (FT-IR) spectra were recorded using a Vertex 80v FT-IR spectrometer (Bruker Germany) equipped with a DTGS detector. Scanning was conducted in transmission mode with a spectral resolution of  $2\text{ cm}^{-1}$ . Small amount of either pristine or carboxyl functionalized MWCNTs were pressed together with KBr to form pellets. Raman spectra were measured with a WITEC alpha300R micro-Raman system (RAMAN Imaging System WITEC alpha300R). The spectra were acquired in the back-scattering geometry and the excitation wavelength was 532 nm from an  $\text{Ar}^+$  ion laser with a laser power of 1mW. Thermogravimetric analysis (TGA) was used to analyze the thermal behavior of pristine and acid modified MWCNTs. Thermal scans were performed under nitrogen flow using a TA instrument (Q 5000) from  $30\text{ }^\circ\text{C}$  to  $800\text{ }^\circ\text{C}$  with a heating rate of  $10\text{ }^\circ\text{C}/\text{min}$ .

In order to study the grafting reaction procedure, XPS studies were carried out by means of an AXIS Ultra X-Ray photoelectron spectrometer (Kratos Analytical, England). Areas of approximately  $300 \times 700\text{ }\mu\text{m}^2$  were analyzed with a monochromatic  $\text{Al K}\alpha$  ( $h\nu = 1486.6\text{ eV}$ ) X-ray source of 300 W operating at 15 kV. The kinetic energy of the photoelectrons was determined with a hemispheric analyzer set to pass energy of 160 eV for the survey spectra and of 20 eV for high-resolution spectra. During all measurements electrostatic charging of the sample was avoided by means of a low-energy electron source working in combination with a magnetic immersion lens. All the recorded peaks were shifted by the same amount which was necessary to set the C 1s peak to 285.00 eV for saturated hydrocarbons or, respectively, 284.5 eV for the carbon atoms, which are bonded in the graphite-like lattice. For all the measurements the base pressure in the analysis chamber was less than  $10^{-8}$  mbar. Quantitative elemental compositions were determined from peak areas using experimentally determined sensitivity factors and the spectrometer transmission function. Spectrum background was subtracted according to Shirley [292]. The high-resolution spectra were deconvoluted by means of a computer routine (Kratos Analytical, Manchester, UK). Free parameters of component peaks were their binding energy (BE), height, full width at half maximum and the Gaussian-Lorentzian ratio. The samples were fixed with double-sided adhesive tape (Scotch 3M) on a sample holder. The maximum information depth of the XPS method is not more than 8 nm. In order to avoid hydrolysis reactions, the sample preparation was carried out under inert atmosphere.

Field-emission scanning electron microscopy (FE-SEM) was performed with a NEON 40 (Carl Zeiss AG, Germany) scanning electron microscope operating at an accelerating voltage of 1.0 kV. Dispersions of pristine or carboxyl functionalized MWCNTs were prepared by adding specific amount in DMF (0.1mg/ml) and sonicated for ten minutes. Three drops of each MWCNT suspension were dispensed onto the surface of cleaned silicon wafers and dried. In order to study the surface morphology of pristine, cleaned-activated, silanized and MWCNT-coated GFs, single fibers were placed onto the surface of cleaned silicon wafers and attached at both sides with a copper adhesive tape. Prior to the SEM analysis, all specimens were coated with a thin layer (3 nm) of platinum using a sputter coater to avoid charging effects.

The surface topography of different GFs was observed by Tapping Mode Atomic Force Microscopy (TM-AFM). AFM images (height data) were recorded with a scanning probe microscope (Nanoscope III, Dimension 3100<sup>TM</sup>, Veeco Digital Instruments) in air at room temperature at a resonant frequency of approximately 300 kHz. Commercially available silicon cantilevers were used (TM Nanoprobe, Veeco) with a cantilever spring constant of 35 N/m, a tip cone angle of 20° and tip radius of about 10nm while the scanning frequency was 1 Hz. The values of surface mean roughness ( $R_a$ ) and maximum height roughness ( $R_{max}$ ) were calculated after 2<sup>nd</sup> flattening operation over the captured area of 2×2 μm. For the AFM investigation, single GFs were stabilized onto clean silicon wafers in a similar way as for the SEM analysis.

In an attempt to visualize the electrically conductive interphases, single fibers were embedded in epoxy and cross-sections were prepared as reported elsewhere [33]. Afterwards, current maps were acquired by the PeakForce TUNA module with a Bruker ICON scanning probe microscope (Bruker Corporation). Electrically conductive tips PPP-EFM supplied by NanoAndMore GmbH were used and as measurement parameters, a scan rate of 0.5 Hz and a direct Voltage bias of 5 V were applied. In the obtained images, only the CNTs are visible which form the conductive paths within the area of investigation. The Nanoscope analysis software (Bruker, ver. 1.40) was used for the image analysis.

The Libra 200 transmission electron microscope (TEM, Carl Zeiss AG, Germany) operating at 200 kV was used to investigate the morphological characteristics of MWCNTs, as well as the interphase microstructures of single fiber composites. Bright field TEM images were recorded, while the energy filtering and contrast apertures were inserted to enhance the contrast of the images. For MWCNT investigations, one drop of pre-dispersed pristine or acid modified CNTs in DMF (0.01 mg/ml) was dispensed onto the surface of a

holey carbon coated grid and the excess solvent was removed by placing the grid on a filter paper. Interphase-sections of single fiber composites were prepared by Focused Ion Beam (FIB) using the NEON 40 FIB/SEM chamber equipped with a gallium ion beam operating at 30 kV. A single filament of either GF-g-CNT or GF-ad-CNT (~30mm length) was placed flat onto a cleaned silicon wafer and stabilized from both sides with an adhesive tape. Afterwards, a thin layer of well-mixed and degassed epoxy resin/hardener mixture (DGEBA-based epoxy resin with amine hardener EPH 960) covered thoroughly the whole GF and cured at 60 °C for 4 h, followed by high temperature post curing at 120 °C for 3 h. Single fiber composites were exposed to the focused ion beam process for the fabrication of the interphase-sections which were investigated further with TEM. Initially, the samples were sputtered with a platinum layer of 60 nm thickness to avoid charging effects during the FIB-cutting (milling) process. By using the ion beam, a localized 15 nm protective platinum layer was also deposited to the surface of each sample over the region of interest selected for the interphase-section preparation. After several steps of milling-polishing, lamellae of 100 nm thickness were obtained and stabilized with a macro-manipulator on a special Cu grid for the TEM investigations. The FIB interphase-sections of GF-g-CNT and GF-ad-CNT composites were acquired following the same preparation steps.

The DC electrical resistance ( $R$ ) of single GFs chemically grafted and physically bonded with MWCNTs, at different fiber lengths, was measured through a standard two-probe method using a Keithley 2400 Source-Measure Unit (Keithley Instruments GmbH, Germany) interfaced with a PC. Single fibers were laid down on a glass slide with pre-patterned sputtered platinum electrodes at 0.5, 1.0, 2.0 and 5.0 mm electrode-electrode distances, respectively, and glued with silver paste to stabilize them. Then, two copper electrodes were adjusted tightly to the gold contacts and electrical resistance measurements were performed at 22 °C and 22% relative humidity ( $RH$ ) providing a voltage source ( $V$ ) of 0-10 V in 100 steps. By recording the current ( $I$ ) which flows through the fiber surface in every step, the average resistance of each fiber was calculated. At least, 20 samples of either GF-g-CNT or GF-ad-CNT were measured and the mean resistance values with the corresponding standard deviations are presented. The distance between the pre-patterned sputtered gold electrodes defines the length of the fiber used for the resistivity ( $\rho$ ) and conductivity ( $\sigma$ ) calculations. The  $I$ - $V$  characteristics of single GF-g-CNT and GF-ad-CNT embedded in epoxy were also determined. A single fiber was placed lengthwise on two prepatterned sputtered platinum contacts on opposite sides of a rectangular shaped Teflon mould at 5.0 mm distance between them. Silver paste was used to contact and glue two copper wires with the platinum contacts in order to be connected further with the Keithley

Source-Measure Unit. Epoxy mixed with the hardener was poured into the mould and cured as previously described. Using a voltage power supply ( $V$ ) of 0-10 V in 100 steps, the current values were recorded and the  $I$ - $V$  curves were plotted. Each measurement set-up is shown schematically in Fig. 6.2.

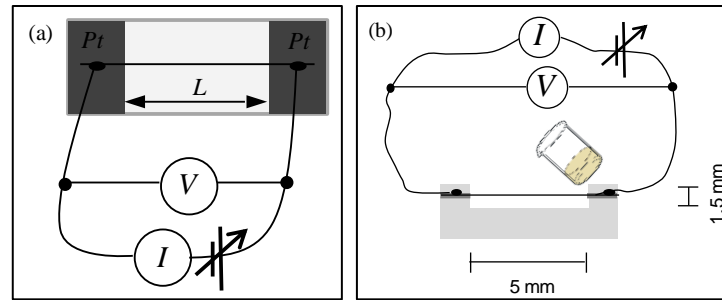


**Fig. 6.2 – Schematic illustration of the set-up used for the electrical investigations of (a) MWCNT-coated glass fibers and (b) single fiber composites.**

In order to study the interfacial adhesion strength, single fiber pull-out tests (SF POT) were performed on single fiber model micro-composites. This micro-mechanical technique is very sensitive to variations of the interfacial adhesion and it has been extensively used in order to study the interphase quality in composite materials as a function of the fiber surface modifications. Model composites were prepared using self-made embedding equipment as previously described elsewhere. [293] Single GFs with a pre-determined embedding length between 50 and 200  $\mu\text{m}$ , were accurately end-embedded perpendicularly into the epoxy matrix under controlled atmosphere and temperature conditions. After curing, the single fiber pull-out tests were carried out using a self-made pull-out apparatus to evaluate the apparent interfacial shear strength ( $\tau_{app}$ ) as a measure of the practical adhesion at the fiber/matrix interphase. [294] All the tests were performed in an ambient atmosphere under quasi-static conditions with force accuracy of 1 mN and displacement accuracy of 0.07  $\mu\text{m}$ . The crosshead displacement rate used throughout all the experiments was set at 0.01  $\mu\text{m/s}$ . From each force-displacement curve, the maximum force ( $F_{max}$ ) required for pulling the fiber out of the matrix and the embedded fiber length ( $l_e$ ) were derived. The apparent interfacial shear strength ( $\tau_{app}$ ) was calculated then according to the following equation:

$$\tau_{app} = \frac{F_{max}}{\pi d_f l_e} \quad (6.1)$$

where  $d_f$  is the fiber diameter measured by optical microscopy. The adhesion bond strength between the fiber and the epoxy matrix was characterized finally by the values of apparent interfacial shear strength for each group of model composites. The average values of shear

strength which are presented with the corresponding error bars representing the standard deviations were determined from at least ten successful pull-out experiments. The pulled-out fibers were collected and their surface morphologies were investigated by SEM.

### 6.1.3 Results and discussion

#### 6.1.3.1 MWCNT analytics

Fig. 6.2 shows the FT-IR spectrum of pristine and acid functionalised MWCNTs, respectively. The appearance of a band at  $1712\text{ cm}^{-1}$  can be assigned to the stretching vibrations of carbonyl groups ( $\text{C}=\text{O}$ ), arising from the  $-\text{COOH}$  moieties introduced to the sidewalls and open ends of MWCNTs after the oxidative treatment. The absorption band at  $2918\text{ cm}^{-1}$  for both pristine and acid modified MWCNTs is attributed to hydrocarbon groups ( $-\text{CH}_x$ ), and it is slightly decreased for the acid treated MWCNTs due to existence of surface  $-\text{COOH}$  functionalities. [24] [295] [192] TEM images of pristine and acid treated MWCNTs are depicted next to the FT-IR spectra. Obviously, the acidic treatment generates some structural defects to the MWCNTs, which appear with not such a smooth surface of the outer wall compared to pristine ones.

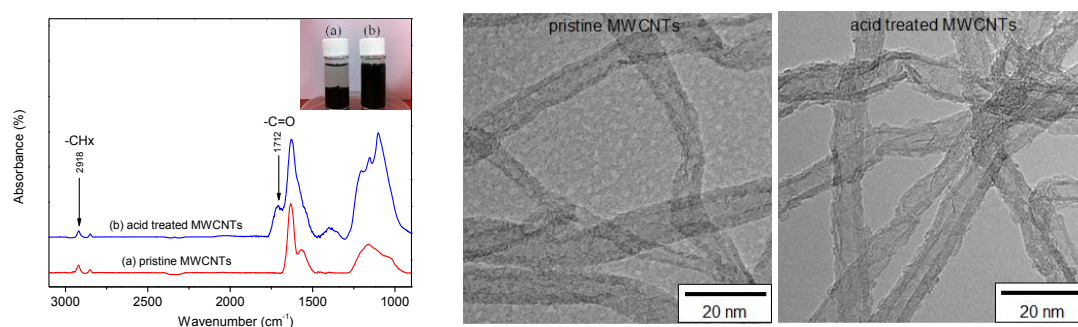


**Fig. 6.2** - FT-IR spectra of pristine (red line) and acid treated (blue line) MWCNTs. The inset image shows the colloidal stability of MWCNTs in water, one month after the CNT-dispersions have been prepared. TEM images of pristine and acid treated MWCNTs are depicted next to the FT-IR spectra.

#### 6.1.3.2 XPS analysis

On molecularly smooth surfaces, the XPS method gives information on the chemical composition of a surface layer, which is not thicker than 8 nm. Hence, XPS was utilized as a suitable tool to show modifications carried out on the MWCNT and GF surfaces but also on the GF-g-CNT and GF-ad-CNT hybrid filaments (areas of approximately  $300 \times 700\ \mu\text{m}^2$  were analyzed). XPS scans were performed to detect the presence of surface elements and determine the chemical composition of MWCNTs, GFs and GFs with chemically and

physically attached MWCNTs. The peaks of carbon, oxygen, nitrogen and chlorine are centered at around 283.9, 532.4, 399.5 and 200.1 eV, respectively. Fig. 6.3 shows the wide-scan and high-resolution element spectra of pristine MWCNTs, MWCNTs modified with carbonic acid (MWCNT-COOH) and acyl halide (MWCNT-COCl) groups. It can be seen from Fig. 6.3a (left column, wide-scan spectrum of pristine MWCNTs) that besides the intensive C 1s peak of carbon (99.14 at.%), MWCNTs contain traces of oxygen (O 1s and O 2s peaks, and O KLL Auger series; 0.66 at.%), which can be mainly a constituent of typical inorganic impurities such as aluminum (0.30 at.%). The asymmetric shape of high-resolution C 1s spectrum for pristine MWCNTs is very characteristic for carbeneous substances having graphite-like lattices. Photoelectrons of carbon atoms of the carbon nanotube graphite-like lattice ( $-\underline{\text{C}}=\underline{\text{C}}- \leftrightarrow =\underline{\text{C}}-\underline{\text{C}}=$ ) contributes to the main component peak *Gr* at 284.5 eV. Excited states caused by the consumption of external energy led to its asymmetric shape. Electron transitions between  $\pi$  and  $\pi^*$  orbitals of the conjugated carbon atoms in the  $sp^2$  hybrid state were observed as shake-up peaks. The endowing of MWCNTs with carbonic acid groups clearly increased the relative amount of oxygen (13.31 at.%) in the sample surface (Fig. 6.3b, left column). Accordingly, it can be observed that the shape of the corresponding C 1s high-resolution spectrum has been slightly changed. The asymmetric shape of the main component peak *Gr* is not significantly affected, however, two additional component peaks, *C* (3.99 at.%) and *E* (5.46 at.%) resulting from surface functional groups were introduced. Component peak *E* (at 288.5 eV) results from carbonyl carbon atoms of carbonic acids ( $\text{HO}-\underline{\text{C}}=\text{O}$ ) and their corresponding carboxylate groups ( $\text{O}=\underline{\text{C}}-\text{O}^- \leftrightarrow \text{O}=\underline{\text{C}}-\text{O}$ ), showing the success of the functionalization reaction. Component peak *C* (at 286.6 eV) indicates oxidative side reaction where phenol-like groups ( $\underline{\text{C}}-\text{OH}$ ) were formed. Furthermore, the acid treatment partly decomposed the graphite-like structures, which is accompanied by the formation of  $sp^3$  hybridized carbon atoms (component peak *A* at 285.00 eV). The oxidation reaction decreased slightly only the intensities of the shake-up peaks. These findings support the assumption that carbonic acids and other functional groups were formed only on the carbon nanotubes' surfaces. The attachment of -COCl groups after treatment with thionyl chloride, introduced chlorine to the carbon nanotube surface which was detected as Cl 2p and Cl 2s peaks (Fig. 6.3c, left column; 4.21 at.%). The high-resolution Cl 2p spectrum (Fig. 6.3c, right column) clearly indicated that the majority of chlorine is organically bonded ( $\underline{\text{C}}-\underline{\text{Cl}}$ ) in intact acyl chloride groups (component peaks *N* [Cl 2p<sub>3/2</sub>] at 199.82 eV and *N'* [Cl 2p<sub>1/2</sub>] at 201.42 eV). Hydrolysis of acyl chloride groups released chloride ions ( $\underline{\text{Cl}}^-$ ) which were observed as component peaks *M* [Cl 2p<sub>3/2</sub>] and *M'* [Cl 2p<sub>1/2</sub>] at lower binding energy values (197.35 eV and 198.95 eV, respectively). The shape of the C 1s narrow scan spectrum



of the MWCNT-COCl sample (Fig. 6.3c, second column) is obviously different from the other C 1s spectra discussed above. Component peak *D* (at 287.2 eV) results from carbonyl carbon atoms of intact acyl chloride groups ( $\text{O}=\underline{\text{C}}-\text{Cl}$ ). Its intensity ( $\approx 3.9$  at.%) excellently agrees with the intensity of the organically bonded chlorine in the high-resolution Cl 2p spectrum. The component peak *E* shows carbonic acid groups and their corresponding carboxylate groups, which were formed by the hydrolysis of some of the acyl chloride groups. The lower intensities of the shake-up peaks suggest that the endowing of MWCNTs with acyl chloride groups has affected the graphite-like lattice stronger than the first step of oxidation treatment to introduce carbonic acid groups.

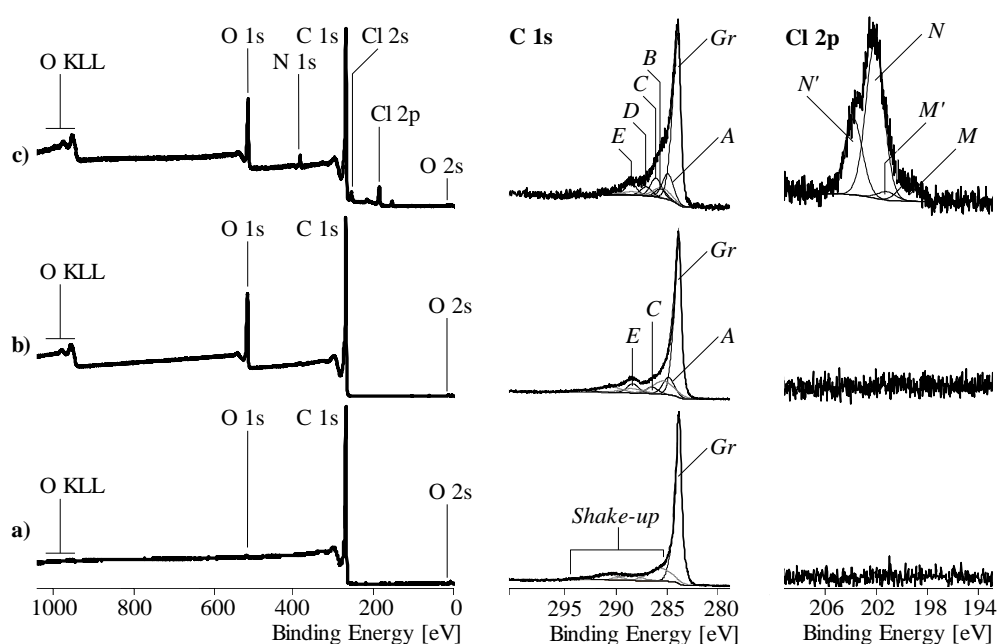


**Fig. 6.3** - Wide-scan XPS spectra, C 1s and Cl 2p high-resolution XPS element spectra of (a) pristine MWCNTs, (b) MWCNT-COOH and (c) MWCNT-COCl.

Differently surface-modified MWCNTs were attached to GFs which were coupled with  $\gamma$ -APS. Fig. 6.4 shows the XPS wide-scan and the corresponding high-resolution C 1s, N 1s and Cl 2p spectra of  $\gamma$ -APS modified GFs (Fig. 6.4a), GF-ad-CNT (Fig. 6.4b) and GF-g-CNT (Fig. 6.4c). The successful silanisation of GFs can be seen by the presence of a considerable amount of nitrogen on the sample surface ( $[\text{N}]:[\text{C}] = 0.125$ ) in Fig. 6.4a (left column). Moreover, the high-resolution C 1s spectrum (Fig. 6.4a, second column) shows a component peak *Si* (at 284.33 eV) appearing from carbon atoms which are bonded to silicon ( $\underline{\text{C}}-\text{Si}$ ). With respect to the stoichiometry of  $\gamma$ -APS, component peak *A* (at 285.00 eV) shows an excess of saturated hydrocarbons ( $\underline{\text{C}}_x\text{H}_y$ ). Such surface contaminations are usually observed on oxide surfaces because the high amount of the material's surface free energy can

be minimized by non-specific adsorption of organic molecules during wet processes or from atmosphere. Component peaks *C* (carbon atoms of alcohol and/or ether groups, alcohol-sided carbon atoms of carbonic ester groups), *E'* (carbonyl carbon atoms of carbonic ester groups) and *E* (carbonyl carbon atoms of carbonic acid groups and their corresponding carboxylate groups) appeared from carbon atoms of functional groups containing oxygen. Carbon atoms bonded to nitrogen ( $\underline{C}-N$ ) contributed to component peak *B* (at 286.02 eV). The N 1s high-resolution spectrum (Fig. 6.4a, third column) shows the two component peaks *G* and *H* which indicate the presence of organically bonded nitrogen. The binding energy found for component peak *G* (at 399.8 eV) is typical for  $C-\underline{N}$  bonds of amino groups. Component peak *H* (at 401.6 eV) arose from protonated amino groups ( $C-\underline{N}^+H$ ). The intensity ratio  $[H]:([G] + [H])$  quantifies the protonation equilibrium of the amino groups. On glass surfaces, it is also possible that the primary amino groups of  $\gamma$ -APS can be partly protonated by their interaction with the Brønsted-acid silanol groups of the glass substrate.

If it is assumed that a small amount of carboxyl modified MWCNTs were attached to the silanized GF surface, the slight decrease observed for the peak intensity of silicone of the substrate material seemed to be plausible (Fig. 6.4b, left column). In the corresponding high-resolution C 1s spectrum it was impossible to separate neither a component peak *Gr* showing the carbon atoms of the graphite-like lattice of the carbon nanotubes nor a component peak *Si* showing  $\underline{C}-Si$  bonds of silanes. Hence, all these carbon atoms contributed to component peak *A*, which is wider than the main component peak in the C 1s spectrum of the silanized GF without MWCNTs. After the attachment of MWCNT-COCl, chlorine was detected on the GF surface as Cl 2s and Cl 2p peaks (Fig. 6.4c, left column). In contrast to the MWCNT-COCl sample, the high-resolution Cl 2p spectrum of the MWCNT-COCl grafted glass fiber shows only chlorine (Fig. 6.4c, right column), which is not organically bonded (component peak *M* [Cl 2p<sub>3/2</sub>] at 197.36 eV and component peak *M'* [Cl 2p<sub>1/2</sub>] at 198.95 eV). The absence of organically bonded chlorine can be explained by taking place of reactions between the carbon nanotube's acyl chloride groups and the primary amino groups of the silane coated fibers. The carbonic amide groups ( $O=C-NH-C$ ) formed during these reaction contributed to component peak *D'* (at 287.83 eV), which was observed in the corresponding C 1s spectrum (Fig. 6.4c, second column). The new component peak *D'* resulted from carbonyl carbon atoms of the amide groups ( $O=\underline{C}-NH-C$ ) while the amine-sided carbon atoms of the amide groups ( $O=C-NH-\underline{C}$ ) contributed to component peak *B*. The intensity of component peak *D'* was approximately the half of the  $[N]:[C]$  ratio, which was determined from the wide-scan spectrum. That means only the half of the amino groups was involved in the reaction with the acyl chloride-modified carbon nanotubes. These

findings correspond to the high amount of protonated amino groups (component peak *H*), which cannot react with acyl chloride groups of the MWCNTs. The formation of amide groups did not significantly shift the position of component peak *G*, which represents now mainly nitrogen atoms of the carbonic amide bonds ( $\text{O}=\text{C}-\underline{\text{N}}\text{H}-\text{C}$ ). In contrast to the formation of covalent bonds between the acyl chloride-functionalized MWCNTs and the GF surface carrying primary amino groups; the attachment of COOH-modified MWCNTs on the fibers is mediated by electrostatic interactions. The Brønsted basic primary amino groups of the silane layer drive the deprotonation of the weak Brønsted acid carbonic acid groups by stabilizing the hydronium ion. As a result, a salt pair between MWCNT-COOH and the  $\gamma$ -APS modified GFs ( $-\text{COO}^- \cdots \text{H}^+ \text{NH}_2-$ ) is formed. The protonated amino groups should contribute to component peak *H* in the N 1s spectrum (Fig. 6.4b, third column). However, the negative charge of the carboxylate group in the immediate neighborhood of the primary amino group apparently neutralized the amino group's electric field and compensated the expected chemical shift in the N 1s spectrum. Hence, in Fig. 6.4b the intensity of component peak *H* seems to be decreased.

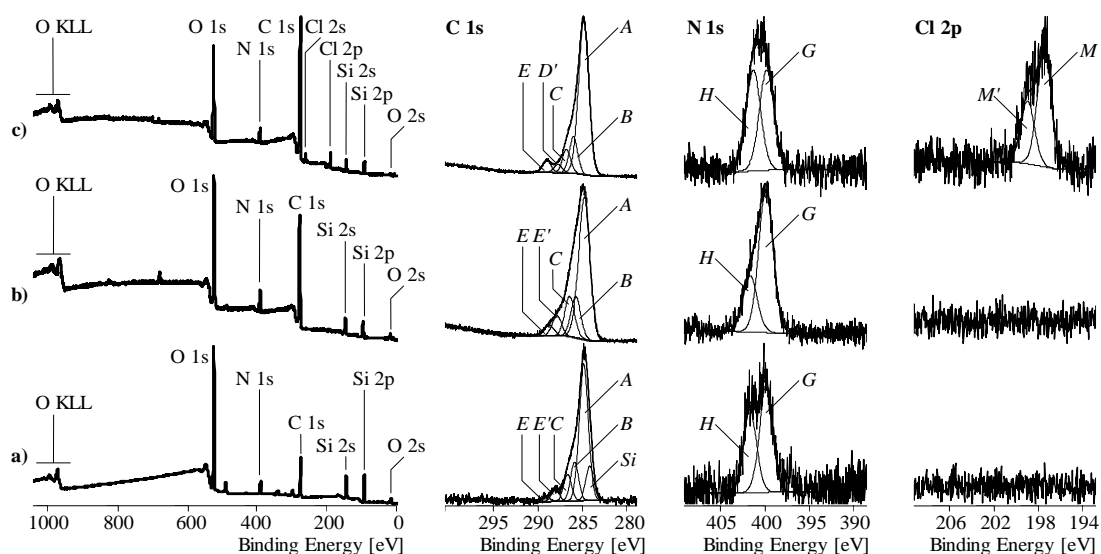
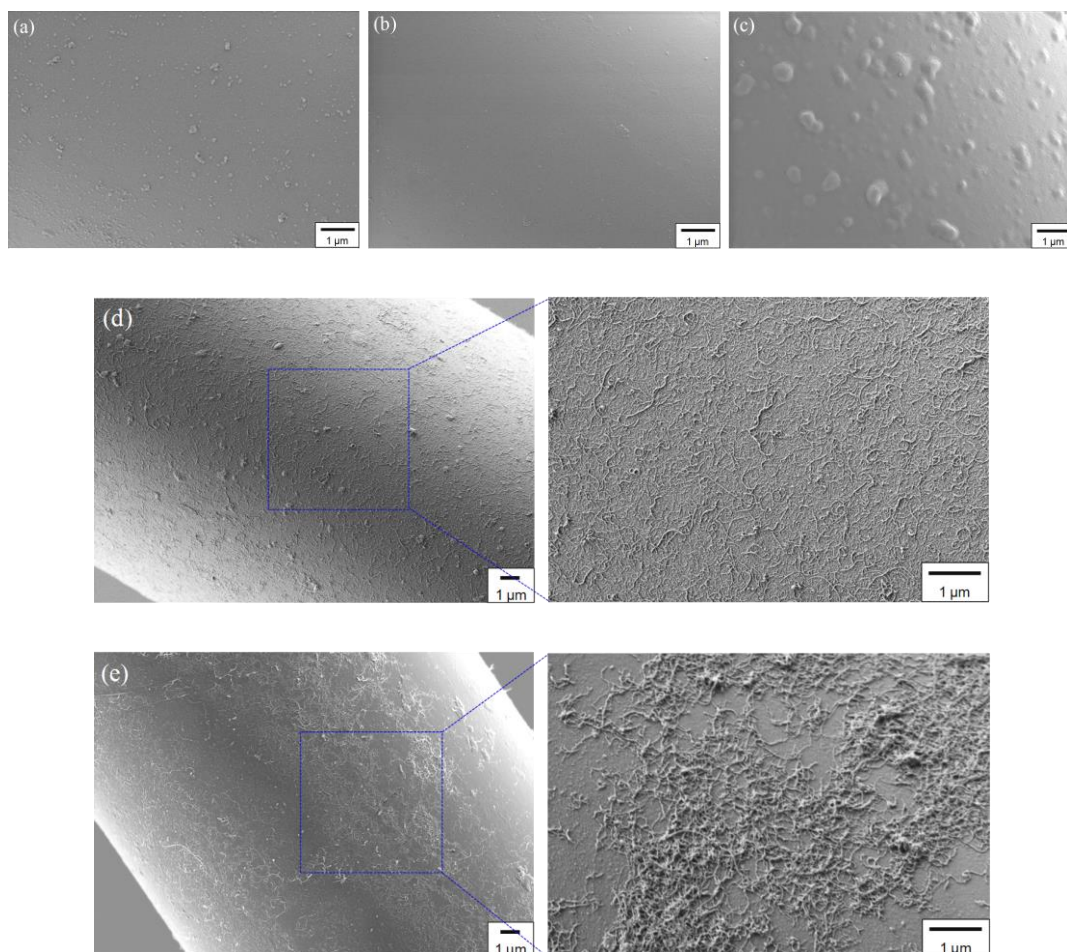


Fig. 6.4 – Wide-scan XPS spectra and C 1s, N 1s, Cl 2p high-resolution XPS element spectra of (a) APS-modified GFs, (b) GFs coated with MWCNT-COOH and (c) grafted with MWCNT-COCl.

### 6.1.3.3 Glass fiber surface microstructures

The SEM images in Fig. 6.5a-c depict the fiber's surface morphology after the spinning process, the cleaning-activation treatment and the silanisation coupling, respectively. The GFs produced by the spinning process expose some small glass particles

on the surface (Fig. 6.5a) which are removed after the basic piranha treatment (Fig. 6.5b). This step yields activated as well as neat and smooth fiber surfaces due to possible hydrolysis of siloxane bonds, which may cause the extraction of the glass particles. The surface modification of GFs with  $\gamma$ -APS generates a mountain-like topography (Fig 5c) which is typical for the condensation of silanes on glass surfaces. [41] Fig. 6.5d and 6.5e demonstrate the microstructures of chemically attached (GF-g-CNT) and physically adsorbed (GF-ad-CNT) MWCNTs to the GF, at two different magnifications. The MWCNT-coating of GF-g-CNT is more uniform compared to GF-ad-CNT, and MWCNTs form an interconnected network with fully surface coverage and very few visible agglomerates. This could be attributed to the covalent bond between GF/MWCNTs, which is strong enough to prevent undesired agglomeration of CNTs upon drying after the dip-coating process. On the other hand, the surface morphology of GF-ad-CNT (Fig. 6.5e) shows that MWCNTs are assembled into arrays due to their native Van der Waals forces or possible electrohydrodynamic and electro-osmotic effects. [20] It can be presumed that the nature of bonding between MWCNTs and GFs plays an important role to obtain a good quality of CNT-coating which may affect the electrical properties as well as the interfacial strength.



**Fig. 6.5 – SEM images of GFs (a) after the spinning process, (b) cleaned-activated and (c) silane treated. (d) GFs grafted with MWCNT-COCl and (e) non-covalently bonded with MWCNT-COOH at two different magnifications.**

Fig. 6.6 illustrates the AFM height images of single GFs showing the variations of fiber surface topographies. Fig. 6.6a corresponds to the GF after the spinning process and small glass impurities can be observed, while, relatively clean and smooth fiber morphology was obtained after the cleaning-activation treatment (Fig. 6.6b). The lowest values of image mean and maximum roughness indicate that the cleaning-activation treatment not only increases the number of surface silanol groups (Si-OH), but also removes the small glass particles originating from the spinning process. In Fig. 6.6c, the silane islands as discussed above are formed due to the condensation of the silane coupling agent. Fig. 6.6d and 6.6e display the CNT-layer characteristics of GF-g-CNT and GF-ad-CNT, respectively, and the observed topographies fully corroborate with the SEM micrographs.

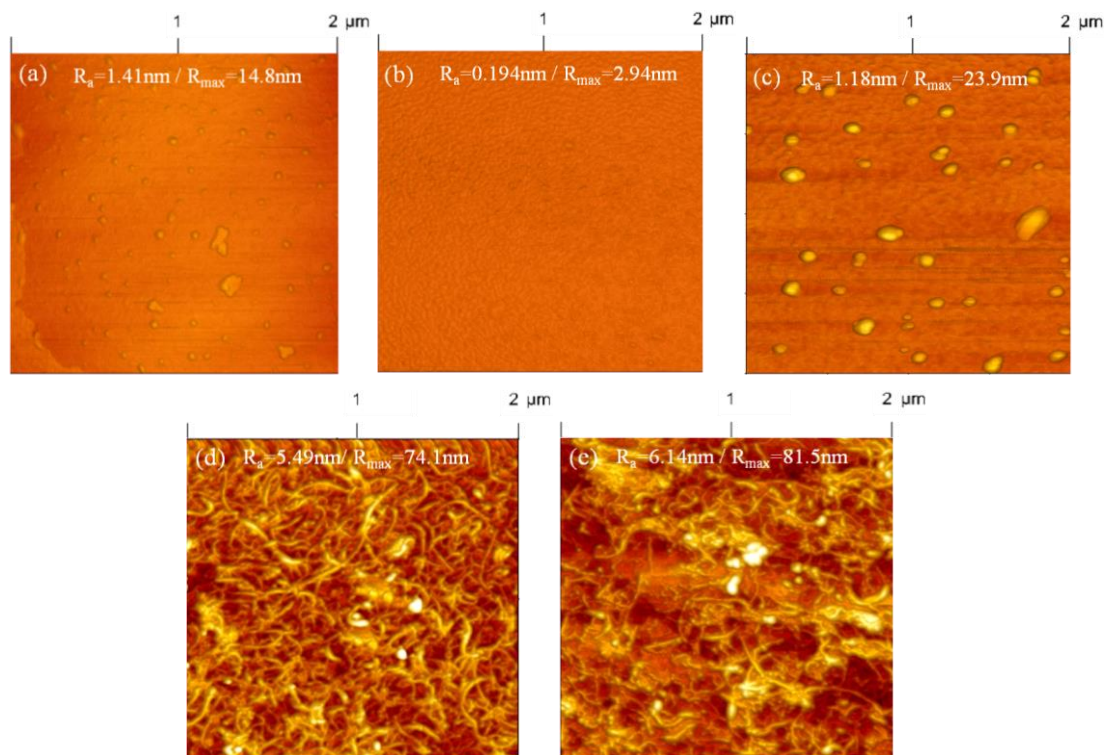
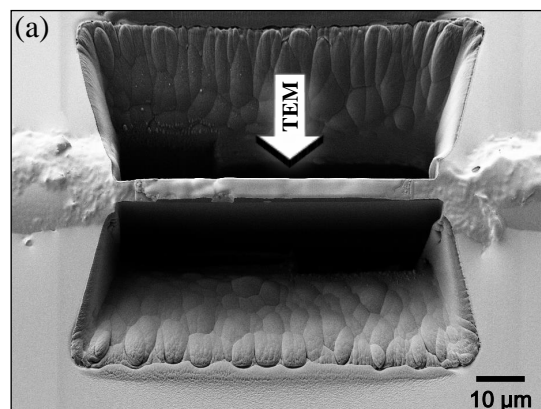


**Fig. 6.6 – AFM height images of (a) GF after the spinning process, (b) cleaned-activated, (c) silane treated, (d) grafted and (e) non-covalently bonded with MWCNTs. Scan size: 2 x 2  $\mu\text{m}$ , Z data scale: 100 nm. The values of image mean and maximum roughness ( $R_a$ ,  $R_{\text{max}}$ ) are inserted in the corresponding AFM image.**

#### 6.1.3.4 TEM interphase microstructures of single fiber composites

Fig. 6.7a demonstrates a representative SEM image of the single fiber composite interphase-section at an intermediate step of the Focused Ion Beam (FIB) milling-polishing

process. Consecutive steps were performed to achieve ~100 nm thickness of the interphase-section lamellae which were investigated by TEM at the direction shown by the arrow. Fig. 6.7b and Fig. 6.7c depict the TEM images of single GF-g-CNT and GF-ad-CNT epoxy composite interphases. These images provide detailed information about the MWCNT-network characteristics along the interphase region. In Fig. 6.7b, a homogeneous and interconnected network can be observed that remains in contact with the GF surface after embedding in epoxy matrix. This could be an indirect proof of the chemical bonding between MWCNTs and GF, which is in a good agreement with the results of the XPS analysis. On the contrary, Fig. 6.7c shows that only few MWCNTs are close to the GF surface and the CNT-network has migrated away, around 40 nm to the epoxy phase. A possible explanation could be that *i*) the chemical reaction of epoxy groups with the GF amine surface functionalities as well as the MWCNT carboxylic groups via a nucleophilic ring opening mechanism, and *ii*) the molecular mobility of the epoxy polymeric chains during the curing process, overcome the strength of zwitterionic interactions (or H-bonds) formed between MWCNT-COOH and amine terminated GFs resulting in the detachment of MWCNTs. From the interfacial characteristics obtained by the TEM analysis, we can deduce that chemically grafted MWCNTs expose high durability to remain attached to the GF when they are introduced in an epoxy matrix. This finding is of utmost importance for further utilization of the hierarchical reinforcement as multifunctional sensor in composite materials.



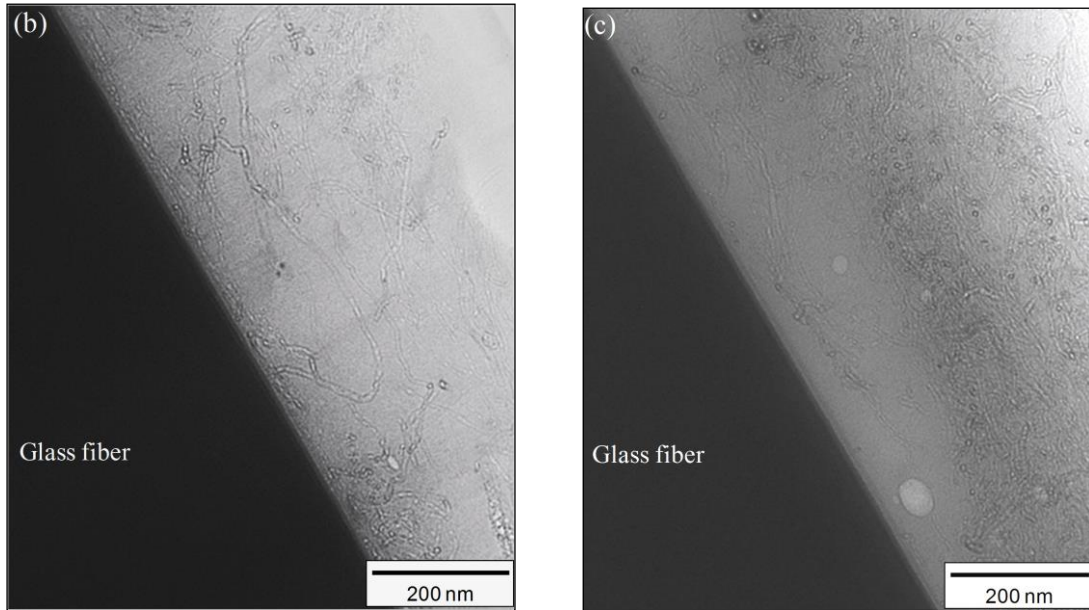


**Fig. 6.7** – (a) SEM image of the FIB interphase-section at an intermediate step of the milling-polishing process. (b and c) TEM interface microstructures of single GF-g-CNT and GF-ad-CNT epoxy composites.

### 6.1.3.5 Electrical properties of single MWCNT-coated glass fibers and single fiber composites

Fig. 6.8a and 6.8b show the arithmetic mean values with the corresponding standard deviations of electrical resistance ( $R$ , black bars) and conductivity ( $\sigma$ , grey bars) for single GF-g-CNT and GF-ad-CNT, respectively. In general, the resistance increased with increasing the electrode-electrode distance, and specifically for the GF-g-CNT was in the range of  $10^4$ - $10^5 \Omega$  while for the GF-ad-CNT about  $10^5$ - $10^6 \Omega$ . It can be observed that the resistance values and their variation are higher for the GF-ad-CNT samples. This can result from the inhomogeneous microstructure of the CNT surface layer which was previously demonstrated by the SEM and AFM images. Accordingly, the specific conductivity of MWCNT-coated GFs (GF-CNT) with an average diameter of  $d \approx 18 \mu\text{m}$  was calculated by the formula:  $\sigma_{GF-CNT} = (4L) / \pi d^2 R$ , and it was  $\sim 20 \text{ S/m}$  for the GF-g-CNT and  $\sim 2 \text{ S/m}$  for the GF-ad-CNT. The conductivity introduced to the intrinsic electrically insulating GFs can be attributed to the ultrathin CNT-networks deposited to the fiber surfaces creating the electron transport pathways. In fact, higher values were achieved for the GF-g-CNT due to the excellent distribution of MWCNTs which were arranged in highly entangled and closely packed networks. The maximum conductivity ( $\sim 20 \text{ S/m}$ ) of the GF-g-CNT is to our knowledge one of the highest values compared to existing ones in literature for similar systems. [33] However, the concentration of the CNT solution ( $0.1 \text{ mg/ml}$ ) used for the dip coating process was five times lower than previously reported protocols. [20, 33] The

aforementioned conductivity values can be explained more precisely if we consider the existence of a continuous MWCNT thin layer with thickness,  $t$ , on the fiber surface with electrical conductivity,  $\sigma_{CNT}$ , attached either by covalent or non-covalent bonds. The conductivity of the CNT layer ( $\sigma_{CNT}$ ) then is given by the following equation: [33] [296]

$$\sigma_{CNT} \approx \frac{d}{4t} \sigma_{GF-CNT} \quad (6.2)$$

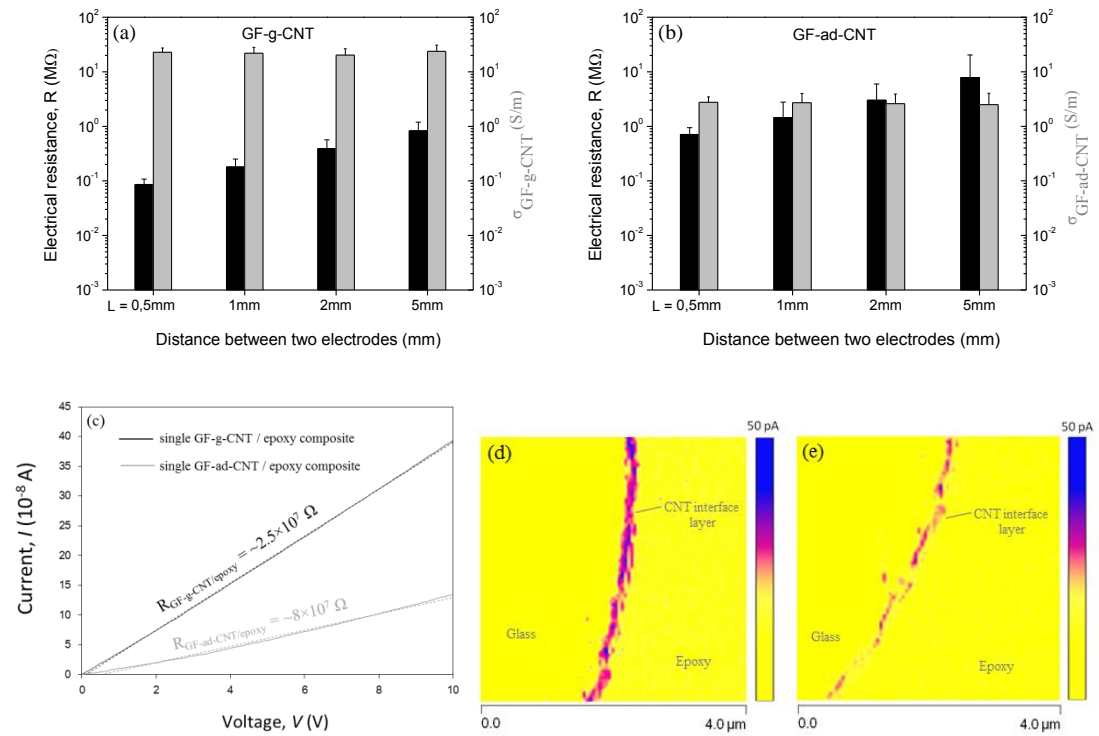
Taking this equation as a rough estimate, the fibers average diameter  $d \approx 18 \mu\text{m}$ , the thickness of the CNT layer about 70-80 nm according to the AFM maximum roughness data, and  $\sigma_{GF-CNT}$  the conductivity of CNT-coated GFs given in Fig 6.8a and 6.8b, the conductivity of the CNT layer is calculated to be  $1.18 \times 10^3 \text{ S/m}$  for GF-g-CNT and  $1.1 \times 10^2 \text{ S/m}$  for GF-ad-CNT, respectively. The difference is assigned as already discussed to the CNT-coating morphology. It should be mentioned that the thin CNT layer which was formed by grafted MWCNTs possesses high electrical conductivity comparable to the aggregated and highly dense structure of CNT-only bucky paper film (calculated to be  $\sim 2.3 \times 10^3 \text{ S/m}$ ; bucky paper CNT films were prepared by vacuum filtering a CNT suspension of the nanotubes used for the fiber coatings). On the other hand, the CNT layer of the GF-ad-CNT exposes a non-uniform morphology which dampers the extended individual CNT junction points resulting in one order of magnitude lower conductivity.

Fig. 6.8c represents the  $I$ - $V$  characteristics of single GF-g-CNT and GF-ad-CNT epoxy composites together with two linear dash lines showing the regression of the experimental data. Obviously, there is a linear dependency of the measured current as a function of the applied voltage and this indicates that Ohmic contacts between GF-CNT and electrodes were formed. Therefore, the contact resistance between the fibers and the electrodes is negligible compared to the resistance of single fiber composites. The resistance of the single GF-g-CNT and GF-ad-CNT composites was calculated from the reciprocal of the corresponding  $I$ - $V$  curve slope and it is inserted in Fig. 6.8c. The specific conductivity of a single GF-CNT in epoxy at the longitudinal direction was given by the formula:  $\sigma_{GF-CNT/epoxy} = (4L) / \pi d^2 R$ , and after calculations was found to be 0.79 S/m and 0.24 S/m, respectively, which is one to two orders of magnitude lower than the conductivity of the bare fibers. This can be explained by the presence of the epoxy insulating macromolecular chains through the MWCNT-networks which generate an insulating layer at the nanotube-nanotube junctions preventing direct physical contact between them. [297] In the same way like previously, considering the thickness,  $t^*$  of the MWCNT-networks after embedding in epoxy as revealed by the TEM interphase-section images ( $t^* \approx 250 \text{ nm}$ ), using Equation 6.2, we can correlate the



conductivity of the nanostructured interphases ( $\sigma_{Interphase}$ ) with the respective specific conductivity of single GF-CNT in epoxy following the expression:  $\sigma_{Interphase} \approx (d/4t^*) \sigma_{GF-CNT/epoxy}$ . After calculations, the interphase conductivity of GF-g-CNT and GF-ad-CNT in epoxy matrix was  $\sim 14.2$  S/m and  $\sim 4.4$  S/m, respectively. The high values of conductivity within the interphases can be compared to CNT/polymer composites with high CNT loadings, [33] and they can be attributed to the dense MWCNT-networks located at the interphase region.

Fig. 6.8d and 6.8e depict the nanoscale electrical current maps of single fiber/epoxy cross-sections investigated by PeakForce TUNA atomic force microscopy (PF-TUNA AFM). We should mention that these images provide a qualitative sense of the interphase electrical properties. Both GF-g-CNT and GF-ad-CNT composite interphases expose conductive characteristics due to the localization of MWCNTs at the interphase area. However, the non-fully surface coverage of GF-ad-CNT results in a non-continuous conductive interphase.



**Fig. 6.8** – DC electrical resistance ( $R$ , black bars) and conductivity ( $\sigma$ , grey bars) of single GFs with (a) chemically grafted (GF-g-CNT) and (b) physically adsorbed (GF-ad-CNT) MWCNTs as a function of the electrode distance (error bars represent the corresponding standard deviations). (c)  $I$ - $V$  characteristics of single GF-g-CNT and GF-ad-CNT epoxy composites showing the linear regression (linear dash lines) in

each case. PeakForce TUNA current maps of single (d) GF-g-CNT and (e) GF-ad-CNT epoxy cross-sections (scale: 50 pA,  $V_{\text{bias}} = 5 \text{ V}$ ).

### 6.1.3.6 Interfacial adhesion properties

The single fiber pull-out test was used to determine the quality of interfacial bonding between the epoxy matrix and the different fibers used in this study. Fig. 6.9a shows the results of apparent interfacial shear strength ( $\tau_{\text{app}}$ ) measurements performed on single fiber model micro-composites. The interfacial shear strength is an evaluation of the efficiency of the interface to transfer the applied stress from the matrix to the fiber. GFs modified with APS (GF-APS); widely used as a coupling agent to improve the adhesion strength of GF/epoxy composites, have been compared with GF-ad-CNT and GF-g-CNT, respectively. As it can be observed, the GF-g-CNT exposed the highest interfacial adhesion strength ( $65.4 \pm 6.4 \text{ MPa}$ ) with an increase of  $\sim 48\%$  compared to the GF-APS. A plausible explanation about this could be that the epoxy monomer interdiffuses through the CNT-grafted network and interacts chemically both with the amine groups of the fiber surface via nucleophilic ring opening reaction, as well as with the carbonyl groups of the CNTs via esterification. Therefore, the covalent bonds of epoxy at the interphase region combined with the high strength of the grafted CNT-network to be attached to the GF surface very effectively hinder the shear flow through the interphase resulting in the highest interfacial strength among the investigated fibers. The SEM images in Fig. 6.9b, 6.9c and 6.9d depict the fracture morphologies of the pulled-out fibers and it is clear that in all cases cohesive failure occurred, since matrix material was observed on the fibers after the pull-out process. Improvement of the  $\tau_{\text{app}}$  for the GF-ad-CNT ( $\sim 13.4\%$ ) and GF-g-CNT compared to GF-APS could be attributed to the local stiffening of the polymeric chains at the interphase region because CNTs act as nucleating agent. The CNT carboxyl groups could be also responsible for an increase of the epoxy cross-linking density which may contribute to the stiffening of the polymer chains. In addition, the nanoscale roughness can further introduce a mechanical interlocking mechanism that was apparently more effective in the case of chemically grafted MWCNTs.

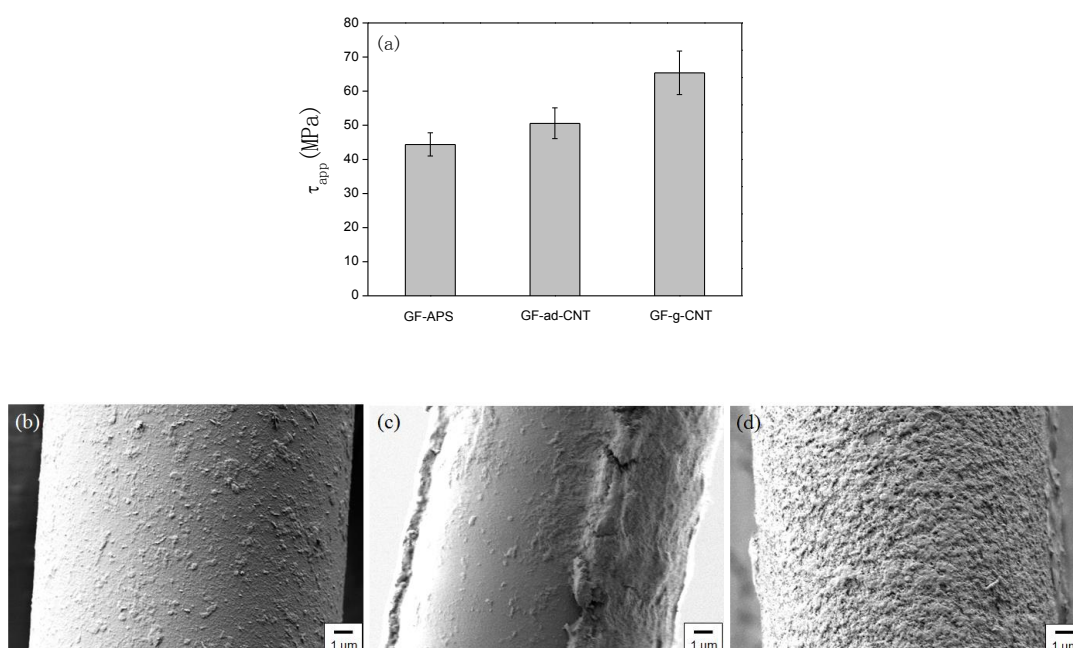
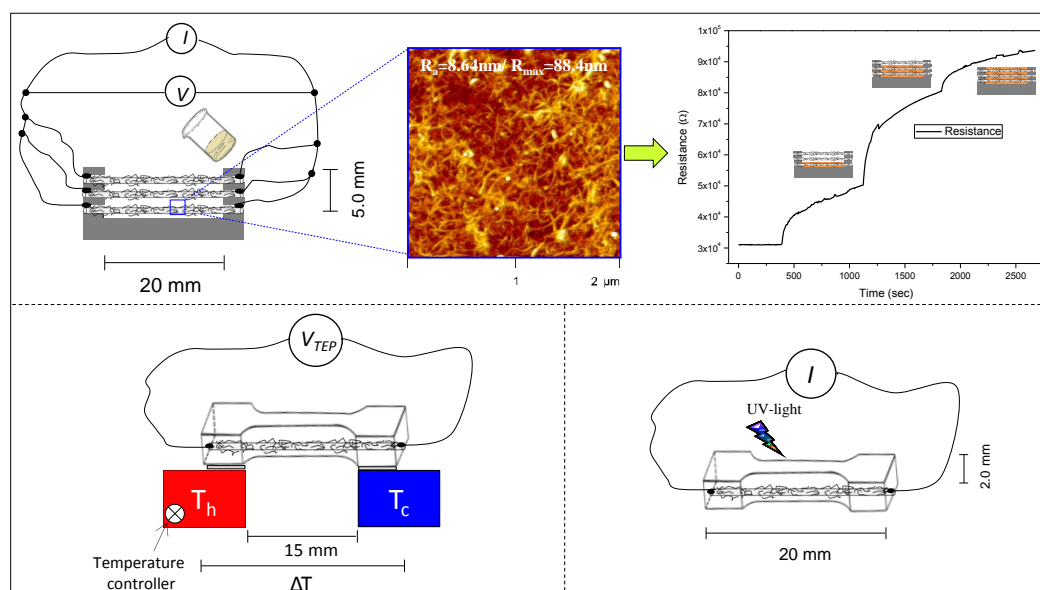


**Fig. 6.9 – (a) Apparent interfacial shear strength ( $\tau_{app}$ ) and (b, c, d) SEM fracture surface morphologies of GF-APS, GF-ad-CNT and GF-g-CNT, respectively.**

In conclusion, MWCNTs were successfully deposited onto the surface of electrically insulating GFs via covalent or non-covalent bonds in a conventional dip coating deposition process. SEM and AFM images of MWCNT-coated fibers demonstrated the surface morphological and topographic characteristics. Homogeneous MWCNT-networks were achieved by chemically grafting carbon nanotubes to the GFs, whereas relatively big areas remained uncovered in the case of non-covalently bonded CNTs. The electrical conductivity of single fibers grafted with MWCNTs was generally more than ten times higher than the physically adsorbed ones, reaching the value of  $\sim 20$  S/m at 0.5 mm fiber length. XPS analyses together with the interfacial microstructures observed by the TEM images, can strongly prove the formation of an amide chemical bond between the GF-APS and the MWCNT-COCl. By using each of the hybrid filaments, single fiber composites were prepared and the resistance in each case was found to be increased approximately one order of magnitude compared to the values of the respective fibers at the same length. For the first time in this work, we presented the cross-sectional interface characteristics of a CNT-coated GF embedded in epoxy matrix. Focused ion beam was employed to prepare the interphase-sections, and it is the only possible technique since conventional ultramicrotomy is not a suitable due to the brittle behavior of GFs which can destroy the diamond knives, used for the cross-sectioning process. The corresponding TEM images of single fiber composite interphase-sections reveal the microstructures of the interfacial area and the durability of the

MWCNT-coating, which is shown to remain attached or to migrate away few nanometers from the GF surface after embedding in epoxy matrix. For possible utilization of the hybrid filaments as in-situ mechanical damage sensors, the fiber fragmentation steps can be more precisely and efficiently monitored when the MWCNTs remain attached to the GF after embedding into the epoxy matrix. The hierarchical GFs chemically grafted with MWCNTs can be easily prepared according to the protocol proposed here, and they show great potential to be used as novel reinforcements in high performance composites.

## 6.2 MWCNT-grafted glass fiber yarns as a smart tool for the epoxy cure monitoring, UV-sensing and thermal energy harvesting



### Abstract

A hierarchical reinforcement structure of glass fiber yarns (GFs) grafted with multiwalled carbon nanotubes (MWCNTs) has been utilised as a smart tool for the epoxy cure monitoring, UV-sensing and thermal energy harvesting. CNT-networks were covalently attached onto the surface of intrinsically insulating GF yarns (GF-CNT) in a dip-coating deposition process at 0.1; GF-CNT(0.1) and 0.5; GF-CNT(0.5) mg/mL CNT solutions, respectively. An electrically conductive layer was formed covering the fiber surfaces, as revealed by the scanning electron microscopy (SEM) images. In turn, GF-CNT(0.5) reached a maximum conductivity of 2020 S/m, very close to the CNT-only bucky paper film value. A GF-CNT yarn in a uni-directional arrangement within a dog-bone shaped mould was used for the epoxy cure monitoring recording the resistance change during the hardening process. Furthermore, three yarns in parallel connection highlighted the potential of detecting the resin position upon filling a mold. The GF-CNT embedded in epoxy matrix has been proposed also to function as a UV-sensor, providing the possibility of the polymer matrix health monitoring, since polymers are known to be sensitive in the UV-light. Besides, the semi-conductive nature of MWCNTs provided the opportunity of harvesting thermal energy by the GF-CNT, operating as a typical thermoelectric material. This work highlights some new insights and potential of CNT/fiber hierarchical structures; and it is envisaged that all

the ideas presented here could be implemented in a bigger scale giving rise to multifunctional structural composites.

### 6.2.1 Introduction

Since their discovery, carbon nanotubes (CNTs) have been widely used for advanced applications due to their unique electrical, mechanical and thermal properties. [6] [254] The incorporation of CNTs in polymer matrices has been the subject of different studies, demonstrating that they are an ideal candidate for fabricating multi-functional polymer nanocomposites. [255] [256] [257] [258] [196] [298] Recently, CNTs have been combined together with micro-scale filaments like glass, carbon [276] or natural fibers resulting in 'hierarchical' [275] or 'fuzzy' [299] multi-scale structures, [260] and have been incorporated further into different polymer matrices. [260] [261] [262] [263] A review could be found where carbon nanotube-based hierarchical composites and the advantages for the formation of a multi-scale reinforcement were elaborately discussed. [264] The methods of CNT deposition onto the fibrous reinforcements include: *i*) chemical vapor deposition (CVD), *ii*) electrophoretic deposition, *iii*) sizing mixtures containing CNTs applied to the fibers during the spinning process and *iv*) dip-coating. The hybrid fibers have been found to enhance the interfacial adhesion strength as well as endowing with multi-functional properties to the final composites. The multi-functional properties arise specifically from the composite hybrid interphases or interphasial regions, and different kinds of functionalities have been established such as strain and temperature sensing. [283]

Glass fiber reinforced polymer composites (GFRPs) offer a flexible design approach for structural materials with significantly enhanced specific properties such as strength and stiffness. [177] Epoxy resins are one of the most important thermosetting polymers used as the matrix in composite materials, due to their ability to be infused in fabrics at room temperature, [300] and their high chemical as well as temperature resistance. [301] It is a well-known fact that fibers are the load-bearing constituent in a composite structure, and the matrix/fiber interface should be designed in an engineered way, since it acts as the bridge for transferring the mechanical stresses from the matrix to the reinforcement. However, the matrix-dominated properties such as interlaminar shear strength, [302] [303] resin failure strain, [304] void content, [305] crosslink density, [306] etc can play a crucial role on the composite's damage development and progression. To that end, factors which can influence the properties of the epoxy matrix include: *i*) chemical composition and stoichiometry of the reagents, i.e relative epoxy/amine concentration; *ii*) cure schedule used to process the resin;

and *iii*) the detection of resin location upon filling a mold containing fibers; for instance prepregs. Hence, there is a demand for sensors which can determine in situ the state of cure of a composite at points remote from the surface. The curing reaction of the resin is one of the major processes in composite materials, and therefore cure monitoring is crucial for the control and optimisation of composites' manufacturing process which influences further the composite mechanical properties. [307] [308] The cure monitoring can rely on various physical or chemical properties that can be used to follow the transformation of an initially liquid thermoset resin into its final rigid solid form. Optical fibre sensors, [177] dielectric analysis, [307] ultrasonic wave propagation, [309] heat-flux measurements [310] and viscosity measurements [311] are some of the techniques that have been already used for the cure monitoring of epoxy resins. Conventional spectroscopic techniques such as near-infrared (NIR), [312] mid-infrared, fluorescence [313] and Raman [314] have been also employed, and they can provide even quantitative information about the relative concentrations of the chemical constituents in the resin. Since the fiber/CNT hierarchical structures have been promising reinforcements increasing the interfacial adhesion strength studied by single fiber model composites, [281] as well as the interlaminar shear strength investigated by laminate composites, [315] it would be ideal if they could provide some information about the curing state of the resin in which they are incorporated.

Besides, polymers are known to be sensitive in UV-light which can cause the shortening of the polymeric chain's by time, phenomenon called as 'photodegradation'. In particular, photodegradation has been explained via different kind of mechanisms for thermosetting and thermoplastic polymers. [316] [317] Consequently, exposition of polymers in UV irradiation can have a negative impact on their mechanical performance by time. Therefore, in polymer composites where the matrix provides the structural integrity, it is very important that it is free of defects. To that end, the possibility of an integrated sensor within the composite structure that can give an output signal when it is exposed to UV irradiation would be beneficial for the composite health state. Then, by testing the resistance and stability of the polymer itself towards the UV illumination, the sensor's data can be correlated to the polymer's structural state. This can give the opportunity to determine whether the polymer has undergone a significant damage or not.

Composite materials are exposed in several cases in environments where there is a temperature gradient, i.e composite parts of airplanes, cars, etc. Thereby, the potential of composites to function as thermoelectric materials is a very intriguing field of research. [318] Thermoelectric materials are one of the potential candidates for energy harvesting

(such as waste heat) due to their ability to generate voltage upon exposure to a temperature difference. This so-called thermoelectric or Seebeck effect is described by the thermoelectric power (TEP), or thermopower, or Seebeck coefficient ( $S$ ), which is the direct solid state conversion of thermal energy to electricity. [319] The thermoelectric power is defined as:

$$S = \frac{\Delta V}{\Delta T} \quad (6.3)$$

where  $\Delta V$  is the electric potential difference (or thermovoltage, or thermoelectric voltage) created by the temperature gradient,  $\Delta T$ , within the material. The Seebeck coefficient is used further to calculate the power factor [ $PF$ ,  $PF = \sigma \times S^2 = \sigma \times (\Delta V / \Delta T)^2$ ,  $\sigma$  is the electric conductivity], as a means to compare the efficiency of different thermoelectric materials. The dimensionless Fig. of merit [ $ZT$ ,  $ZT = (\sigma \times S^2 / \kappa) T$ ,  $\kappa$  is the thermal conductivity and  $T$  is the absolute temperature] is also used to compare the thermoelectric efficiency; [320] however in this study due to the difficulties to determine the thermal conductivity of the composite interface, alternately the values of power factor are given, often used to compare materials to one other. [321] It should be mentioned that the Seebeck coefficient,  $S$ , is positive for p-type materials, and negative for n-type material, [322] and it is an intrinsic property of the materials related to their electronic properties, and independent of their geometry. [323] It can be realised that for an optimum thermoelectric efficiency, a high electrical conductivity and Seebeck coefficient, combined with low thermal conductivity are required. Traditional thermoelectric materials are known to be fabricated from low band gap semiconductors like  $\text{Bi}_2\text{Te}_3$ ,  $\text{PbTe}$ , etc., however they are toxic and expensive to mass produce. [324] CNT-based polymer nanocomposites have been already reported as thermoelectrics, and they are of particular interest due to their low thermal conductivities (due to phonon scattering at the CNT-polymer-CNT interphase) which can sustain a temperature difference across the material, high electrical conductivities, ease of production, relatively low cost, flexibility and high specific properties. Especially, highly loaded SWCNT nanocomposites [325] have reached very promising power factors ( $\sigma \times S^2$ ), and values in the range of  $\sim 140 \mu\text{W m}^{-1} \text{K}^{-2}$  have been reported. [326] The optimisation of the power factor by increasing both the conductivity as well as the Seebeck coefficient, remains still an open field for further investigation, and for that different approaches have been adopted such as doping of CNTs with different molecules, [327] creation of structural geometries like a p/n heterojunction, [328] different kind of conjugated polymers, [329] etc. Until now, the thermoelectric power of mainly solution processed CNT filled polymer nanocomposites, [328] as well as for long carbon fiber reinforced laminates [318] [330] and short carbon fiber/polycarbonate composites [331] have been investigated. Indeed,



thermoelectric structural materials are very promising for large-scale thermal energy harvesting, and several factors should be addressed in order to increase their thermoelectric efficiency, making them an attractive technology for the composite market. To the best of our knowledge, GF/CNT hierarchical reinforcements embedded in a polymer matrix with a great potential to harvest thermal energy has not been yet reported.

Herein, an effective wet chemical method for grafting MWCNTs onto the surface of GFs (GF-CNT) is presented. GF yarns exhibiting amine surface functionalities were dipped in a solution of acyl chloride modified MWCNTs (MWCNT-COCl), and amide chemical bonds were formed (GF-CNT) as revealed by the XPS analysis. The fiber surface morphology was investigated by scanning electron microscopy (SEM). MWCNTs were found to be arranged into entangled and densely packed networks homogeneously distributed onto the fiber surfaces. The interphase microstructure of single GF-CNT embedded in epoxy was studied by transmission electron microscopy (TEM). The electrical properties of the hybrid fibers attributed to the surface anchored CNTs were investigated by ‘two probe’ electrical resistance measurements. A GF-CNT yarn has been proposed as a smart tool for the in-situ cure monitoring of a commercial DGEBA-based epoxy resin upon fabricating single fiber yarn uni-directional model composites. Recording the fiber resistance changes as a function of time was found to give a fingerprint of the epoxy degree of cure, and correlated further to the real state of cure investigated by isothermal dynamic scanning calorimetry (DSC). The principle of this study can be simply implemented to big-scale composites, since the GF-CNT yarns can be incorporated in the composite during the manufacturing process, for example in prepregs, woven fabrics, pultrusion and filament winding. The fibers could allow to monitor in real time the curing process as well as to detect the resin infiltration, in different composite fabrication routes such as RTM, infusion, autoclave and pultrusion. The GF-CNT exhibited also excellent response to UV-light illumination facilitating the use as an integrated UV-sensor within the composite. This could be an important feature for the health monitoring of the polymer matrix. Thermal energy harvesting was finally demonstrated by the GF-CNT before and after being embedded in the epoxy matrix and more investigation is required to increase the thermoelectric efficiency. The use of GF-CNT yarns for the epoxy cure monitoring, UV-sensing and thermoelectric energy harvesting is for the first time addressed in this work.

## **6.2.2 Experimental**

### **6.2.2.1 Materials**

E-glass fiber yarns (GFs) without sizing and with a fineness of 120 tex consisting of 204 filaments (aver. diameter of 18  $\mu\text{m}$ ) were manufactured by a continuous spinning process at the Leibniz Institute of Polymer Research Dresden. Commercially available MWCNTs (Nanocyl, NC 7000) with a carbon purity  $>90\%$ , average length 1.5  $\mu\text{m}$  and diameters around 10 nm were received from Nanocyl S.A. (Sambreville, Belgium). The silane coupling agent, 3-aminopropyltriethoxysilane ( $\gamma$ -APS, 98%) was supplied by ABCR (Karlsruhe, Germany) and used for the fiber's surface modification. Ammonium hydroxide (28 wt% ammonia), hydrogen peroxide, absolute ethanol, acetone, sulfuric-nitric acid, thionyl chloride ( $\text{SOCl}_2$ ), dichloromethane, extra dry toluene, dimethylformamide (DMF) and tetrahydrofuran (THF) were purchased from Sigma-Aldrich (Steinheim, Germany). A commercial low viscosity diglycidyl ether of bisphenol-A (DGEBA) based epoxy resin ( $\eta \sim 0.7 \text{ Pa s}$ ) with triethylenetetramine (TETA) hardener (Epofix, Struers) was used, known to cure under a ring-opening addition polymerisation reaction. According to the supplier's specification, the epoxy fully cures at room temperature (cold curing) within 24 h. The stoichiometric ratio was 100:12 (w/w) epoxy resin:hardener, and the chemical formula of the two constituents are depicted in Fig. 6.10. All the chemical reagents were analytical grade and used as received without further purification.

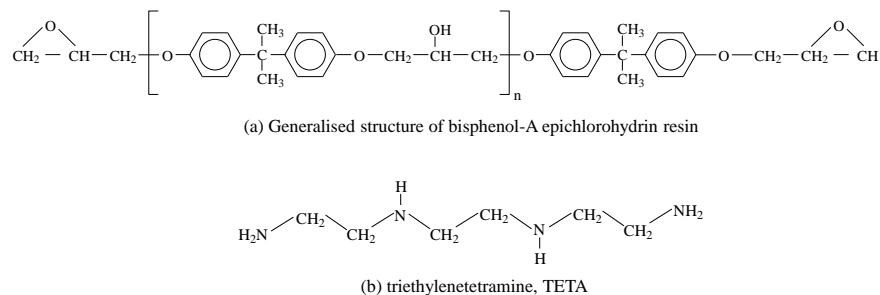


Fig. 6.10 – Chemical structure of (a) Epofix Struers resin and (b) triethylenetetramine hardener.

### 6.2.2.2 Chemical grafting of MWCNTs onto the GF surface

Initially, 5 cm long tow of GFs (containing 204 filaments) was cut from the spin cake and cleaned followed by a silanisation treatment similar to the procedure described in 6.1.1.2 section. As already mentioned in 6.1 of this chapter, MWCNTs were chemically modified with carbonyl chloride groups in order to facilitate the chemical grafting reaction with the amine terminal groups of the glass fiber surfaces. In brief, MWCNT-COCl solutions of 0.1 and 0.5 mg/ml were prepared, and  $\gamma$ -APS modified GF yarns were immersed using a dip-coating apparatus, similar to the steps described in 6.1.13 paragraph. Hereafter, GFs grafted with MWCNTs at a 0.1 mg/mL solution are denoted as GF-CNT(0.1), and at a 0.5

mg/mL as GF-CNT(0.5), respectively. All the reaction steps were carried out under argon (Ar) atmosphere. Fig. 6.11 illustrates schematically the chemical procedure followed to covalently attach CNTs onto the GFs.

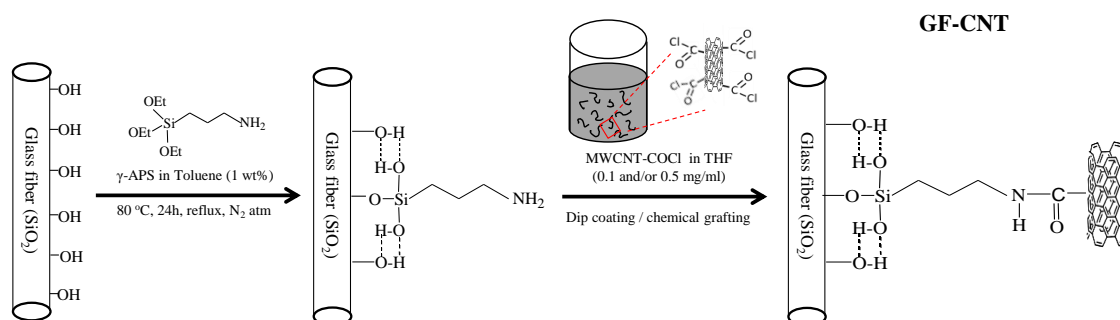


Fig. 6.11 - Schematic illustration of the steps followed to attach covalently MWCNTs onto the GF surface.

### 6.2.3 Characterisation techniques

#### 6.2.3.1 Scanning and Transmission electron microscopy (SEM, TEM)

A NEON 40 (Carl Zeiss AG, Germany) scanning electron microscope operating at 1.0 kV was used to study the surface morphology of GF-CNT(0.1) and GF-CNT(0.5). Single fibers were placed onto the surface of cleaned silicon wafers and attached from both end-sides with a copper adhesive tape. Prior to the SEM analysis, all specimens were sputter-coated with platinum (~3 nm) to avoid charging effects. The Libra 200 transmission electron microscope (TEM, Carl Zeiss AG, Germany) operating at 200 kV was used to investigate the interphase microstructures of single fiber composites. Bright field TEM images were recorded, while the energy filtering and contrast apertures were inserted to enhance the image quality. Interphase-sections of single GF-CNT composites were prepared by Focused Ion Beam (FIB) using the NEON 40 FIB/SEM chamber equipped with a gallium ion beam operating at 30 kV.

#### 6.2.3.2 Electrical resistance and conductivity measurements

The electrical resistance,  $R$ , of GF-CNT(0.1) and GF-CNT(0.5) yarns was represented by measuring the resistance on a single fiber level. More specific, single filaments were thoroughly detached from the corresponding fiber yarns, and resistance measurements were carried out at 20.0 mm fiber length by a standard two-probe method using a semiconductor characterization system (Keithley 2400 Source-Measure Unit, Keithley Instruments GmbH, Germany). An individual filament was laid down on a glass

slide with pre-patterned sputtered platinum electrodes at 20.0 mm electrode-electrode distance, and glued with silver paste to be stabilized. Then, two copper electrodes were tightly adjusted to the gold contacts. A voltage source ( $V$ ) of 0-10 V in 100 steps has been provided, and by recording the current ( $I$ ) which flows through the fiber surface, the resistance values were derived. At least 20 samples of GF-CNT(0.1) and GF-CNT(0.5) were tested in order to obtain significant statistical averages. The resistance mean values with the corresponding standard deviations are finally presented. The distance between the two gold electrodes defines the length of the fiber used for the resistivity ( $\rho$ ) and conductivity ( $\sigma$ ) calculations. The  $I$ - $V$  characteristics of a single GF-CNT(0.1) and GF-CNT(0.5) embedded in epoxy were also determined in order to evaluate the interphasial electrical properties. A single filament was placed lengthwise on two sputtered platinum contacts on the opposite sides of a rectangular shaped teflon mould at 20.0 mm distance. Silver paste was used to contact two copper wires with the fiber and connected further to the Keithley Source-Measure Unit. Epoxy mixed with the hardener was poured into the mould and left 24 h at room temperature for curing. By using voltage of 0-10 V, the current values were recorded and the  $I$ - $V$  curves were plotted.

### 6.2.3.3 In-situ cure monitoring of epoxy using the GF-CNT smart tool

In order to conduct the epoxy cure monitoring measurements, a GF-CNT(0.1) yarn was placed lengthwise on a dog-bone shaped teflon mold and two silver wires were contacted at the ends of the fiber yarn using silver paste. The epoxy mixture was prepared within 1 min, and then was thoroughly added into the mold until it was entirely filled. Afterwards, the current was immediately recorded providing a constant voltage of 0.1 V every two seconds for a period of 24 h. The resistance values were derived by the Ohm's law and used for the cure monitoring evaluation. For the detection of the epoxy position upon filling a mold, three GF-CNT yarns were connected in parallel, and the current measurement started using a constant voltage of 0.1 V, as previously. After one minute, the epoxy mixture was added within three time intervals, covering fully each of the three yarns. The experimental set-up used for the epoxy cure monitoring and the epoxy position detection using the GF-CNT sensor is depicted in Fig. 6.12a. In order to correlate the GF-CNT resistance change with the state of cure of the epoxy resin, similarly to the 'optical degree of cure' which has been defined in other publications [332] in which an optical fiber sensor has been utilised as the cure monitoring tool, here we define for the first time the 'electrical degree of cure' as:

$$a_R = \frac{R_t - R_0}{R_f - R_0} \quad (6.4)$$

where  $R_t$  is the resistance of the GF-CNT at any time,  $t$ , after the start of cure,  $R_0$  is the resistance of the sensor 10 sec after the epoxy was introduced in the mold fully covering the GF-CNT sensor (this time is considered as the beginning of the cure reaction), and  $R_f$  is the resistance at the end of the cure. The above equation assumes a linear relationship between the degree of cure and the resistance during the entire course of the cure. Therefore, the equation presented below relates the ‘electrical degree of cure’ to the real conversion values determined by the DSC experiments.

$$\alpha_{(t)} = a_R \alpha_{DSC}^{max}(t) \quad (6.5)$$

where  $\alpha_{(t)}$  is the fractional conversion at time  $t$  for an isothermal cure at temperature  $T$ , and  $\alpha_{DSC}^{max}(t)$  is the maximum conversion attainable at temperature  $T$ .

#### 6.2.3.4 Thermal analysis of the resin cure by differential scanning calorimetry (DSC)

Thermal characterisation was performed using a Q2000 dynamic scanning calorimeter (TA Instruments Inc., USA) in order to analyze the epoxy cure behavior and establish the degree of cure. Prior to the DSC experiments, epoxy was mixed with the hardener under magnetic stirring for 1 min, to ensure a homogeneous mixture. The curing process was studied then using isothermal scans at 23 °C for 24 h, performed on ~10 mg sample by hermetically sealed aluminum sample pans. The experiments were carried out isothermally at 23 °C, under a constant flow of nitrogen at a rate of 50 mL/min. The room temperature isothermal measurements allowed to compare and correlate the curing process with the electrical resistance change results of the GF-CNT sensor, thus avoiding any impact of temperature on the electronic transport properties of CNTs. For isothermal cure measurements, the degree of cure can be estimated as the reaction progresses by monitoring the DSC heat flow during the curing reaction. From the DSC scan, the degree of cure ( $\alpha$ ) was calculated then from the enthalpy per unit mass ( $\Delta H_t$ ) at any time during the isothermal cure, divided by the total heat of the reaction ( $H_T$ ) obtained by integrating the area under the heat flow curve. The degree of cure ( $\alpha$ ) can range from 0 (completely uncured) to 1 (fully cured) and it is defined as follows:

$$\alpha = \frac{\Delta H_t}{H_T} \quad (6.6)$$

The degree of cure was plotted as a function of time for direct comparison with the resistance change results.

### 6.2.3.5 Rheology

Rheological experiments were conducted by an AR2000 rheometer (TA Instruments Inc., Delaware), in a rate control mode, using a parallel plate geometry at a frequency of 1 Hz. Isothermal time sweeps were performed at 23 °C for 24 h using a gap of 1 mm and a strain of 1 %. The sample (pure epoxy mixture) was placed on the lower plate, and the upper plate was lowered to make contact with the resin. The experiment started after the system was allowed to come to thermal equilibrium (1-2 min).

### 6.2.3.6 UV-sensing

The response of a GF-CNT yarn embedded in epoxy matrix to UV-light has been detected by recording the generated photocurrent. This property is attributed to the excellent behavior of CNTs to induce charge carriers upon photon excitation. In particular, a continuous constant voltage bias ( $V_{\text{bias}}$ ) of 0.1 V with a step of 0.1 sec was applied to the GF-CNT through the two wires as shown in Fig. 6.12b. Then, the current under the UV lamp (Deutsche Mechatronics, Inc.,  $\lambda=254$  nm, typical peak UV-intensity:  $640 \mu\text{W}/\text{cm}^2$  @ 25 cm) was measured using as previously the Keithley 2400 Source-Measure Unit. ON/OFF (UV-irradiation/UV-turned off) cycles at time intervals of 650 sec with the sample enclosed in a dark experimental chamber were carried out. To evaluate the GF-CNT sensor characteristics, the  $I_{\text{UV}}/I_{\text{D}}$  is defined as the ratio of the UV illuminating current ( $I_{\text{UV}}$ ) versus the dark current ( $I_{\text{D}}$ ) measured at a constant voltage of 0.1 V, while the distance between the sample and the lamp was kept at around 25 cm.

### 6.2.3.7 Thermoelectric energy harvesting

The thermoelectric power (or Seebeck coefficient,  $S$ ) measurements were carried out using an experimental set-up which is schematically shown in Fig. 6.12c. The Seebeck coefficient is an intrinsic property of materials related to the material's electronic properties, and independent of their geometry. [323] To measure the  $S$ , a single GF-CNT yarn or GF-CNT/epoxy model composite (like the one used for the UV-sensing) was mounted on two copper blocks. Then, one block was kept at room temperature ( $\sim 298$  K), while the other block was heated up in a controlled way by 10 K steps up to 373 K. This created the temperature difference between the ends of the investigated sample. The generated electric

potential difference, or thermovoltage ( $\Delta V$ ), was measured across the electrodes, while the temperature of the two blocks was continuously measured with K-type thermocouples to determine the temperature gradient,  $\Delta T$  within the material. The Seebeck coefficient ( $S = \Delta V/\Delta T$ ) was derived then from the slope of  $\Delta V$  vs  $\Delta T$  curves by linear fitting, and the power factors have been calculated as well.

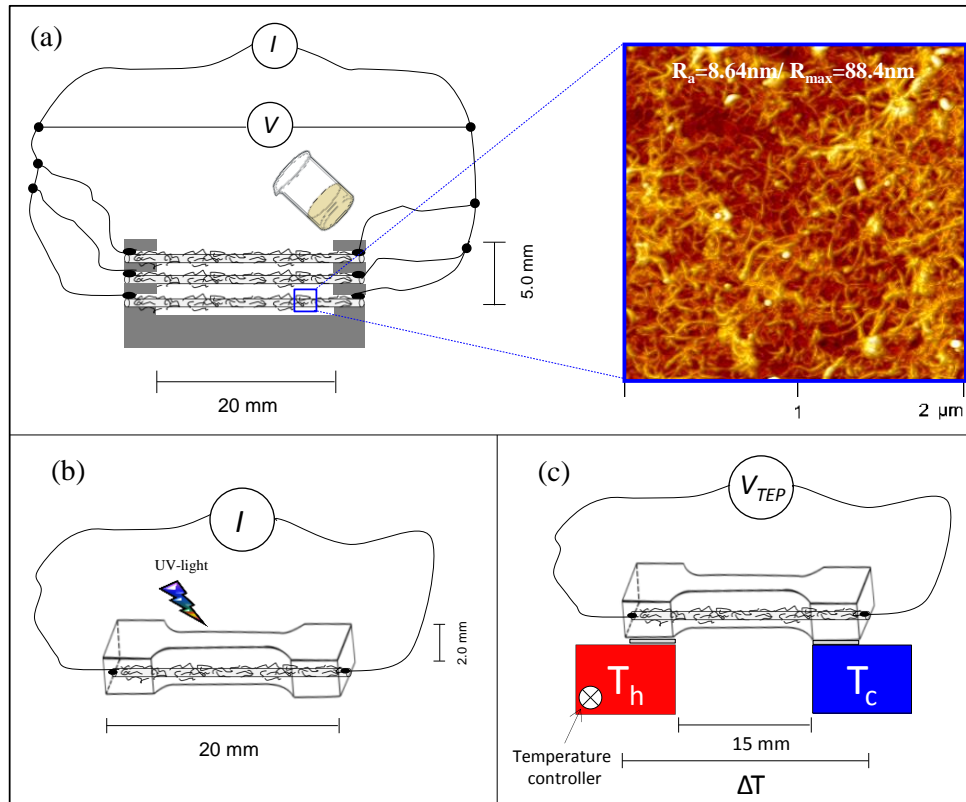


**Fig. 6.12** – Schematic illustration of the set-up used for (a) the epoxy position detection (in a similar way the epoxy cure monitoring has been performed using a single GF-CNT(0.1) yarn), (b) UV-sensing and (c) thermoelectric power measurements. For all measurements a single GF-CNT(0.1) yarn has been used. For simplicity in the schematics a single fiber is drawn representing the single GF-CNT yarn which was utilized throughout all the measurements.

## 6.2.3 Results and discussion

### 6.2.3.1 Surface morphology of MWCNT-grafted glass fibers

Fig. 6.13 shows the microstructures of GF-CNT(0.1) and GF-CNT(0.5), respectively. As it can be observed, the higher the CNT concentration of the solution used for the dip-coating process, the denser the resulting CNT surface layer. This is an important finding which had an effect on the electrical conductivity of the fibers as well as on their thermoelectric properties before and after embedding into the epoxy matrix.

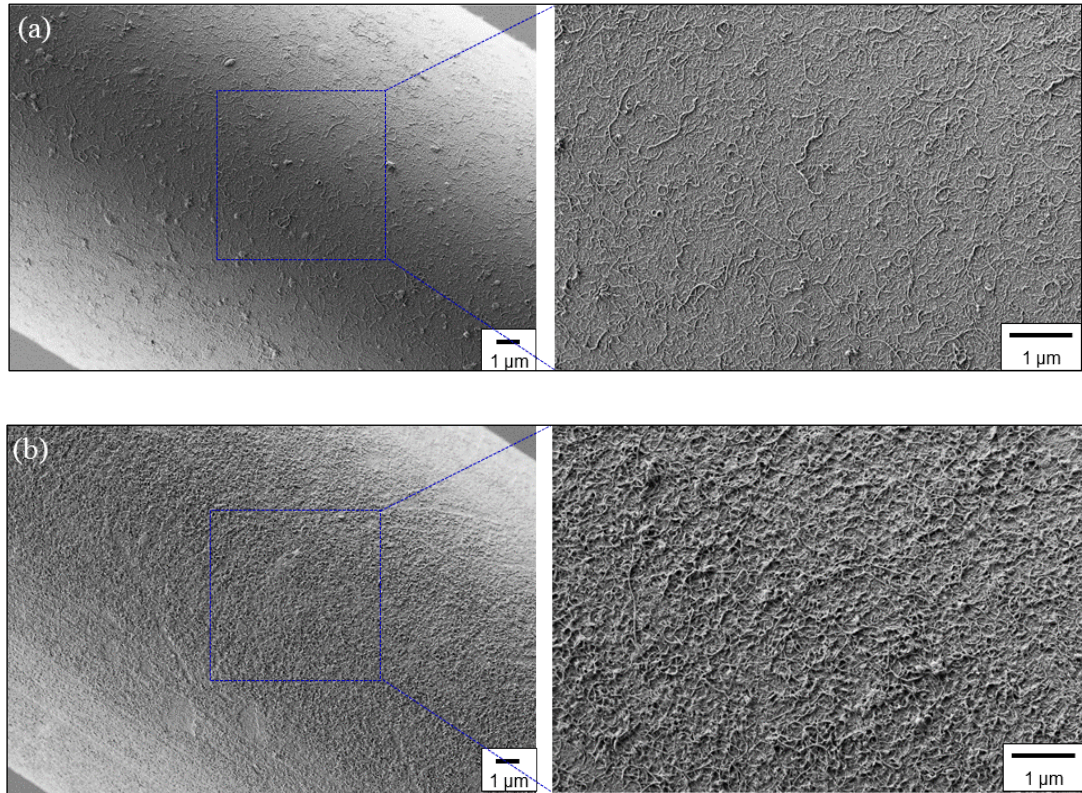


**Fig. 6.13** – SEM images of GFs grafted with MWCNT-COCl at (a) 0.1 and (b) 0.5 mg/ml respectively, shown at two different magnifications.

### 6.2.3.2 Single fiber composite interphase microstructures

Fig. 6.14a and Fig. 6.14b depict the TEM images of single GF-CNT(0.1) and GF-CNT(0.5) composite interphases. These images provide detailed information about the MWCNT-network characteristics along the interphase region. It can be easily realised that the CNT-network microstructure is affected by the polymerization and cross-linking of the epoxy resin during the hardening process. The GF-CNT(0.5) as it was expected exhibits a higher loading of CNTs at the interfacial area with almost the double of the thickness as compared with the GF-CNT(0.1). The thickness of the CNT rich interphase is about 120 nm for the GF-CNT(0.1) and about 250 nm for the GF-CNT(0.5) epoxy composite. The difference of the CNT coating thickness before embedding in epoxy (calculated from AFM height images; 44.6 and 88.4 respectively), and afterwards as revealed by the TEM micrographs, could be attributed to the epoxy interdiffusion through the CNT network. More precisely, this occurs due to the chemical reaction of the epoxy groups with the MWCNT carboxylic groups via a ring opening addition mechanism resulting in the grafting of the epoxy monomer on the CNT surface. By the time, due to the increase of the epoxy molecular weight during the polymerisation process, the distance between CNT-CNT also increases



speculating that the epoxy results finally in a kind of ‘swelling’ of the fiber CNT surface layer. The increase of the CNT coating thickness is around three times in each case after embedding the fibers in the epoxy matrix. This finding is of utmost importance for the calculation of the electrical conductivity of this CNT-rich interphase, as well as for the thermoelectric power factor determination.

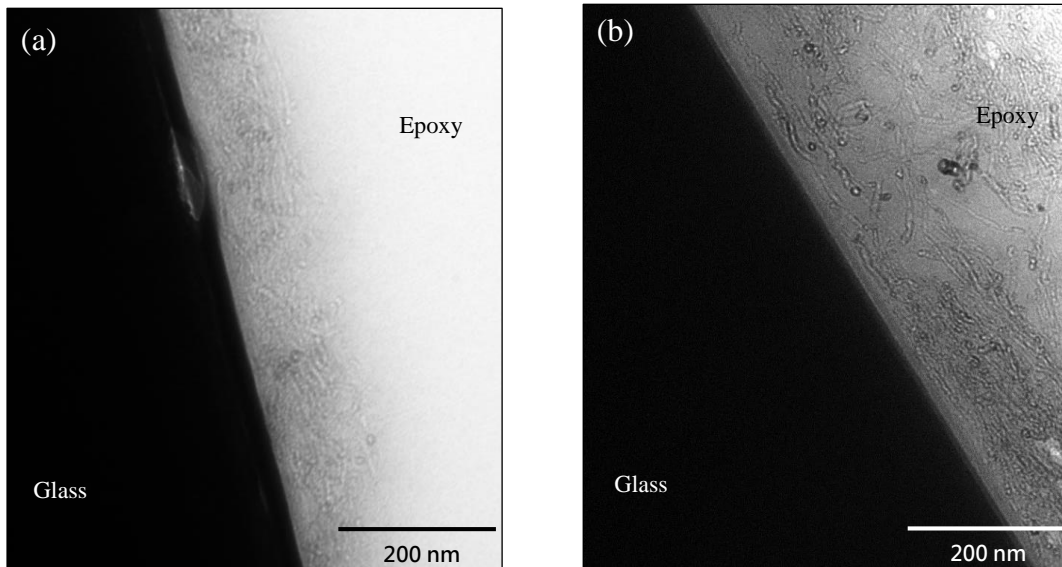
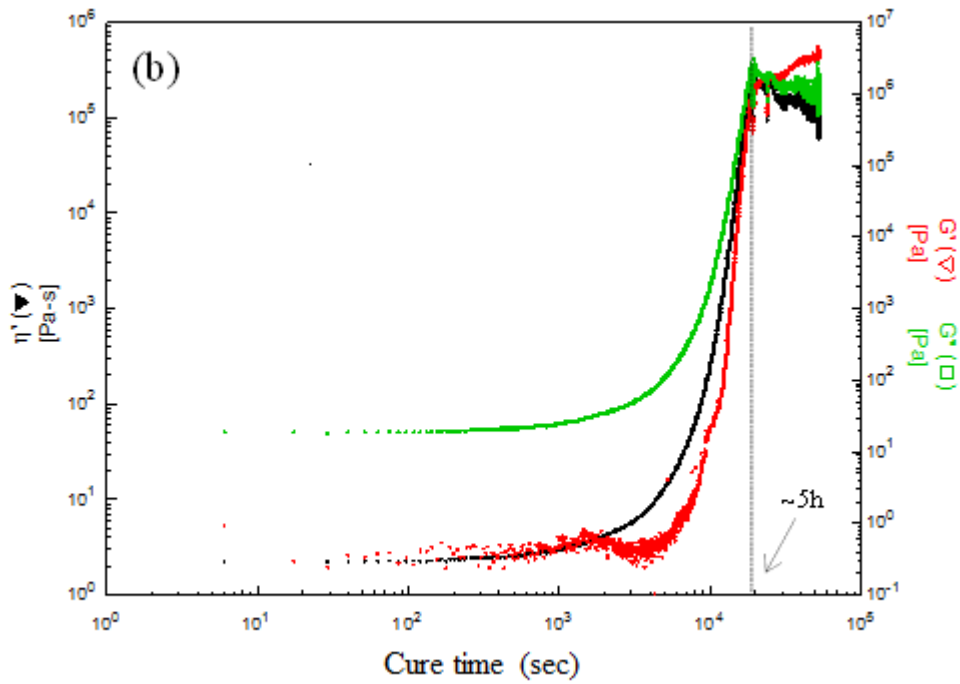
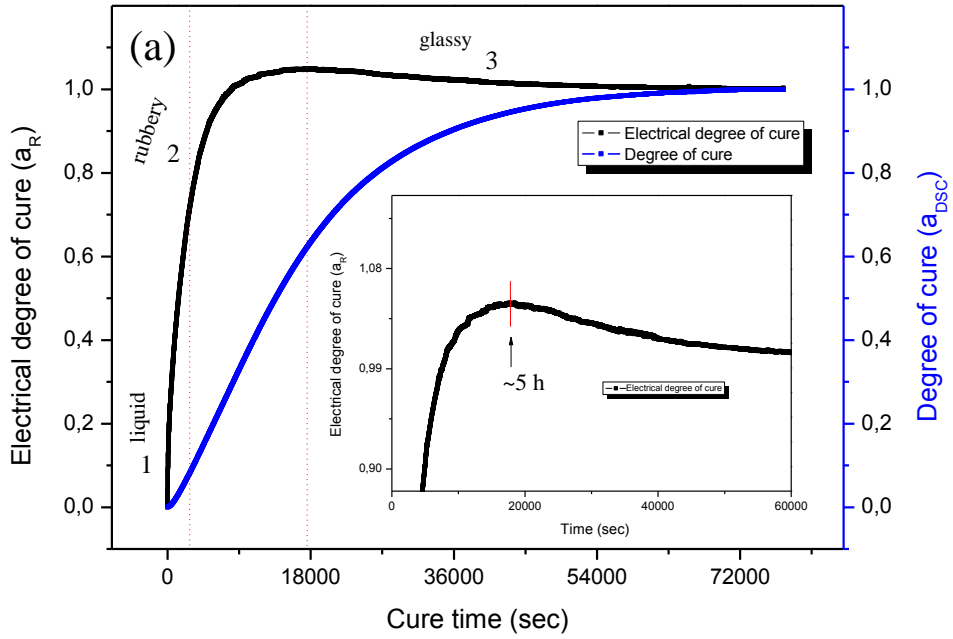


Fig. 6.14 – TEM interface microstructures of single (a) GF-CNT(0.1) and (b) GF-CNT(0.5) epoxy composites.

### 6.2.3.3 Epoxy cure monitoring and position detection using the GF-CNT sensor

Fig. 6.15a depicts the electrical degree of cure,  $a_R$ , (black line) as a function of time within the 24 h curing cycle. At the same Fig., the DSC degree of cure (blue line) is also plotted for direct comparison. As it was expected, the conversion increases with increasing time, and 24 h were found to be sufficient time for the fully-cure of the particular epoxy resin, being in a good agreement with the manufacturers’ data sheet. Fig. 6.15b demonstrates the epoxy rheological properties showing that about 5 h are required for the epoxy to become a gel. The time between the onset of the rapid increase of the dynamic viscosity ( $\sim 3000$  sec = 50 min), and that at which it exceeded 100 KPa-s was taken as the gelation period, similarly to other studies. [332] [333] At the end of gelation period, the gel point is reached and it is considered as the point in which storage and loss modulus cross. [334] At that time, the onset of vitrification occurs and the curing reaction continues until the end of vitrification, which is considered practically as the end of the epoxy curing. The DSC and rheological investigations were performed in order to have a full image about the curing reaction and its completion, as well as for the epoxy molecular mobility during hardening. Regarding the

electrical degree of cure, it can be observed that it increases by the time until it reaches a certain maximum, and then slightly decreases until a final plateau. This can be explained by two factors: *i*) predominant one is that the epoxy interdiffuses/penetrates through the fiber surface CNT-networks increasing the distance between adjacent CNTs and hampering the direct physical contact of the CNT-CNT junctions, both of which affect the electron transport via a tunneling or a hopping mechanism, and *ii*) alternation of the CNT surface electronic properties by the absorption of the epoxy molecules, due to their chemical reaction with the CNT carboxylic groups via a ring opening addition mechanism. More specific, taking into account the epoxy's reaction progression, and its molecular mobility as revealed by the rheological analysis, we can distinguish three areas of the electrical degree of cure curve. In the first one, the epoxy is in a liquid state and penetrates very fast and easily through the CNT network, therefore the resistance changes with a high rate. The rate of resistance change starts to decrease at a time around 3000 sec which is consistent with the rapid increase of the viscosity from the rheological investigation (onset of gelation). Further, the resistance changes with a lower rate and the epoxy comes into the rubbery state until it reaches a maximum at around 18000 sec or 5 h, shown to be the gel point. At this point, the molecular mobility of the epoxy starts to become very slow, thereby interdiffusion through the CNT network becomes practically zero without increasing any more the CNT-CNT distances. Comparing this point with the DSC degree of cure, we can claim that at the maximum of the electrical degree of cure, epoxy has been 62 % cured, and the maximum of the electrical degree of cure corresponds to the gelation point. It should be mentioned that the slight decrease of the electrical degree of cure afterwards is attributed to the chemical interaction of the epoxy and/or the amine hardener with the carboxyl groups of CNTs which can act as a doping decreasing slightly the CNT resistance. Fig. 6.15c demonstrates that three GF-CNT yarns can very effectively give a fast response of their resistance change when epoxy has reached and wetted them. The resistance like previously increases due to the reasons which were already mentioned. The response of the GF-CNT sensor at each time that epoxy came in contact can be utilised to detect the location of epoxy resin upon filling a mold in big-scale composite manufacturing processes.



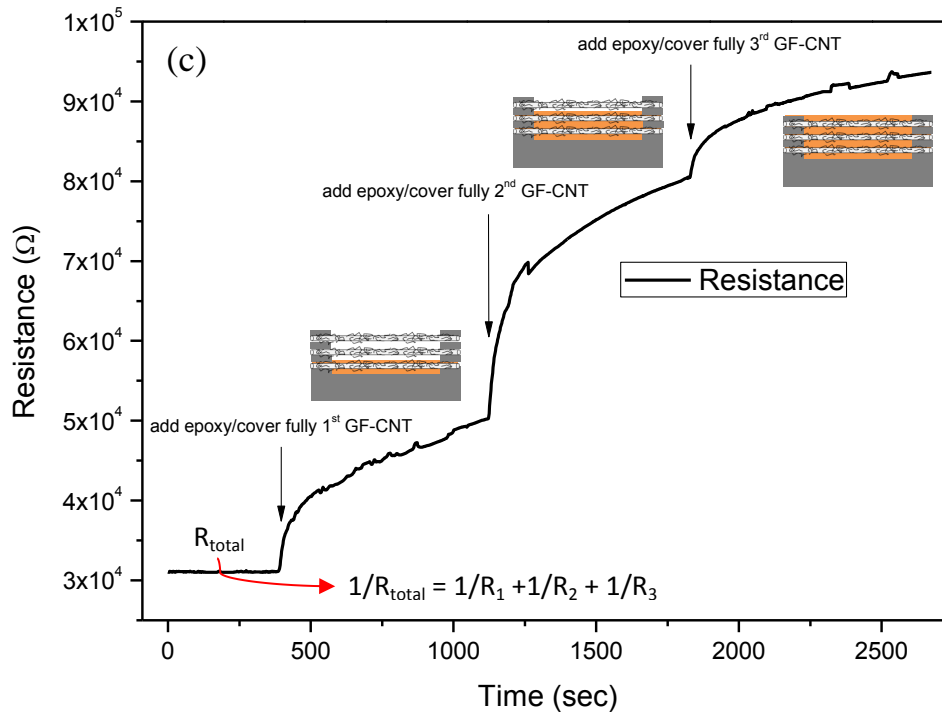
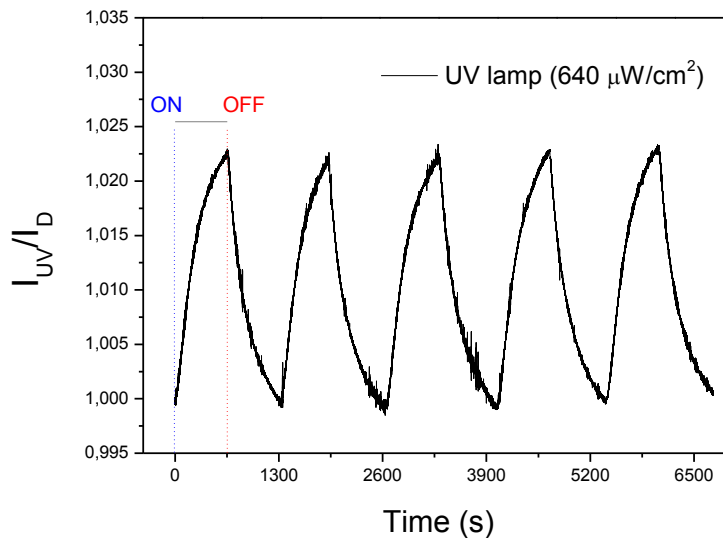


Fig. 6.15 – (a) Electrical and DSC degree of cure at an isothermal cure cycle within 24 h (b) Epoxy rheological properties within 24 h. (c) Illustration of the fast resistance change upon filling a mold with epoxy resin.

#### 6.2.3.4 UV sensing properties

Fig. 6.16 depicts the ON or OFF state of the UV-light illumination ( $\lambda \approx 254$  nm,  $640 \mu\text{W}/\text{cm}^2$ ) and the fast response of the GF-CNT sensor to the incidence of UV-light. A significant increase of the forward current could be observed upon UV illumination which showed complete elastic and recoverable behavior. Since the MWCNTs used for coating the GFs contained  $-\text{COCl}$  functionalities (considered to have been transformed to  $-\text{COOH}$  groups by hydrolysis after the grafting reaction), the CNTs attached onto the fiber are p-doped because the carboxyl groups facilitate the  $e^-$  withdrawing from the CNT-backbone, creating holes as charge carriers. Therefore, the observed response of the GF-CNT sensor was due to the presence of photo-excited holes and slightly due to the rise in temperature. [335] The responsivity of the GF-CNT/epoxy device with an active area of  $15 \times 0.15 \text{ mm}^2$  was found to be  $3.61 \times 10^{-3} \text{ A/W}$  at a forward bias of 0.1 V. The fast response of the GF-CNT can be attributed to the highly entangled and concentrated CNT network located at the interphase region (illustrated by the TEM image in Fig. 6.13) which allows high carrier mobility due to its high conductance and enables fast transfer of the generated photocarriers. It was also observed from test experiments that the measured light-induced current increased

as the UV power was increased, corroborating the results found in literature. [336] In addition, the current changes very slightly under visible light illumination and considering its high response to UV illumination, the hierarchical GF-CNT can act as an excellent UV sensor. The UV-sensing ability could be utilized to health monitor the condition of the polymer matrix, by counting the time that a composite material has been exposed to UV-light and how much this time could affect the degradation of the polymer due to the shortening of the polymeric chains.



**Fig. 6.16** – The ratio of photocurrent divided by the dark current at a constant bias of 0.1 V versus time. The time intervals between On/Off state of the UV-irradiation has been 650 sec.

### 6.2.3.5 Electrical resistance and conductivity of GF-CNT and GF-CNT/epoxy composites

Fig. 6.17a shows the arithmetic mean values with the corresponding standard deviations of the electrical resistance ( $R$ , black bars) and conductivity ( $\sigma$ , grey bars) of single GF-CNT(0.1) and GF-CNT(0.5), respectively. The average resistance of GF-CNT(0.1) was  $136.24 \pm 18.5 \text{ M}\Omega$ , while for GF-CNT(0.5)  $4.91 \pm 0.50 \text{ M}\Omega$ . It should be noted that the variation of the resistance values in both cases is relatively low as a result of the homogeneous CNT-coating characteristics observed previously by the SEM microstructural analysis. The specific conductivity of a GF-CNT with an average diameter of  $d \approx 18 \text{ }\mu\text{m}$  was derived from the formula:  $\sigma_{\text{GF-CNT}} = (4L) / \pi d^2 R$ , and after calculations, it was found to be  $5.78 \pm 0.74 \text{ S/m}$  for the GF-CNT(0.1), and  $160.15 \pm 16.84 \text{ S/m}$  for the GF-CNT(0.5), respectively. Higher values have been achieved for the GF-CNT(0.5) due to the highly

loaded CNT-coating which facilitates a more efficient electron transport through the CNT-networks. The conductivity introduced to the electrically insulating GFs arises from the interconnected ultrathin CNT-networks deposited onto the fiber surfaces, with the CNT-CNT extensive junctions to create the electron transport pathways. The conductivity values can be explained more precisely if we consider the existence of a continuous CNT thin layer with thickness,  $t$ , and with electrical conductivity,  $\sigma_{CNT}$ . The conductivity of the CNT layer ( $\sigma_{CNT}$ ) then is given by the following equation. [33] [296]

$$\sigma_{CNT} \approx \frac{d}{4t} \sigma_{GF-CNT} \quad (6.7)$$

Taking this formula as a rough estimate, the fiber average diameter  $d \approx 18 \mu\text{m}$ , the thickness of the CNT layer 44.6 and 88.4 nm for GF-CNT(0.1) and GF-CNT(0.5) respectively (according to the AFM maximum roughness data), and  $\sigma_{GF-CNT}$  the conductivity of CNT-coated GFs given in Fig. 6.17a, the conductivity of the CNT layer is calculated to be  $5.84 \times 10^2 \text{ S/m}$  for GF-CNT(0.1) and  $8.15 \times 10^3 \text{ S/m}$  for the GF-CNT(0.5). The difference is assigned as already discussed above to the CNT-coating structure. The thin CNT layer which was formed in both cases possesses high electrical conductivity comparable to the aggregated and highly dense structure of CNT-only bucky paper film. The maximum conductivity of the GF-CNT(0.5) is to our knowledge the highest value compared to existing ones in literature for similar systems. [33]

Fig. 6.17b represents the  $I$ - $V$  characteristics of single GF-CNT(0.1) and GF-CNT(0.5) epoxy composites together with two linear dash lines showing the regression of the experimental data. Obviously, there is a linear dependency of the measured current as a function of the applied voltage, indicating the formation of Ohmic contacts between GF-CNT and the electrodes. The resistance of the single fiber composites was calculated from the reciprocal of the corresponding  $I$ - $V$  curve slope and it is inserted in Fig. 6.17b. The specific conductivity of single GF-CNT(0.1) and GF-CNT(0.5) in epoxy at the longitudinal direction was given by the formula:  $\sigma_{GF-CNT/epoxy} = (4L) / \pi d^2 R$ , and after calculations was found to be 2.71 S/m and 70.21 S/m, respectively, which is around two times lower than the conductivity of the respective fibers. This can be explained by the presence of the epoxy insulating chains through the CNT-networks generating an insulating layer at the nanotube-nanotube junctions preventing direct physical contact between them. [297] In the same way like previously, if we consider the thickness,  $t^*$  of the CNT-networks after embedding in epoxy, as revealed by the TEM interphase-section images ( $t^*_{GF-CNT(0.1)} \approx 120 \text{ nm}$  and  $t^*_{GF-CNT(0.5)} \approx 250 \text{ nm}$ ), using Equation 6.7, we can correlate the conductivity of the nanostructured

interphases ( $\sigma_{\text{Interphase}}$ ) with the respective specific conductivity of single GF-CNT in epoxy following the expression:  $\sigma_{\text{Interphase}} \approx (d/4t^*) \sigma_{\text{GF-CNT/epoxy}}$ . After calculations, the  $\sigma_{\text{Interphase}}$  of GF-CNT(0.1) and GF-CNT(0.5) was  $1.01 \times 10^2 \text{ S/m}$  and  $1.05 \times 10^3 \text{ S/m}$ , respectively. The high conductivity values within the interphases can be compared to CNT/polymer composites with high CNT loadings, [33] and this is of utmost importance for utilising the GF-CNT as thermoelectric elements in composite materials.

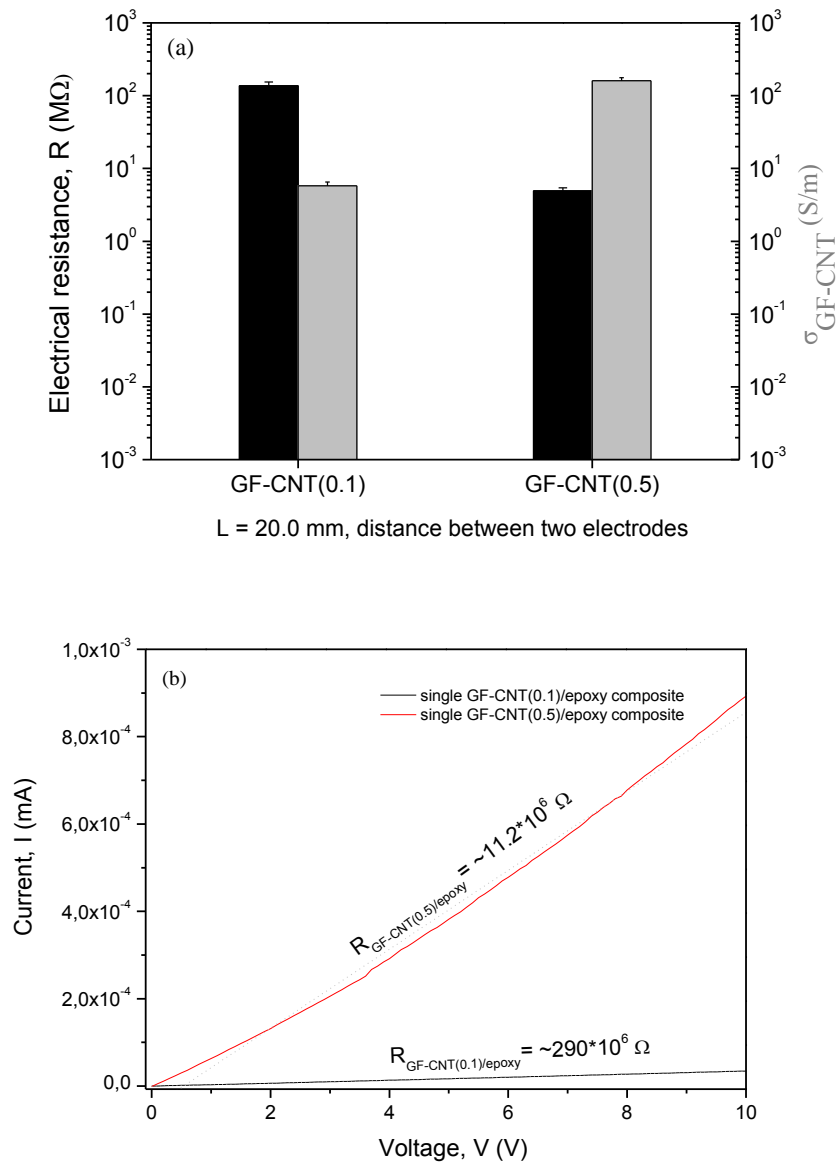
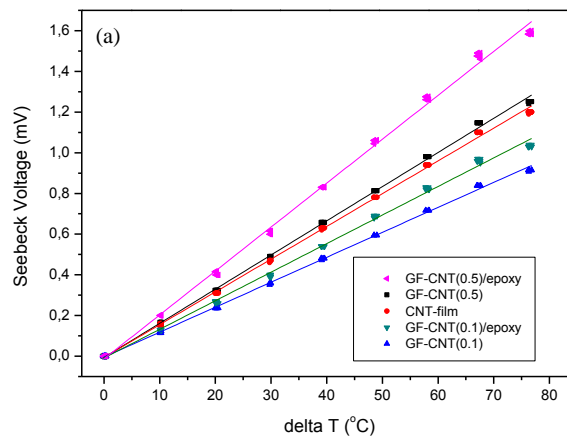


Fig. 6.17 – (a) DC electrical resistance ( $R$ , black bars) and conductivity ( $\sigma$ , grey bars) of single GF yarns chemically grafted with MWCNTs in 0.1 and 0.5 mg/mL CNT solutions at  $L=20 \text{ mm}$  electrode-electrode distance (error bars represent the standard deviations). (b)  $I$ - $V$  curves of single GF-CNT(0.1) and GF-CNT(0.5) epoxy composites showing the linear regression (linear dash lines) in each case.

### 6.2.3.6 Thermoelectric power generation

Fig. 6.18a demonstrates the generated thermovoltage upon exposition to a temperature gradient, for the different samples tested. It could be observed that within the temperature range, the generated voltage increased linearly with the increased temperature, as revealed by the perfectly matching linear regressions. The slope of the voltage versus temperature difference (Seebeck coefficient) was found to be  $12.26 \mu\text{V/K}$  for GF-CNT(0.1),  $16.79 \mu\text{V/K}$  for GF-CNT(0.5),  $14.05 \mu\text{V/K}$  for GF-CNT(0.1)/epoxy,  $21.59 \mu\text{V/K}$  for GF-CNT(0.5)/epoxy and  $16.1 \mu\text{V/K}$  for the CNT film (bucky paper film). It is easily observed that the GF-CNT(0.5) exhibits a Seebeck coefficient very close to that of the bucky paper CNT film. Accordingly, the power factors after calculations have shown the best value for the CNT film [ $6.49 \times 10^{-7} \text{ Wm}^{-1}\text{K}^{-2}$ ], while the GF-CNT(0.5) and GF-CNT(0.5)/epoxy showed  $5.56 \times 10^{-7}$  and  $1.61 \times 10^{-7}$ , respectively. Both of the fiber yarns depict higher values after being incorporated in the epoxy matrix due to the phonon scattering which facilitates the remaining of the temperature gradient within the material. Moreover, due to the high electrical conductivity of the highly loaded CNT interphase regions, high power factors can be achieved reaching the value of CNTs. By increasing also the CNT loading onto the fiber surface, it was found to have a positive effect to the power factor. The extremely high conductivity of the filaments which is endowed to the resulting composite interphases, combined with the high Seebeck coefficients exceeded that of CNTs used for the fiber coatings, are very promising values higher than highly filled MWCNT composites prepared via solution blending techniques. [326]





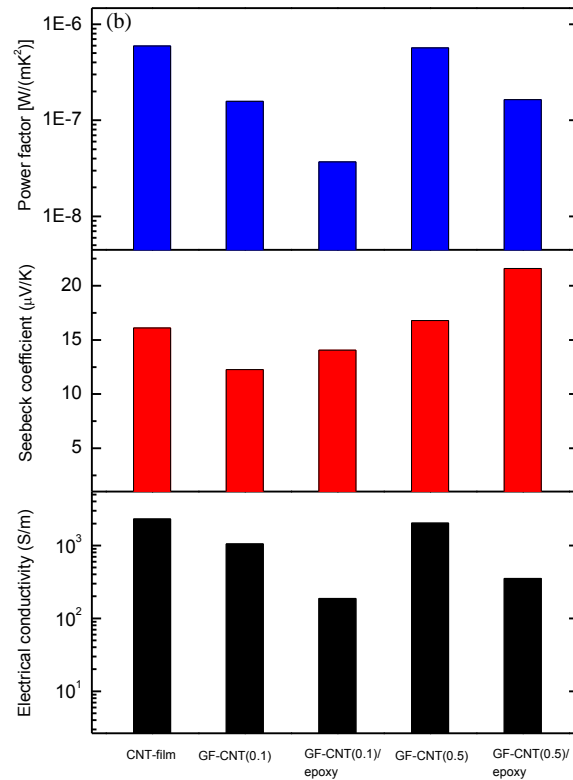
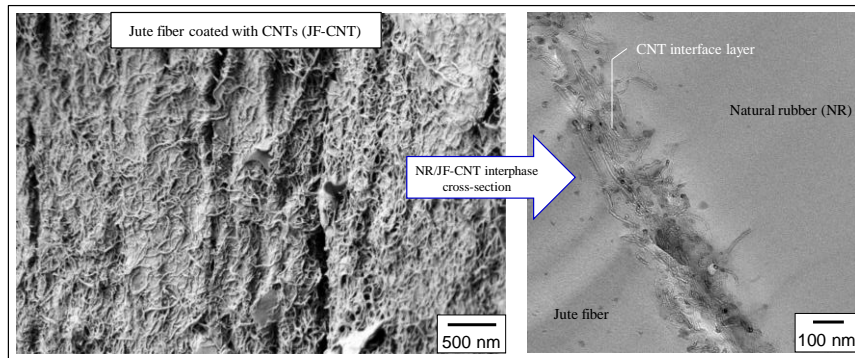


**Fig. 6.18 – (a) Seebeck voltage (or thermovoltage) versus  $\Delta T$  with the corresponding linear regression fits giving the values of Seebeck coefficients from the slopes. (b) Electrical conductivity, Seebeck coefficients and Power factors calculated for the materials investigated in this study.**

In summary, the development of glass fibres coated with MWCNTs (GF-CNT) by covalent bonds following a solution based dip-coating deposition process has been achieved. The CNT coating was found to be sensitive in the epoxy molecular mobility during the hardening process, and therefore GF-CNT can serve as a non-invasive sensor for the real time epoxy cure monitoring. The GF-CNT embedded in epoxy matrix exhibited also a high sensitivity to UV-light offering the possibility to be used as an integrated composite UV-sensor. Finally, a major finding of this study is the utilization of the GF-CNT multi-scale structure for harvesting thermal energy, when a model composite with a single fiber yarn was exposed to a temperature gradient. All the properties investigated in this study are for the first time reported, and they arise from the CNT-rich composite interphases. The use of GF-CNT yarns with p- and n-type conductivity characteristics connected in series, as well as decoration of effective thermoelectric nanoparticles onto the CNT network covering the fiber surface, is ongoing research to increase the efficiency of the thermoelectric interphases.

## Chapter 7

### Jute fibers covered with CNT-networks as hybrid fillers for the effective reinforcement of a natural rubber matrix



#### Abstract

A simple and facile method is reported for depositing multiwall carbon nanotubes (MWCNTs) onto the surface of naturally occurring short jute fibers (JFs). Hierarchical multi-scale structures were formed with CNT-networks uniformly distributed and fully covering the JFs (JF-CNT), as depicted by scanning electron microscopy (SEM) images. The impact of these hybrid fillers on the mechanical properties of a natural rubber (NR) matrix was systematically investigated. Pristine JFs were cut initially to an average length of 2.0 mm and exposed to an alkali treatment (a-JFs) to remove impurities existing in the raw jute. MWCNTs were treated under mild acidic conditions following the protocol of Aviles *et al.* to generate carboxylic acid moieties [295]. Afterwards, MWCNTs were dispersed in an aqueous media and short a-JFs were allowed to react with them. Raman spectroscopy confirmed the chemical interaction between CNTs and JFs. The JF-CNT exposed quite hydrophobic behavior as revealed by the water contact angle measurements, improving the wettability of the non-polar NR. Consequently, the composite interfacial adhesion strength was significantly enhanced while a micro-scale "mechanical interlocking" mechanism was observed from the interphase-section transmission electron microscopy (TEM) images. SEM analysis of the composite fracture surfaces demonstrated the interfacial strength of NR/a-JF and NR/JF-CNT composites, at different fiber loadings. It can be presumed that the CNT-coating effectively compatibilised the composite structure acting as a macromolecular coupling agent. A detailed analysis of stress-strain and dynamic mechanical spectra confirmed the high mechanical performance of the natural-based hierarchical composites.

## 7.1 Introduction

Natural fiber reinforced polymer composites have been introduced since 1908 when for the first time cellulose fibers were incorporated in phenolic resins. [337] Nowadays, natural fibers such as jute, flax or hemp have attracted considerable scientific interest in the field of polymer composites due to their intrinsic low density as well as the high specific mechanical properties at a very low price. Therefore, it can be easily realised that natural fibers possess great potential to replace synthetic ones, like glass, carbon or aramid for specific applications, since they are recyclable, biodegradable and non-polluting. Accordingly, environment-friendly biodegradable composites can be achieved exposing comparable mechanical properties with that of glass fiber composites [338], but with lower weight and significantly reduced carbon footprint. [339]

Recently, natural fibers have been used as alternative reinforcements of conventional glass fibers for petroleum-based polymer composites in the automotive and building product industry. [164] However, the use of natural fibers has to face some specific drawbacks, e.g. the relatively poor thermal stability and especially the poor compatibility and interfacial bond strength with the hydrophobic polymer matrices, due to their basically hydrophilic nature. [340] [341] This can result further in weak fiber/matrix interfaces and poor mechanical properties of the final composites. Nevertheless, it has been reported in several studies that most of these drawbacks can be overcome utilising specific surface modifications. [342] [343] [344] [345] In composite materials, it is a well-known fact that the strength and modulus are both dominated by the reinforcement phase which is considered to be the main load bearing constituent. The interphase between fibers and matrix acts as an intermediate bridge which transfers the load from the matrix to the reinforcing fibers through the shear flow. Therefore, it is considered as a critical parameter in controlling the overall composite's performance. [282] [346] Optimized engineered interfaces can guarantee a "good adhesion" between the composite constituents resulting in enhanced interfacial strength; a key parameter for the effective stress transfer upon mechanical loading. Indeed, the high quality of the interphase is a precondition for the optimal composite's mechanical performance as concluded in various studies. [266] [281] [289]

The reinforcement of rubbers by particulate and fibrous fillers is quite common method to enhance their mechanical properties, however, useful products and their commercial viability have been found only when these two parameters, viz., lowest dimension of the dispersed phase and strong interaction between the filler/matrix are achieved. [347] Much investigation has been focused on the reinforcement of rubbers by using both synthetic as well as natural fibers. Especially, the incorporation of short fibers in a

rubber matrix has become an attractive field of research due to the versatile processing which lowers the production costs compared to unidirectional fiber composites. Short fiber rubber composites can be used in a wide range of applications such as belts, hoses, seals, complex-shaped mechanical goods and tire industries. [348] Several studies are available on the use of short synthetic fibers like glass, carbon, rayon, nylon, aramid and asbestos in various natural and synthetic rubbers. [349] [350] [351] [352] Sreeja and Kutty [353] investigated the mechanical properties of rubber composites reinforced with short nylon fibers. In another work, Senapati [354] embedded short polyester fibers in a natural rubber matrix. Generally, the mechanical properties of short fiber reinforced composites are largely governed by the fiber/matrix adhesion strength as well as the state of fiber dispersion, concentration, aspect ratio and orientation which may directly be affected by the processing method and processing parameters. [355] Hintze *et al.* [352] described that the reinforcement of an EPDM rubber matrix was significantly influenced by the process induced orientation and the residual length of aramid type short fibers. Due to the fact that natural fibers are renewable in nature, a lot of attention is given to achieve rigid rubber-based composites. Many researchers have reported the use of natural fibers, viz., pineapple leaf fiber [356], short jute fiber [357], short coir fiber [358], bamboo [359], sisal/oil palm [360] in elastomer compounds. Murthy [361] and Chakraborty [357] investigated the reinforcing effect of short jute fibers in natural and carboxylated nitrile rubber composites. Recently, Götze *et al.* [351] reported that short cellulose type fibers offered much reinforcement at lower filler content compared to conventional synthetic fillers in a solution processed styrene butadiene rubber.

The fabrication of natural rubber/jute fiber composites is in general a quite new research field and the effective reinforcement could be a challenging topic. Obviously, the dispersion of JFs in NR and the formation of a strong interphase between them is a difficult task which requires extensive investigation. It is reported that partial modification of either the fiber surface or the polymer matrix can develop an improved bonding leading to satisfying reinforcing effects. [294] The JFs in the as grown state consist of a cellulose rich core and their outside surface is dominated by cementing which includes waxes, fats, lignin, pectin and hemicellulose. This cementing prevents from the formation of a good interface and normally it is removed by an alkali treatment. However, the hydrophilic and polar nature of JFs after alkali treatment still remains not suitable for direct incorporation with the apolar NR. A lot of different approaches have been utilised to rendering the JFs more compatible with polymer matrices. [343] [345] [294] A first step usually contains as mentioned above an alkali treatment so that the fibers will expose their cellulosic nature. [362] Silane coupling agents and/or other chemical substances [363] have been further used to promote the

fiber/matrix adhesion and endow the desired interfacial strength. Garcia-Hernandez [364] reported an apparent influence of the natural fiber surface modifications on the interfacial shear strength of polystyrene composites. Another method to improve the compatibility between natural fibers and polymeric matrices is to use modified polymers, e.g. the addition of a small amount of maleic anhydride grafted PP to a polypropylene matrix. [345] Recently, carbon nanotubes (CNTs) have been regarded as excellent candidates to modify the fiber surfaces and improve the interfacial strength as well as to introduce interphase functionality due to their unique electrical, mechanical and thermal properties. [365] [366] In particular, deposition of CNTs onto glass or carbon fibers using chemical vapour deposition, simple solution dip-coating methods or spray coating techniques has been found to increase the interfacial interaction via increased chemical bonding, mechanical interlocking and local stiffening of the polymer chains at the interphase region, all of which may improve the stress transfer from the matrix to the reinforcement. [275] Subsequently, high loadings of CNTs in the final composites can be achieved while alleviating the critical problems encountered during the composite fabrication related to the high viscosity of the polymer melts and the CNT agglomeration. [281] A review could be found where carbon nanotube-based hierarchical composites and the advantages for the formation of a multi-scale reinforcement were elaborately discussed. [264] The influence of CNT-modified fibers, e.g., on static tensile and dynamic mechanical properties of elastomer composite materials with the aim to be applied finally in products under dynamic loading, are not established yet. Meanwhile, the chemical vapour deposition (CVD) process which is already reported for CNT deposition [367] [263] [368] onto fibrous reinforcements cannot be employed in the case of JFs and/or other kind of natural fibers, because they are not stable at high temperatures required for the CVD CNT-growth.

The main objective of the current study is to develop an engineered interface in short jute fiber reinforced NR composites, using CNTs as a novel interphase coupling agent. JFs were coated with CNTs (JF-CNT) via non covalent interactions and hierarchical structures were created. The resulting JF-CNT hybrid fillers were embedded in a NR matrix, and exposed a significant reinforcing effect as revealed by the static tensile tests and dynamic mechanical analysis (DMA). This was mainly attributed to the NR improved wettability towards the CNT-coated JFs at 10, 20 and 30 phr (parts per hundred gram of rubber) loadings, compared to the respective a-JF composites. JF-CNT exposed less polar and less hydrophilic behaviour as shown by the water contact angle measurements explaining more precisely the improved wetting of the NR resin. SEM fractographic analysis exhibited limited JF-CNT pulled-out from the NR matrix, and also no significant interfacial

debonding. The CNT-networks introduced a mechanical interlocking mechanism illustrated by the TEM interphase-section images. In addition, the JFs were endowed with nano-scale roughness which is responsible for the local stiffening of the NR chains at the fiber/matrix interphase region. Overall, it can be envisaged that the CNT surface layer played an important role on the enhanced interfacial adhesion strength reflecting to the mechanical properties of the final composites. The different micro-scale toughening mechanisms correlated to the improved mechanical performance of the hierarchical natural-based rubber composites will be discussed further more in detail.

## 7.2 Experimental

### 7.2.1 Materials

The natural rubber used in our study is Standard Malaysian Rubber (SMR-10). Jute yarn was obtained from Gloster Jute Mills, (TD 4 grade, Howrah, India). Stearic acid was purchased from Acros Organics (Geel Belgium, 97 % purity) and N-cyclohexyl-2-mercapto benzothiazole sulfonamide from Rhein Chemie (Rheinau, Mannheim Germany). Sulfur, zinc oxide, ethanol, toluene and sodium hydroxide were supplied by Sigma-Aldrich (Steinheim, Germany) and used as received. Commercially available pristine MWCNTs (Nanocyl, NC 7000) with carbon purity > 90 %, average length 1.5  $\mu\text{m}$  and diameters around 10 nm were provided by Nanocyl S.A (Belgium). All the chemicals were analytical grade and used as received without further purification.

### 7.2.2 Purification and functionalization of MWCNTs

Pristine MWCNTs (0.3 g) were mixed with 70 ml of  $\text{HNO}_3$  (3.0 M) and dispersed by magnetic stirring and short time of sonication alternatingly at 60  $^\circ\text{C}$  for 15 min. [295] The mixture was left to cool down, diluted with one liter of distilled water and subsequently filtered through a polycarbonate membrane (47 mm diameter and 0.4  $\mu\text{m}$  pore size) using a vacuum filtration apparatus. The bucky paper CNT-film formed onto the filter membrane was cleaned with copious amount of distilled water up to the neutral pH value, and dried under vacuum at 60  $^\circ\text{C}$  for 24 h.

### 7.2.3 Jute fiber alkali treatment and deposition of MWCNTs

Chopped JFs were ground to powder with the help of a mixer grinder and subsequently de-waxed in a mixture of ethanol and toluene (100:50 volume ratio) for 48 h at 50  $^\circ\text{C}$ . The solvent mixture was removed by filtration and the obtained fibers were cleaned several times with distilled water followed by drying at 60  $^\circ\text{C}$  for 12 h. Dried JFs were added

then in a flask containing 1.0 wt% sodium hydroxide aqueous solution and remained under stirring for 4 h at room temperature. After alkali treatment, the fibers were washed with distilled water, neutralized with diluted acetic acid to remove any freed from the alkali substance followed by rinsing again with distilled water. Finally, the a-JFs were dried at 60 °C overnight in a vacuum oven. [294] The length of the fibers was about 2.0 mm and the average diameter 30.0  $\mu\text{m}$  as observed by optical microscopy micrographs. In order to deposit MWCNTs onto the a-JF surfaces, dry acid modified MWCNTs (100 mg) were dispersed in 100 ml of distilled water with the help of an ultrasonic bath to obtain a stable suspension with a concentration of 1.0 mg/ml. Alkali treated JFs (5.0 g) were dispersed in 1000 ml of distilled water under magnetic stirring for 6 h and then MWCNTs were added drop by drop into the beaker containing the a-JFs. The mixture was kept for 24 h under vigorous stirring at room temperature and finally filtered through a glass filter and washed with distilled water to remove excess of MWCNTs which have not interacted with the hydroxyl groups of the JF-surface. Finally, the JF-CNT were annealed at 100 °C for 30 min, and afterwards kept in a vacuum oven overnight at 60 °C. After the complete drying, JF-CNT were stored in a desiccator until the preparation of NR composites and other analytic investigations. The plausible interaction mechanism based on the formation of H-bonds between the hydroxyl functionalities of the a-JFs and the carboxyl groups of MWCNTs is illustrated in Fig.7.1.

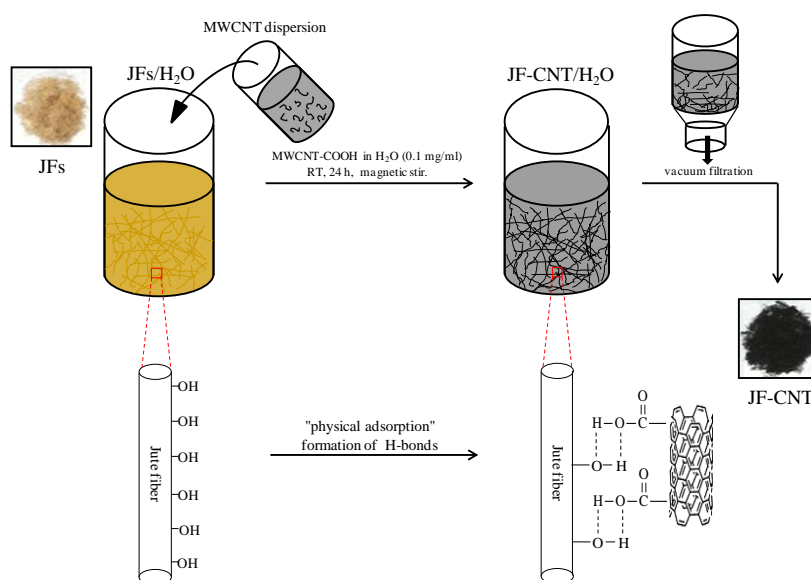


**Fig. 7.1 - Schematic illustration of the preparation and the interaction mechanism between a-JFs and MWCNTs. The optical image of JFs coated with CNTs (JF-CNT) in dry state depicts the color change of JFs from light yellow to black after deposition of MWCNTs.**

#### 7.2.4 Preparation of NR/a-JF and NR/JF-CNT composites

For the fabrication of NR/JF composites, initially the NR mixture containing all the components for the cross-linking process was prepared. In brief, requisite amount of ZnO and stearic acid were incorporated sequentially in previously masticated rubber in an open two-roll mixing mill (Polymix 110L, Servitech GmbH, Wustermark, Germany) at 70 °C with 15-min compounding cycle. Then, different amounts of a-JF and JF-CNT were added in the elastomer mixture followed by adding finally the accelerator and the sulphur. The stocks were cured under pressure at 150 °C using an optimum cure time. The mixture formulation used in our study is given in Table 1. The optical images of the different types of short JFs used for the preparation of NR compounds as well as the resulting composite dog-bone shaped samples used for the mechanical tensile test investigations are depicted in Fig. 7.2.

**Table 1 The mixture formulation of NR/JF composites**

Mix. No. & composition*	1	2	3	4	5	6	7
NR	100	100	100	100	100	100	100
ZnO	5	5	5	5	5	5	5
Stearic Acid	5	5	5	5	5	5	5
CBS	1.5	1.5	1.5	1.5	1.5	1.5	1.5
S	1.5	1.5	1.5	1.5	1.5	1.5	1.5
a-JF	-	10	20	30	-	-	-
JF-CNT	-	-	-	-	10	20	30

\* Numbers for components in recipe are in phr (parts per hundred rubber)

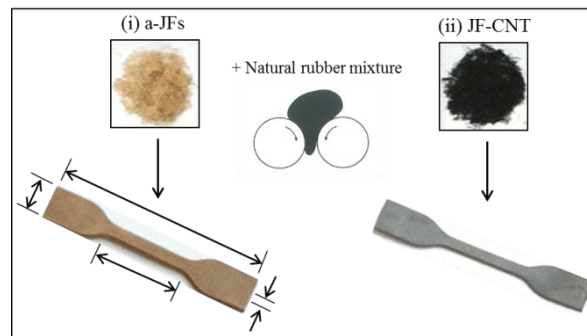


**Fig. 7.2 - Schematic illustration of the fabrication of NR composites and the final dog-bone shaped samples used for the tensile test investigations. The arrows illustrated to the dog-bone sample show the dimensions of the samples used for the mechanical characterization according to the ASTM D 412-92.**

### 7.2.5 Characterization techniques

Fourier-transform infrared (FT-IR) spectra were recorded with spectral resolution of 2 cm<sup>-1</sup> using a Vertex 80v FT-IR spectrometer (Bruker Optics, Germany) equipped with a DTGS detector by signal averaging of 256 scans in transmission mode. Very small amount of either pristine or carboxyl functionalized MWCNTs were pressed together with KBr to form pellets. Raman spectra were measured with an alpha300R Raman spectrometer system



(WITEC GmbH, Germany). The spectra were acquired in the back-scattering geometry and the excitation wavelength was 532 nm from an Nd:YAG laser with a laser power of 1mW used for all the measurements in our study. The 20× magnifying objective of the microscope focused the beam into a spot of about 1µm in diameter. Thermogravimetric analysis (TGA) was carried out in order to study the thermal behavior of neat NR as well as the NR/JF composites. The alkali treated and CNT-coated JFs were studied also by TGA and the weight difference obtained at 800 °C can be attributed to the amount of CNTs which were attached onto the JF-surface. The TGA scans were performed using a TA instrument (Q 5000) under nitrogen flow from 30 °C to 800 °C with a heating rate of 10 °C/min. Curie point standards were utilized for the temperature calibration and all the investigated samples were dried overnight at 60 °C prior to the thermogravimetric analysis. The wettability of a-JF and JF-CNT were evaluated by the sessile drop method using the Dataphysics OCA 20 (Dataphysics, Germany) contact angle analyser system. All the experiments were performed at  $25 \pm 1$  °C and at about 65 % relative humidity. Alkali treated and CNT-coated JFs were pressed to form pellets using the same pressure conditions and the same amount of material (200 mg). The fiber pellets were kept then for drying at 60 °C under vacuum overnight before conducting the contact angle measurements. A droplet of deionized water with 2 µl volume was suspended onto the surface of jute fiber pellets and after standing for 5 s, the droplet profile was recorded with a CCD video camera. A microsyringe was used to form the water droplets and from each single droplet profile, the corresponding contact angles were determined. The reported values are representative of at least five different samples of which three measurements were performed at different positions in order to obtain clear and statistically valid values. Field-emission scanning electron microscopy (FE-SEM) investigations were performed with the NEON 40 (Carl Zeiss AG, Germany) scanning electron microscope operating at an accelerating voltage of 1.0 KV, and the images were recorded using the secondary electron (SE2) detector. In order to study the surface morphology of pristine, alkali treated and CNT-coated JFs, a small amount of fibers was stabilized onto the surface of an adhesive copper tape. Scanning electron microscopy was used also for the fractographic analysis of the composite samples by investigating the fracture surface morphologies of all the specimens after the tensile testing. Prior to the SEM analysis, all the samples were sputter coated with a 3 nm platinum layer in order to avoid charging effects. Interphase-sections of the NR/JF-CNT hierarchical composite with approximately 60-80 nm thickness, have been prepared by means of cryo-ultramicrotomy using the Leica Ultramicrotome (Reichert Ultracut S). Diamond knives for cryo-temperatures (Diatome) were used for the trimming (model cryotrim 45°) as well as the

cutting process (model cryo 35°). The cutting has been carried out at temperatures between -120 and -160 °C. The thin sections were placed on a copper grid (300 mesh Cu, Agar), and investigated further using the Libra 200 transmission electron microscope operating at 200 kV acceleration voltage (HR-TEM, Carl Zeiss AG, Germany). Bright field TEM images were recorded and the energy filtering and contrast apertures were inserted in order to enhance the contrast of the images. Curing studies were performed using a rubber processing analyzer (Scarabaeus SIS-V50, Langgöns Germany) in the isothermal time sweep mode for all the samples at 150 °C for 60 min. Tensile test experiments of the cured samples were carried out using a material testing equipment Zwick 1456 (model 1456, z010, Ulm Germany) at room temperature with a crosshead speed of 200 mm/min (ISO527) according to ASTM D 412-92 after 24 h of maturation of the same. The hardness was determined according to ASTM D 2240-85 with a Shore A durometer (Zwick & Co., Germany). Dynamic mechanical thermal analysis (DMTA) was performed on strips using a dynamic mechanical spectrometer (Gabo Qualimeter, Ahlden, Germany, model Eplexor-2000N). Temperature sweep analysis was carried out using a constant frequency of 10 Hz in a temperature range of -80 to +80 °C. For the measurement of the complex modulus ( $E^*$ ), a static tensile load of 1 % pre-strain was applied and then the samples were oscillated to a dynamic load of 0.5 % strain. Measurements were performed with a heating rate of 2 °C/min under liquid nitrogen flow. Strain sweep analysis was performed for the crosslinked samples in isochronal frequency of 10 Hz and dynamic strain of 0.2 – 30 %, with a static load of 30 % strain at room temperature.

### 7.3 Results and Discussions

#### 7.3.1 Infrared spectroscopy (FT-IR)

The FT-IR spectrum of pristine and functionalized MWCNTs using mild acidic treatment is shown in Fig. 7.3. The appearance of a small band at  $1712\text{ cm}^{-1}$  for the modified CNTs, can be assigned to stretching vibrations of the carbonyl groups (C=O) which are introduced after the acid treatment. The optical image which is given as an inset in Fig.3 represents the colloidal stability of pristine and acid functionalized CNTs in water media at equal concentrations (1 mg/mL). The image has been recorded six hours after the CNT dispersions have been prepared by ultrasonication and as it can be observed, CNTs containing small amount of oxygen groups remain well-dispersed.

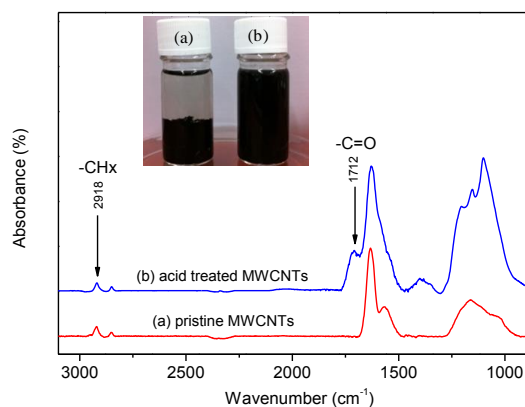


**Fig. 7.3 - FT-IR spectra of (a) pristine (red line) and (b) acid-treated (blue line) MWCNTs. The optical image given as an inset shows the colloidal stability of pristine (left) and functionalized MWCNTs (right) in water six hours after the CNTs have been dispersed by ultrasonication.**

### 7.3.2 Raman spectroscopy

Raman spectroscopy is a powerful tool to characterize structural changes of materials which contain hexagonally packed aromatic hydrocarbons, and this is due to the stretching vibrations of the C-C bonds of the aromatic rings. Therefore, Raman spectroscopy has been utilized as a useful experimental technique to probe sensitively the non-covalent interactions of CNTs with various molecular moieties. [369] In our case, both the MWCNTs as well as the JFs are Raman active materials due to presence of aromatic benzene rings and the hemicellulosic structure, respectively. Fig. 7.4 shows the room temperature Raman spectra of pristine and mild acid treated CNTs, as well as a-JFs and JF-CNT. The spectra in Fig. 7.4a display three characteristic bands corresponding to the CNT tangential modes. The D-band at  $\sim 1340\text{ cm}^{-1}$  indicates the density of defects of CNTs ( $\text{sp}^3$  hybridization) and the G-band at  $\sim 1575\text{ cm}^{-1}$  is assigned to the in-plane tangential stretching from the C-C bonds in the graphene sheets ( $\text{sp}^2$  hybridization). The  $\text{G}^+$  band at  $\sim 1610\text{ cm}^{-1}$  is a weak shoulder of the G-band and originates also from defects and disorder in the graphitic lattice. Comparing the  $\text{G}^+$  band intensity of pristine and acid-treated CNTs, we note that it is not significantly increased for the acid treated material, and also the intensity of G-band remains almost the same in both cases. The  $I_{\text{D}}/I_{\text{G}}$  relative band intensity ratio is 1.40 for pristine and 1.42 for acid treated CNTs. This fact can prove further that the mild acidic treatment has not generated significant defects to the graphitic structure of pristine CNTs. The Raman spectra of a-JF and JF- CNT, compared to the spectra of acid treated CNTs are depicted in Fig 7.4b. In Fig. 7.4c, the spectra region of  $1250\text{--}1450\text{ cm}^{-1}$  is demonstrated and it can be clearly observed that there is a relative shift of the  $\text{CH}_2$  deformation band of the a-JF from  $1335$  to  $1352\text{ cm}^{-1}$ . At the same time, as shown from the spectra region of  $1525\text{--}1700\text{ cm}^{-1}$  in Fig.

7.4d, a shift of the CNT G-band from 1560 to 1576  $\text{cm}^{-1}$  occurs in the case for the JF-CNT sample. Both shifts provide strong evidence that CNTs have interacted chemically with the a-JFs by means of non-covalent bonds.

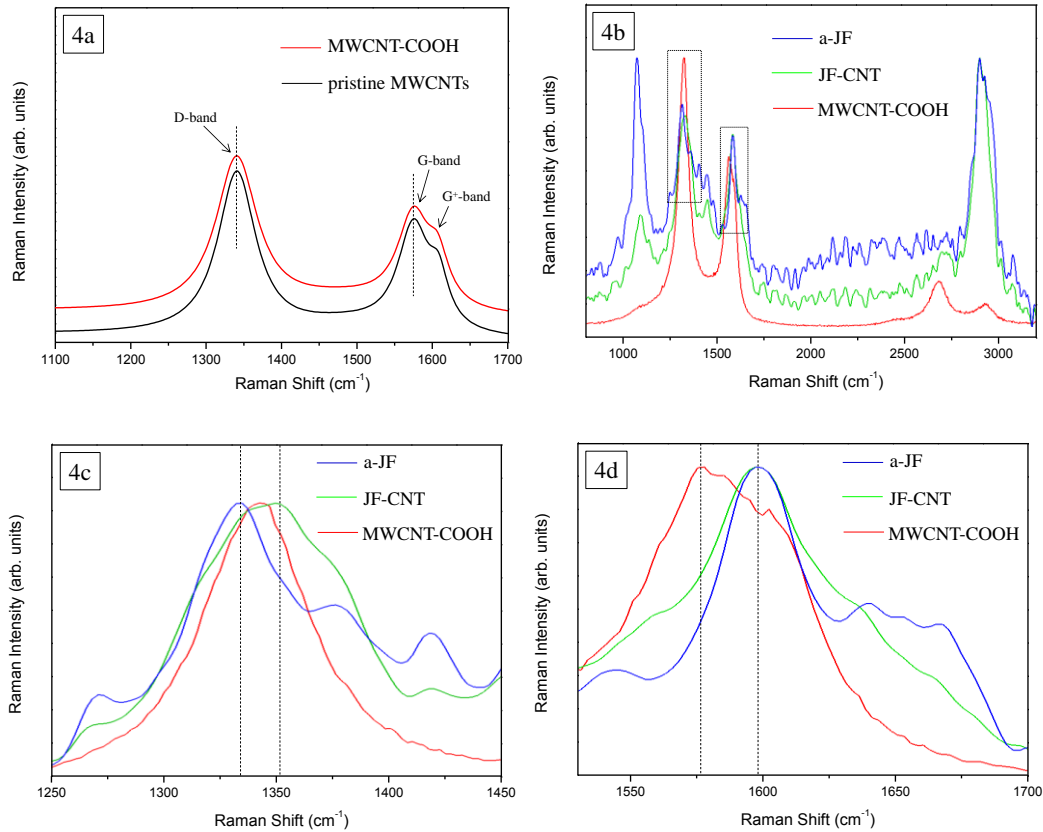


**Fig. 7.4 - Raman spectra of pristine and acid treated MWCNTs (Fig. 7.4a) and comparison of MWCNT-COOH, a-JF and JF-CNT (Fig. 7.4b). Fig 7.4c and 7.4d depict the spectral regions indicated by dashed-line boxes in Fig. 7.4b, showing the relative shifts of the bands.**

### 7.3.3 Thermogravimetric analysis (TGA)

In order to study the thermal degradation behavior of NR and the corresponding composites containing a-JF and JF-CNT, the thermal decomposition temperatures ( $T_d$ ) were studied by thermogravimetric analysis under  $\text{N}_2$  atmosphere. Fig. 7.5a illustrates the TGA scans of neat NR and NR/JF composites, respectively. The results suggest that the incorporation of 10 phr JFs in the NR matrix increases slightly its thermal stability. Since CNTs are highly thermally conductive fillers [196], the thermal stability of NR loaded with 10 phr JF-CNT has been additionally increased. A quite remarkable enhanced thermal degradation behavior was observed for the NR/JF-CNT composite. This is a very important finding considering that the CNT loading is less than 0.6 wt% in relation to the final NR/JF-CNT composite, as revealed by the TGA investigations depicted in Fig. 7.5b. The weight

difference of the residue at the temperature range of 700 °C for a-JF compared to JF-CNT was around 6 wt% as shown from the TGA scan in Fig. 7.5b. Apparently, the weight difference between the dried a-JFs and JF-CNT corresponds to the amount of CNTs deposited onto the surface of a-JFs.

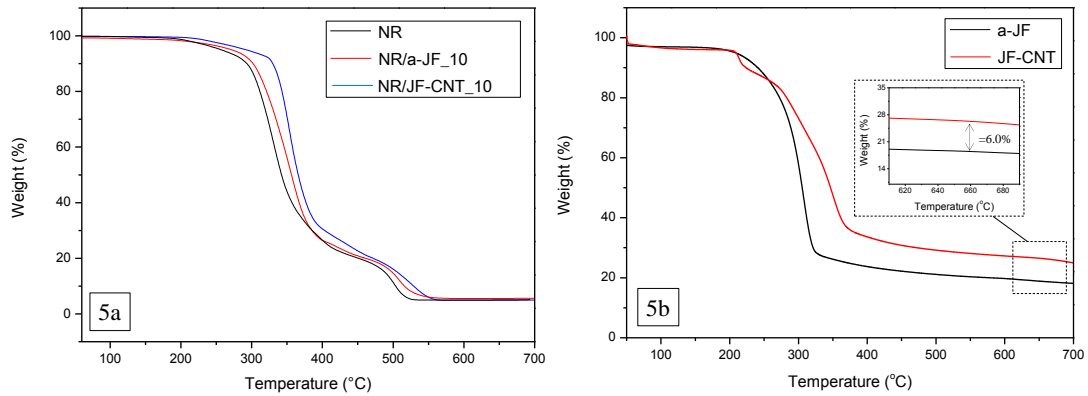


**Fig. 7.5 - TGA curves of (a) neat NR and NR filled with 10 phr a-JFs and JF-CNT, respectively, and (b) a-JF and JF-CNT showing the residue at the temperature range of 700 °C which corresponds to the CNTs adsorbed to the a-JF surface.**

### 7.3.4 Contact angle measurements

Contact angle is a sensitive tool for the characterization of the outermost surface layer of materials (about 0.5 nm). In order to get more insight into the surface properties of JFs used for the fabrication of NR composites, the static water contact angles of a-JF and JF-CNT pressed in the form of pellets were measured. [370] The wetting of fibers by deionized water can clearly indicate their hydrophilicity which is apparently a non-desired factor to achieve a good adhesion and interfacial compatibility with the apolar and hydrophobic NR matrix. From the contact angle experiments, the nature and the expected compatibility of a-JFs as well as JF-CNT with the natural rubber were elucidated. Typical results are given in Fig. 7.6 showing the contact angle images of a-JFs (Fig. 7.6a) and JF-CNT (Fig. 7.6b) JFs including as inserts the arithmetic values of the contact angles given by the software (Dataphysics) for each captured droplet profile. The images were captured five seconds after the drop was suspended onto the surface of the fiber pellets, and several experiments were performed in different positions which have shown relatively small variations of the values which are finally presented. The water contact angle of a-JF was found to be around 49.5° being in good agreement with the reported data of Doan *et al.* [294], whereas the JF-CNT showed a contact angle of around 70°. It can be speculated that the deposited CNT-networks endow quite hydrophobic behavior of the hybrid JF-CNT fillers compared to their inherent hydrophilic properties. Jute fibers surface modified with silane coupling agents have exposed

similar contact angles with the values obtained in our study. [294] The increased hydrophobicity of the CNT-modified JFs can be explained mainly by two factors, *i*) the low amount of CNT functional groups which form the CNT-coating as compared to the high content of hydroxyl functionalities of the a-JFs and *ii*) the nanoscale surface roughness [371] induced by the CNT-networks on the microscale jute fiber. The JF-CNT micro-nanoscale binary hierarchical structure formed results in the formation of an artificial lotus leaf structure on the JF surface. Liu *et al.* [371] has reported even super hydrophobic properties of the inherently hydrophilic cotton fibers after coating with CNT-networks.

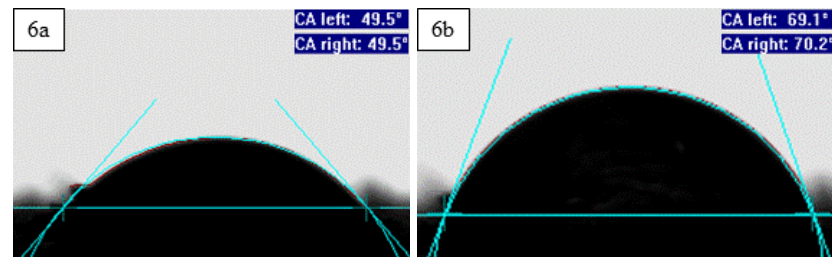


**Fig. 7.6 - Contact angle images of a water droplet in contact with (a) a-JFs and (b) JF-CNT, pressed in the form of pellets, showing the static contact angles measured by a goniometer.**

### 7.3.5 Electron microscopy investigations

Fig. 7.7 represents the SEM images showing the surface microstructures of pristine, a-JFs and JF-CNT (Fig. 7.7a, 7.7b and 7.7c). Pristine JFs in Fig. 7.7a appear with a lot of structural defects and small parts of jute as well as hemicellulosic impurities and/or other impurities like waxes, fats, lignin, pectin, all of which they are part of the cementing which exists on the JF-surface in the as grown state. After the alkali treatment, the cementing layer and small jute parts are hydrolyzed and removed as can be observed in Fig.7.7b, yielding a quite smooth and uniform surface with visible the natural fiber's veins. Fig.7.7c and the corresponding micrograph at a higher magnification depicts the surface morphology of JF-CNT hierarchical structure. It can be obviously seen that CNT-networks cover fully the JF surface forming a uniform, homogeneous and interconnected CNT-layer. The resulting CNT coating endows nanoscale roughness to the microscale jute fiber which is responsible for the hydrophobic properties of the JF-CNT as mentioned above. In addition, the CNT-coating effectively increases the surface area of the JF-CNT compared to the a-JFs, promoting mechanical interlocking for the NR/JF-CNT hierarchical composites.

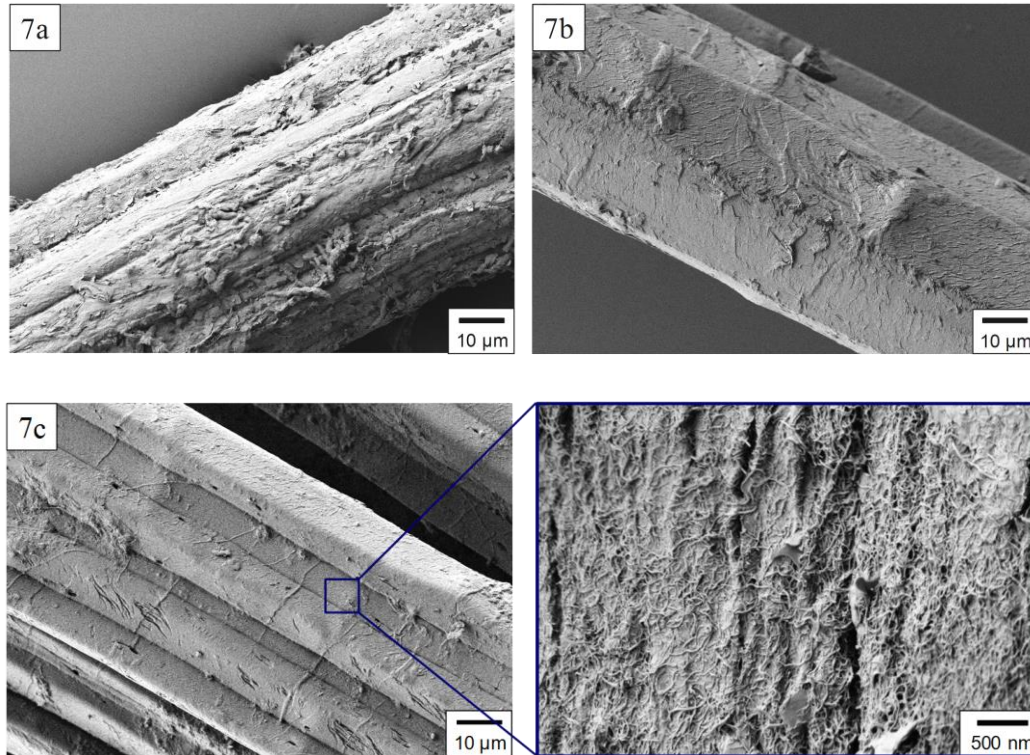
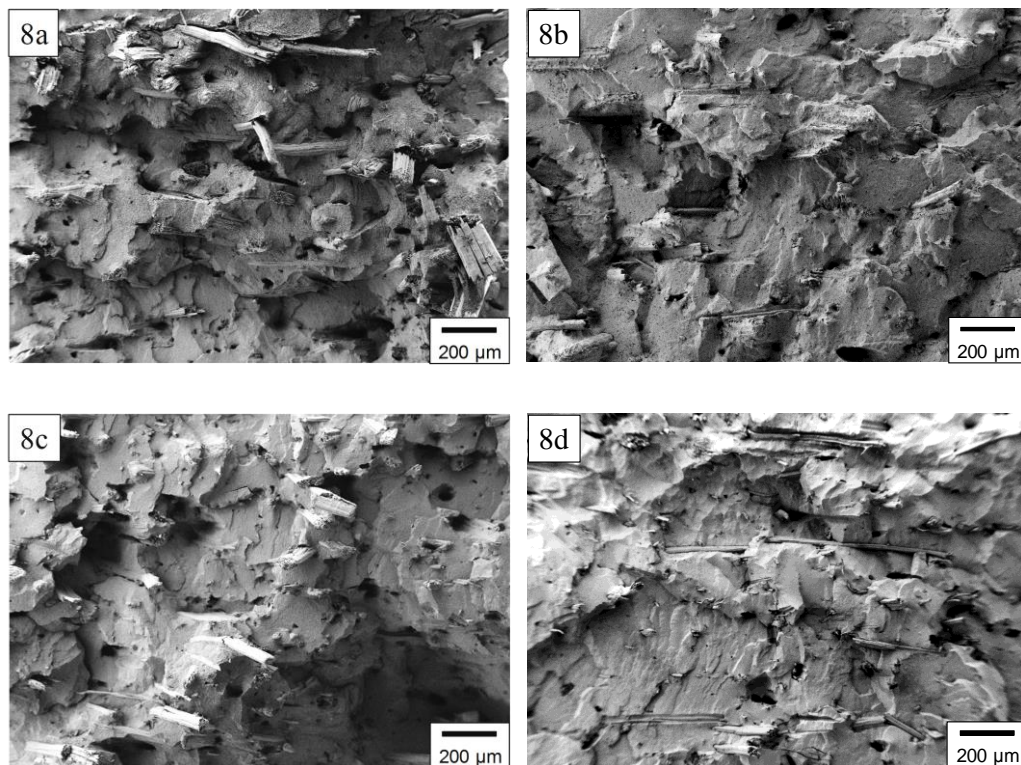


**Fig.7.7 - SEM images showing the surface morphology of pristine (Fig 7.7a), a-JFs (Fig 7.7b) and JF-CNT (Fig 7.7c).**

Fig. 7.8 depicts the SEM fracture surface images after tensile testing for the NR/JF composites containing 10 phr (Fig. 7.8a and 7.8b), 20 phr (Fig. 7.8c and 7.8d) and 30 phr (Fig 7.8e and 7.8f) a-JFs and JF-CNT, respectively. In Fig. 7.8, the composite interphase microstructures are also illustrated by the SEM (Fig 7.8g and 7.8h) and TEM (Fig 7.8i) micrographs. In Fig. 7.8a, 7.8c and 7.8e, the images correspond to the fractured surfaces of the NR composites with different loadings of a-JFs (10, 20 and 30 phr), while Fig. 7.8b, 7.8d and 7.8f depict the NR composites containing JF-CNT at different loadings. It can be clearly seen that a-JFs are pulled out from the NR matrix after the tensile test fracturing process. On the other hand, the JF-CNT due to the improved interfacial adhesion and compatibility with the NR in conjunction with the occurring mechanical interlocking mechanism remain embedded in the NR matrix. From the fractographic analysis, it can be also observed that the fibers for both NR/a-JF and NR/JF-CNT composites are well separated and dispersed in the matrix indicating our optimized processing parameters. Consequently, the good state of dispersion of the short JF-CNT hierarchical reinforcement combined with the enhanced interfacial adhesion should result in high mechanical performance of the final composites due to the apparent potential to efficiently transfer the load from the matrix to the reinforcement. Fig. 7.8g and 7.8h show the NR composite's interphase section characteristics

at high magnification focusing on the single fiber/matrix interphase level. These images demonstrate more precisely the interfacial adhesion and highlight the wettability of the NR to the a-JFs (Fig. 7.8g) and JF-CNT (Fig. 7.8h). In the first case, it is observed that the fiber is detached from the NR after the tensile fracturing whereas in the second case, JF-CNT remains in contact with the NR showing the interfacial integrity and the good wetting of the NR to the JF-CNT.

Fig. 7.8i shows the TEM interphase cross-section image of the NR/JF-CNT hierarchical composite. The thickness of the CNT-coating was found to be around 100 nm and it can be seen that the NR fully wets the JF-CNT without any cracks or microvoids generated during the fabrication process. The TEM image at higher magnification represents a more detailed overview for the interfacial microstructure of the NR/JF-CNT composite. In specific, the CNT-coating consists of a dense and interconnected assembly of CNTs attached to the JF surface. Another important factor is that the nano-sized CNT-particles are acting probably as a healing agent for the a-JF which as a natural material even after the alkali treatment still contains some defects and some cracks on the outer surface.





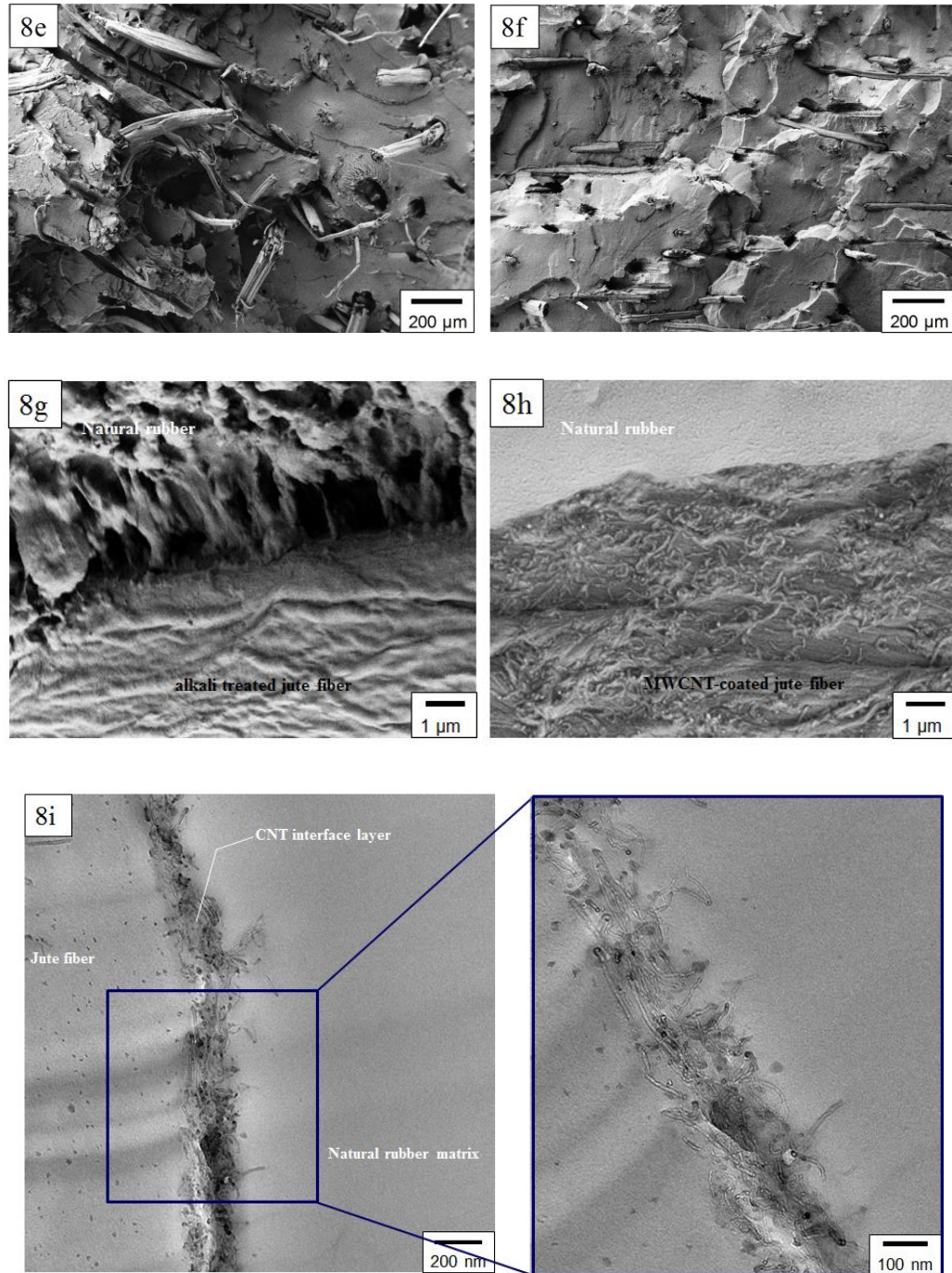


**Fig. 7.8** - SEM images of the fracture surfaces of NR composites after tensile testing containing 10 phr (Fig 7.8a, 7.8b), 20 phr (Fig 7.8c, 7.8d) and 30 phr (Fig 7.8e, 7.8f) a-JFs (left side) and JF-CNT (right side). High magnification of the 7.8a and 7.8b images shows the interphase section area of a single JF in the NR matrix (Fig 7.8g and 7.8h). Fig 7.8i depicts the TEM interphase cross-section image of the NR/JF-CNT hierarchical composite and the selected area at a higher magnification.

### 7.3.6 Cure and physical properties of NR and NR/JF composites

The maximum rheometric torque ( $S_{\max}$ ), scorch time ( $t_2$ ) and optimum curing time ( $t_{90}$ ) obtained from this study are recorded in Table 2. It has been found from the values presented in this table that the maximum rheometric torque for the composites is always higher as compared with neat NR gum and the value is increasing with the increased JF loading. However, the JF-CNT did not show much difference with a-JFs with respect to the maximum torque. A slight decrease in scorch time was observed with JF-CNT filled compounds. The curing time was not affected too much with addition of JFs and this is also true for the cure rate index.

**Table 2 Cure and physical properties of NR compounds**

Mix. No. & cure properties	$S_{\min}$ (dNm)	$S_{\max}$ (dNm)	$t_2$ (min)	$t_{90}$ (min)	*Cure rate index
NR	0.39	4.91	4.92	16.0	9.02
NR/a-JF_10	0.40	6.98	4.05	20.8	5.97
NR/a-JF_20	0.36	7.31	5.28	16.55	8.87
NR/a-JF_30	0.45	8.85	5.30	16.16	9.20
NR/JF-CNT_10	0.42	6.29	5.09	17.02	8.38
NR/JF-CNT_20	0.48	7.03	4.17	16.79	7.92
NR/JF-CNT_30	0.65	9.12	3.81	14.14	9.68

\*The cure rate index (CRI) is given by the formula  $CRI = 100/(t_{90} - t_2)$  and after calculations is given in the last column of Table 2.

Natural rubber shows an excellent flexibility as a typical elastomeric material. However, its mechanical properties should be improved for certain applications like truck tires tread application where abrasion resistance, cut growth resistance, structural long term durability, reliability at speed, blow-out resistance, impact resistance are the major concerns. Nano-sized fillers like reinforcing carbon black need to be added at a relatively large amount into a NR matrix in order to gain sufficient mechanical properties, due to weak interfacial adhesion of the fillers with the NR. [372] [373] In silica filled synthetic rubbers, the amount of nano-fillers is also very high; even higher compared to rubber composites reinforced with carbon black. [374] In the present work, it is aimed to understand the effect of addition of a relatively smaller amount of micro-scale sized anisotropic fillers on the final mechanical properties of NR composites. The modulus, tensile strength, elongation at break and hardness of the resulting composites were measured and presented in Table 3. In one hand, the NR composites with 10, 20 and 30 phr JF-CNT depict a more prominent increase at 100 % modulus, 200 % modulus and 300 % modulus, respectively (Table 3), as compared to the composites filled with the same amounts of a-JFs. On the other hand, the tensile strength of composites filled with both a-JFs and JF-CNT is increased with the addition of only 10 phr of fibers. However, tensile strength found to decrease at higher loading of both fibers

(especially after 20 phr). NR/JF-CNT<sub>20</sub> exhibits higher tensile strength together with higher modulus at different elongations compared to a-JF filled compound with similar fiber loading. Such behaviour can be explained in terms of enhanced interfacial adhesion strength which can result in higher crosslinking density in the system. In general, the mechanical properties of a rubber intensely depend on crosslinking density. [375] Modulus and hardness increase gradually with increasing cross-linked density. Tensile strength passes through a maximum as cross-linked density is increased. When a rubber is deformed externally, part of the applied energy stored elastically in the chains and is available as driving force for fracture. The remaining energy is dissipated through molecular motions into heat and in this way is made inaccessible to break further chains. At high cross-links level, chain motions become restricted and the tight network is incapable of dissipating much energy. The enhanced modulus of NR/JF-CNT hierarchical composites shows a strong correlation with the morphology obtained from their SEM fracture surface images. Although, it was found that the elongation at break values did not follow any trend.

The filler reinforcement and filler-polymer affinity of both a-JFs and JF-CNT based NR composites are further analyzed using Mooney-Rivlin (MR) equation which is often used by rubber scientists to discuss the stress-strain curves. [376] The stress-strain relationship was studied from the stress-strain behavior illustrated by a phenomenological expression suggested by Mooney [377] and Rivlin and Saunders. [378]

$$\frac{\sigma}{\lambda - \lambda^{-2}} = 2(C_1 + C_2\lambda^{-1}) \quad (7.1)$$

where,  $\sigma$  is the applied stress,  $\lambda$  is the extension ratio, and  $C_1$ ,  $C_2$  are the Mooney-Rivlin (MR) constants.

However, the original MR equation does not explain the steep increase at large elongation. It is believed in many publications that the upturn or steep increase in the stress-strain plot of rubbers is frequently attributed to the limited polymer chain extensibility and also to the strain-induced crystallization, especially for natural rubber. [379] Hence, both crystallizable and non-crystallizable rubbers can exhibit a steep increase of elastic force due to the limitation of polymer chain extensibility if the rupture is avoided. Furukawa *et al.* [380] proposed a modified MR equation, based on the assumption of uniform stress rather than uniform strain. The effect of limited chain extensibility was also considered in the aforementioned equation in deriving the stress strain relationship. According to this modified MR equation, one can obtain Eq. 7.2

$$\sigma = 2(C_1 + C_2/\lambda)F(\lambda) \quad (7.2)$$

where, the  $F(\lambda)$  can be denoted as:

$$F(\lambda) = \lambda - \frac{1}{\lambda^2} + \frac{\lambda^3}{3\lambda_m^2} + \dots \quad (7.3)$$

$\lambda_m$  being the maximum extension ratio, i.e.  $\lambda$  at the break point.

It is worth to be noted that at  $\lambda \ll \lambda_m$ , the function  $F(\lambda)$  approaches to  $\lambda - 1/\lambda^2$ , and the Eq. 3 becomes again the original MR equation. According to the modified MR equation, a plot of  $\sigma/F(\lambda)$ , generally known as reduced stress, as a function of inverse extension ratio,  $1/\lambda$ , should yield a linear curve, from which the values of  $C_1$  and  $C_2$  can be obtained from the stress-strain curves. An upturn is observed in unfilled and JF filled NR compounds particularly at high deformations. Unfilled NR exhibits an upturn at high deformations attributed to the phenomenon commonly known as ‘strain-induced crystallization’. However, in JF filled NR compounds, the elongation at which the upturn occurs, decreases with the filler loading. NR/JF-CNT\_20 shows upturn even at lower elongations and this result indicates the presence of some strong interaction between the JF-CNT and the macromolecular rubber chains (Fig. 7.9b).

**Table 3 Physical properties of NR, NR/a-JF and NR/JF-CNT composites**

Mix No. & Properties	E-mod. (MPa)	Mod. (100%) (MPa)	Mod. (200%) (MPa)	Mod. (300%) (MPa)	Tensile Strength (MPa)	Elongation at break (%)	Hardness Shore-A
NR	1.33	0.85	1.33	1.91	10.00	560	42.8
NR/a-JF_10	3.18	1.40	1.70	2.27	14.08	580	56.2
NR/a-JF_20	5.88	1.77	2.00	2.53	9.98	552	60.0
NR/a-JF_30	10.57	2.27	2.44	3.06	8.02	502	63.8
NR/JF-CNT_10	4.00	1.41	1.80	2.47	17.60	636	58.1
NR/JF-CNT_20	7.51	2.45	2.93	3.97	11.92	530	62.2
NR/JF-CNT_30	12.33	2.89	3.33	4.28	9.32	503	65.8

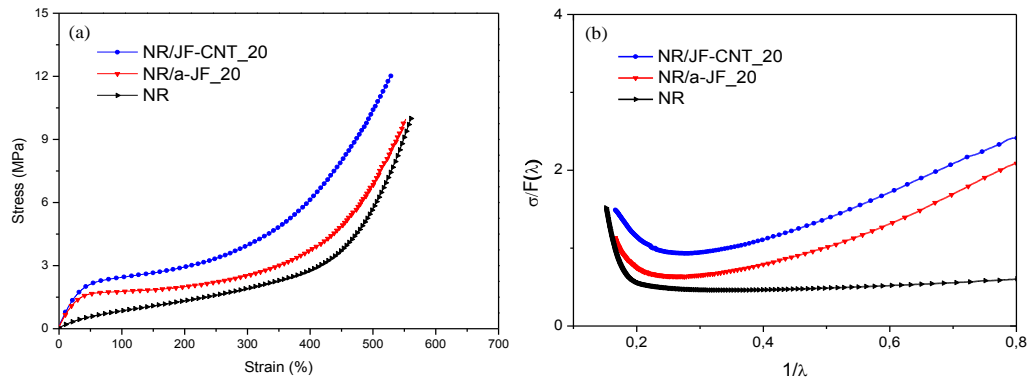


**Fig. 7.9 - (a) Stress-strain behavior and (b) Mooney-Rivlin plot of NR composites reinforced with 20 phr of a-JFs and JF-CNT.**

To understand further the reinforcing mechanism of JF filled NR composites, tensile properties of different systems were analyzed using the Halpin-Tsai composite model. [381] The Halpin-Tsai equation serves as a model in this case since it is accurately utilized to determine the reinforcement effect of incorporated fillers in the composites. Specifically, the elastic modulus of composites filled with fibrous reinforcing particulates is given by the Halpin-Tsai as follows: [381]

$$\frac{E_c}{E_m} = \frac{1+2f\eta\phi}{1-\eta\phi} \quad (7.4)$$

where  $f$  is the aspect ratio,  $\eta = \frac{E_{filler}/E_m - 1}{E_{filler}/E_m + 2f}$  and  $E_{filler}$  the Young's modulus of the filler. For most of the fibrous fillers, the value of  $E_{filler}/E_m$  is  $\sim 10^5$  and  $\eta$  is  $\sim 1$ .

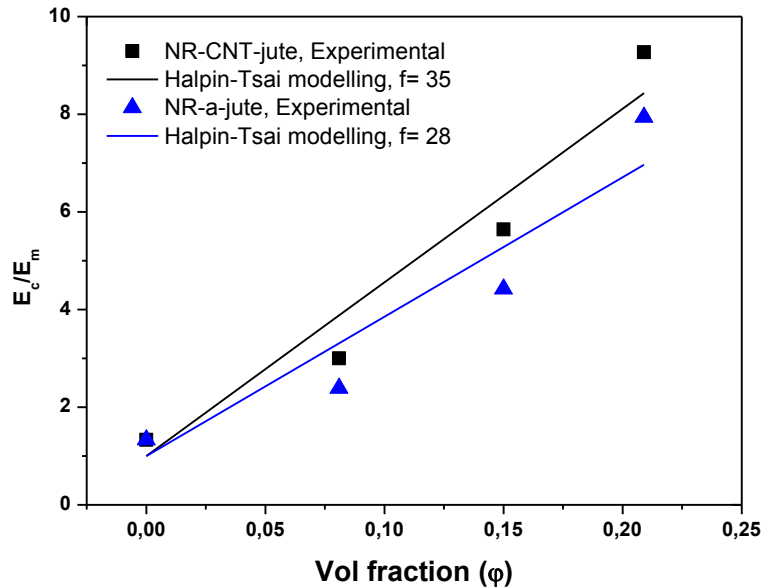


Fig. 7.10 - Modeling of E- modulus using the Halpin-Tsai model.

In this study, the aforesaid H-T model has been utilized to fit the mechanical properties of the NR/JF composites. It has been observed that the H-T equation gives a reasonable fit at low fiber concentration but under-predicts the reinforcement factor at higher filler concentrations. The aspect ratio ( $f$ ), which is a fitting parameter, obtained corresponding to the best fit are 35 and 28, respectively. Similar aspect ratio is also reported elsewhere. [382] Higher aspect ratio is obtained in the case of JF-CNT fillers attributed to a possible better dispersion of these fibers in the NR matrix after modification or the enhanced interfacial strength that the CNT-coating provided. The reinforcement factors ( $E_c/E_m$ ) are

plotted as a function of filler volume fraction ( $\phi$ ) in the Fig.7.10. It is interesting to note that the reinforcement factor is increased with the increase of both a-JF and JF-CNT volume fraction. Nevertheless, this increment in reinforcement factor is more pronounced in the case of NR/JF-CNT compared to NR/ a-JF composites.

### 7.3.7 Dynamic mechanical thermal analysis of NR and NR/JF composites

Dynamic mechanical thermal analysis (DMTA) has been performed to understand the dynamic response of the blend after the addition of JFs. The dependency of storage modulus obtained from oscillatory tension deformation as a function of temperature is given in Fig.7.11a. All samples show a steep decrease of  $E'$  value at the temperature range between  $T = -50$  and  $-20$  °C followed by a rubbery plateau. The most exciting information observed in Fig. 7.11a is the increase of modulus values at room temperature by the addition of JFs. With the increase of JF content, the modulus values also increase but in the case of JF-CNT, the increase is more prominent than the same loading of a-JFs. It has to be mentioned that the good state of dispersion of the JFs into the NR matrix was also a critical parameter for an optimum reinforcing effect of the incorporated fillers. At the glass transition temperature ( $T_g$ ), the stiffness of materials is strongly reduced; the storage modulus decreases strongly and the loss modulus reaches a maximum. When the loss factor  $\tan \delta$  ( $\tan \delta = E''/E'$ ) is plotted versus the temperature, the glass transition temperature is indicated by a peak. Addition of the filler reduces the peak height. The reduction of polymer fraction in a certain volume of the vulcanized rubber (dilution effect) might be the main reason. A strong interaction between the rubber molecules with the filler surface can restrict the movement of the chains and can decrease the peak height. The large variation in the height of the  $\tan \delta$  peaks for the different rubber samples filled with the alkali treated and CNT-coated JFs, clearly suggest different interactions between the NR with each type of JFs used (Figs. 7.11a, 7.11b, 7.11c). Fig.7.11c shows the  $\tan \delta$ -temperature plots of the filled and the gum samples of NR. Addition of JF-CNT reduced more strongly the  $\tan \delta$  peak height than the addition of a-JFs. In order to understand the pronounced effect of JF-CNT on height of the  $\tan \delta$  peak of NR vulcanizates, the plots of  $E'$  and  $E''$  with temperature were considered (Fig. 7.11a, 7.11b). Natural rubber filled with a-JFs shows less increase of  $E'$  value compared to gum whereas NR filled with JF-CNT shows higher increase of  $E'$  value compared to gum above the glass transition temperature.  $E''$  values are also following the same trend throughout the whole temperature range. The reduction of polymer fraction in a certain volume of the vulcanized rubber (dilution effect) might be the main reason.

The strain sweep analysis of a filled and crosslinked rubber can give some information about the filler-filler interaction and rubber-filler interaction. [383] Generally, an unfilled rubber does not show any dependencies of the dynamic modulus with strain, but filled rubber composite shows strong dependencies. At higher strain the filler-filler network is destroyed and the dynamic modulus values are decreased with strain. Fig.7.11d describes the results obtained from strain sweep analysis. As expected the gum rubber did not show any change of the storage modulus with strain but all the filled rubbers showed a strong effect. The higher the fiber content, the higher is the effect. However, the effect of JF-CNT in the filler-filler network is stronger as compared with the a-JFs at same loading. This observation leads to conclude that CNTs remaining on the surface of the fibers are mechanically interlocking two neighbour fiber particles and impart the strong filler-filler networks.

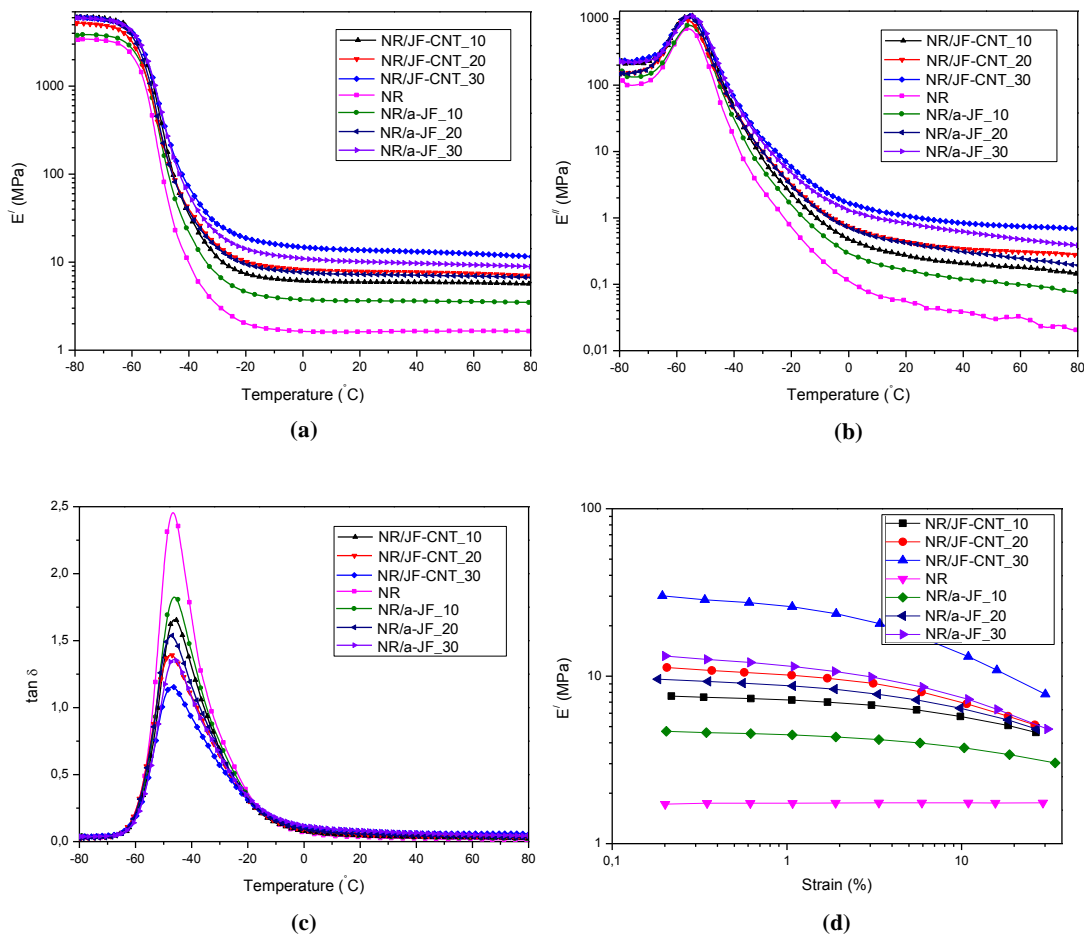


**Fig. 7.11 - Dynamic mechanic thermal analysis of neat NR and NR/JF composites showing  $E'$ ,  $E''$  and loss factor  $\tan \delta$  versus temperature scans (Fig. 7.11a, 7.11b, 7.11c) and the dependency of the dynamic moduli  $E'$  versus strain amplitude measured at room temperature (Fig. 7.11d).**

In conclusion, the introduction of CNT-networks onto the surface of short JFs created a hierarchical structure which showed a promising reinforcing effect in the resulting short fiber reinforced NR composites. The hybrid JF-CNT fillers improved significantly the composite mechanical performance, as revealed by the tensile tests and the dynamic mechanical thermal analysis, via improved wetting of the NR resin as well as the occurring interfacial mechanical interlocking. The excellent interfacial adhesion of CNT-coated JFs with the NR matrix contributes to a significant improvement in tensile strength and tensile modulus at different elongations up to the 20 phr filled compounds. Additionally, a remarkable improvement of the thermal degradation temperature of the NR/JF-CNT hierarchical composites was observed. Raman spectra evaluation supports directly the interaction between CNTs and JFs. The hybrid fillers seem to be the leading effect of the improved mechanical properties offering a satisfactory reinforcing effect to the final NR composites. The application of these novel elastomeric materials could be realized where good mechanical properties of the composites are required at lower loading of fillers. This finding also triggers to develop and design lightweight elastomer products where a good dynamic mechanical performance is a crucial factor for long service life. Namely, the products like truck tyres, conveyor and power transmission belts, engine mounts and vibration dampers could be the items for the application of this high performance elastomeric material based on NR and natural JFs.



## Chapter 8

### General Conclusions and Outlook

In this work, multi-walled carbon nanotubes (MWCNTs) have been deposited onto the surface of fibrous reinforcements (Glass and Jute fibers) via wet chemical methods, resulting in multi-scale hierarchical reinforcements. CNTs in general convert the insulating fibers to semi-conductors, impart a nanoscale roughness increasing the fiber surface area, and they change significantly the fiber surface chemistry endowing with the chemical functionalities that CNTs contain.

Initially, glass fibers were modified with MWCNTs via covalent and non-covalent bonds, and the interfacial mechanical as well as the electrical properties of single fiber/epoxy composites were investigated. This allowed determining the deposition process parameters such as CNT concentration, time of completion for the reaction between CNTs and glass fiber, etc. Single fiber pull-out tests and resistance measurements demonstrated that there is a prominent increase of the interfacial strength and the interphasial conductivity when the CNTs are covalently attached onto the fiber surface. Moreover, the results obtained on single fiber level gave us the opportunity to up scale the chemical methods and modify single glass fiber yarns with CNTs (GF-CNT). A single GF-CNT yarn was incorporated in a uni-directional arrangement within an epoxy matrix, and served as epoxy cure monitoring sensor, integrated UV-detector, and thermal energy harvesting element, giving rise to multi-functional structural composites. Further research is required to increase the thermoelectric efficiency arising actually from the hybrid nanostructured interphases, either by engineering the band gap of CNTs (with different kind of dopants), or modifying the fibers with p- and n-doped CNTs which can facilitate the formation of p/n heterojunction by connecting the fibers in series. Additionally, another possibility that can increase the thermoelectric efficiency is to attach onto the highly conductive CNT networks which cover the fiber surfaces some kind of narrow band gap thermoelectric nanoparticles like for e.g. PbTe or Bi<sub>2</sub>Te<sub>3</sub>.

Having a general image and overview about the impact of CNT-modified glass fibers on the interfacial interactions in model epoxy composites, we extended the idea of CNT deposition by using natural jute fibers. MWCNTs were deposited by a very simple and facile method onto the surface of short jute fibers, and the hybrid fillers exposed a significant interfacial enhancement when incorporated in a natural rubber matrix. This affected further macroscopically the mechanical (static and dynamic) properties of the natural rubber,

making these novel natural-based elastomeric materials appropriate where good mechanical properties are required at lower loading of fillers. This finding also triggers to develop and design lightweight elastomer products where a good dynamic mechanical performance is a crucial factor for long service life. Namely, the products like truck tyres, conveyor and power transmission belts, engine mounts and vibration dampers could be the items for the application of this high performance elastomeric material based on NR and natural JFs. It should be mentioned that it is the first time that CNTs have been introduced onto the surface of jute fibers to act as a macromolecular coupling agent for the enhanced interfacial adhesion with an apolar rubber matrix. In future, higher content of CNTs can be introduced onto the fiber surfaces in order to achieve reasonable electrical conductivity values of the final composites, thus alleviating the well-known problem of viscosity increase during the processing of rubbers with nanoparticulate reinforcements.

Since in this study it has been given a special interest on the utilization of epoxy resins; widely used as a matrix in composite materials, epoxy was blended with a block copolymer. The resulting blends exhibited spherical nanostructured morphology, and appropriate modification of the block copolymer with an ionic liquid endowed with remarkable magnetic properties. It can be easily realised that the novel thermosetting materials could be of great interest to introduce fiber/CNT reinforcements, and investigate both the mechanical as well as the physical properties, i.e electrical conductivity, magnetic response, etc

Finally, due to our interest to synthesize different kind of colloidal particles and stabilize them onto the CNT-coated fibers, silica particles have been decorated with Ag dots and used as SERS substrates as well as redox catalysts. Potential applications of these hybrid colloids when combined together with the hierarchical fiber/CNT structures are under investigation.

## References

- [1] Popov VN. Carbon nanotubes: properties and application. *Materials Science and Engineering: R: Reports*. 2004;43(3):61-102.
- [2] Kroto HW, Heath JR, O'Brien SC, Curl RF, Smalley RE. C<sub>60</sub>: Buckminsterfullerene. *Nature*. 1985;318(6042):162-3.
- [3] Radushkevich L, Lukyanovich V. *Zurn Fisic. Chim* 1952.
- [4] Iijima S. Helical microtubules of graphitic carbon. *Nature*. 1991;354(6348):56-8.
- [5] Meyyappan MIE, In : *Carbon Nanotubes Science and Applications*, Boca Raton London NY, Washington, D.C: CRC Press LLC, Chapter 1, 2005.
- [6] Dresselhaus MS DG, Avouris P. *Carbon nanotubes: synthesis, structure, properties and applications*. Berlin: Springer-Verlag. 2001.
- [7] Thostenson ET, Ren Z, Chou T-W. Advances in the science and technology of carbon nanotubes and their composites: a review. *Composites Science and Technology*. 2001;61(13):1899-912.
- [8] Dresselhaus MS, Dresselhaus G, Saito R. Physics of carbon nanotubes. *Carbon*. 1995;33(7):883-91.
- [9] Terrones M. Science and technology of the twenty-first century: Synthesis, properties and applications of carbon nanotubes. *Annual Review of Materials Research*. 2003;33:419-501.
- [10] Dai H. Carbon nanotubes: opportunities and challenges. *Surface Science*. 2002;500(1-3):218-41.
- [11] Journet C, Maser WK, Bernier P, Loiseau A, de la Chapelle ML, Lefrant S, et al. Large-scale production of single-walled carbon nanotubes by the electric-arc technique. *Nature*. 1997;388(6644):756-8.
- [12] Rinzler AG, Liu J, Dai H, Nikolaev P, Huffman CB, Rodríguez-Macias FJ, et al. Large-scale purification of single-wall carbon nanotubes: process, product, and characterization. *Appl Phys A*. 1998;67(1):29-37.
- [13] Nikolaev P, Bronikowski MJ, Bradley RK, Rohmund F, Colbert DT, Smith KA, et al. Gas-phase catalytic growth of single-walled carbon nanotubes from carbon monoxide. *Chemical Physics Letters*. 1999;313(1-2):91-7.
- [14] Endo M, Takeuchi K, Kobori K, Takahashi K, Kroto HW, Sarkar A. Pyrolytic carbon nanotubes from vapor-grown carbon fibers. *Carbon*. 1995;33(7):873-81.
- [15] Hamada N, Sawada S-i, Oshiyama A. New one-dimensional conductors: Graphitic microtubules. *Physical Review Letters*. 1992;68(10):1579-81.
- [16] Saito R, Fujita M, Dresselhaus G, Dresselhaus MS. Electronic structure of chiral graphene tubules. *Applied Physics Letters*. 1992;60(18):2204-6.
- [17] Mintmire JW, Dunlap BI, White CT. Are fullerene tubules metallic? *Physical Review Letters*. 1992;68(5):631-4.
- [18] Dresselhaus MS, Dresselhaus G, Saito R. Carbon fibers based on C<sub>60</sub> and their symmetry. *Physical Review B*. 1992;45(11):6234-42.
- [19] Tanaka K, Okahara K, Okada M, Yamabe T. Electronic properties of bucky-tube model. *Chemical Physics Letters*. 1992;191(5):469-72.
- [20] Wilder JWG, Venema LC, Rinzler AG, Smalley RE, Dekker C. Electronic structure of atomically resolved carbon nanotubes. *Nature*. 1998;391(6662):59-62.
- [21] *Carbon Nanotubes: Synthesis S, Properties and Applications*; Dresselhaus, M. S.; Dresselhaus GA, Ph., Eds.; Springer: Berlin, 2001.
- [22] Odom TW, Huang J-L, Kim P, Lieber CM. Atomic structure and electronic properties of single-walled carbon nanotubes. *Nature*. 1998;391(6662):62-4.
- [23] Avouris P. Carbon nanotube electronics. *Chemical Physics*. 2002;281(2-3):429-45.
- [24] Liu K, Avouris P, Martel R, Hsu WK. Electrical transport in doped multiwalled carbon nanotubes. *Physical Review B*. 2001;63(16):161404.
- [25] Ebbesen TW, Lezec HJ, Hiura H, Bennett JW, Ghaemi HF, Thio T. Electrical conductivity of individual carbon nanotubes. *Nature*. 1996;382(6586):54-6.
- [26] Qing C, Sheng W, Lian-Mao P. Establishing Ohmic contacts for in situ current-voltage characteristic measurements on a carbon nanotube inside the scanning electron microscope. *Nanotechnology*. 2006;17(4):1087.
- [27] de Heer WA, Châtelain A, Ugarte D. A Carbon Nanotube Field-Emission Electron Source. *Science*. 1995;270(5239):1179-80.
- [28] Bockrath M, Cobden DH, McEuen PL, Chopra NG, Zettl A, Thess A, et al. Single-Electron Transport in Ropes of Carbon Nanotubes. *Science*. 1997;275(5308):1922-5.
- [29] Tans SJ, Verschueren ARM, Dekker C. Room-temperature transistor based on a single carbon nanotube. *Nature*. 1998;393(6680):49-52.
- [30] Kim P, Lieber CM. Nanotube Nanotweezers. *Science*. 1999;286(5447):2148-50.
- [31] Dai H, Hafner JH, Rinzler AG, Colbert DT, Smalley RE. Nanotubes as nanoprobe in scanning probe microscopy. *Nature*. 1996;384(6605):147-50.
- [32] Wong SS, Joselevich E, Woolley AT, Cheung CL, Lieber CM. Covalently functionalized nanotubes as nanometre-sized probes in chemistry and biology. *Nature*. 1998;394(6688):52-5.

- [33] Baughman RH, Cui C, Zakhidov AA, Iqbal Z, Barisci JN, Spinks GM, et al. Carbon Nanotube Actuators. *Science*. 1999;284(5418):1340-4.
- [34] Dillon AC, Jones KM, Bekkedahl TA, Kiang CH, Bethune DS, Heben MJ. Storage of hydrogen in single-walled carbon nanotubes. *Nature*. 1997;386(6623):377-9.
- [35] Rueckes T, Kim K, Joselevich E, Tseng GY, Cheung C-L, Lieber CM. Carbon Nanotube-Based Nonvolatile Random Access Memory for Molecular Computing. *Science*. 2000;289(5476):94-7.
- [36] Choi WB, Chung DS, Kang JH, Kim HY, Jin YW, Han IT, et al. Fully sealed, high-brightness carbon-nanotube field-emission display. *Applied Physics Letters*. 1999;75(20):3129-31.
- [37] Cooper EB, Manalis SR, Fang H, Dai H, Matsumoto K, Minne SC, et al. Terabit-per-square-inch data storage with the atomic force microscope. *Applied Physics Letters*. 1999;75(22):3566-8.
- [38] Kong J, Franklin NR, Zhou C, Chapline MG, Peng S, Cho K, et al. Nanotube Molecular Wires as Chemical Sensors. *Science*. 2000;287(5453):622-5.
- [39] Krishnan A, Dujardin E, Ebbesen TW, Yianilos PN, Treacy MMJ. Young's modulus of single-walled nanotubes. *Physical Review B*. 1998;58(20):14013-9.
- [40] Lu JP. Elastic Properties of Carbon Nanotubes and Nanoropes. *Physical Review Letters*. 1997;79(7):1297-300.
- [41] Popov VN, Van Doren VE, Balkanski M. Elastic properties of single-walled carbon nanotubes. *Physical Review B*. 2000;61(4):3078-84.
- [42] Yu M-F, Lourie O, Dyer MJ, Moloni K, Kelly TF, Ruoff RS. Strength and Breaking Mechanism of Multiwalled Carbon Nanotubes Under Tensile Load. *Science*. 2000;287(5453):637-40.
- [43] Treacy MMJ, Ebbesen TW, Gibson JM. Exceptionally high Young's modulus observed for individual carbon nanotubes. *Nature*. 1996;381(6584):678-80.
- [44] Wong EW, Sheehan PE, Lieber CM. Nanobeam Mechanics: Elasticity, Strength, and Toughness of Nanorods and Nanotubes. *Science*. 1997;277(5334):1971-5.
- [45] Falvo MR, Clary GJ, Taylor RM, Chi V, Brooks FP, Washburn S, et al. Bending and buckling of carbon nanotubes under large strain. *Nature*. 1997;389(6651):582-4.
- [46] Shaffer MSP, Windle AH. Fabrication and Characterization of Carbon Nanotube/Poly(vinyl alcohol) Composites. *Advanced Materials*. 1999;11(11):937-41.
- [47] Zhang X, Liu T, Sreekumar TV, Kumar S, Moore VC, Hauge RH, et al. Poly(vinyl alcohol)/SWNT Composite Film. *Nano Letters*. 2003;3(9):1285-8.
- [48] Cooper CA, Ravich D, Lips D, Mayer J, Wagner HD. Distribution and alignment of carbon nanotubes and nanofibrils in a polymer matrix. *Composites Science and Technology*. 2002;62(7-8):1105-12.
- [49] Bhattacharyya AR, Sreekumar TV, Liu T, Kumar S, Ericson LM, Hauge RH, et al. Crystallization and orientation studies in polypropylene/single wall carbon nanotube composite. *Polymer*. 2003;44(8):2373-7.
- [50] Sandler JKW, Kirk JE, Kinloch IA, Shaffer MSP, Windle AH. Ultra-low electrical percolation threshold in carbon-nanotube-epoxy composites. *Polymer*. 2003;44(19):5893-9.
- [51] Sennett M, Welsh E, Wright JB, Li WZ, Wen JG, Ren ZF. Dispersion and alignment of carbon nanotubes in polycarbonate. *Appl Phys A*. 2003;76(1):111-3.
- [52] Dalton AB, Collins S, Munoz E, Razal JM, Ebron VH, Ferraris JP, et al. Super-tough carbon-nanotube fibres. *Nature*. 2003;423(6941):703-.
- [53] Sreekumar TV, Liu T, Min BG, Guo H, Kumar S, Hauge RH, et al. Polyacrylonitrile Single-Walled Carbon Nanotube Composite Fibers. *Advanced Materials*. 2004;16(1):58-61.
- [54] Banerjee S, Hemraj-Benny T, Wong SS. Covalent Surface Chemistry of Single-Walled Carbon Nanotubes. *Advanced Materials*. 2005;17(1):17-29.
- [55] Sun Y-P, Fu K, Lin Y, Huang W. Functionalized Carbon Nanotubes: Properties and Applications. *Accounts of Chemical Research*. 2002;35(12):1096-104.
- [56] Dyke CA, Tour JM. Covalent Functionalization of Single-Walled Carbon Nanotubes for Materials Applications. *The Journal of Physical Chemistry A*. 2004;108(51):11151-9.
- [57] Fu K, Sun Y-P. Dispersion and Solubilization of Carbon Nanotubes. *Journal of Nanoscience and Nanotechnology*. 2003;3(5):351-64.
- [58] <http://www.cheaptubesinc.com/cntpricelist.htm>.
- [59] Hunter RJI. MCSOUP, USA, 1994.
- [60] Society AC, Bergna HE, Colloid ACSDo, Chemistry S, Meeting ACS. The Colloid Chemistry of Silica: Developed from a Symposium Sponsored by the Division of Colloid and Surface Chemistry, at the 200th National Meeting of the American Chemical Society, Washington, DC, August 26-31, 1990: American Chemical Society; 1994.
- [61] Yu Y-Y, Chen W-C. Transparent organic-inorganic hybrid thin films prepared from acrylic polymer and aqueous monodispersed colloidal silica. *Materials Chemistry and Physics*. 2003;82(2):388-95.
- [62] Hommel H, Touhami A, Legrand AP, Balard H, Papirer E. Segmental mobility of model compounds for rubber reinforcement. *Die Makromolekulare Chemie*. 1993;194(3):879-89.
- [63] Wei Y, Fan LM, Chen LR. Effect of different pore diameter silica based polymer-bonded phases and mobile phase on separation of proteins. *Chromatographia*. 1997;46(11-12):637-40.
- [64] Mathew JP, Srinivasan M. Silica-supported polymer-palladium complexes as catalysts for the reduction of nitro and azo groups. *Polymer International*. 1992;29(3):179-84.

- [65] Mizutani Y, Nagō S. Microporous polypropylene films containing ultrafine silica particles. *Journal of Applied Polymer Science*. 1999;72(11):1489-94.
- [66] Mittal KL, Ed. *Adhesion Aspects of Polymeric Coatings*; Plenum: New York., 1983.
- [67] Brook MASiO, *Organometallic, and Polymer Chemistry*; 1st ed.; Wiley-, Interscience.
- [68] Iler RKTcoss, *polymerization, colloid and surface, properties abW*, , 1979.
- [69] Plueddemann EPScanePP, , 1991.
- [70] Stöber W, Fink A, Bohn E. Controlled growth of monodisperse silica spheres in the micron size range. *Journal of Colloid and Interface Science*. 1968;26(1):62-9.
- [71] Hutter E, Fendler JH. Exploitation of Localized Surface Plasmon Resonance. *Advanced Materials*. 2004;16(19):1685-706.
- [72] Ipe BI, Thomas KG, Barazzouk S, Hotchandani S, Kamat PV. Photoinduced Charge Separation in a Fluorophore–Gold Nanoassembly. *The Journal of Physical Chemistry B*. 2001;106(1):18-21.
- [73] Ghosh SK, Pal T. Interparticle Coupling Effect on the Surface Plasmon Resonance of Gold Nanoparticles: From Theory to Applications. *Chemical Reviews*. 2007;107(11):4797-862.
- [74] El-Sayed MA. Some Interesting Properties of Metals Confined in Time and Nanometer Space of Different Shapes. *Accounts of Chemical Research*. 2001;34(4):257-64.
- [75] Turkevich J. Colloidal gold. Part I. *Gold Bull*. 1985;18(3):86-91.
- [76] Faraday M. The Bakerian Lecture: Experimental Relations of Gold (and Other Metals) to Light. *Philosophical Transactions of the Royal Society of London*. 1857;147:145-81.
- [77] Alivisatos AP. Perspectives on the Physical Chemistry of Semiconductor Nanocrystals. *The Journal of Physical Chemistry*. 1996;100(31):13226-39.
- [78] Kreibig UV, M. . *Optical Properties of Metal Cluster*. Springer Series in Material Science. 1995;Vol 25.
- [79] Link S, El-Sayed MA. Shape and size dependence of radiative, non-radiative and photothermal properties of gold nanocrystals. *International Reviews in Physical Chemistry*. 2000;19(3):409-53.
- [80] Mie G. Contributions to the optics of turbid media, particularly of colloidal metal solutions. *Ann Phys*. 1908;25(3): 377-445.
- [81] Moskovits M. Surface-enhanced spectroscopy. *Reviews of Modern Physics*. 1985;57(3):783-826.
- [82] Vo-Dinh T. Surface-enhanced Raman spectroscopy using metallic nanostructures. *TrAC Trends in Analytical Chemistry*. 1998;17(8–9):557-82.
- [83] Contreras-Cáceres R, Abalde-Cela S, Guardia-Girós P, Fernández-Barbero A, Pérez-Juste J, Alvarez-Puebla RA, et al. Multifunctional Microgel Magnetic/Optical Traps for SERS Ultradetection. *Langmuir*. 2011;27(8):4520-5.
- [84] Fang N, Lee H, Sun C, Zhang X. Sub-Diffraction-Limited Optical Imaging with a Silver Superlens. *Science*. 2005;308(5721):534-7.
- [85] Ebbesen TW, Lezec HJ, Ghaemi HF, Thio T, Wolff PA. Extraordinary optical transmission through sub-wavelength hole arrays. *Nature*. 1998;391(6668):667-9.
- [86] Campion A, Kambhampati P. Surface-enhanced Raman scattering. *Chemical Society Reviews*. 1998;27(4):241-50.
- [87] Johnson PB, Christy RW. Optical Constants of the Noble Metals. *Physical Review B*. 1972;6(12):4370-9.
- [88] Johnson PB, Christy RW. Optical constants of copper and nickel as a function of temperature. *Physical Review B*. 1975;11(4):1315-23.
- [89] Evanoff DD, Chumanov G. Size-Controlled Synthesis of Nanoparticles. 2. Measurement of Extinction, Scattering, and Absorption Cross Sections. *The Journal of Physical Chemistry B*. 2004;108(37):13957-62.
- [90] Evanoff DD, Chumanov G. Synthesis and Optical Properties of Silver Nanoparticles and Arrays. *ChemPhysChem*. 2005;6(7):1221-31.
- [91] Herves P, Perez-Lorenzo M, Liz-Marzan LM, Dzubielia J, Lu Y, Ballauff M. Catalysis by metallic nanoparticles in aqueous solution: model reactions. *Chemical Society Reviews*. 2012;41(17):5577-87.
- [92] Moores A, Goettmann F. The plasmon band in noble metal nanoparticles: an introduction to theory and applications. *New Journal of Chemistry*. 2006;30(8):1121-32.
- [93] Lu X, Rycenga M, Skrabalak SE, Wiley B, Xia Y. Chemical Synthesis of Novel Plasmonic Nanoparticles. *Annual Review of Physical Chemistry*. 2009;60(1):167-92.
- [94] Willets KA, Van Duyne RP. Localized Surface Plasmon Resonance Spectroscopy and Sensing. *Annual Review of Physical Chemistry*. 2007;58(1):267-97.
- [95] Horechyy A. Ordered structures from nanoparticles/Block copolymer hybrids: Ex-situ approaches toward binary and ternary composites, PhD thesis. 2011.
- [96] Link S, El-Sayed MA. Spectral Properties and Relaxation Dynamics of Surface Plasmon Electronic Oscillations in Gold and Silver Nanodots and Nanorods. *The Journal of Physical Chemistry B*. 1999;103(40):8410-26.
- [97] Fleischmann M, Hendra PJ, McQuillan AJ. Raman spectra of pyridine adsorbed at a silver electrode. *Chemical Physics Letters*. 1974;26(2):163-6.
- [98] Séquaris JM, Koglin E. Subnanogram colloid surface-enhanced Raman spectroscopy (SERS) of methylated guanine on silica gel plates. *Z Anal Chem*. 1982;321(8):758-9.
- [99] Moskovits M. Surface selection rules. *The Journal of Chemical Physics*. 1982;77(9):4408-16.

- [100] Moskovits M, Suh JS. Surface selection rules for surface-enhanced Raman spectroscopy: calculations and application to the surface-enhanced Raman spectrum of phthalazine on silver. *The Journal of Physical Chemistry*. 1984;88(23):5526-30.
- [101] Gao X, Davies JP, Weaver MJ. Test of surface selection rules for surface-enhanced Raman scattering: the orientation of adsorbed benzene and monosubstituted benzenes on gold. *The Journal of Physical Chemistry*. 1990;94(17):6858-64.
- [102] Guzonas DA, Irish DE, Atkinson GF. Evidence for a photon-driven charge-transfer enhancement in the surface-enhanced Raman scattering of 1,4-diazabicyclo[2.2.2]octane at a silver electrode. *Langmuir*. 1990;6(6):1102-12.
- [103] Cáceres RC. New hybrid nanoparticles with tuneable optical and magnetic responses for surface enhanced raman spectroscopy (SERS), PhD thesis. 2011.
- [104] Otto A, Mrozek I, Grabhorn H, Akemann W. Surface-enhanced Raman scattering. *Journal of Physics: Condensed Matter*. 1992;4(5):1143.
- [105] Gersten J, Nitzan A. Electromagnetic theory of enhanced Raman scattering by molecules adsorbed on rough surfaces. *The Journal of Chemical Physics*. 1980;73(7):3023-37.
- [106] Gersten JI, Nitzan A. Photophysics and photochemistry near surfaces and small particles. *Surface Science*. 1985;158(1-3):165-89.
- [107] Otto A. Surface-enhanced Raman scattering of adsorbates. *Journal of Raman Spectroscopy*. 1991;22(12):743-52.
- [108] Campion A, Ivanecy JE, Child CM, Foster M. On the Mechanism of Chemical Enhancement in Surface-Enhanced Raman Scattering. *Journal of the American Chemical Society*. 1995;117(47):11807-8.
- [109] Albrecht MG, Creighton JA. Anomalously intense Raman spectra of pyridine at a silver electrode. *Journal of the American Chemical Society*. 1977;99(15):5215-7.
- [110] Sánchez-Gil JA, García-Ramos JV. Calculations of the direct electromagnetic enhancement in surface enhanced Raman scattering on random self-affine fractal metal surfaces. *The Journal of Chemical Physics*. 1998;108(1):317-25.
- [111] Rivas L, Sanchez-Cortes S, García-Ramos JV, Morcillo G. Growth of Silver Colloidal Particles Obtained by Citrate Reduction To Increase the Raman Enhancement Factor. *Langmuir*. 2001;17(3):574-7.
- [112] Moskovits M. Surface-enhanced Raman spectroscopy: a brief retrospective. *Journal of Raman Spectroscopy*. 2005;36(6-7):485-96.
- [113] Kneipp K, Kneipp H, Corio P, Brown SDM, Shafer K, Motz J, et al. Surface-Enhanced and Normal Stokes and Anti-Stokes Raman Spectroscopy of Single-Walled Carbon Nanotubes. *Physical Review Letters*. 2000;84(15):3470-3.
- [114] Pieczonka NPW, Aroca RF. Single molecule analysis by surfaced-enhanced Raman scattering. *Chemical Society Reviews*. 2008;37(5):946-54.
- [115] Braun G, Pavel I, Morrill AR, Seferos DS, Bazan GC, Reich NO, et al. Chemically Patterned Microspheres for Controlled Nanoparticle Assembly in the Construction of SERS Hot Spots. *Journal of the American Chemical Society*. 2007;129(25):7760-1.
- [116] Gunnarsson L, Bjerneld EJ, Xu H, Petronis S, Kasemo B, Käll M. Interparticle coupling effects in nanofabricated substrates for surface-enhanced Raman scattering. *Applied Physics Letters*. 2001;78(6):802-4.
- [117] Grand J, de la Chapelle ML, Bijeon JL, Adam PM, Vial A, Royer P. Role of localized surface plasmons in surface-enhanced Raman scattering of shape-controlled metallic particles in regular arrays. *Physical Review B*. 2005;72(3):033407.
- [118] Grand J, Kostcheev S, Bijeon JL, de la Chapelle ML, Adam PM, Romyantseva A, et al. Optimization of SERS-active substrates for near-field Raman spectroscopy. *Synthetic Metals*. 2003;139(3):621-4.
- [119] Creighton JA, Blatchford CG, Albrecht MG. Plasma resonance enhancement of Raman scattering by pyridine adsorbed on silver or gold sol particles of size comparable to the excitation wavelength. *Journal of the Chemical Society, Faraday Transactions 2: Molecular and Chemical Physics*. 1979;75(0):790-8.
- [120] Lee PC, Meisel D. Adsorption and surface-enhanced Raman of dyes on silver and gold sols. *The Journal of Physical Chemistry*. 1982;86(17):3391-5.
- [121] Brust M, Walker M, Bethell D, Schiffrin DJ, Whyman R. Synthesis of thiol-derivatised gold nanoparticles in a two-phase Liquid-Liquid system. *Journal of the Chemical Society, Chemical Communications*. 1994(7):801-2.
- [122] He S, Yao J, Jiang P, Shi D, Zhang H, Xie S, et al. Formation of Silver Nanoparticles and Self-Assembled Two-Dimensional Ordered Superlattice. *Langmuir*. 2001;17(5):1571-5.
- [123] Wang TC, Rubner MF, Cohen RE. Polyelectrolyte Multilayer Nanoreactors for Preparing Silver Nanoparticle Composites: Controlling Metal Concentration and Nanoparticle Size. *Langmuir*. 2002;18(8):3370-5.
- [124] Zhao YP, Ye DX, Wang GC, Lu TM. Novel Nano-Column and Nano-Flower Arrays by Glancing Angle Deposition. *Nano Letters*. 2002;2(4):351-4.
- [125] Mafuné F, Kohno J-y, Takeda Y, Kondow T, Sawabe H. Structure and Stability of Silver Nanoparticles in Aqueous Solution Produced by Laser Ablation. *The Journal of Physical Chemistry B*. 2000;104(35):8333-7.
- [126] Zhu J, Liu S, Palchik O, Koltypin Y, Gedanken A. Shape-Controlled Synthesis of Silver Nanoparticles by Pulse Sonoelectrochemical Methods. *Langmuir*. 2000;16(16):6396-9.

- [127] Kotov NA, Zaniquelli MED, Meldrum FC, Fendler JH. Two-dimensional silver electrocrystallization under monolayers spread on aqueous silver nitrate. *Langmuir*. 1993;9(12):3710-6.
- [128] Park J, Joo J, Kwon SG, Jang Y, Hyeon T. Synthesis of Monodisperse Spherical Nanocrystals. *Angewandte Chemie International Edition*. 2007;46(25):4630-60.
- [129] Hiramatsu H, Osterloh FE. A Simple Large-Scale Synthesis of Nearly Monodisperse Gold and Silver Nanoparticles with Adjustable Sizes and with Exchangeable Surfactants. *Chemistry of Materials*. 2004;16(13):2509-11.
- [130] Pastoriza-Santos I, Liz-Marzán LM. Formation and Stabilization of Silver Nanoparticles through Reduction by N,N-Dimethylformamide. *Langmuir*. 1999;15(4):948-51.
- [131] Bastys V, Pastoriza-Santos I, Rodríguez-González B, Vaisnoras R, Liz-Marzán LM. Formation of Silver Nanoprisms with Surface Plasmons at Communication Wavelengths. *Advanced Functional Materials*. 2006;16(6):766-73.
- [132] Gupta S, Uhlmann P, Agrawal M, Chapuis S, Oertel U, Stamm M. Immobilization of Silver Nanoparticles on Responsive Polymer Brushes. *Macromolecules*. 2008;41(8):2874-9.
- [133] Liu Z, Wang X, Wu H, Li C. Silver nanocomposite layer-by-layer films based on assembled polyelectrolyte/dendrimer. *Journal of Colloid and Interface Science*. 2005;287(2):604-11.
- [134] Chen C-W, Serizawa T, Akashi M. Synthesis and Characterization of Poly(N-isopropylacrylamide)-Coated Polystyrene Microspheres with Silver Nanoparticles on Their Surfaces†. *Langmuir*. 1999;15(23):7998-8006.
- [135] Lu Y, Mei Y, Drechsler M, Ballauff M. Thermosensitive Core–Shell Particles as Carriers for Ag Nanoparticles: Modulating the Catalytic Activity by a Phase Transition in Networks. *Angewandte Chemie International Edition*. 2006;45(5):813-6.
- [136] Gupta S, Agrawal M, Conrad M, Hutter NA, Olk P, Simon F, et al. Poly(2-(dimethylamino)ethyl methacrylate) Brushes with Incorporated Nanoparticles as a SERS Active Sensing Layer. *Advanced Functional Materials*. 2010;20(11):1756-61.
- [137] Contreras-Caceres R, Dawson C, Formanek P, Fischer D, Simon F, Janke A, et al. Polymers as Templates for Au and Au@Ag Bimetallic Nanorods: UV–Vis and Surface Enhanced Raman Spectroscopy. *Chemistry of Materials*. 2012;25(2):158-69.
- [138] Jiang Z-J, Liu C-Y, Sun L-W. Catalytic Properties of Silver Nanoparticles Supported on Silica Spheres. *The Journal of Physical Chemistry B*. 2005;109(5):1730-5.
- [139] Oldenburg SJ, Hale GD, Jackson JB, Halas NJ. Light scattering from dipole and quadrupole nanoshell antennas. *Applied Physics Letters*. 1999;75(8):1063-5.
- [140] Ung T, Liz-Marzán LM, Mulvaney P. Redox Catalysis Using Ag@SiO<sub>2</sub> Colloids. *The Journal of Physical Chemistry B*. 1999;103(32):6770-3.
- [141] Deng Z, Chen M, Wu L. Novel Method to Fabricate SiO<sub>2</sub>/Ag Composite Spheres and Their Catalytic, Surface-Enhanced Raman Scattering Properties. *The Journal of Physical Chemistry C*. 2007;111(31):11692-8.
- [142] Zhu M, Qian G, Hong Z, Wang Z, Fan X, Wang M. Preparation and characterization of silica–silver core-shell structural submicrometer spheres. *Journal of Physics and Chemistry of Solids*. 2005;66(5):748-52.
- [143] Kobayashi Y, Salgueiriño-Maceira V, Liz-Marzán LM. Deposition of Silver Nanoparticles on Silica Spheres by Pretreatment Steps in Electroless Plating. *Chemistry of Materials*. 2001;13(5):1630-3.
- [144] Hamley IW. *The physics of block copolymers*. Oxford ; New York: Oxford University Press; 1998.
- [145] Abetz V, Simon PW. Phase Behaviour and Morphologies of Block Copolymers. In: Abetz V, ed. *Block Copolymers I*: Springer Berlin Heidelberg 2005, p. 125-212.
- [146] Hadjichristidis N, Pitsikalis M, Iatrou H. Synthesis of Block Copolymers. In: Abetz V, ed. *Block Copolymers I*: Springer Berlin Heidelberg 2005, p. 1-124.
- [147] F. S. Bates and G. H. Fredrickson *ARPC*, 41, 525-557.
- [148] Braunecker WA, Matyjaszewski K. Controlled/living radical polymerization: Features, developments, and perspectives. *Progress in Polymer Science*. 2007;32(1):93-146.
- [149] G. H. Fredrickson and F. S. Bates *ARMS*, 501 (1996).
- [150] Matsen MW, Bates FS. Origins of Complex Self-Assembly in Block Copolymers. *Macromolecules*. 1996;29(23):7641-4.
- [151] Almdal K, Mortensen K, Ryan AJ, Bates FS. Order, Disorder, and Composition Fluctuation Effects in Low Molar Mass Hydrocarbon–Poly(dimethylsiloxane) Diblock Copolymers. *Macromolecules*. 1996;29(18):5940-7.
- [152] Alberda van Ekenstein GOR, Meyboom R, ten Brinke G, Ikkala O. Determination of the Flory–Huggins Interaction Parameter of Styrene and 4-Vinylpyridine Using Copolymer Blends of Poly(styrene-co-4-vinylpyridine) and Polystyrene. *Macromolecules*. 2000;33(10):3752-6.
- [153] Clarke CJ, Eisenberg A, La Scala J, Rafailovich MH, Sokolov J, Li Z, et al. Measurements of the Flory–Huggins Interaction Parameter for Polystyrene–Poly(4-vinylpyridine) Blends. *Macromolecules*. 1997;30(14):4184-8.
- [154] Schulz MF, Khandpur AK, Bates FS, Almdal K, Mortensen K, Hajduk DA, et al. Phase Behavior of Polystyrene–Poly(2-vinylpyridine) Diblock Copolymers. *Macromolecules*. 1996;29(8):2857-67.
- [155] Dai KH, Kramer EJ. Determining the temperature-dependent Flory interaction parameter for strongly immiscible polymers from block copolymer segregation measurements. *Polymer*. 1994;35(1):157-61.

- [156] Zha W, Han CD, Lee DH, Han SH, Kim JK, Kang JH, et al. Origin of the Difference in Order–Disorder Transition Temperature between Polystyrene-block-poly(2-vinylpyridine) and Polystyrene-block-poly(4-vinylpyridine) Copolymers. *Macromolecules*. 2007;40(6):2109-19.
- [157] Castelletto V, Hamley IW. Morphologies of block copolymer melts. *Current Opinion in Solid State and Materials Science*. 2004;8(6):426-38.
- [158] Drzal LT, Madhukar M. Fibre-matrix adhesion and its relationship to composite mechanical properties. *J Mater Sci*. 1993;28(3):569-610.
- [159] Madhukar MS, Drzal LT. Fiber-Matrix Adhesion and Its Effect on Composite Mechanical Properties. III. Longitudinal (0°) Compressive Properties of Graphite/Epoxy Composites. *Journal of Composite Materials*. 1992;26(3):310-33.
- [160] Rotheron RN. Particulate-filled polymer composites. Shawbury: Rapra Technology Limited; 2003.
- [161] Hamerton I. Recent developments in epoxy resins. Shawbury, Shrewsbury: Rapra Technology Ltd.; 1996.
- [162] Hartman D, Greenwood M, Miller D. High strength glass fibers. *Moving Forward With 50 Years of Leadership in Advanced Materials*. 1994;39:521-33.
- [163] Bledzki AK, Faruk O, Huque M. Physico-mechanical studies of wood fiber reinforced composites. *Polymer-Plastics Technology and Engineering*. 2002;41(3):435-51.
- [164] Bledzki AK, Gassan J. Composites reinforced with cellulose based fibres. *Progress in Polymer Science*. 1999;24(2):221-74.
- [165] Youngquist JAIWHWaaEMUS, Department of Agriculture FS, Forest Products Laboratory., Madison W, 1999.
- [166] *Plast Additives Compound 6 JA*, 18-21 (2004).
- [167] Khalil HPSA, Ismail H, Rozman HD, Ahmad MN. The effect of acetylation on interfacial shear strength between plant fibres and various matrices. *European Polymer Journal*. 2001;37(5):1037-45.
- [168] Rong MZ, Zhang MQ, Liu Y, Yang GC, Zeng HM. The effect of fiber treatment on the mechanical properties of unidirectional sisal-reinforced epoxy composites. *Composites Science and Technology*. 2001;61(10):1437-47.
- [169] Mishra S, Naik JB, Patil YP. The compatibilising effect of maleic anhydride on swelling and mechanical properties of plant-fiber-reinforced novolac composites. *Composites Science and Technology*. 2000;60(9):1729-35.
- [170] *Plast Additives Compound 5 JA*, 24-28, (2003).
- [171] Bledzki AK, Faruk O, Sperber VE. Cars from Bio-Fibres. *Macromolecular Materials and Engineering*. 2006;291(5):449-57.
- [172] Bledzki AK, Gassan J, Theis S. Wood-filled thermoplastic composites. *Mech Compos Mater*. 1998;34(6):563-8.
- [173] Ashori A. Wood–plastic composites as promising green-composites for automotive industries! *Bioresource Technology*. 2008;99(11):4661-7.
- [174] Vepa R. Fundamentals of Structural Control. *Dynamics of Smart Structures*: John Wiley & Sons, Ltd 2010, p. 75-116.
- [175] Pocius AV. Adhesion and adhesives technology : an introduction. Munich [u.a.: Hanser; 2002.
- [176] Pascault J-P, Williams RJJ. General Concepts about Epoxy Polymers. *Epoxy Polymers*: Wiley-VCH Verlag GmbH & Co. KGaA 2010, p. 1-12.
- [177] Crosby PA, Powell GR, Fernando GF, France CM, Spooncer RC, Waters DN. In situ cure monitoring of epoxy resins using optical fibre sensors. *Smart Materials and Structures*. 1996;5(4):415.
- [178] Kim JK MYEiifrcNYE, 1998.
- [179] Hoecker F, Karger-Kocsis J. Effects of the interface on the mechanical response of CF/EP microcomposites and macrocomposites. *Composites*. 1994;25(7):729-38.
- [180] *Spectroscopy Volume Two*; Straughan BP, Walker S., Eds.; Chapman and Hall: London, Ed.
- [181] Maiman TH. Stimulated Optical Radiation in Ruby. *Nature*. 1960;187(4736):493-4.
- [182] Nakamoto K. Theory of Normal Vibrations. *Infrared and Raman Spectra of Inorganic and Coordination Compounds*: John Wiley & Sons, Inc. 2008, p. 1-147.
- [183] Kneipp K, Kneipp H, Itzkan I, Dasari RR, Feld MS. Ultrasensitive Chemical Analysis by Raman Spectroscopy. *Chemical Reviews*. 1999;99(10):2957-76.
- [184] Nie S, Emory SR. Probing Single Molecules and Single Nanoparticles by Surface-Enhanced Raman Scattering. *Science*. 1997;275(5303):1102-6.
- [185] Cotton TM, Kim J-H, Chumanov GD. Application of surface-enhanced Raman spectroscopy to biological systems. *Journal of Raman Spectroscopy*. 1991;22(12):729-42.
- [186] Baker G, Moore D. Progress in plasmonic engineering of surface-enhanced Raman-scattering substrates toward ultra-trace analysis. *Anal Bioanal Chem*. 2005;382(8):1751-70.
- [187] Dieringer JA, McFarland AD, Shah NC, Stuart DA, Whitney AV, Yonzon CR, et al. Introductory Lecture Surface enhanced Raman spectroscopy: new materials, concepts, characterization tools, and applications. *Faraday Discussions*. 2006;132(0):9-26.
- [188] Burgess C, Frost T. Standards and Best Practice in Adsorption Spectrometry: Wiley-Blackwell; 1999.
- [189] Reichardt C, Welton T. Solvents and solvent effects in organic chemistry: John Wiley & Sons; 2011.



- [190] Moulder JF, Chastain J, King RC. Handbook of X-ray photoelectron spectroscopy: a reference book of standard spectra for identification and interpretation of XPS data: Physical Electronics Eden Prairie, MN; 1995, 261p.
- [191] Binnig G, Rohrer H, Gerber C, Weibel E. Tunneling through a controllable vacuum gap. *Applied Physics Letters*. 1982;40(2):178-80.
- [192] Datsyuk V, Kalyva M, Papagelis K, Parthenios J, Tasis D, Siokou A, et al. Chemical oxidation of multiwalled carbon nanotubes. *Carbon*. 2008;46(6):833-40.
- [193] Gao C, Jin YZ, Kong H, Whitby RLD, Acquah SFA, Chen GY, et al. Polyurea-Functionalized Multiwalled Carbon Nanotubes: Synthesis, Morphology, and Raman Spectroscopy. *The Journal of Physical Chemistry B*. 2005;109(24):11925-32.
- [194] Lou XD, Detrembleur C, Sciannamea V, Pagnouille C, Jerome R. Grafting of alkoxyamine end-capped (co)polymers onto multi-walled carbon nanotubes. *Polymer*. 2004;45(18):6097-102.
- [195] Lou X, Detrembleur C, Pagnouille C, Jérôme R, Bocharova V, Kiriya A, et al. Surface Modification of Multiwalled Carbon Nanotubes by Poly(2-vinylpyridine): Dispersion, Selective Deposition, and Decoration of the Nanotubes. *Advanced Materials*. 2004;16(23-24):2123-7.
- [196] Wode F, Tzounis L, Kirsten M, Constantinou M, Georgopoulos P, Rangou S, et al. Selective localization of multi-wall carbon nanotubes in homopolymer blends and a diblock copolymer. Rheological orientation studies of the final nanocomposites. *Polymer*. 2012;53(20):4438-47.
- [197] An Y, Chen M, Xue Q, Liu W. Preparation and self-assembly of carboxylic acid-functionalized silica. *Journal of Colloid and Interface Science*. 2007;311(2):507-13.
- [198] Kobayashi S, Hiroishi K, Tokunoh M, Saegusa T. Chelating properties of linear and branched poly(ethylenimines). *Macromolecules*. 1987;20(7):1496-500.
- [199] Yang Z, Lin Y-W, Tseng W-L, Chang H-T. Impacts that pH and metal ion concentration have on the synthesis of bimetallic and trimetallic nanorods from gold seeds. *Journal of Materials Chemistry*. 2005;15(25):2450-4.
- [200] Kalapathy U, Proctor A, Shultz J. A simple method for production of pure silica from rice hull ash. *Bioresource Technology*. 2000;73(3):257-62.
- [201] Lu X, Mi Y. Characterization of the Interfacial Interaction between Polyacrylamide and Silicon Substrate by Fourier Transform Infrared Spectroscopy. *Macromolecules*. 2005;38(3):839-43.
- [202] Sanchez-Cortes S, Berenguel RM, Madejón A, Pérez-Méndez M. Adsorption of Polyethyleneimine on Silver Nanoparticles and Its Interaction with a Plasmid DNA: A Surface-Enhanced Raman Scattering Study. *Biomacromolecules*. 2002;3(4):655-60.
- [203] Nerapusri V, Keddie JL, Vincent B, Bushnak IA. Swelling and Deswelling of Adsorbed Microgel Monolayers Triggered by Changes in Temperature, pH, and Electrolyte Concentration. *Langmuir*. 2006;22(11):5036-41.
- [204] Rodríguez-Fernández J, Pérez-Juste J, García de Abajo FJ, Liz-Marzán LM. Seeded Growth of Submicron Au Colloids with Quadrupole Plasmon Resonance Modes. *Langmuir*. 2006;22(16):7007-10.
- [205] Liou T-H, Chang F-W, Lo J-J. Pyrolysis Kinetics of Acid-Leached Rice Husk. *Industrial & Engineering Chemistry Research*. 1997;36(3):568-73.
- [206] Hildebrandt P, Stockburger M. Surface-enhanced resonance Raman spectroscopy of Rhodamine 6G adsorbed on colloidal silver. *The Journal of Physical Chemistry*. 1984;88(24):5935-44.
- [207] Joseph V, Matschulat A, Polte J, Rolf S, Emmerling F, Kneipp J. SERS enhancement of gold nanospheres of defined size. *Journal of Raman Spectroscopy*. 2011;42(9):1736-42.
- [208] Kim K, Yoon JK. Raman Scattering of 4-Aminobenzenethiol Sandwiched between Ag/Au Nanoparticle and Macroscopically Smooth Au Substrate. *The Journal of Physical Chemistry B*. 2005;109(44):20731-6.
- [209] Su KH, Wei QH, Zhang X, Mock JJ, Smith DR, Schultz S. Interparticle Coupling Effects on Plasmon Resonances of Nanogold Particles. *Nano Letters*. 2003;3(8):1087-90.
- [210] Sánchez-Iglesias A, Aldeanueva-Potel P, Ni W, Pérez-Juste J, Pastoriza-Santos I, Alvarez-Puebla RA, et al. Chemical seeded growth of Ag nanoparticle arrays and their application as reproducible SERS substrates. *Nano Today*. 2010;5(1):21-7.
- [211] Zhang W, Tan F, Wang W, Qiu X, Qiao X, Chen J. Facile, template-free synthesis of silver nanodendrites with high catalytic activity for the reduction of p-nitrophenol. *Journal of Hazardous Materials*. 2012;217-218(0):36-42.
- [212] Gangula A, Podila R, M R, Karanam L, Janardhana C, Rao AM. Catalytic Reduction of 4-Nitrophenol using Biogenic Gold and Silver Nanoparticles Derived from *Breynia rhamnoides*. *Langmuir*. 2011;27(24):15268-74.
- [213] Signori AM, Santos KdO, Eising R, Albuquerque BL, Giacomelli FC, Domingos JB. Formation of Catalytic Silver Nanoparticles Supported on Branched Polyethyleneimine Derivatives. *Langmuir*. 2010;26(22):17772-9.
- [214] Huang X, Xiao Y, Zhang W, Lang M. In-situ formation of silver nanoparticles stabilized by amphiphilic star-shaped copolymer and their catalytic application. *Applied Surface Science*. 2012;258(7):2655-60.
- [215] Yuan J, Wunder S, Warmuth F, Lu Y. Spherical polymer brushes with vinylimidazolium-type poly(ionic liquid) chains as support for metallic nanoparticles. *Polymer*. 2012;53(1):43-9.

- [216] Maity D, Choo S-G, Yi J, Ding J, Xue JM. Synthesis of magnetite nanoparticles via a solvent-free thermal decomposition route. *Journal of Magnetism and Magnetic Materials*. 2009;321(9):1256-9.
- [217] Matsen MW, Thompson RB. *Macromolecules*. 2008;41:1853-60.
- [218] Zhang D, Chung R, Karki AB, Li F, Young DP, Guo Z. *J Phys Chem C*. 2010;114:212-9.
- [219] Diaz L, Santos M, Ballesteros C, Marysko M, Pola J. *J Mater Chem*. 2005;15:4311-7.
- [220] Cao H, Huang G, Xuan S, Wu Q, Gu F, Li C. *J Alloys Compd*. 2008;448:272-6.
- [221] Fan N, Ma X, Ju Z, Li J. *J Mater Res Bull*. 2008;43:1549-54.
- [222] Wei X-W, Zhu G-X, Xia C-J, Ye Y. *Nanotechnology* 2006;17:4307-11.
- [223] Guo Z, Lei K, Li Y, Ng HW, Prikhodko S, Hahn HT. *Compos Sci Technol*. 2008;68:1513-20.
- [224] Gyergyek S, Huskic M, Makovec D, Drogenik M. *Colloids Surf, A*. 2008;317:49-55.
- [225] Baker C, Ismat Shah S, Hasanain SK. *J Magn Magn Mater* 2004;280:412-8.
- [226] Guo Z, Lin H, Karki AB, Wei S, Young DP, Park S, et al. *Compos Sci Technol*. 2008;68:2551-6.
- [227] Garcia I, Tercjak A, Rueda L, Mondragon I. *Macromolecules*. 2008;41:9295-8.
- [228] Garcia I, Tercjak A, Gutierrez J, Rueda L, Mondragon I. *J Phys Chem C*. 2008;112:14343-7
- [229] Garcia I, Ruiz de Luzuriaga A, Grande H, Jeandupeux L, Charmet J, Laux E, et al. *Mater Chem Phys* 2010;124:780-4.
- [230] Binnemans K. *Chem Rev*. 2007;107:2592-614.
- [231] Marcilla R, Curri ML, Cozzoli PD, Martínez MT, Loinaz I, Grande H, et al. *Small* 2006;2:507-12.
- [232] Xie Y, Zhang Z, Jian T, He J, Han B, Wu T, et al. *Angew Chem Int Ed*. 2007;46:7255-8.
- [233] Matsumoto K, Endo TI. *Macromolecules*. 2008;41:6981-6.
- [234] Green O, Grubjesic S, Lee S, Firestone MA. *Polym Rev*. 2009;49:339-60.
- [235] Green MD, Long TE. *Polym Rev*. 2009;49:291-314.
- [236] Hayasi S, Hamaguchi H. *Chem Lett*. 2004;33:1590-1.
- [237] Mallick B, Balke B, Felsler C, A-V. M. *Angew Chem Int Ed*. 2008;47:7635 -8
- [238] Peppel T, Kockerling M, Geppert-Rybczynska M, Ralys RV, Lehmann JK, Verevkin SP, et al. *Angew Chem Int Ed*. 2010;49:7116 -9.
- [239] Mecerreyes D. *Prog Polym Sci*. 2011;36:1629-48.
- [240] Uhrig D, W. MJ. *J Polym Sci Part A: Polym Chem*. 2005;43:6179-222.
- [241] Tsitsilianis C, Sfika V. *Macromol Rapid Commun*. 2001;22:647-51.
- [242] Sung HH, Jin KK. *React Funct Polym*. 2009;69: 493-7.
- [243] Stavrouli ND, Tsitsilianis C, Kiriy A, Gorodyska G, Stamm M. *Journal of Nanostructured Polymers and Nanocomposites*. 2005;1:13-21.
- [244] Hadjichristidis N, Iatrou H, Pispas S, Pitsikalis M. *J Polym Sci Pol Chem*. 2000;38:3211-34.
- [245] Carrasco PM, Ruiz de Luzuriaga A, Constantinou M, Georgopoulos P, Rangou S, Avgeropoulos A, et al. *Macromolecules*. 2011;44:4936-41.
- [246] Dobbelin M, Jovanovski V, Llarena I, Claros Marfil LJ, Cabañero G, Rodriguez J, et al. *Polym Chem* 2011;2:1275-8.
- [247] Carrasco P, Ruiz de Luzuriaga A, Kirsten M, Constantinou M, Georgopoulos P, Rangou S, et al. *J Mater Sci* 2012;47:4348-53.
- [248] Ruiz de Luzuriaga A, Pomposo JA, Grande H, Etxeberria A. *Macromol Rapid Commun*. 2009;30:932-5.
- [249] Joule JA, Mills K. *Heterocyclic chemistry: Willey-Blackwell*; 2010.
- [250] Meng F, Xu Z, Zheng S. *Macromolecules*. 2008;41:1411-20.
- [251] Blanco M, Lopez M, Kortaberria G, Mondragon I. *Polym Int*. 2010;59:523-8.
- [252] Ramos J, Millán A, Palacio F. *Polymer*. 2000;41:8461-4.
- [253] Marcilla R, Blazquez JA, Rodriguez J, Pomposo JA, Mecerreyes D. *J Polym Sci Pol Chem* 2004;41:208-12.
- [254] Baughman RH, Zakhidov AA, de Heer WA. *Carbon Nanotubes--the Route Toward Applications*. *Science*. 2002;297(5582):787-92.
- [255] Ajayan PM, Stephan O, Colliex C, Trauth D. *Aligned Carbon Nanotube Arrays Formed by Cutting a Polymer Resin—Nanotube Composite*. *Science*. 1994;265(5176):1212-4.
- [256] Sandler J, Shaffer MSP, Prasse T, Bauhofer W, Schulte K, Windle AH. *Development of a dispersion process for carbon nanotubes in an epoxy matrix and the resulting electrical properties*. *Polymer*. 1999;40(21):5967-71.
- [257] Li C, Chou T-W. *Electrical Conductivities of Composites with Aligned Carbon Nanotubes*. *Journal of Nanoscience and Nanotechnology*. 2009;9(4):2518-24.
- [258] Ma P-C, Siddiqui NA, Marom G, Kim J-K. *Dispersion and functionalization of carbon nanotubes for polymer-based nanocomposites: A review*. *Composites Part A: Applied Science and Manufacturing*. 2010;41(10):1345-67.
- [259] Chou T-W, Gao L, Thostenson ET, Zhang Z, Byun J-H. *An assessment of the science and technology of carbon nanotube-based fibers and composites*. *Composites Science and Technology*. 2010;70(1):1-19.
- [260] Bekyarova E, Thostenson ET, Yu A, Kim H, Gao J, Tang J, et al. *Multiscale Carbon Nanotube—Carbon Fiber Reinforcement for Advanced Epoxy Composites*. *Langmuir*. 2007;23(7):3970-4.

- [261] Zhang F-H, Wang R-G, He X-D, Wang C, Ren L-N. Interfacial shearing strength and reinforcing mechanisms of an epoxy composite reinforced using a carbon nanotube/carbon fiber hybrid. *J Mater Sci.* 2009;44(13):3574-7.
- [262] Zhang L, Su D, Jin L, Li C. Polyamide 6 composites reinforced with glass fibers modified with electrostatically assembled multiwall carbon nanotubes. *J Mater Sci.* 2012;47(14):5446-54.
- [263] Rahmanian S, Thean KS, Suraya AR, Shazed MA, Mohd Salleh MA, Yusoff HM. Carbon and glass hierarchical fibers: Influence of carbon nanotubes on tensile, flexural and impact properties of short fiber reinforced composites. *Materials & Design.* 2013;43(0):10-6.
- [264] Qian H, Greenhalgh ES, Shaffer MSP, Bismarck A. Carbon nanotube-based hierarchical composites: a review. *Journal of Materials Chemistry.* 2010;20(23):4751-62.
- [265] Kim JK MYIcICT, editor. *Materials science and technology: structure and properties of composites*, 13. Weinheim, Germany: VCH, 1993. p. 229-89, chapter 6.
- [266] Kim J-K, Mai Y-w. High strength, high fracture toughness fibre composites with interface control—A review. *Composites Science and Technology.* 1991;41(4):333-78.
- [267] Drzal L. The interphase in epoxy composites. In: Dušek K, ed. *Epoxy Resins and Composites II*: Springer Berlin Heidelberg 1986, p. 1-32.
- [268] Pisanova E ZSF-rhcIBW, editor. *Performance of plastics*. Cincinnati: Hanser, Munich; 2000. p. 461-518.
- [269] Hull D CTSasis-ftirAitcmCUPp-.
- [270] Zhang J, Zhuang R, Liu J, Mäder E, Heinrich G, Gao S. Functional interphases with multi-walled carbon nanotubes in glass fibre/epoxy composites. *Carbon.* 2010;48(8):2273-81.
- [271] Gao L, Chou T-W, Thostenson ET, Godara A, Zhang Z, Mezzo L. Highly conductive polymer composites based on controlled agglomeration of carbon nanotubes. *Carbon.* 2010;48(9):2649-51.
- [272] Gao L, Chou T-W, Thostenson ET, Zhang Z, Coulaud M. In situ sensing of impact damage in epoxy/glass fiber composites using percolating carbon nanotube networks. *Carbon.* 2011;49(10):3382-5.
- [273] Fan Z, Hsiao K-T, Advani SG. Experimental investigation of dispersion during flow of multi-walled carbon nanotube/polymer suspension in fibrous porous media. *Carbon.* 2004;42(4):871-6.
- [274] Thostenson ET, Li WZ, Wang DZ, Ren ZF, Chou TW. Carbon nanotube/carbon fiber hybrid multiscale composites. *Journal of Applied Physics.* 2002;91(9):6034-7.
- [275] Qian H, Bismarck A, Greenhalgh ES, Kalinka G, Shaffer MSP. Hierarchical Composites Reinforced with Carbon Nanotube Grafted Fibers: The Potential Assessed at the Single Fiber Level. *Chemistry of Materials.* 2008;20(5):1862-9.
- [276] Sager RJ, Klein PJ, Lagoudas DC, Zhang Q, Liu J, Dai L, et al. Effect of carbon nanotubes on the interfacial shear strength of T650 carbon fiber in an epoxy matrix. *Composites Science and Technology.* 2009;69(7-8):898-904.
- [277] Zhu S, Su C-H, Lehoczyk SL, Muntele I, Ila D. Carbon nanotube growth on carbon fibers. *Diamond and Related Materials.* 2003;12(10-11):1825-8.
- [278] Zhao Z-G, Ci L-J, Cheng H-M, Bai J-B. The growth of multi-walled carbon nanotubes with different morphologies on carbon fibers. *Carbon.* 2005;43(3):663-5.
- [279] Riccardis MFD, Carbone D, Makris TD, Giorgi R, Lisi N, Salernitano E. Anchorage of carbon nanotubes grown on carbon fibres. *Carbon.* 2006;44(4):671-4.
- [280] Agnihotri P, Basu S, Kar KK. Effect of carbon nanotube length and density on the properties of carbon nanotube-coated carbon fiber/polyester composites. *Carbon.* 2011;49(9):3098-106.
- [281] Qian H, Bismarck A, Greenhalgh ES, Shaffer MSP. Carbon nanotube grafted silica fibres: Characterising the interface at the single fibre level. *Composites Science and Technology.* 2010;70(2):393-9.
- [282] Lv P, Feng Y-y, Zhang P, Chen H-m, Zhao N, Feng W. Increasing the interfacial strength in carbon fiber/epoxy composites by controlling the orientation and length of carbon nanotubes grown on the fibers. *Carbon.* 2011;49(14):4665-73.
- [283] Gao S-I, Zhuang R-C, Zhang J, Liu J-W, Mäder E. Glass Fibers with Carbon Nanotube Networks as Multifunctional Sensors. *Advanced Functional Materials.* 2010;20(12):1885-93.
- [284] Schaefer JD, Rodriguez AJ, Guzman ME, Lim C-S, Minaie B. Effects of electrophoretically deposited carbon nanofibers on the interface of single carbon fibers embedded in epoxy matrix. *Carbon.* 2011;49(8):2750-9.
- [285] Godara A, Gorbatiikh L, Kalinka G, Warriar A, Rochez O, Mezzo L, et al. Interfacial shear strength of a glass fiber/epoxy bonding in composites modified with carbon nanotubes. *Composites Science and Technology.* 2010;70(9):1346-52.
- [286] He X, Zhang F, Wang R, Liu W. Preparation of a carbon nanotube/carbon fiber multi-scale reinforcement by grafting multi-walled carbon nanotubes onto the fibers. *Carbon.* 2007;45(13):2559-63.
- [287] Laachachi A, Vivet A, Nouet G, Ben Doudou B, Poilâne C, Chen J, et al. A chemical method to graft carbon nanotubes onto a carbon fiber. *Materials Letters.* 2008;62(3):394-7.
- [288] Vivet A, Doudou B, Poilâne C, Chen J, Ayachi MH. A method for the chemical anchoring of carbon nanotubes onto carbon fibre and its impact on the strength of carbon fibre composites. *J Mater Sci.* 2011;46(5):1322-7.

- [289] Zhao F, Huang Y, Liu L, Bai Y, Xu L. Formation of a carbon fiber/polyhedral oligomeric silsesquioxane/carbon nanotube hybrid reinforcement and its effect on the interfacial properties of carbon fiber/epoxy composites. *Carbon*. 2011;49(8):2624-32.
- [290] Peng Q, He X, Li Y, Wang C, Wang R, Hu P, et al. Chemically and uniformly grafting carbon nanotubes onto carbon fibers by poly(amidoamine) for enhancing interfacial strength in carbon fiber composites. *Journal of Materials Chemistry*. 2012;22(13):5928-31.
- [291] Turrión SG, Olmos D, González-Benito J. Complementary characterization by fluorescence and AFM of polyaminosiloxane glass fibers coatings. *Polymer Testing*. 2005;24(3):301-8.
- [292] Shirley DA. High-Resolution X-Ray Photoemission Spectrum of the Valence Bands of Gold. *Physical Review B*. 1972;5(12):4709-14.
- [293] Pisanova E, Zhandarov S, Mäder E, Ahmad I, Young RJ. Three techniques of interfacial bond strength estimation from direct observation of crack initiation and propagation in polymer–fibre systems. *Composites Part A: Applied Science and Manufacturing*. 2001;32(3–4):435-43.
- [294] Doan T-T-L, Brodowsky H, Mäder E. Jute fibre/epoxy composites: Surface properties and interfacial adhesion. *Composites Science and Technology*. 2012;72(10):1160-6.
- [295] Avilés F, Cauch-Rodríguez JV, Moo-Tah L, May-Pat A, Vargas-Coronado R. Evaluation of mild acid oxidation treatments for MWCNT functionalization. *Carbon*. 2009;47(13):2970-5.
- [296] Fan Q, Qin Z, Gao S, Wu Y, Pionteck J, Mäder E, et al. The use of a carbon nanotube layer on a polyurethane multifilament substrate for monitoring strains as large as 400%. *Carbon*. 2012;50(11):4085-92.
- [297] Grossiord N, Loos J, van Laake L, Maugey M, Zakri C, Koning CE, et al. High-Conductivity Polymer Nanocomposites Obtained by Tailoring the Characteristics of Carbon Nanotube Fillers. *Advanced Functional Materials*. 2008;18(20):3226-34.
- [298] Wardle BL, Saito DS, García EJ, Hart AJ, de Villoria RG, Verploegen EA. Fabrication and Characterization of Ultrahigh-Volume- Fraction Aligned Carbon Nanotube–Polymer Composites. *Advanced Materials*. 2008;20(14):2707-14.
- [299] García EJ, Wardle BL, John Hart A, Yamamoto N. Fabrication and multifunctional properties of a hybrid laminate with aligned carbon nanotubes grown In Situ. *Composites Science and Technology*. 2008;68(9):2034-41.
- [300] Pandey G, Deffor H, Thostenson ET, Heider D. Smart tooling with integrated time domain reflectometry sensing line for non-invasive flow and cure monitoring during composites manufacturing. *Composites Part A: Applied Science and Manufacturing*. 2013;47(0):102-8.
- [301] Ooi SK, Cook WD, Simon GP, Such CH. DSC studies of the curing mechanisms and kinetics of DGEBA using imidazole curing agents. *Polymer*. 2000;41(10):3639-49.
- [302] Bowles KJ, Frimpong S. Void Effects on the Interlaminar Shear Strength of Unidirectional Graphite-Fiber-Reinforced Composites. *Journal of Composite Materials*. 1992;26(10):1487-509.
- [303] Soni HK, Patel RG, Patel VS. Structural, physical and mechanical properties of carbon fibre-reinforced composites of diglycidyl ether of bisphenol-A and bisphenol-C. *Die Angewandte Makromolekulare Chemie*. 1993;211(1):1-8.
- [304] Morgan RJ. Structure-property relations of epoxies used as composite matrices. *Epoxy Resins and Composites I: Springer Berlin Heidelberg* 1985, p. 1-43.
- [305] de Almeida SFM, Neto ZdsN. Effect of void content on the strength of composite laminates. *Composite Structures*. 1994;28(2):139-48.
- [306] Lau CH, Hodd KA, Wright WW. Structure and Properties Relationships of Epoxy Resins Part 1: Crosslink Density of Cured Resin: (II) Model Networks Properties. *British Polymer Journal*. 1986;18(5):316-22.
- [307] Hardis R, Jessop JLP, Peters FE, Kessler MR. Cure kinetics characterization and monitoring of an epoxy resin using DSC, Raman spectroscopy, and DEA. *Composites Part A: Applied Science and Manufacturing*. 2013;49(0):100-8.
- [308] Zhang J. Multifunctional composite interphase, PhD thesis. 2012.
- [309] Davis A, Ohn MM, Liu K, Measures RM. Study of an opto-ultrasonic technique for cure monitoring. p. 264-74.
- [310] Perry MJ, Lee LJ, Lee CW. On-Line Cure Monitoring of Epoxy/Graphite Composites Using a Scaling Analysis and a Dual Heat Flux Sensor. *Journal of Composite Materials*. 1992;26(2):274-92.
- [311] Kim J-S, Lee DG. On-line cure monitoring and viscosity measurement of carbon fiber epoxy composite materials. *Journal of Materials Processing Technology*. 1993;37(1–4):405-16.
- [312] St John NA, George GA. Cure kinetics and mechanisms of a tetraglycidyl-4,4'-diaminodiphenylmethane/diaminodiphenylsulphone epoxy resin using near i.r. spectroscopy. *Polymer*. 1992;33(13):2679-88.
- [313] Pyun E, Sung CSP. Network structure in diamine-cured tetrafunctional epoxy by UV-visible and fluorescence spectroscopy. *Macromolecules*. 1991;24(4):855-61.
- [314] Merad L, Cochez M, Margueron S, Jauchem F, Ferriol M, Benyoucef B, et al. In-situ monitoring of the curing of epoxy resins by Raman spectroscopy. *Polymer Testing*. 2009;28(1):42-5.
- [315] An Q, Rider AN, Thostenson ET. Hierarchical Composite Structures Prepared by Electrophoretic Deposition of Carbon Nanotubes onto Glass Fibers. *ACS Applied Materials & Interfaces*. 2013;5(6):2022-32.

- [316] Woo RSC, Chen Y, Zhu H, Li J, Kim J-K, Leung CKY. Environmental degradation of epoxy–organoclay nanocomposites due to UV exposure. Part I: Photo-degradation. *Composites Science and Technology*. 2007;67(15–16):3448–56.
- [317] Çaykara T, Güven O. UV degradation of poly(methyl methacrylate) and its vinyltriethoxysilane containing copolymers. *Polymer Degradation and Stability*. 1999;65(2):225–9.
- [318] Han S, Chung DDL. Through-thickness thermoelectric power of a carbon fiber/epoxy composite and decoupled contributions from a lamina and an interlaminar interface. *Carbon*. 2013;52(0):30–9.
- [319] Vineis CJ, Shakouri A, Majumdar A, Kanatzidis MG. Nanostructured Thermoelectrics: Big Efficiency Gains from Small Features. *Advanced Materials*. 2010;22(36):3970–80.
- [320] Boukai AI, Bunimovich Y, Tahir-Kheli J, Yu J-K, Goddard Iii WA, Heath JR. Silicon nanowires as efficient thermoelectric materials. *Nature*. 2008;451(7175):168–71.
- [321] Tritt TM, Subramanian MA. Thermoelectric Materials, Phenomena, and Applications: A Bird's Eye View. *MRS Bulletin*. 2006;31(03):188–98.
- [322] Baxendale M, Lim KG, Amaratunga GAJ. Thermoelectric power of aligned and randomly oriented carbon nanotubes. *Physical Review B*. 2000;61(19):12705–8.
- [323] Terry MT. Electrical and Thermal Transport Measurement Techniques for Evaluation of the Figure-of-Merit of Bulk Thermoelectric Materials. *Thermoelectrics Handbook: CRC Press* 2005, p. 23–1--0.
- [324] Choi Y, Kim Y, Park S-G, Kim Y-G, Sung BJ, Jang S-Y, et al. Effect of the carbon nanotube type on the thermoelectric properties of CNT/Nafion nanocomposites. *Organic Electronics*. 2011;12(12):2120–5.
- [325] Yu C, Kim YS, Kim D, Grunlan JC. Thermoelectric Behavior of Segregated-Network Polymer Nanocomposites. *Nano Letters*. 2008;8(12):4428–32.
- [326] Moriarty GP, De S, King PJ, Khan U, Via M, King JA, et al. Thermoelectric behavior of organic thin film nanocomposites. *Journal of Polymer Science Part B: Polymer Physics*. 2013;51(2):119–23.
- [327] Yu C, Murali A, Choi K, Ryu Y. Air-stable fabric thermoelectric modules made of N- and P-type carbon nanotubes. *Energy & Environmental Science*. 2012;5(11):9481–6.
- [328] Piao M, Na J, Choi J, Kim J, Kennedy GP, Kim G, et al. Increasing the thermoelectric power generated by composite films using chemically functionalized single-walled carbon nanotubes. *Carbon*. 2013;62(0):430–7.
- [329] Bubnova O, Khan ZU, Malti A, Braun S, Fahlman M, Berggren M, et al. Optimization of the thermoelectric figure of merit in the conducting polymer poly(3,4-ethylenedioxythiophene). *Nat Mater*. 2011;10(6):429–33.
- [330] Guerrero VH, Chung DDL. Enhancement of the absolute thermoelectric power of carbon fiber polymer–matrix composite in the through-thickness direction. *Composite Interfaces*. 2002;9(4):395–401.
- [331] Saq'an S, Zihlif AM, Al-Ani SR, Ragosta G. Thermoelectric power and AC electrical properties of PAN-based carbon fiber composites. *J Mater Sci: Mater Electron*. 2008;19(11):1079–85.
- [332] Dimopoulos A, Buggy SJ, Skordos AA, James SW, Tatam RP, Partridge IK. Monitoring cure in epoxies containing carbon nanotubes with an optical-fiber Fresnel refractometer. *Journal of Applied Polymer Science*. 2009;113(2):730–5.
- [333] Karkanias PI, Partridge IK. Cure modeling and monitoring of epoxy/amine resin systems. I. Cure kinetics modeling. *Journal of Applied Polymer Science*. 2000;77(7):1419–31.
- [334] Abdalla M, Dean D, Robinson P, Nyairo E. Cure behavior of epoxy/MWCNT nanocomposites: The effect of nanotube surface modification. *Polymer*. 2008;49(15):3310–7.
- [335] Pradhan B, Kohlmeyer RR, Setyowati K, Owen HA, Chen J. Advanced carbon nanotube/polymer composite infrared sensors. *Carbon*. 2009;47(7):1686–92.
- [336] Cuong TV, Tien HN, Luan VH, Pham VH, Chung JS, Yoo DH, et al. Solution-processed semitransparent p–n graphene oxide:CNT/ZnO heterojunction diodes for visible-blind UV sensors. *physica status solidi (a)*. 2011;208(4):943–6.
- [337] Gordon JE. *Structure et materiaux: l' explication mecanique des forms PIS*, Paris; 1994.
- [338] Bodros E, Pillin I, Montrelay N, Baley C. Could biopolymers reinforced by randomly scattered flax fibre be used in structural applications? *Composites Science and Technology*. 2007;67(3–4):462–70.
- [339] Mohanty AK, Misra M, Drzal LT. Sustainable Bio-Composites from Renewable Resources: Opportunities and Challenges in the Green Materials World. *Journal of Polymers and the Environment*. 2002;10(1–2):19–26.
- [340] De Rosa IM, Kenny JM, Puglia D, Santulli C, Sarasini F. Morphological, thermal and mechanical characterization of okra (*Abelmoschus esculentus*) fibres as potential reinforcement in polymer composites. *Composites Science and Technology*. 2010;70(1):116–22.
- [341] Peponi L, Biagiotti J, Torre L, Kenny JM, Mondragon I. Statistical analysis of the mechanical properties of natural fibers and their composite materials. I. Natural fibers. *Polymer Composites*. 2008;29(3):313–20.
- [342] Mohanty AK, Misra M, Drzal LT. Surface modifications of natural fibers and performance of the resulting biocomposites: An overview. *Composite Interfaces*. 2001;8(5):313–43.
- [343] Arbelaz A, Cantero G, Fernández B, Mondragon I, Gañán P, Kenny JM. Flax fiber surface modifications: Effects on fiber physico mechanical and flax/polypropylene interface properties. *Polymer Composites*. 2005;26(3):324–32.

- [344] Scarponi C, Pizzinelli CS. Interface and mechanical properties of Natural Fibres reinforced composites: a review. *International Journal of Materials and Product Technology*. 2009;36(1):278-303.
- [345] Doan T-T-L, Gao S-L, Mäder E. Jute/polypropylene composites I. Effect of matrix modification. *Composites Science and Technology*. 2006;66(7–8):952-63.
- [346] Biagiotti J, Fiori S, Torre L, López-Manchado MA, Kenny JM. Mechanical properties of polypropylene matrix composites reinforced with natural fibers: A statistical approach. *Polymer Composites*. 2004;25(1):26-36.
- [347] Yang J, Tian M, Jia Q-X, Shi J-H, Zhang L-Q, Lim S-H, et al. Improved mechanical and functional properties of elastomer/graphite nanocomposites prepared by latex compounding. *Acta Materialia*. 2007;55(18):6372-82.
- [348] Goettler LA, Shen KS. Short Fiber Reinforced Elastomers. *Rubber Chemistry and Technology*. 1983;56(3):619-38.
- [349] Shibulal GS, Naskar K. RFL coated aramid short fiber reinforced thermoplastic elastomer: Mechanical, rheological and morphological characteristics. *J Polym Res*. 2011;18(6):2295-306.
- [350] G. S. Shibulal KN. Exploring a novel multifunctional agent to improve the dispersion of short aramid fiber in polymer matrix. *Express Polymer Letters*. 2012;6(4):329-44.
- [351] Götze T KH, Stöckelhuber KW, Heinrich G. *Kautschuk Gummi Kunststoffe* 2013, in press.
- [352] Hintze C WS, Wagenknecht U, Heinrich G. *Gummi Fasern Kunststoffe* 2012;65:562.
- [353] Sreeja TD, Kutty SKN. Cure Characteristics and Mechanical Properties of Natural Rubber—Short Nylon Fiber Composites. *Journal of Elastomers and Plastics*. 2001;33(3):225-38.
- [354] Senapati AK, Kutty SKN, Pradhan B, Nando GB. Short Polyester Fiber Reinforced Natural Rubber Composites. *International Journal of Polymeric Materials and Polymeric Biomaterials*. 1989;12(3):203-24.
- [355] Shibulal GS, Naskar K. Scrutinizing the influence of strain-induced fiber orientation on the melt rheological behavior of short aramid fiber/thermoplastic elastomer composite using rubber process analyzer. *Journal of Applied Polymer Science*. 2013;128(6):4151-63.
- [356] Lopattananon N, Panawarangkul K, Sahakaro K, Ellis B. Performance of pineapple leaf fiber–natural rubber composites: The effect of fiber surface treatments. *Journal of Applied Polymer Science*. 2006;102(2):1974-84.
- [357] Chakraborty SK, Setua DK, De SK. Short Jute Fiber Reinforced Carboxylated Nitrile Rubber. *Rubber Chemistry and Technology*. 1982;55(5):1286-307.
- [358] Geethamma VG, Thomas Mathew K, Lakshminarayanan R, Thomas S. Composite of short coir fibres and natural rubber: effect of chemical modification, loading and orientation of fibre. *Polymer*. 1998;39(6–7):1483-91.
- [359] Ismail H, Shuhelmy S, Edyham MR. The effects of a silane coupling agent on curing characteristics and mechanical properties of bamboo fibre filled natural rubber composites. *European Polymer Journal*. 2002;38(1):39-47.
- [360] Jacob M, Thomas S, Varughese KT. Mechanical properties of sisal/oil palm hybrid fiber reinforced natural rubber composites. *Composites Science and Technology*. 2004;64(7–8):955-65.
- [361] Murty VM, De SK. Effect of particulate fillers on short jute fiber-reinforced natural rubber composites. *Journal of Applied Polymer Science*. 1982;27(12):4611-22.
- [362] Gassan J, Bledzki AK. Possibilities for improving the mechanical properties of jute/epoxy composites by alkali treatment of fibres. *Composites Science and Technology*. 1999;59(9):1303-9.
- [363] Mwaikambo LY, Ansell MP. Chemical modification of hemp, sisal, jute, and kapok fibers by alkalization. *Journal of Applied Polymer Science*. 2002;84(12):2222-34.
- [364] García-Hernández E, Licea-Claverie A, Zizumbo A, Alvarez-Castillo A, Herrera-Franco PJ. Improvement of the interfacial compatibility between sugar cane bagasse fibers and polystyrene for composites. *Polymer Composites*. 2004;25(2):134-45.
- [365] Montazeri A, Javadpour J, Khavandi A, Tcharkhtchi A, Mohajeri A. Mechanical properties of multi-walled carbon nanotube/epoxy composites. *Materials & Design*. 2010;31(9):4202-8.
- [366] Suryasarathi B, Arup RB, Rupesh AK, Ajit RK, Patro TU, Sivaraman P. Tuning the dispersion of multiwall carbon nanotubes in co-continuous polymer blends: a generic approach. *Nanotechnology*. 2008;19(33):335704.
- [367] An F, Lu C, Li Y, Guo J, Lu X, Lu H, et al. Preparation and characterization of carbon nanotube-hybridized carbon fiber to reinforce epoxy composite. *Materials & Design*. 2012;33(0):197-202.
- [368] Shazed MA, Suraya AR, Rahmanian S, Mohd Salleh MA. Effect of fibre coating and geometry on the tensile properties of hybrid carbon nanotube coated carbon fibre reinforced composite. *Materials & Design*. 2014;54(0):660-9.
- [369] Tasis D, Mikroyannidis J, Karoutsos V, Galiotis C, Papagelis K. Single-walled carbon nanotubes decorated with a pyrene–fluorenevinylene conjugate. *Nanotechnology*. 2009;20(13):135606.
- [370] Sever K, Seki Y, Tavman IH, Erkan G, Cecen V. The structure of  $\gamma$ -glycidoxypropyltrimethoxysilane on glass fiber surfaces: Characterization by FTIR, SEM, and contact angle measurements. *Polymer Composites*. 2009;30(5):550-8.
- [371] Liu Y, Wang X, Qi K, Xin JH. Functionalization of cotton with carbon nanotubes. *Journal of Materials Chemistry*. 2008;18(29):3454-60.

- [372] Rooj S, Das A, Stöckelhuber KW, Mukhopadhyay N, Bhattacharyya AR, Jehnichen D, et al. Pre-intercalation of long chain fatty acid in the interlayer space of layered silicates and preparation of montmorillonite/natural rubber nanocomposites. *Applied Clay Science*. 2012;67–68(0):50-6.
- [373] Poikelispää M, Das A, Dierkes W, Vuorinen J. The effect of partial replacement of carbon black by carbon nanotubes on the properties of natural rubber/butadiene rubber compound. *Journal of Applied Polymer Science*. 2013;130(5):3153-60.
- [374] Byers JT. Fillers for Balancing Passenger Tire Tread Properties. *Rubber Chemistry and Technology*. 2002;75(3):527-48.
- [375] Rooj S, Das A, Morozov IA, Stöckelhuber KW, Stoczek R, Heinrich G. Influence of “expanded clay” on the microstructure and fatigue crack growth behavior of carbon black filled NR composites. *Composites Science and Technology*. 2013;76(0):61-8.
- [376] Bhattacharyya S, Sinturel C, Bahloul O, Saboungi M-L, Thomas S, Salvétat J-P. Improving reinforcement of natural rubber by networking of activated carbon nanotubes. *Carbon*. 2008;46(7):1037-45.
- [377] Mooney M. A Theory of Large Elastic Deformation. *Journal of Applied Physics*. 1940;11(9):582-92.
- [378] Rivlin RS, Saunders DW. Large Elastic Deformations of Isotropic Materials. VII. Experiments on the Deformation of Rubber. *Philosophical Transactions of the Royal Society of London Series A, Mathematical and Physical Sciences*. 1951;243(865):251-88.
- [379] Qu L, Huang G, Liu Z, Zhang P, Weng G, Nie Y. Remarkable reinforcement of natural rubber by deformation-induced crystallization in the presence of organophilic montmorillonite. *Acta Materialia*. 2009;57(17):5053-60.
- [380] Furukawa J, Onouchi Y, Inagaki S, Okamoto H. Rubber elasticity at very large elongation. *Polymer Bulletin*. 1982;6(7):381-7.
- [381] Guzmán de Villoria R, Miravete A. Mechanical model to evaluate the effect of the dispersion in nanocomposites. *Acta Materialia*. 2007;55(9):3025-31.
- [382] Soykeabkaew N, Supaphol P, Rujiravanit R. Preparation and characterization of jute- and flax-reinforced starch-based composite foams. *Carbohydrate Polymers*. 2004;58(1):53-63.
- [383] Das A, Mahaling RN, Stöckelhuber KW, Heinrich G. Reinforcement and migration of nanoclay in polychloroprene/ethylene–propylene–diene–monomer rubber blends. *Composites Science and Technology*. 2011;71(3):276-81.

## Full list of publications and contribution to conferences

### Publications

1. F. Wode, **L. Tzounis**, M. Kirsten, M. Constantinou, P. Georgopoulos, S. Rangou, N. E. Zafeiropoulos, A. Avgeropoulos, M. Stamm. Selective Localization of Multi-Wall Carbon Nanotubes in Homopolymer Blends and a Diblock Copolymer. Rheological Orientation Studies of the Final Nanocomposites. *Polymer* 2012;53(20):4438-47.
2. P. M. Carrasco, **L. Tzounis**, F. J. Mompean, K. Strati, P. Georgopoulos, M. Garcia-Hernandez, M. Stamm, G. Cabañero, I. Odriozola, A. Avgeropoulos, I. Garcia. Thermoset Magnetic Materials Based on Poly(ionic liquid)s Block Copolymers. *Macromolecules* 2013;46(5):1860-67.
3. M. Liebscher, **L. Tzounis**, P. Pötschke, G. Heinrich. Influence of the viscosity ratio in PC/SAN blends filled with MWCNTs on the morphological, electrical, and melt rheological properties. *Polymer* 2013;54(25):6801-08.
4. **L. Tzounis**, S. Debnath, S. Rooj, D. Fischer, E. Mäder, A. Das, M. Stamm, G. Heinrich. High performance natural rubber composites with a hierarchical reinforcement structure of CNT-modified natural fibers. *Materials & Design* 2014;58:1-11.
5. **L. Tzounis**, M. Kirsten, F. Simon, E. Mäder, M. Stamm. The interphase microstructure and electrical properties of glass fibers covalently and non-covalently bonded with multiwall carbon nanotubes. *accepted from Carbon*
6. **L. Tzounis**, R. Contreras-Caceres, L. Schellkopf, D. Jehnichen, D. Fischer, C. Cai, P. Uhlmann, M. Stamm. Controlled growth of silver nanoparticles decorated onto the surface of silica spheres: A nanohybrid system with combined SERS and catalytic properties. *accepted from RSC Advances*
7. **L. Tzounis**, M. Liebscher, F. Simon, E. Mäder, M. Stamm. MWCNT-grafted glass fiber yarns as a smart tool for the epoxy cure monitoring, UV-sensing and thermal energy harvesting. *under preparation*
8. **L. Tzounis**, F. Simon, E. Mäder, M. Stamm. Thermoelectric properties of glass fiber-MWCNT hierarchical reinforcements and their epoxy composites: Effect of the MWCNT loading. *under preparation*
9. M. Liebscher, T. Gärtner, **L. Tzounis**, W. Jenschke, D. Fischer, P. Pötschke, M. Stamm, B. Voit, G. Heinrich. Influence of the MWCNT functional groups on the thermoelectric properties of melt-mixed PC/CNT composites. *under preparation*



10. **L. Tzounis**, T. Gärtner, M. Liebscher, D. Fischer, P. Pötschke, M. Stamm, B. Voit, G. Heinrich. The effect of a cyclic oligomer additive on the thermoelectric properties of Polycarbonate/CNT nanocomposites prepared by melt-mixing. *under preparation*
11. **L. Tzounis**, S. Debnath, S. Rooj, D. Fischer, E. Mäder, A. Das, M. Stamm, G. Heinrich. Natural rubber reinforced with multi-scale natural resources: A synergetic effect of short jute fibers and montmorillonite nanoclays. *under preparation*

### **Conferences**

1. **L. Tzounis**, M. Kirsten, E. Mäder, M. Stamm. Study of the surface morphology and electrical properties of glass fibers covalently and non-covalently bonded with MWCNTs. 7<sup>th</sup> International Conference on nanostructured polymers and nanocomposites. Prague, Czech Republic, 2012 (poster presentation)
2. **L. Tzounis**, E. Mäder, M. Stamm. Surface morphologies and interfacial characteristics of glass fibers covalently and non-covalently bonded with MWCNTs. Decoration of SiO<sub>2</sub> nanoparticles onto the grafted CNT-networks. International Workshop on nanocarbon composites - From fundamental to industrial applications. Valencia, Spain, 2012 (poster presentation)
3. L. Casaban, **L. Tzounis**, M. Kirsten, P. M. Carrasco, I. Garcia, M. Stamm, J. M. Kenny. Orientation and alignment of Block Copolymers (BCPs)/Carbon nanotubes (CNTs) in thermosetting epoxy resins. International Workshop on nanocarbon composites - From fundamental to industrial applications. Valencia, Spain, 2012 (poster presentation)
4. **L. Tzounis**, M. Stamm. Transparent and electrically conductive MWCNT thin films grafted to SiO<sub>2</sub> substrates for sensoric applications. 10<sup>th</sup> IPF Colloquium on Functional Polymers and Composites for Applications in Organic Electronics and Sensorics (combined with the Industrial Workshop of the European Centre for Nanostructured Polymers, ECNP). Dresden, Germany, 2012 (poster presentation)
5. G. He, D. Pospiech, D. Jehnichen, A. Janke, P. Friedel, **L. Tzounis**, M. Stamm, B. Voit. Au NPs Modified Inorganic/Organic Hybrids Thin Films Based on PPMA-b-PMMA. Third International Conference on Multifunctional, Hybrid and Nanomaterials (Hybrid Materials 2013). Sorrento, Italy, 2013 (oral presentation)
6. **L. Tzounis**, F. Simon, E. Mäder, M. Stamm. CNT-based nanostructured glass fiber coatings for novel composites with multi-functional interphases. Eurofillers 2013 – 10<sup>th</sup> anniversary meeting. Bratislava, Slovakia, 2013 (oral presentation)

7. M. Liebscher, **L. Tzounis**, W. Jenschke, M. T. Müller, M. Stamm, P. Pötschke. Thermoelectric energy harvesting with highly conductive CNT-filled polycarbonate composites prepared by melt-mixing. 6<sup>th</sup> International Conference on Carbon Nanoparticle Based Composites (CNPComp2013). Dresden, Germany, 2013 (poster presentation)
8. D. Fischer, H. Kreyenschulte, M. Liebscher, V. S. Raman, A. Das, **L. Tzounis**. Raman spectroscopy and Raman imaging applications for the investigation of carbon based polymer composites. 6<sup>th</sup> International Conference on Carbon Nanoparticle Based Composites (CNPComp2013). Dresden, Germany, 2013 (oral presentation)
9. M. Liebscher, **L. Tzounis**, P. Pötschke. Variation of the viscosity ratio of PC / SAN blends with MWCNTs: Investigation on morphology, electrical and rheological properties. 6<sup>th</sup> International Conference on Carbon Nanoparticle Based Composites (CNPComp2013). Dresden, Germany, 2013 (oral presentation)
10. **L. Tzounis**, E. Mäder, M. Stamm. Hybrid nanostructured interphases of glass fiber polymer composites with unique mechanical and electrical properties. 6<sup>th</sup> International Conference on Carbon Nanoparticle Based Composites (CNPComp2013). Dresden, Germany, 2013 (poster presentation; **winner of the first poster award**)

## VERSICHERUNG

Hiermit versichere ich, dass ich die vorliegende Arbeit ohne unzulässige Hilfe Dritter und ohne Benutzung anderer als der angegebenen Hilfsmittel angefertigt habe; die aus fremden Quellen direkt oder indirekt übernommenen Gedanken sind als solche kenntlich gemacht. Die Arbeit wurde bisher weder im Inland noch im Ausland in gleicher oder ähnlicher Form einer anderen Prüfungsbehörde vorgelegt.

Die Dissertation wurde in der Zeit von December 2010 bis Januar 2014 unter der Betreuung von Herrn Prof. Dr. Manfred Stamm am Leibniz-Institut für Polymerforschung Dresden e.V. in der Abteilung Nanostrukturierte Materialien angefertigt. Es haben keine früheren erfolglosen Promotionsverfahren stattgefunden. Ich erkenne die Promotionsordnung der Fakultät Mathematik und Naturwissenschaften an der Technischen Universität Dresden von 01. April 2011 an.

---

Datum

---

Unterschrift